THÈSE

En vue de l'obtention du

DOCTORAT DE L'UNIVERSITÉ DE TOULOUSE

Délivré par : *l'Université Toulouse 3 Paul Sabatier (UT3 Paul Sabatier)*

Présentée et soutenue le *06/12/2017* **par :**

HANNAH WEHR

Modélisation 3D des Pyrénées à partir des données géologiques, gravimétriques et sismiques

---

JURY

SÉBASTIEN CHEVROT	Directeur de Recherche	Directeur de thèse
GUILLAUME CAUMON	Professeur	Rapporteur
FLORIAN WELLMANN	Professeur	Rapporteur
HÉLÈNE LYON-CAEN	Directrice de Recherche	Rapporteure
GYÖRGY HÉTÉNYI	Professeur	Examinateur
FRÉDÉRIC MOUTHEREAU	Professeur	Président
GABRIEL COURRIOUX	Chercheur	Invité
ROLAND MARTIN	Directeur de Recherche	Invité

École doctorale et spécialité :
SDU2E : Sciences de la Terre et des Planètes Solides
Unité de Recherche :
Géosciences Environnement Toulouse (GET - UMR 5563)
Directeur de Thèse :
Sébastien CHEVROT

Résumée Un modèle géologique tridimensionnel des Pyrénées et de leurs bassins d'avant-pays est construit avec le logiciel `GeoModeller`. Ce modèle tient compte de toutes les informations géologiques et géophysiques disponibles et couvre l'ensemble des Pyrénées, de l'Océan Atlantique à la Méditerranée, et du Système Ibérique au Massif Central, jusqu'à une profondeur de 70 km. La structure géologique est modelée avec une pile stratigraphique composée de couches superposées représentant le manteau, la croûte inférieure, moyenne, et supérieure ainsi que les sédiments. Les bassins sédimentaires sont décrits par deux couches afin de distinguer entre les sédiments consolidés mésozoïques et les sédiments cénozoïques non consolidés. Comme les Pyrénées résultent de la convergence entre les plaques ibérique et européenne, chaque plaque a sa propre colonne stratigraphique. Ceci permet la modélisation de l'indentation et la superposition des croûtes ibériques et européennes. En outre, deux unités supplémentaires décrivant le prisme d'accrétion et la colonne d'eau dans le Golfe de Gascogne et dans la mer Méditerranée sont introduites. Le dernier ingrédient est une unité qui représente les corps du manteau serpentinisé, peu profond et exhumé, qui sont supposés de produire les anomalies positives de Bouguer observées sous la Zone Nord-Pyrénéene. Un premier modèle 3D est construit en utilisant uniquement l'information géologique provenant de cartes géologiques, des relevés de forage et des sections sismiques. L'interpolation entre ces données géologiques est réalisée avec la méthode des champs potentiels implémentée dans `GeoModeller`. Afin de mieux expliquer les anomalies gravimétriques de Bouguer observées, le modèle est ensuite raffiné en ajoutant de nouvelles contraintes sur les principales interfaces lithologiques par essai/erreur. Le modèle final explique les anomalies Bouguer observées avec des erreurs inférieures à 3.5 mGal.

Les caractéristiques principales du modèle géologique sont la subduction de la croûte ibérique dans les Pyrénées occidentales et centrales et les corps de manteau exhumés à une profondeur de ∼12 km dans la zone de l'ouest et du centre de la zone pyrénéenne du nord. À l'est, aucune subduction ne peut être observée et un corps de faible densité est nécessaire pour reproduire les anomalies Bouguer négatives dans la Zone Axiale orientale.

Les temps de trajet des ondes P et S sont modélisés avec le modèle 3D. Pour cela, les densités utilisées pour la modélisation des anomalies de Bouguer sont converties en vitesses des ondes P. Les données régionales des temps d'arrivée révèlent un rapport v_P/v_S de 1,71. Les temps de trajet prédits du modèle 3D sont conformes avec les données observées, avec un écart type de 0,5 s (0,7 s pour les ondes S), et valident ainsi le modèle.

Le modèle géologique 3D est utilisé comme modèle a priori dans une inversion stochastique conjointe des données géologiques, gravimétriques et sismiques. Pour celà, un module permettant l'inversion des données sismiques est implémentée dans `GeoModeller`.

Les résultats révèlent la nécessité d'ajouter d'autres contraintes dans l'inversion, comme une matrice de covariance pour lisser le modèle ou une fonction de pénalité sur la norme du modèle pour pénaliser des perturbations trop fortes et stabiliser l'inversion. L'inversion des données sismiques avec `GeoModeller` n'ayant pas donné de résulats satisfaisants, nous avons réalisé des inversions directes basés sur la méthode LSQR. Dans ces nouvelles inversions, les hétérogénéités proches de la surface sont bien résolues, que l'on utilise le modèle 3D, ou le modèle tabulaire comme modèle a priori. Cependant, les anomalies plus profondes sont mieux résolues en utilisant le modèle a-priori 3D. L'inversion des donnés gravimétriques localise l'anomalie négative qui est nécessaire pour expliquer les anomalies de Bouguer à l'est des Pyrénées dans les 15 premiers kilomètres en utilisant une grille régulière avec des blocs de faible épaisseur, mais à des profondeurs plus grandes lorsque les épaisseurs de blocs augmentent avec la profondeur. L'inversion LSQR ne révèle aucune anomalie de grande échelle dans la zone axiale orientale, comme prévu par la modélisation des anomalies de Bouguer. Ceci indique que l'anomalie pourrait être située plus profondément, à un niveau mal résolu par l'inversion.

Summary A three-dimensional geological model of the Pyrenees and their foreland basins is constructed with the `GeoModeller` software. This model accounts for all available geological and geophysical information and covers the whole Pyrenees, from the Atlantic Ocean to the Mediterranean Sea, and from the Iberian Range to the Massif Central, down to 70 km depth. The geological structure is modeled with a stratigraphic pile composed of superposed layers representing the mantle, lower, middle, and upper crust, and sediments. The sedimentary basins are described by two layers in order to make the distinction between the Mesozoic consolidated sediments and the Cenozoic unconsolidated sediments. Since the Pyrenees result from the convergence between the Iberian and European plates, each plate has its own stratigraphic column. This allows the modeling of the indentation and superposition of the Iberian and European crusts. Moreover, two additional units describing the accretionary prism and the water column in the Bay of Biscay and in the Mediterranean Sea are introduced. The last ingredient is a unit representing the bodies of shallow exhumed, serpentinized mantle, which are assumed to produce the positive gravity Bouguer anomalies observed in the North Pyrenean Zone. A first 3D model is built using only geological information coming from geological maps, drill-hole surveys, and seismic sections. The interpolation between these geological data is performed with the potential field method implemented in `GeoModeller`. In order to better explain the observed gravimetric Bouguer anomalies, the model is then refined by adding new constraints on the main lithological interfaces by trial-and-error. The final model explains the observed Bouguer anomalies within errors less than 3.5 mGal.

The main features of the geological model are the subduction of the Iberian crust in the western and central Pyrenees and the exhumed mantle bodies at ∼12 km depth in the western and central North Pyrenean Zone. In the east, no subduction can be observed, and a low density body is needed to reproduce the negative Bouguer anomalies in the eastern Axial Zone.

Seismic P and S wave travel times are predicted with the 3D model. For this, the densities used for gravity modeling are converted into seismic P wave velocities, but velocities of the crustal units have to be modified in order to obtain better travel time residuals. Regional seismic travel time data reveal a v_P/v_S ratio of 1.71. Predicted travel times agree with the observed data within a standard deviation of 0.5 s (0.7 s for S waves) and thus validate the model.

The 3D geological model is used as an a-priori model in stochastic gravimetric and seismic inversions performed with `GeoModeller`. However, the results reveal the necessity of implementing further constraints, such as a covariance matrix for smoothing or a penalty function on the model norm to prevent too strong perturbations. Since seismic inversion in `GeoModeller` does not yield satisfying results, we also perform direct inversion with the LSQR method. In these new inversions, near-surface heterogeneities are well resolved, either starting from the 3D model or from a 1D layered model. Deeper anomalies, however, are better resolved with the 3D a-priori model. Gravity inversion in a regular grid with a small cell thickness localizes the low-density body needed in the eastern Pyrenees in the uppermost 15 km. Using a grid with block thicknesses increasing with depth, however, localizes it at greater depths. The LSQR inversion does not reveal any large-scale low-velocity anomaly in the eastern Axial Zone, as expected from gravity modeling. This indicates that the anomaly might be located deeper, at a depth that cannot be resolved by the seismic data set.

Acknowledgments

I thank my supervisor Sébastien Chevrot for offering me the chance to work on this thesis. He introduced me to the world of seismic inversion and sustained me during the three years. My deep gratitude goes to Gabriel Courrioux and Antonio Guillen, for introducing me to the `GeoModeller` software and for the close collaboration during the compilation of the 3D geological model and the implementation of seismic inversion. I thank Christelle Loiselet and the BRGM 3D working group for the fruitful discussions and for making me feel like being one of them during my stays at Orléans. Finally, I deeply thank my husband, who did not only encourage me to go abroad for this thesis but who followed me and stayed here with me despite of all the difficulties the French Administration held for him.

Contents

List of Figures

List of Tables

Chapter 1

Introduction

Contents

1.1 Introduction (French)

Cette thèse s'inscrit dans le cadre du RGF (Référentiel Géologique de la France[1]) qui a été lancé en 2013 par le Bureau de Recherches Géologiques et Minières (BGRM). Le but de ce projet est la création d'une base de données numérique et cohérente des connaissances géologiques tridimensionnelles (3D) du sous-sol français, une évolution de la carte géologique de la France au 1/50 000. De plus, la dimension temporelle, c'est-à-dire l'histoire géologique, doit être incluse afin de connaître les processus qui ont façonné la croûte terrestre depuis sa genèse jusqu'à présent. Cette recherche est motivée par des objectifs socio-économiques liés au développement durable, á une meilleure protection du sous-sol, á la maintenance des aquifères et de l'approvisionnement en eau, á la production géothermique ou á la prévention des risques environnementaux. Une première zone d'investigation s'est focalisée sur les Vosges [Vassal and Derenne, 2013]. Dans cette thèse, nous allons nous intéresser aux Pyrénées qui constituent la deuxième zone d'étude du RGF.

Les Pyrénées forment la partie la plus jeune du système orogénique alpin-himalayen et s'étendent sur environ 450 km d'est en ouest et 125 km du nord au sud. Elles sont délimitées par le Bassin

[1] http://rgf.brgm.fr/

Aquitain en France et par le Bassin de l'Ebre en Espagne. Cette chaîne de montagne s'est développée suite à la collision entre la plaque ibérique et l'Eurasie au cénozoïque [Le Pichon et al., 1971; Vergés et al., 2002; Choukroune, 1992; Beaumont et al., 2000; Muñoz, 1992; Mouthereau et al., 2014]. Il existe différentes théories décrivant la cinématique de la plaque ibérique au cours du Mésozoïque [p.e. Sibuet et al., 2004; Jammes et al., 2009; Vissers and Meijer, 2012; Barnett-Moore et al., 2016], qui reste très mal contrainte.

L'exploration de la structure crustale sous les Pyrénées a commencé à la fin des années 1970. Les deux principaux profils de réflexion sismique du programme ECORS ont donné des premières images de l'architecture profonde et ont mis en évidence des racines crustales épaisses sous les Pyrénées centrales ainsi qu'un décalage de 15 km entre le Moho ibérique et le Moho européen [Daignières et al., 1982; Choukroune, 1989; Roure et al., 1989; Teixell, 1998]. De nouveaux profils ont été déployés au travers des Pyrénées pendant les expériences temporaires IBERARRAY et PYROPE [Chevrot et al., 2014]. Cependant, l'architecture profonde des Pyrénées reste encore mal connue.

Un autre sujet débattu est l'origine des fortes anomalies positives de Bouguer dans la partie ouest de la zone pyrénéenne, près du massif de Labourd et de la ville de Saint-Gaudens. Torné et al. [1989] et Casas et al. [1997] ont étudié les profils gravimétriques traversant ces anomalies et ont proposé de les expliquer par des écailles de manteau exhumé ensérées dans la croûte supérieure. Cependant, ces études sont limitées par une modélisation bidimensionnelle (2D) supposant une extension latérale infinie des structures modélisées, alors que les anomalies de Labourd et Saint Gaudens s'étendent sur quelques dizaines de kilomètres seulement. Les modélisations 2D sont donc susceptibles de surestimer l'influence d'une écaille de manteau. Le seul modèle de densité tridimensionnelle (3D) à l'échelle lithosphérique [Vacher and Souriau, 2001] souffre d'une description très schématique des structures crustales profondes. De plus, les résidus entre les anomalies de Bouguer modélisées et observées restent importants. De nouvelles informations sur l'origine des anomalies de Bouguer positives sont venues d'une inversion de formes d'ondes [Wang et al., 2016], montrant une anomalie de vitesse rapide superficielle, connectée au manteau européen, sous l'anomalie de gravité de Labourd. Cette structure a été interprétée comme du manteau exhumé, vestige de l'épisode de rifting crétacé.

Cette thèse décrit la construction d'un modèle géologique 3D avec le logiciel `GeoModeller` [Calcagno et al., 2008; Guillen et al., 2008]. Il couvre la région pyrénéenne, de l'océan Atlantique à la mer Méditerranée et du Massif Central à la Chaîne Ibérique, de la surface jusqu'à 70 km de profondeur. Un premier modèle est construit sur la base des données géologiques disponibles, puis affiné par essai-et-erreur afin de mieux reproduire les anomalies de Bouguer. Le modèle est ensuite validé par la prédiction des temps de trajet sismiques et sert d'information a-priori pour une inversion stochastique et conjointe de la géologie, de la gravité et des temps de propagation des ondes P et S. Pour cela, les temps de trajet théoriques sont calculés avec la méthode de différences finies de Podvin and Lecomte [1991], et un module d'inversion sismique est implémenté dans `GeoModeller`.

Dans les sections suivantes nous allons d'abord décrire les résultats des études géophysiques antérieures dans les Pyrénées, puis exposer les bases de la modélisation du champs de gravité et du logiciel `GeoModeller` dans la section 2. La section 3 traîte les bases de la modélisation sismique et l'implémentation de l'inversion de temps de trajet dans `GeoModeller`. La section 4 décrit la construction du modèle géologique et présente une discussion sur les anomalies de Bouguer prédites. La section 5 présente la modélisation et l'inversion 3D, et finalement, la section 6 contient les conclusions et les perspectives de ce travail.

1.2 Overview (English)

This thesis is part of the RGF (Référentiel Géologique de la France[2]) project that has been launched by the BGRM (Bureau de Recherches Géologiques et Minères[3]) in 2013. The aim of this project is to create a coherent, numerical data base of the three-dimensional (3D) geological knowledge of the French subsurface, an evolution of the two-dimensional (2D) 1/50 000 geological map of France. In addition, the dimension of time, i.e. the geological history, shall be included, in order to describe the processes that have shaped the rocks from their genesis up to now. The research is motivated

[2]engl.: geological reference of France; http://rgf.brgm.fr/
[3]engl.: French Geological Survey; www.brgm.fr

by socio-economical objectives such as a better development and protection of the subsurface, maintenance of aquifers and ground water supply, geothermal production, or environmental risk prevention. A first investigation area has been the Vosges, in Eastern France [Vassal and Derenne, 2013]. The Pyrenees in southern France and northern Spain form the second study area of the RGF and constitute the focus of this thesis.

The Pyrenees are the youngest part of the Alpine-Himalayan orogenic system. They extend over about 450 km EW and 125 km NS and are delimited by the Aquitaine foreland basin in France and by the Ebro foreland basin in Spain. The mountain belt has grown as a consequence of the continent-continent collision between Iberia and Eurasia during Cenozoic times [Le Pichon et al., 1971; Vergés et al., 2002; Choukroune, 1992; Beaumont et al., 2000; Muñoz, 1992; Mouthereau et al., 2014]. Many different theories exist describing the Iberian plate kinematics during the Mesozoic [e.g. Sibuet et al., 2004; Jammes et al., 2009; Vissers and Meijer, 2012; Barnett-Moore et al., 2016], but the relative motion between the Iberian and the Eurasian plates remains highly controversial.

The exploration of the crustal structure beneath the Pyrenees started in the late 1970s. Two deep seismic reflection profiles of the ECORS program [Daignières et al., 1982; Choukroune, 1989; Roure et al., 1989; Teixell, 1998] yielded first insights into the deep architecture. They evidenced thick crustal roots beneath the central Pyrenees and a sharp 15 km offset between the Iberian and European Moho. Moreover, passive seismic profiles were recently deployed during the IBERARRAY and PYROPE temporary experiments [Chevrot et al., 2014]. However, large parts of the Pyrenean architecture remain poorly known. Furthermore, the origin of the regional seismicity remains unexplained, the present-day velocity field being negligibly small.

Another debated topic is the origin of the strong positive Bouguer anomalies in the western North Pyrenean Zone, near the Labourd Massif and the city of Saint-Gaudens. Torné et al. [1989] and Casas et al. [1997] focused on gravity profiles across these anomalies and postulated slices of exhumed mantle enclosed in the upper crust. Their studies are limited by the fact that two-dimensional (2D) gravity modeling assumes an infinite lateral extension of the modeled structures but the Labourd and Saint-Gaudens anomalies extend over a few tens of kilometers only. 2D gravity modeling is thus likely to overestimate the influence of these finite mantle slices. The only

three-dimensional (3D) density model at lithospheric scale [Vacher and Souriau, 2001] suffers from a coarse description of deep crustal structures and relatively large misfits between modeled and observed Bouguer anomalies. New insights in the origin of the positive Bouguer anomalies recently came from full wave-form inversion of teleseismic P-waves [Wang et al., 2016], which evidenced a high-velocity anomaly at a crustal level but linked to the European mantle, beneath the Labourd gravity anomaly. This structure has been interpreted as serpentinized mantle, exhumed during the cretaceous phase of rifting.

This thesis describes the construction of a 3D geological model with the software `GeoModeller` [Calcagno et al., 2008; Guillen et al., 2008]. The model covers the Pyrenean region, from the Atlantic Ocean to the Mediterranean Sea and from the Massif Central to the Iberian Range, from the surface down to 70 km depth. A first model is built on the basis of available geological data and then refined by trial-and-error in order to better fit the Bouguer anomalies. The model is then validated by travel time prediction for regional tomography and serves as a-priori information for a stochastic, joint inversion of geology, gravimetric, and seismic data. For this, travel times are predicted with the finite difference routine from Podvin and Lecomte [1991], and a seismic inversion module is implemented into `GeoModeller`.

The following sections in this chapter will highlight the results of previous geophysical studies. The background for gravity modeling in `GeoModeller` is given in 2. Section 3 describes the bases of seismic modeling and the implementation of travel time inversion into `GeoModeller`. Section 4 describes the construction of the geological model and presents a discussion with regard to the predicted Bouguer anomalies. Section 5 describes geophysical 3D modeling and inversion, and finally, section 6 contains the conclusions and perspectives.

1.3 Present-day Structures of the Pyrenees

Together with the Catambrian Mountains in Spain, the Pyrenees form the westernmost part of the Alpine-Himalayan orogenic system [Martín González, 2011]. They extend over about 450 km EW between the Atlantic Ocean and the Mediterranean Sea, and approximately 125 km NS between

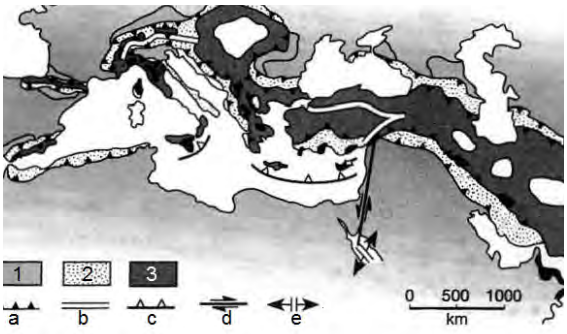

(a) Western segment of the Alpine-Himalayan orogen (after Twiss and Moores [2007]). 1- Foredeep, 2- Miogeoclinal fold-thrust-belt, 3- Core Zone: metamorphic, volcanic rocks, batholiths, ophiolites, etc, a- Thrust complex, b- Rectilinear fault zone, c- consuming plate boundary, d- Transform fault, e- Ridge axis.

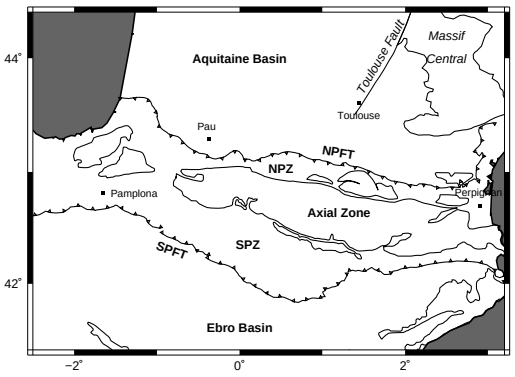

(b) Main units of the Pyrenees. NPFT- North Pyrenean Frontal Thrust, NPZ- North Pyrenean Zone, SPFT- South Pyrenean Frontal Thrust, SPZ- South Pyrenean Zone.

Figure 1.1

France and Spain (e.g. Vissers and Meijer [2012]).

The Pyrenean belt is bordered by the Aquitaine foreland basin in the north and the Ebro foreland basin in the south. It can be subdivided into three zones (five including the foreland basins; cf. Figure 1.1b and e.g. Choukroune [1989], Roure et al. [1989], Teixell [1998]): The Axial Zone (AZ) in the center, and the North and South Pyrenean Zones (NPZ, SPZ) to the north and to the south, overthrusting parts of the meso-cenozoic foreland basins. The North Pyrenean Fault (NPF) describes the limit between the AZ and the NPZ, and is more pronounced in the East than in the West. The North Pyrenean Frontal Thrust (NPFT) separates the NPZ from the Aquitaine basin [Velasque et al., 1989; Teixell, 1998; Roure et al., 1989; Choukroune, 1989]. Similarly, the South Pyrenean Frontal Thrust (SPFT) separates the SPZ and the Ebro Basin.

The Axial Zone presents a fan-like geometry in the central Pyrenees with north-vergent thrusts in the north and south-vergent thrusts in the south. Hercynian rocks are present in the central and eastern parts, while paleozoic units are found in the west [Daignières et al., 1982]. The NPZ, in contrast, shows mainly mesozoic sediments (flysch deposits); hercynian ages are rare. Between the AZ and the NPZ, a low-pressure/high-temperature (LPHT) belt of 1 to 5 km width and parallel

to the North Pyrenean Fault [Choukroune, 1989] is observed. Inside this belt, highly metamorphic rocks (in the "LPHT facies") and lherzolithes can be found, whereas only little metamorphism can be observed for the Mesozoic and Tertiary rocks outside [Choukroune, 1989; Daignières et al., 1982]. The stratigraphy of Pyrenean structures is described in more detail in Velasque et al. [1989].

In terms of crustal thickness, one can describe a thickening of the Iberian crust towards the north with a maximum thickness of 65 km [Torné et al., 1989] and a thickening of the European crust to the south with a maximum thickness of 40 km [Vergés et al., 2002]. The maximum crustal thickness can be found in the Central Pyrenees, where topography is the highest. It flattens towards the atlantic coast with an estimated crustal shortening of 80 km [Vergés et al., 2002; Teixell, 1998] to the west of the range. To the east, the thickness decrease is more pronounced, a fact that Gallart et al. [2001] explain by the "late overprint of Neogene extension related to the opening of the Valencia Trough in the western Mediterranean" [Vergés et al., 2002].

1.4 Problematic Reconstruction of Iberian Plate Kinematics

The formation of the Pyrenees is linked to the opening of the Bay of Biscay, produced by the $\sim$35° counter-clockwise rotation of the Iberian peninsula with respect to Eurasia [Le Pichon et al., 1971; Choukroune and Mattauer, 1978; Choukroune, 1989; Sibuet et al., 2004; Jammes et al., 2009]. However, different models have been proposed for the kinematics of the Iberian plate during the Mesozoic. These models can be classified into three major models, but important discrepancies exist even within these models:

1. Cretaceous strike-slip motion, followed by convergence [e.g. Le Pichon and Sibuet, 1971; Rosenbaum et al., 2002],

2. Cretaceous transtensional motion and extension, followed by convergence [e.g. Vergés et al., 2002; Jammes et al., 2009], and

3. Convergence during the whole Cretaceous [e.g. Sibuet et al., 2004; Vissers and Meijer, 2012; Teixell et al., 2016].

	Ma	P.S., 1971 [a]	R., 2002 [b]	V., 2002 [c]	S., 2002 [d]	J., 2009 [e]	V.M., 2012 [f]	T., 2016 [g]
Oligoc.	33.9	.	conversion	collision, subduction, uplift	85 Ma: beg. of cont. subd., inv. of the back-arc basins(2) 120 - 90 Ma: convergence lith. subd. back-arc basins(1)	.	convergence	full collision
Eocene	56	compression: 45-38 Ma	right-lateral strike-slip			"major collision": Pyrenean uplift, formation of S foreland basin		
Paleoc.	66	.	stagnation (67-55)					proto-collision 70-75 Ma
Late Cret.	71 Maastr. 84 Camp. 86 Sant. 89 Conia. 94 Turon.	strike-slip	conversion	.		.	stagnation	convergence
	100 Cenom.		left-lateral strike-slip + convergence (120 - 83 Ma)	transtensional motion, pull-apart basins		HTLP metamorphism (95 Ma)		
Early Cret.	112 Albian 125 Aptian 130 Barrem. 136 Hauter. 140 Valang. 146 Berrias.		left-lateral strike-slip (170-120 Ma)	rifting	NS extension (157-118 Ma)	orth. extension, crustal thinning	convergence	.
Late Jur.	161					transtension, left-lateral strike-slip	rifting, opening of Neothetys Ocean	
Middle Jur.	176	.		.	.	.	.	
Rotation		30° northern France	between Australia and New Zealand	35°	(1): Bay of Biscay (2): west of Portugal	.	35°	.

Table 1.1: Kinematic Evolution of the Pyrenees. References:[a]-Le Pichon and Sibuet [1971] [b]-Rosenbaum et al. [2002] [c]-Vergés et al. [2002] [d]-Sibuet et al. [2004] [e]-Jammes et al. [2009] [f]-Vissers and Meijer [2012], [g]-Teixell et al. [2016].

For the first group, considering a strike-slip motion during Cretaceous, Le Pichon and Sibuet [1971] propose a rotation of about 30° around a pole situated in the north-east of Paris, France, leading to the opening of the Bay of Biscay and to a left-lateral strike-slip motion starting at late Jurassic (∼160 Ma). They assume that this motion continued until the end of Cretaceous (∼66 Ma), along the North Pyrenean Fault which is thought to represent the plate boundary between Iberia and Eurasia at that time. Subsequently, the "main phase of creation" [Le Pichon and Sibuet, 1971] of the Pyrenean mountain belt took place, caused by a compressional phase in Upper Eocene (45 Ma to 38 Ma). Mattauer [1968] estimates a shortening of 50 ± 20 km during this period.

In contrast, Rosenbaum et al. [2002] describe a strike-slip motion only from Middle and Late Cretaceous (120 Ma - 83 Ma) yielding to the opening of the Bay of Biscay. According to this theory, the continent-continent collision started at the beginning of Campanian (83 Ma) but stopped between 67 Ma and 55 Ma (Paleocene) before continuing as a right-lateral strike-slip movement in Eocene (55 Ma - 46 Ma). It then returned into conversion until the Oligocene. Rosenbaum et al. [2002] present a series of consecutive poles of rotation, all lying between Australia and New Zealand.

The model of Jammes et al. [2009] can be regarded as a compromise between the first and the second group, with a strong strike-slip component of the trans-tensional motion assumed to occur from Late Jurassic to late Aptian times (160 Ma - 125 Ma). In their study, focused on the Mauléon-Labourd region, the extensional component then dominates, going along with "extreme crustal thinning" [Jammes et al., 2009], until Albian, which may explain the presence of dense material and exhumed mantle rocks in the Labourd area. The high-temperature-low-pressure (HTLP) metamorphism is of Cenomanian age (∼ 95 Ma). The beginning of convergence occurred at Campanian (∼84 Ma), with a major Pyrenean uplift during Eocene.

According to Vergés et al. [2002], the opening of the Bay of Biscay, the Iberian anticlockwise 35° rotation, and the trans-tensional motion along the North Pyrenean Fault Zone yielding the development of pull-apart basins are "major concurrent geodynamic events" occurring "from middle Albian to the end of Cenomanian". Referring to Fabriès et al. [1998] and Montigny et al. [1992], they ascribe the presence of upper mantle material, magmatism and metamorphism to the development

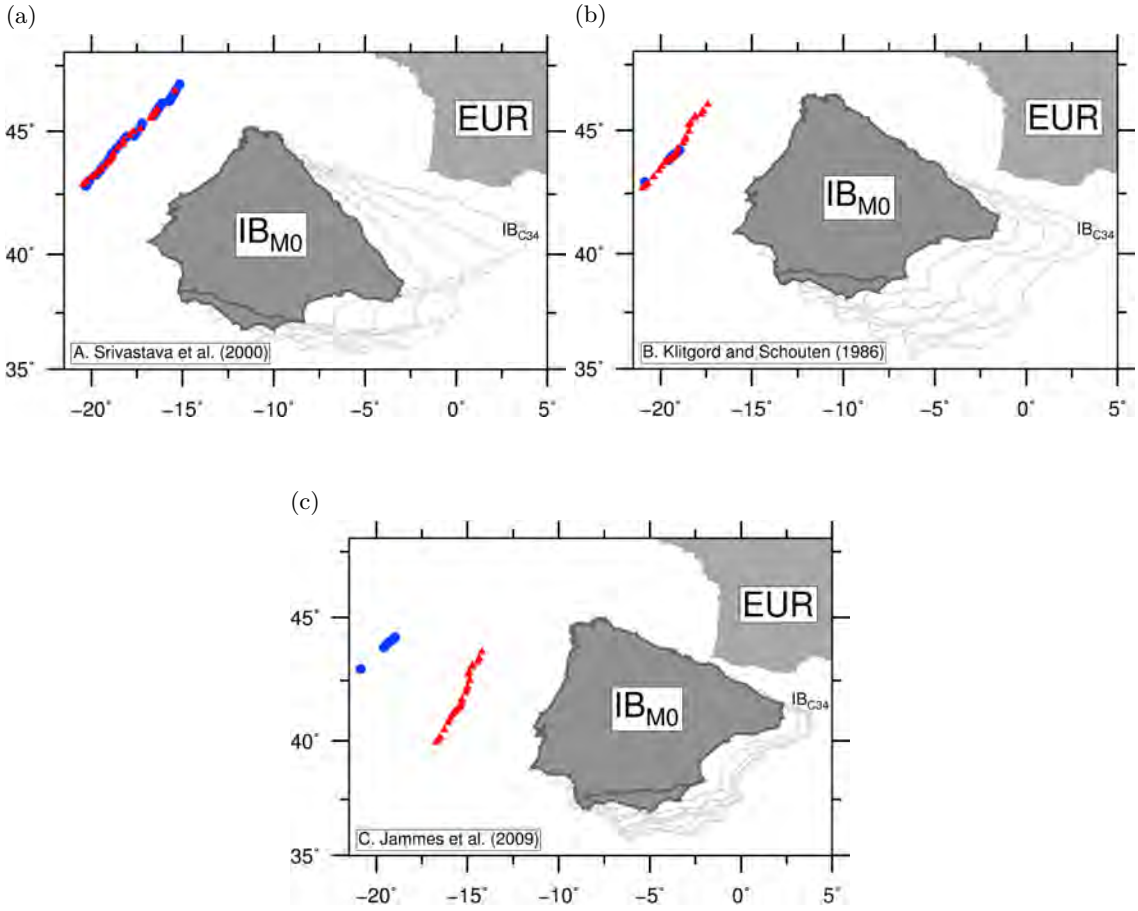

Figure 1.2: Kinematic reconstruction models of the Iberian plate with respect to a fixed European plate at chron M0, modified after Barnett-Moore et al. [2016]. Gray lines represent the Iberian contours every 10 Ma from C34 to M0. Blue circles show M0 along the Newfoundland margin, red triangles along the west Iberian margin. **(a):** scissor-type opening of the Bay of Biscay as proposed by Sibuet et al. [2004], Vissers and Meijer [2012]. **(b):** left-lateral strike-slip motion as postulated by Le Pichon and Sibuet [1971]. **(c):** trans-tensional motion motion as postulated by Jammes et al. [2009].

of pull-apart basins. Vergés et al. [2002] date the beginning of continental collision of Eurasia and Iberia to Tertiary times, with a partial subduction of the Iberian plate and the uplift of the Pyrenees.

Finally, in the third model, Sibuet et al. [2004] argue for a convergence between Iberia and Eurasia from late Aptian (118 Ma) to Eocene, with a formation of back-arc basins due to the subduction of the Neothetys Ocean, and a pole of rotation in the Bay of Biscay roughly from 120 Ma to 90 Ma. They date the beginning of continental subduction and the inversion of the back-arc basins at late Satonian (85 Ma) and the end of the opening of the Bay of Biscay, as well as a displacement of the pole of rotation from the Bay of Biscay to the west of Portugal 80 Ma ago, together with a change in motion from SW-NE to SSE-NNW direction.

This theory is very similar to the one proposed by Teixell et al. [2016] describing "early convergence" from Mid to Late Cretaceous with a crustal shortening of 15 km and "protocollision" in late Campanian implying a shortening of 54 km. They finally see a "full collision" from Eocene to Early Miocene with 45 km shortening.

Vissers and Meijer [2012], however, describe a 35° counter-clockwise rotation of the Iberian plate, yielding the opening of the Bay of Biscay and Iberian-Eurasian conversion, only during the Aptian. From Albian to Santonian (∼110 Ma - 84 Ma), the evolution stagnates, before a new phase of continental collision occurs from Campanian to Tertiary, leading to the present-day structure of the Pyrenees.

The ∼35° anti-clockwise rotation going along with both the left-lateral strike-slip (Figure 1.2b) and the scissor-type motion (Figure 1.2a) is in good agreement with paleomagnetic date [Van der Voo and Zijderveld, 1971]. The scissor-type movement matches better with the magnetic M_0 anomaly [Sibuet et al., 2004] but implies the opening of the neo-Tethys Ocean before and its closure during Aptian. This closure should have left a suture in the northern Ebro Basin [Sibuet et al., 2004], but none was ever seen there. The trans-tensional motion (Figure 1.2c) proposed by Jammes et al. [2009] is supported by inverted rift structures [Barnett-Moore et al., 2016], but shows a large mismatch between the Iberian and the Newfoundland margins.

To summarize, the kinematic evolution of the Pyrenees is highly controversial. Models range from Cretaceous pure strike-slip motion [Le Pichon and Sibuet, 1971; Rosenbaum et al., 2002] over trans-tension [Vergés et al., 2002; Jammes et al., 2009] to pure compression [Sibuet et al., 2004; Vissers and Meijer, 2012; Teixell et al., 2016], from a continuous process [Le Pichon and Sibuet, 1971; Sibuet et al., 2004] to stagnant phases [Rosenbaum et al., 2002; Vissers and Meijer, 2012], and from a pole of rotation located in the west of Portugal [Sibuet et al., 2004], the Bay of Biscay [Sibuet et al., 2004], or Northern France [Le Pichon and Sibuet, 1971] to a series of poles in the vicinity of Australia and New Zealand [Rosenbaum et al., 2002]. Barnett-Moore et al. [2016] present an overview of these different types of models.

While the kinematics of the Iberian plate during Mesozoic and Cenozoic remain uncertain, the present day deformation in the Pyrenees, if any, is extremely small. Only week horizontal motion across the mountain belt can be observed by geodesy nowadays, with estimates of the extension rate ranging from 0.2 mm/yr [Nocquet, 2012] over (0.5 ± 1.5) mm/yr [Nocquet and Calais, 2004] to 1.5 mm/yr [Asensio et al., 2012].

1.5 Previous Geophysical Work

Deep geophysical exploration of the Pyrenees started in the late 1970s. Based on explosion seismic data, Hirn et al. [1980] observed a Moho jump of more than 10 km beneath the NPF, with a thinner crust in the European plate. However, the Moho remained poorly defined over an about 10 km wide zone between the Iberian and the European crust. Nevertheless, their interpretation is supported by two east-west (EW) seismic refraction profiles north and south of the mountain belt [Daignières et al., 1982] revealing the Iberian crust to be 10 km to 15 km thicker than the European one and confirming local crustal thinning beneath the North Pyrenean Zone. Daignières et al. [1982] conclude that the North Pyrenean Fault marks the plate boundary.

In 1985/86, the 250 km long ECORS[4]-Pyrenees deep seismic reflection survey was shot across the central Pyrenees, approximately between the cities of Toulouse (France) and Balaguer (Spain)

[4]Étude continentale et Océanique par Réflexion et Réfraction Sismique; engl.: continental and oceanic seismic reflection and refraction study

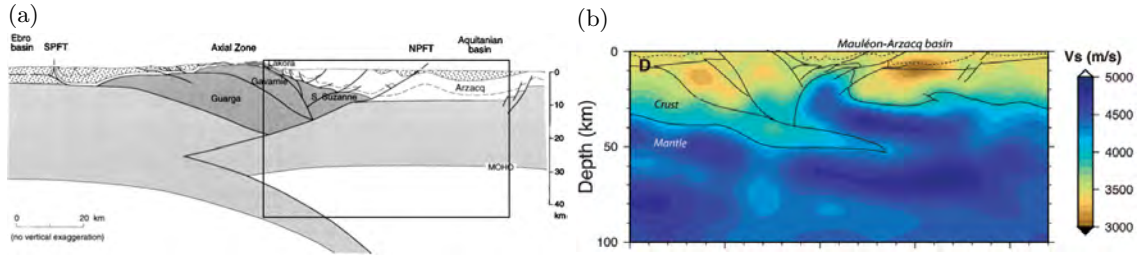

Figure 1.3: **a:** Interpretation of the ECORS-Arzacq profile after Teixell [1998]. The black rectangle shows the area covered with seismic data. **b:** Seismic velocity and geological interpretation of PYROPE 2 profile [Wang et al., 2016].

(cf. Choukroune [1989], Roure et al. [1989]; Teixell [1998]). A second profile, ECORS-Arzacq, followed in 1989 [Teixell, 1998], crossing the Western Pyrenees. Both profiles show a sharp contrast of Moho depth between Eurasia and Iberia just beneath the surface trace of the North Pyrenean Fault, with a 10-15 km thicker Iberian crust. Seismic and gravity modeling suggest an Iberian Moho depth of about 60-65 km for the ECORS-Pyrenees profile [Daignières et al., 1989]. For the ECORS-Arzacq profile, Teixell [1998] observed an Iberian Moho down to 55 km depth (Figure 1.3a) and proposed that it may reach 90 km.

Grandjean [1994] combines seismic reflection, tele-seismic travel times, and gravimetric modeling to analyze the structure around the ECORS-Arzacq profile. He concludes that the European Moho is at 30 km depth, with a deeper Iberian Moho at 50 km at the center of the profile. Between the two plates, he proposes a lower crustal block at upper crustal depth, resulting from the convergence after crustal thinning, to explain the positive Labourd gravity anomaly.

Another explanation for the positive gravity anomaly was proposed by Velasque et al. [1989]. They refer to the poorly defined zone of Moho depth in the work of Hirn et al. [1980] and suggest a significant crustal thinning, going along with a mantle uplift up to about 14 km depth. This theory is supported by a recent study showing a mantle uplift up to 10 km beneath the Mauléon-Arsacq basin [Wang et al., 2016] (Figure 1.3b). Further details of seismic studies in the Pyrenees are given in section 4.3.3.

Interfaces revealed from deep seismic sounding can be used to constrain the geometry of density

models [Torné et al., 1989; Vacher and Souriau, 2001]. Torné et al. [1989] present two 2D models, each explaining the Bouguer gravity anomalies along the ECORS Pyrenees profile using densities of 2.50-2.65 g/cm^3 for sediments, 2.75 g/cm^3 and 2.98 g/cm^3 for the upper and lower crust, and 3.23 g/cm^3 for the mantle. They conclude that a middle crustal unit needs to be inserted between Iberian upper and lower crusts in order to fit the gravity data, as already proposed by Gallart et al. [1981], and ascribe a density of 2.80 g/cm^3 to this unit. Furthermore, they estimate a maximum Iberian crustal thickness of 65 km with a northern limit "between two extreme models, a vertical limit or a 70° sloping interface" [Torné et al., 1989]. Finally, they explain the positive Saint-Gaudens gravity anomaly by "either lower crustal rocks or mantle slices" [Torné et al., 1989] enclosed in the upper crust.

Casas et al. [1997] propose three geological sections crossing the Labourd anomaly, the Saint-Gaudens anomaly, and the eastern Pyrenees, respectively. Half width, gradient/amplitude, and 2D power spectrum analyses of the Labourd gravity anomaly yield a maximum source depth in the upper crust, between 9.2 km and 13.6 km. On this basis and with the same crustal and mantle densities as Torné et al. [1989] but without considering a middle crust, they include mantle bodies in the upper European plate to fit the Bouguer anomalies on the Labourd and Saint-Gaudens profiles. For the eastern profile, where the positive anomaly is far less pronounced, they enclose a lower crustal body in the upper crust.

Both Casas et al. [1997] and Torné et al. [1989] reproduce the Labourd and the St Gaudens gravity anomalies with their respective 2D models. However, 2D gravity modeling implies an infinite horizontal extension of the geological structures, while the lateral extend of the gravity anomalies is limited to less than 20 km. In such a case, 2D gravity calculations as performed in the above mentioned studies strongly overestimate the effect of density anomalies and thus underestimate the amplitude of density anomalies. Vacher and Souriau [2001] reproduced the positive Labourd and Saint Gaudens Bouguer anomalies with finite high-density bodies enclosed in the upper crust of a 3D model covering the whole Pyrenean belt. Apart from these two bodies, however, their model remains rather coarse, allowing no topography on crustal interfaces and only three different Moho depths beneath the western, central, and eastern Pyrenees. No detailed 3D density model is

available.

1.6 Seismicity

Although recent GPS studies [Rigo et al., 2015; Asensio et al., 2012; Nocquet and Calais, 2003; Souriau and Pauchet, 1998] failed to detect significant motion in the Pyrenees, the belt experiences a continuous, moderate seismicity. Indeed, more than 3500 events with magnitudes >2 in the Pyrenees between 1973 and 2011 are reported in the NEIC catalog [Asensio et al., 2012].

Figure 1.4 gives the distribution of the seismic events at different depths. Most of the sources are located in the uppermost 15 km of the crust. A well defined cluster follows an east-west trend north of the NPF between -1.5° and +0.5° of longitude. Two other clusters are observed south and north-east of the Labourd gravity anomaly. The latter is mostly located between 5 km and 10 km depth. This cluster represents the induced seismicity produced by gas extraction and fluid injection in the Lacq reservoir [Bardainne et al., 2008]. The former is most pronounced above 10 km and is related to an irrigation system at the Spanish city Itoiz [Durá-Gómez and Talwani, 2010]. In the eastern part of the Pyrenees, seismic events are scattered all over the Axial Zone down to 10 km depth. Beneath 15 km, only rare events can be observed, most of them around the Labourd area.

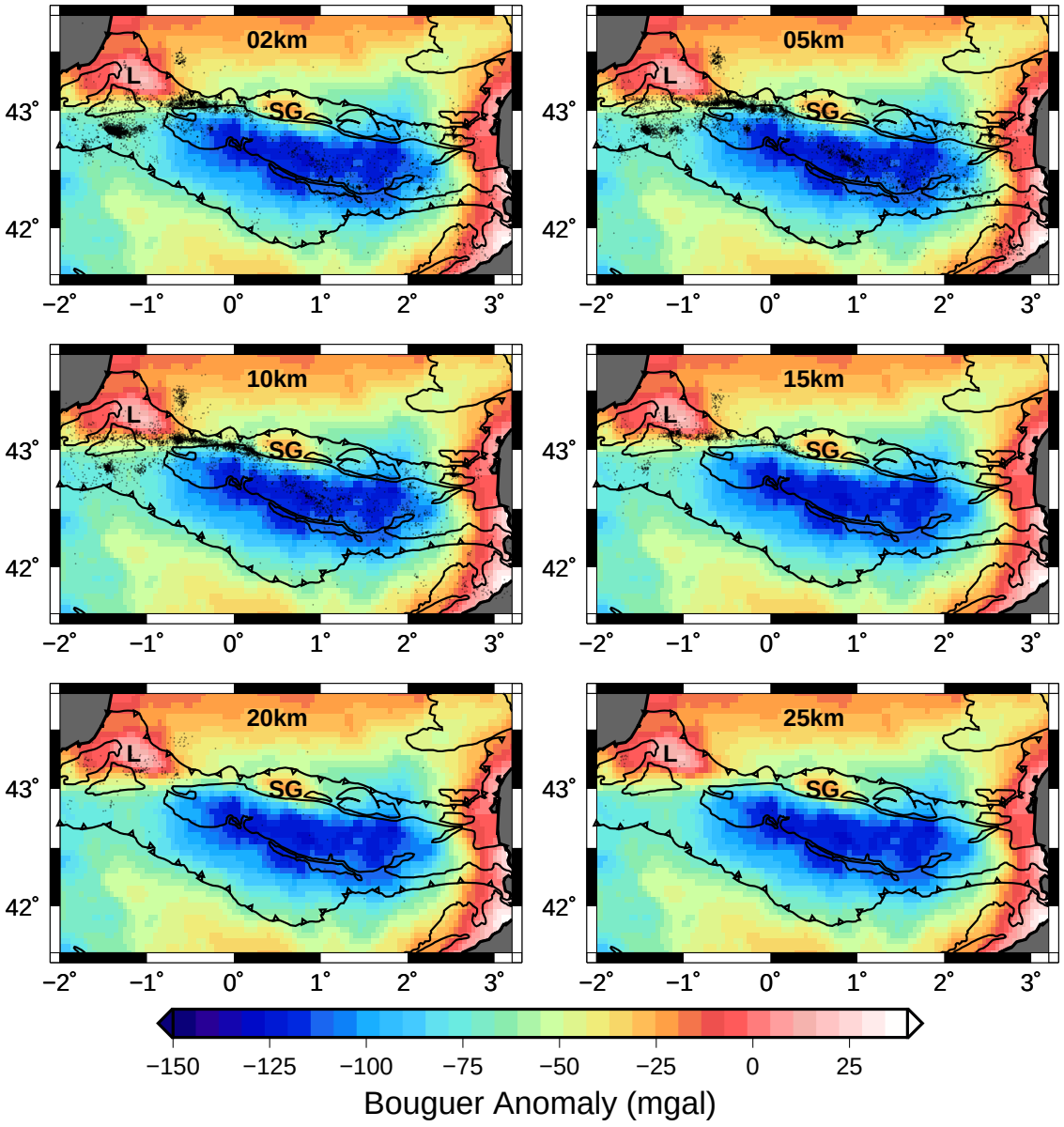

Figure 1.4: Distribution of earthquakes at different depth levels. The letters L and SG indicate the locations of the Labourd and Saint-Gaudens gravity anomalies.

Chapter 2

Gravity Modeling with the `GeoModeller` Software

Contents

The construction of the 3D geological model as well as gravity direct and inverse modeling are done with the `GeoModeller` software developed by the BRGM [Calcagno et al., 2008; Guillen et al., 2008]. This software allows us to import, visualize, and edit different kinds of geological data (cross-sections, maps, boreholes). After an overview on the principles of gravimetry (section 2.1), this chapter presents the `GeoModeller` software. The 3D model is computed from the geological data by using the method of potential field interpolation (2.2), respecting the relationships between the geological units which are defined in a stratigraphic pile (section 2.3). Furthermore, `GeoModeller` offers built-in tools for gravimetric direct (section 2.4) and inverse (section 2.5) modeling, which are exploited to improve and validate the model.

2.1 Principles of Gravimetry

The gravity field strongly depends on the density distribution in the Earth. The analysis of gravity anomalies thus helps us to create an image of the Earth's interior. Two point bodies of masses m and m' separated by a distance r attract each other by the gravitational force

$$\mathbf{F} = G\frac{mm'}{r^2} \tag{2.1}$$

with the universal constant of gravitation $G = 6.673 \cdot 10^{-8}$ m^3/(g s^2) [BGI, 2012]. From (2.1), the gravitational acceleration g_a on the mass m' caused by mass m is given by:

$$g_a = G\frac{m}{r^2} \tag{2.2}$$

Consequently, each point $P(x, y, z)$ on, above, and beneath the Earth's surface is attracted by the gravitational acceleration of the Earth:

$$g_E = G\frac{m_{Earth}}{r^2_{Earth}} \tag{2.3}$$

This quantity represents the main component of Earth's gravitational field $g(P)$. However, centrifugal and tidal accelerations g_C and g_T contribute, too. The centrifugal acceleration is caused by Earth's rotation and is thus latitude-dependent. The tidal acceleration is caused by the gravitational forces of Moon and Sun and is thus position- and time-dependent.

The global gravity field of an ideal Earth is given by the sum of the above mentioned accelerations:

$$g(P) = g_E(P) + g_C(P) + g_T(P). \tag{2.4}$$

In SI units, gravity shall be described in m/s^2. In geophysics, however, the unit mGal is still in use. It stands for milliGalilei and 1 mGal= 10^{-5} m/s^2 [Lindner and Casten, 2005].

Any density anomaly will cause a so-called gravity anomaly Δg. The anomaly caused by a density heterogeneity $\Delta\rho V$ in a volume V is given by

$$\Delta g(P) = G\frac{\Delta\rho V}{r^2}. \tag{2.5}$$

The Earth's total gravity potential (or geopotential) W at a point (x, y) is defined as the sum of the gravitational potential V and the potential $\frac{1}{2}\omega(x^2 + y^2)$ produced by the Earth's rotation,

Property	Notation	Value
Equatorial radius (semi major axis)	a	6378137.0 m
Polar radius (semi minor axis)	b	6356752.3142 m
Flattening	f	298.257223563^{-1}
Earth's gravitational constant(1)	Gm_{Earth}	$(3986004.418 \pm 0.008) \cdot 10^8 \frac{m^3}{s^2}$
Earth's gravitational constant(2)	Gm_{Earth}	$(3986000.9 \pm 0.1) \cdot 10^8 \frac{m^3}{s^2}$
Angular velocity	ω	$7292155.0 \cdot 10^{-11} \frac{rad}{s}$
Eccentricity	e	$8.1819190842662 \cdot 10^{-2}$

Table 2.1: Geometrical properties of reference ellipsoid WGS 84 [NIMA, 1997]. 1. - Earth's atmosphere included. 2. - Earth's atmosphere excluded.

with the angular velocity ω and the geocentric coordinates x, y [NIMA, 1997; Parasnis, 1997]:

$$W = V + \frac{1}{2}\omega(x^2 + y^2) \tag{2.6}$$

Gravity is the vertical gradient of the geopotential and describes the acceleration of a freely falling body perpendicular to an equipotential surface. The unperturbed surface of the ocean constitutes such an equipotential surface. This equipotential surface beneath the continents defines the geoid and represents approximately the Earth's shape. A simple approximation of this surface is an ellipsoid with the polar axis coinciding with the Earth's rotational axis, the mass corresponding to the Earth's mass. Different reference ellipsoids have been proposed (examples are listed in Parasnis [1997]), but the WGS 84 ellipsoid is by far the most frequently used. Its properties are listed in table 2.1.

Gravity studies usually consider anomalies, i.e. differences between measured and theoretical values of gravity, rather than absolute gravity. A widely used observable is the so-called Bouguer anomaly. The procedure involved in the computation of Bouguer anomaly Δg_B from the gravity g measured at a station [BGI, 2012] is described in the following:

- Normal gravity γ, i.e. the reference value on the ellipsoid's surface, is given by NIMA [1997]:

$$\gamma = \gamma_e \frac{1 + k \sin^2(\Phi)}{\sqrt{1 - e^2 \sin^2(\Phi)}}, \qquad k = \frac{b\gamma_p}{a\gamma_e} - 1 \tag{2.7}$$

  with a, b describing the semi-major and semi-minor axes of the ellipsoid, $\gamma_{e,p}$ the gravity at the equator and the poles, e^2 the squared eccentricity, and Φ the geodetic latitude.

- When using the WGS84 ellipsoid, an atmospheric gravity correction δg_A has to be applied, because the WGS84 gravitational constant contains atmospheric mass [BGI, 2012]:

$$\delta g_A = \begin{cases} 0.87 \cdot e^{-0.116(\frac{h}{1000})^{1.047}} \text{ mgal} & \text{for } h \geq 0 \\ 0.87 \text{ mgal} & \text{for } h < 0 \end{cases}. \tag{2.8}$$

  Here, h describes the height above sea level.

- The vertical normal gravity gradient at the ellipsoidal surface is:

$$\frac{\delta\gamma}{\delta h} = -2\frac{\gamma}{a}\left(1 + f + m - 2f\sin^2(\Phi)\right) \tag{2.9}$$

  with $m = \omega^2 a^2 b/(GM)$ (constant), a and b describing the semi-major and semi-minor axes, f the flattening, and ω the angular velocity.

  At high altitudes, the second-order term can be approximated by:

$$\frac{\delta^2\gamma}{\delta h^2} \approx 6\frac{\gamma}{a}. \tag{2.10}$$

- The measured gravity g has to be corrected for deviations caused by instrumental drift and tidal effects. This can be done either directly by the instrument, or by a computer software [Lindner and Casten, 2005]. Let us define the drift and tidal corrected gravity as $g(P)$.

- Free air anomaly Δg_F: Let us define a telluroid as the surface at which the potential of the normal gravity equals the measured gravity. With γ_0 being the normal gravity on the ellipsoid

surface, the normal gravity γ_Q on the telluroid surface is given as:

$$\gamma_Q = \gamma_0 + \frac{\delta g}{\delta h} H^* + \frac{1}{2} \frac{\delta^2 g}{\delta h^2} H^{*^2}, \tag{2.11}$$

where the normal height H^* describes the difference between ellipsoidal and telluroidal surface and is assumed to equal the station elevation above the sea level. Parasnis [1997] estimates the term $\frac{\delta g}{\delta h} H^* + \frac{1}{2} \frac{\delta^2 g}{\delta h^2} H^{*^2}$ to be -3.072 h at the equator and -3.088 h at the poles. Lindner and Casten [2005] and Sleep and Fujita [1997] propose an average value of -0.3086 h, with h the elevation above sea level. Taking into account the atmospheric gravity correction δg_A, the free air anomaly is defined as:

$$\Delta g_F = g(P) - \gamma_Q + \delta g_A. \tag{2.12}$$

- Finally, the Bouguer corrections compensate mass deficiencies beneath and mass excesses above the ellipsoidal surface. They are represented as plates of finite thickness h and infinite lateral extension with a gravitational attraction of

$$\delta g_B = 2\pi G \rho h, \tag{2.13}$$

where ρ describes the difference between the density of the plate and a reference density. The Bouguer anomaly is then defined as:

$$\Delta g_B = \Delta g_F - \delta g_B. \tag{2.14}$$

2.2 Potential Field Interpolation

Interpolation in `GeoModeller` follows the approach of potential fields [Lajaunie et al., 1997; Calcagno et al., 2008]. Geological contact points and orientation data are summarized in potential fields so

that geological interfaces are represented as isopotential surfaces while orientation data are described by the potential gradient.

Let the potential field at any point p be defined as $T(p)$. The potential increment $T(p) - T(p_0)$ between the point p and an arbitrarily chosen origin p_0 can be calculated via cokriging of the potential field and its gradient [Calcagno et al., 2008]:

$$T(p) - T(p_0) = \sum_{i=1}^{M} \mu_i \left(T(p_i) - T(p_i')\right) + \sum_{j=1}^{N} \nu_j \frac{\partial T}{\partial x_j}(p_j). \tag{2.15}$$

Here, $\partial T/\partial x_j$ is the gradient of the potential along direction j. The weights μ_i and ν_j are determined automatically by the cokriging system so that the interpolated potential field is the same at points p_i and p_i'.

The value $T(p) - T(p_0)$ can be calculated at any point p of the model. It is positive, negative, or equal to zero, depending on whether the point p lies in the younger formation, in the older one, or on the interface between two formations. Potential fields corresponding to eroding units always dominate over fields of older units.

2.3 Stratigraphic Pile

Before interpolating the geological data to get a 3D model, relationships between the different geological units have to be defined. The stratigraphic pile in `GeoModeller` does not necessarily correspond to the geological time scale. It describes the structural relations between the different units. A series is marked as 'onlap' if it deposits above another series without changing the latter's geometry (the corresponding potential field is of less consequence than the field of the series below and is truncated by the latter), or it is marked as 'erode' if it erodes the series beneath (the potential field takes precedence over the field of the lower series).

2.4 Gravity Forward Modeling

For this study, forward modeling of Bouguer anomalies is performed with the software `GeoModeller` as described in Guillen et al. [2008]. The geological model is discretized with cuboid cells of dimensions $dx \times dy \times dz$. The horizontal dimensions dx, dy of the cells are the same throughout the entire model, but the vertical extension dz may increase with depth. A homogeneous density is assigned to each geological unit. If a cell contains more than one geological unit, the unit in the center of the cell is selected.

The gravity response of the model is computed following Holstein [2003], Okabe [1979], and Plouff [1976]. At a position $\mathbf{r}$ defined in a cartesian coordinate system, the contribution of a volume V to the gravitational potential is given by:

$$U = G \int_V \frac{\rho}{u} dV, \tag{2.16}$$

where $u = \sqrt{x^2 + y^2 + z^2}$ is the distance between $\mathbf{r}$ and the center of the volume [Okabe, 1979; Guillen et al., 2008]. The gravity field at $\mathbf{r}$ can be obtained from the gradient of the potential:

$$\mathbf{g} = \nabla U(r) = \frac{\partial U}{\partial x}\mathbf{r_1} + \frac{\partial U}{\partial y}\mathbf{r_2} + \frac{\partial U}{\partial z}\mathbf{r_3}, \tag{2.17}$$

where $\mathbf{r_i}$ defines the direction vector along the i-direction [Guillen et al., 2008]. The gravity gradient describes the variation of the gravity field along the k-direction (k being x, y, or z):

$$g_k(r + \delta r) = g_k(r) + \frac{\partial^2 U}{\partial x \partial k}dx + \frac{\partial^2 U}{\partial y \partial k}dy + \frac{\partial^2 U}{\partial z \partial k}dz \tag{2.18}$$

$$= g_k(r) + E_{xk}dx + E_{yk}dy + E_{zk}dz. \tag{2.19}$$

Here, E_{ij} are the components of the symmetric gravity tensor [Guillen et al., 2008]:

$$\nabla\left(g(r)\right) = \begin{pmatrix} E_{xx} & E_{xy} & E_{xz} \\ E_{yx} & E_{yy} & E_{yz} \\ E_{zx} & E_{zy} & E_{zz} \end{pmatrix}. \tag{2.20}$$

The Bouguer anomaly is calculated with the following assumptions:

1. All relevant information for gravity computation is contained in the geological model [Guillen, 2016, pers. com.]. No reference ellipsoid is taken into account. The Bouguer anomaly is thus computed within a constant depending on the modeled density distribution.

2. The Universal Gravity Constant used in `GeoModeller` is $G = 6.668 \cdot 10^{-8}\mathrm{cm}^3/(\mathrm{g}{\cdot}\mathrm{s}^2)$ [Guillen et al., 2008]. The BGI data set we want to explain with our model was computed using $G = 6.673 \cdot 10^{-8}\mathrm{cm}^3/(\mathrm{g}{\cdot}\mathrm{s}^2)$ [BGI, 2012]. According to equation (2.13), this implies a constant offset in the resulting Bouguer anomalies.

The total constant offset resulting from assumptions 1 and 2 between the observed and modeled Bouguer anomalies can be computed automatically in `GeoModeller`.

For each of the cell, the elementary effect is computed according to its geophysical property. From these elementary effects, the gravity can then be computed as a function of the property distribution over the entire model [Guillen et al., 2008]. Thus, the modeling of the Bouguer anomaly for $n_x \times n_y$ cells in the horizontal directions and n_z depth layers requires $(n_x n_y)(n_x n_y)n_z$ computations. The choice of horizontal discretization is thus crucial for computation time because doubling the number of blocks in both x and y directions implies 16 times more computations.

2.5 Inversion Scheme

The inversion in `GeoModeller` is based on a probabilistic approach proposed by Mosegaard and Tarantola [1995] and was first developed in 2D by Bosch et al. [2001]. The 3D algorithm is described

in Guillen et al. [2008]. The a-priori 3D geological model is defined by lithology, shape, and topology (geometry of geological formations and their relationships with other formations, e.g. formation A always above formation B). Uniform petrophysical properties such as mass density are assigned to each geological unit. The geological model can then be used as an a-priori model for geophysical inversion as described in Guillen et al. [2008] and Figure 2.1:

1. Discretization of the model and mapping of the topology:
   The lithological model is discretized into cells of dimension dx×dy×dz, and each voxel is filled with the geological unit that was modeled at its center. Furthermore, a list of all cells at layer boundaries is created.

2. Assignment of petrophysical properties and calculation of the geophysical effects:
   Probability density functions (pdf) are defined for the petrophysical parameters of each formation. The properties of each cell are defined according to the pdf of its geological formation, and the elementary effect of each petrophysical property (field or tensor) is computed for all cells.

3. Sampling of physical parameters and initialization of the misfit:
   For each geophysical property j, the field or tensor effect is calculated by integrating over the entire current model m_{cur}. The initial global misfit is defined as

   $$\Delta_{cur} = \frac{1}{n}\Sigma_{i=1}^{n}(d_i^{obs} - d_i^{cal})^2 \tag{2.21}$$

   with n being the number of data and d_i^{obs} and d_i^{cal} the observed and calculated data.

4. Perturbation of the current model m_{cur} and calculation of the new geophysical effect:
   During the inversion process, the model is perturbed, and the new physical effect is calculated and compared to the observed data. At each step, there are two options to perturb the model with a probability given by the user at the beginning of the inversion: Either the geometry of the model or the geophysical property of a cell is modified.

- Modifying geophysical properties:

  The algorithm chooses randomly one cell and selects at random new values for each property as described in step 2. It then computes the new geophysical effect of the perturbed cell.

- Changing the geometry:

  The algorithm chooses randomly a frontier cell c_m. The model may be subdivided into a data set $\{p_0\}$ that may be changed during inversion and a set $\{pc_0\}$ that may not be modified. If c_m or one of its neighbors is element of $\{p_0\}$, a new lithology is chosen randomly within the neighbored formations and is assigned to the cell. Petrophysical properties of the cell are updated according to step 2, and the new effects on the geophysical fields are computed.

The geophysical effects of the model, i.e. the sum of the effects for all geophysical fields are then calculated.

5. Keep or reject the perturbation:

   The misfit Δ_{pert} of the perturbed model is computed in analogy to equation (2.21) for each field j, and the perturbation is kept or rejected according to the following rule:

   - Accept the perturbation if $\Delta_{pert} < \Delta_{cur}$.
   - Randomly keep or reject the perturbation if $\Delta_{pert} \geq \Delta_{curr}$. In this case, the corresponding likelihoods

     $$L_{j,curr} = ke^{-\Delta_{j,cur}/\sigma_j^2} \tag{2.22}$$

     and, in analogy, $L_{j,pert}$ are calculated with the misfit Δ as described in equation (2.21), σ_j^2 being the variance of the geophysical field's data (calculated from the measurement error), and k describing a normalization factor. The perturbation of the model is accepted if the ratio $L_{j,pert}/L_{j,cur}$ is bigger than a probability chosen at random. In this case, the current model is replaced by the perturbed model: $m_{cur} = m_{pert}$. Otherwise, it remains unchanged. The random decision whether to accept or to reject a bigger residual prevents

the inversion from being stopped by a local misfit minimum.

6. Jump to step 4 for the next iteration.

The algorithm iterates around steps 4 and 6 until the maximum number of iterations is reached. The accepted models are stored so that after the inversion, the a-posteriori probabilities of finding the different lithologies in a given cell can be calculated. It is also possible to compute from the accepted models the average petrophysical properties for each cell .

The above algorithm explains the inversion scheme for one geophysical field only. For the joint inversion of multiple fields, the scheme can roughly be subdivided into two parts:

- Run steps 2 and 3 for all fields.
- Start with steps 4 and 5 for the first field. If a perturbation is accepted, do the same steps for the next field until all fields are done, then go to step 6 to start the next iteration. If at any point of this second part the perturbation of one field is not accepted, the responses of the remaining fields are not calculated. The perturbation is rejected and the algorithm goes directly to step 6.

Gravimetric and electromagnetic data are already handled by `GeoModeller`; the implementation of seismic inversion is part of this thesis and described in section 3.3.

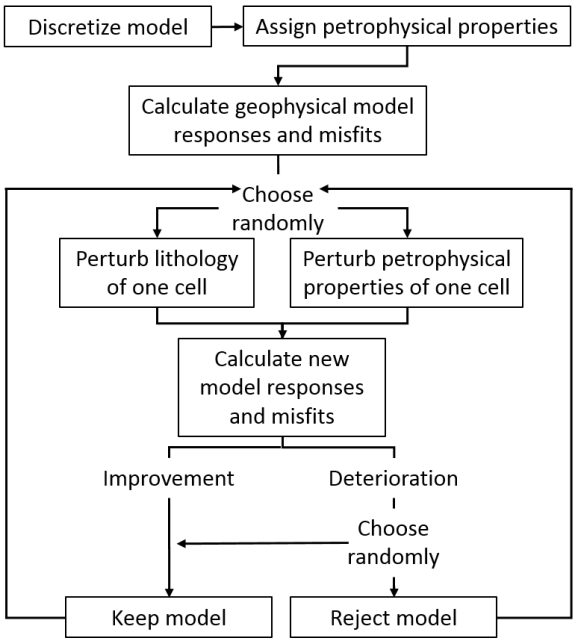

Figure 2.1: Inversion in `GeoModeller` as described in Guillen et al. [2008].

Chapter 3

A Toolbox to Implement Seismic Inversion into `GeoModeller`

Contents

3.1 Travel Time Calculation and Ray Tracing

Seismic tomography exploits travel times of seismic waves to image the Earth's interior. Figure 3.1 shows the principles of the tomographic method: Seismic waves emitted by a source propagate through the subsurface before being recorded by a receiver. Reflection and refraction methods determine depths of interfaces from known or assumed seismic velocities. Seismic tomography uses travel times to invert the seismic velocities in the underlying medium.

Travel times are computed in a velocity model described by blocks of constant velocities. Starting at the source location at time zero, the first arrivals at each node of the discretized model are calculated following the Huygen's Principle, which states that each point of a wave front can be regarded as a secondary source emitting a new signal [e.g. Flood and West, 1952]. As a consequence, to calculate the first arrival time at a given point, we consider the neighboring points that have already been assigned to an arrival time as secondary Huygen's sources. Additional sources can be obtained by interpolation between these neighbors. Each of these Huygen's sources is now assumed to emit a signal at the time it is reached by the wave front. The arrival time at the current point

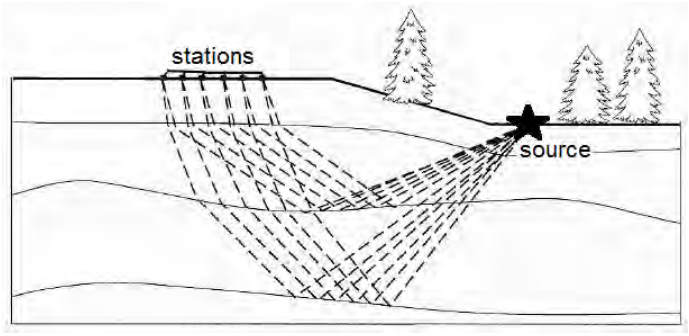

Figure 3.1: The principle of seismic tomography (modified from Brückl et al. [2005]). Seismic waves emitted by a source may be reflected or refracted at seismic interfaces before being recorded by a receiver. Knowledge of source position and arrival times allows us to invert the seismic velocities of the underlying medium. Note that, especially for passive seismic sounding, in which earthquake data are exploited, sources may lay at depth.

of investigation is calculated by considering the different possible paths from the points that have already been reached by a wavefront and by keeping the one that gives the lowest arrival time for this point.

The estimation of the arrival times requires the solution either of the standard or of the factored eikonal equation. If the distance between the wave front and the source is large enough to neglect the curvature of the wave front, i.e. to assume a plane wave, we may solve the standard eikonal equation [Fomel et al., 2009; Noble et al., 2014]:

$$\left(\frac{\partial t}{\partial x}\right)^2 + \left(\frac{\partial t}{\partial y}\right)^2 + \left(\frac{\partial t}{\partial z}\right)^2 = s^2(x, y, z) \tag{3.1}$$

where t is the travel time, defined on cell corners, s the slowness, constant in each cell, and x, y, z the cartesian coordinates. For distances shorter than five to ten nodes from the source, however, the plane wave approach is too imprecise, and spherical wave fronts have to be considered. This requires the solution of the factored eikonal equation [Noble et al., 2014]

$$t_0^2 \left(\nabla\tau\right)^2 + \tau^2 s_0^2 + 2\tau t_0 \nabla t_0 \nabla\tau = \left(s_0\alpha\right)^2 \tag{3.2}$$

where $t = t_0\tau$ and $s = s_0\alpha$. If for all cells s_0 is set to the slowness value at the source, t_0 can be calculated analytically at all grid points. The parameter τ describes the perturbation of travel time

```
for all stations:
   for all events recorded at this station:
        do while distance (actual point - station) > ε:
             calculate and normalize gradient at source point:   norm = 1 / (2 · sqrt(grad_x^2 + grad_y^2 + grad_z^2))
             calculate next point:   x_{i+1} = x_i − h · grad_x · norm
                                     y_{i+1} = y_i − h · grad_y · norm
                                     z_{i+1} = z_i − h · grad_z · norm
             adjust last 5 points to reach station position:   l_j = j/5
                                     x_{i−5+j} → x_{i−5+j} + l_j · (x_sta − x_i)
                                     y_{i−5+j} → y_{i−5+j} + l_j · (y_sta − y_i)
                                     z_{i−5+j} → z_{i−5+j} + l_j · (z_sta − z_i)
for all rays:
   get length of ray segment for each cell and corresponding seismic velocity
   Calculate travel time:   t_cell = l_cell / v_cell
                            t_ray = Σ t_cell
```

Figure 3.2: Pseudo-code used for raytracing.

resulting from the slowness perturbation α [Fomel et al., 2009; Noble et al., 2014].

The reciprocity principle states that the travel time is the same, whether a signal propagates from A to B or from B to A. Since for this work, we have a much smaller number of receivers than sources, the code is parallelized over the stations. The stations are thus considered as the starting point of waves, and time tables containing the arrival times at all grid nodes are computed for each station. The arrival time at the source can then be interpolated from the values at the surrounding nodes. This reciprocity of sources and receivers allows us to save computation time. In the following, however, we will use the common terminology of source for the starting point and receiver for the arrival point of a wave.

Once the time table for a receiver is calculated, a-posteriori raytracing can be performed. This allows to increase the precision of the calculated travel time [Monteiller et al., 2005] and to save computation time during seismic inversion because updated travel times can be integrated along

the ray paths instead of being computed for the complete model.

In a first step, the ray paths from the different sources to the receiver are determined using the steepest gradient method, as illustrated by the pseudo-code in Figure 3.2. For this, we use a code written by V. Monteiller (pers. comm.). Starting at the source, the normalized gradient ∇ is calculated:

$$\nabla = \frac{1}{2 \cdot \sqrt{\nabla_x^2 + \nabla_y^2 + \nabla_z^2}} \tag{3.3}$$

The next point $(x_{i+1}, y_{i+1}, z_{i+1})$ of the ray is then computed as follows, with h describing the grid spacing:

$$x_{i+1} = x_i - h \cdot \nabla_x \cdot norm \tag{3.4}$$

$$y_{i+1} = y_i - h \cdot \nabla_y \cdot norm \tag{3.5}$$

$$z_{i+1} = z_i - h \cdot \nabla_z \cdot norm \tag{3.6}$$

This loop is repeated until the distance between point $(x_{i+1}, y_{i+1}, z_{i+1})$ and the station position is less then a threshold value ϵ. The last five points of the ray are then adjusted so that the ray arrives exactly at the receiver:

for j=1,5: $$l_j = \frac{j}{5} \tag{3.7}$$

$$x_{i-5+j} \rightarrow x_{i-5+j} + l_j \cdot (x_{sta} - x_i) \tag{3.8}$$

$$y_{i-5+j} \rightarrow y_{i-5+j} + l_j \cdot (y_{sta} - y_i) \tag{3.9}$$

$$z_{i-5+j} \rightarrow z_{i-5+j} + l_j \cdot (z_{sta} - z_i) \tag{3.10}$$

In a second step, a-posteriori raytracing is performed. For this, the positions at which a ray crosses a grid line are calculated and stored. The length of a ray segment in a given cell and the

corresponding seismic velocity value give the time that the ray spends inside the cell:

$$t_{cell} = \frac{l_{cell}}{v_{cell}} \tag{3.11}$$

The sum of these times yields the total travel time from the source to the receiver:

$$t_{ray} = \sum t_{cell} \tag{3.12}$$

We will show in section 3.2 that travel times obtained from a-posteriori raytracing are more precise than the calculation described above.

3.2 Computation Time and Precision

In order to choose the most adequate code to perform the travel time calculation, two routines, respectively developed by Podvin and Lecomte [1991] and Noble et al. [2014], are compared in terms of computation time and precision. The routines are presented first, and then their performances are compared.

3.2.1 `time3d` [Podvin and Lecomte, 1991]

Podvin and Lecomte [1991] provide the routine `time3d` written in C for calculating the time of the first arrival at each node with the plane wave approach, i.e. by solving the standard eikonal equation (3.1). The partial derivatives of the travel time are computed by finite differences from the travel times at neighboring points. Depending on which nodes the arrival times have already been calculated and how the wave front is considered to be transmitted, up to 170 arrival times are calculated in order to determine the first arrival at the considered node. The different operators are sketched in Figure 3.3; for their derivations, see Podvin and Lecomte [1991].

Six 1D operators are defined from the values at the nearest neighbors of the actual point, i.e. by the points directly connected to the point of investigation. They represent head waves traveling along the intersection between two cells with different slowness values. Twelve 2D operators defined

by the corners lying in the same planes as the actual point describe diffracted arrivals arriving from these corners. Eight 3D operators describe diffracted arrivals from the corners that are in diagonal position with the current point, and 24 2D operators describe diffraction from co-planar edges. 24 3D operators describe the arrivals from non-co-planar edges, and finally, 96 3D operators calculate the travel time from opposite planes. Each of this 96 operators is defined by three points, halving the plane, i.e. each plane provides four operators.

The plane wave assumption is valid only far away from the source. If the source is located in a homogeneous velocity zone with a radius of at least 10 nodes, travel times for the points inside may be computed directly. Otherwise, Podvin and Lecomte [1991] propose to refine the grid spacing around the source until this criterion is fulfilled.

3.2.2 `FTeik3D-3.0` [Noble et al., 2014]

For the routine `FTeik3D-3.0` (in the following: `FTeik3D`), Noble et al. [2014] follow the suggestion of Afnimar and Kazuki Koketsu [2000] to calculate 16 arrival times per point and per direction of propagation. The operators are sketched in Figure 3.4 (for their derivations, see Noble et al. [2014]).

One 3D operator defined by seven neighboring nodes describes the transmission through the cell after Vidale [1990]. Three 3D operators defined respectively by the four points of opposite planes allow the arrival time calculation separately for converging wave fronts or if not all eight neighbors are defined as proposed by Afnimar and Kazuki Koketsu [2000]. In case one of those points is missing, six 2D operators are defined using only two neighboring points as proposed by Podvin and Lecomte [1991]. Three 2D operators defined by the three neighboring points of the surfaces containing the actual point describe arriving head waves as proposed by Hole and Zelt [1995]. Three 1D operators defined by one neighboring point describe head wave arrivals along edges as proposed by Podvin and Lecomte [1991]. Exactly as in the code of Podvin and Lecomte [1991], all possible arrival times are calculated for the current point, according to the previously described operations. The minimal time is then taken as the first arrival at this point.

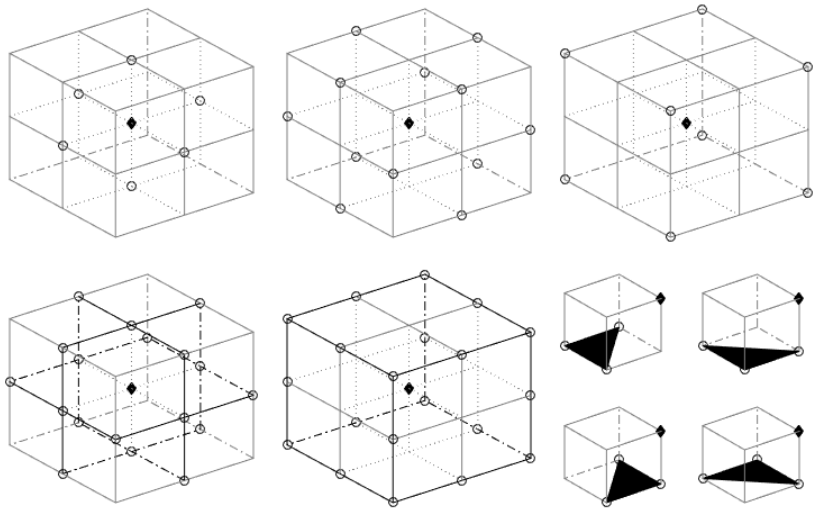

Figure 3.3: Operators for travel time calculation after Podvin and Lecomte [1991]. The black diamond represents the current point; the open circles describe the points used for traveltime interpolation. The method considers (top, from the left to the right) six 1D operators defined by the nearest neighbors of the current node, 12 2D operators defined by the corners surrounding the current node, i.e. defined by the second nearest neighbors, and eight 3D operators defined by the third nearest neighbors, i.e. by the eight outer corners. These operators interpolate the travel time directly form each point to the current node. Furthermore (bottom, left and center), it considers 24 2D operators defined by the edges lying in the same planes as the current point and 34 3D operators defined by the non-co-planar edges. These edges are marked in black. Finally, 96 3D operators may be calculated, each defined by three points building a half of a non-coplanar plane. Each of the eight cubes surrounding the current point have three planes that are non-coplanar with the point. Each of these planes can be described by four different halves as depicted in the bottom right pannel.

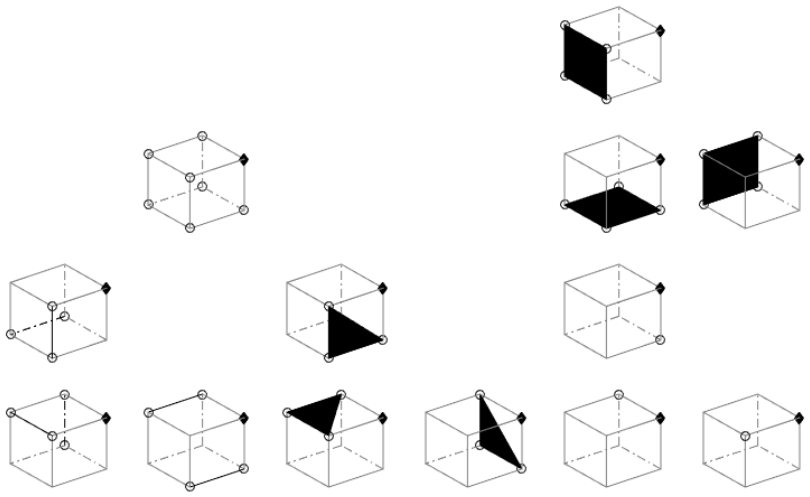

Figure 3.4: Operators for traveltime calculation after Noble et al. [2014]. The black diamond describes the current node and the circles define the points used for travel time interpolation. If these points define an edge or a plane, these are marked in black. For each direction of wave propagation, the method uses one 3D operator defined by seven neighboring points (top, left), three 3D operators defined each by the four points of an opposite plane (top, right), six 2D operators defined by opposite edges (bottom, left), three 2D operators defined each by three points lying in the same plane as the current node (bottom, center), and three 1D operators described by the nearest neighbors (bottom, right).

At the beginning of the routine by Noble et al. [2014], the arrival time is set to zero at the source location and to infinity at all the other points. The time table is then calculated applying the 16 operators described above over the entire model and along eight possible directions of propagation. The lowest time value is stored at each point, and the algorithm is repeated until all the nodes have been reaches by a wave-front.

However, the main difference to `time3d` is the calculation near the source. While Podvin and Lecomte [1991] use the plane wave assumption for the entire model and refine the grid around the source if necessary, Noble et al. [2014] take the plane wave assumption for a large part of the model, but the spherical wave approach given by the factored eikonal equation (3.2) for points that are closer than five to ten nodes from the source.

grid spacing	no. of nodes				velocity at depth
(m)	total (10^3)	x	y	z	(m/s)
2000	576.0	120	160	30	9789.00
1000	4631.2	240	320	59	9753.50
500	36249.6	480	640	118	9771.25

Table 3.1: Setup for comparison of travel time computations. The origin is the same for all cases (x = 240 000 m, y = 6 050 000 m, z = −4 000 m in Lambert 93 or $lon = -2.4899062\,\text{deg}$, $lat = 41.4078155\,\text{deg}$ in WGS84). The indicated P wave velocity at depth is reached with a surface value of 5600 m/s and a constant gradient of 0.071 (m/s)/m.

3.2.3 Comparison

For the comparison of the two routines, we compute seismic travel times in a 1D model made of a constant velocity gradient, i.e. with a seismic velocity $v(z)$ increasing linearly with depth z:

$$v(z) = v_0 + bz \tag{3.13}$$

Here, b describes the vertical velocity gradient. The analytical travel time t from a source to a station, both at the surface ($z = 0$) of a medium with such a velocity gradient, is given by [Slawinski and Slawinski, 1999]:

$$t = \frac{2}{b} \ln \left| \frac{1}{pv_0} \left(1 - \sqrt{1 - p^2 v_0^2} \right) \right| \tag{3.14}$$

with

b velocity gradient

p ray parameter $p^2 = 1/(x^2 b^2 + v_0^2)$, x: distance to source

v_0 velocity at the surface

For our tests, we place a source at the surface and compute the travel times for a profile of ten receivers separated by 10 km. The space between the source and the first station is 10 km. The origin of the test box coincides with the origin of the Pyrenees model, that is x = 240 000 m,

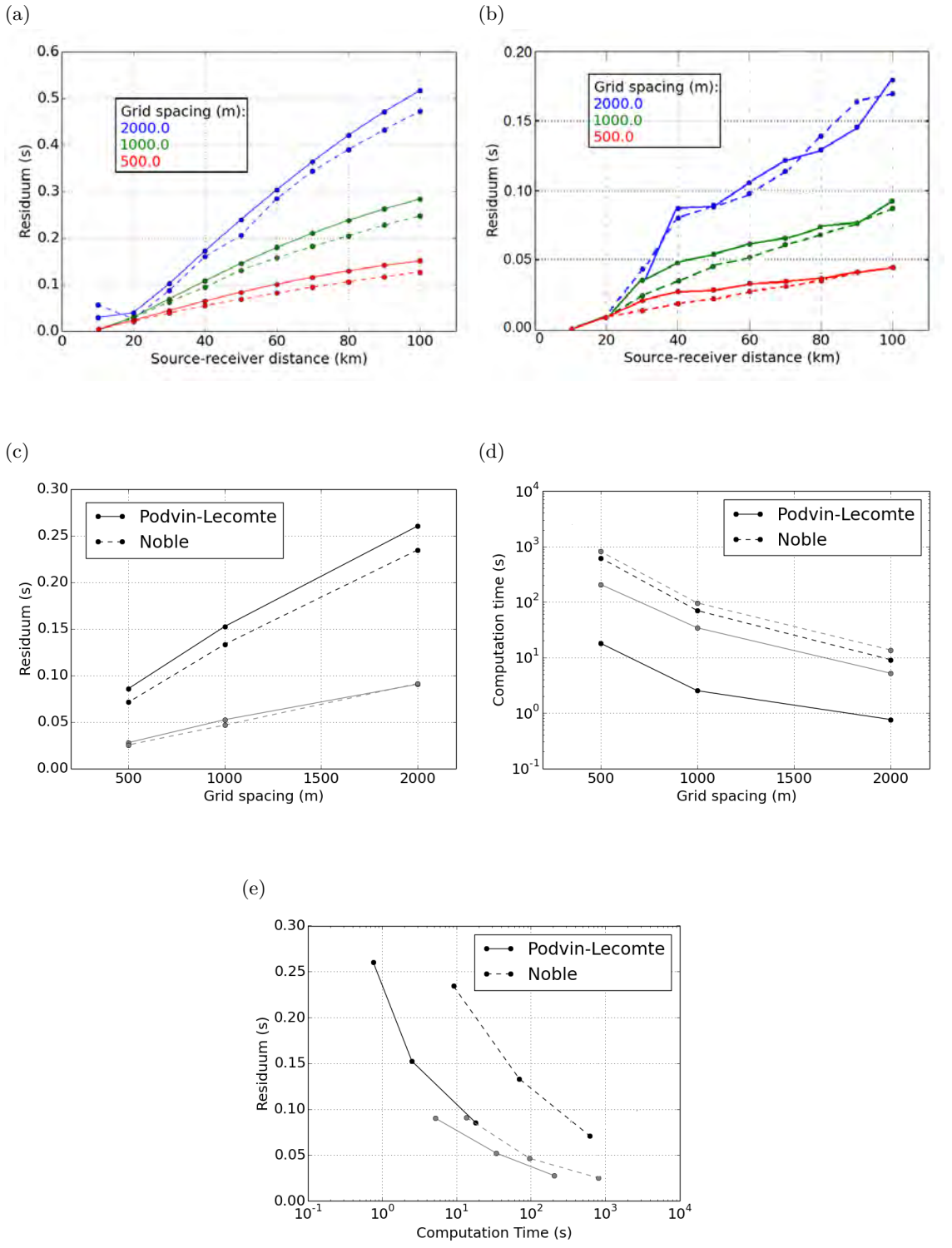

Figure 3.5: Comparison of the raytracing codes of Podvin and Lecomte [1991] (solid lines) and Noble et al. [2014] (dashed lines). **a-b:** Travel time residuals before (**a**) and after (**b**) back-raytracing as a function of distance. **c-e:** Comparisons between residuals, computation times, and grid spacings, averaged over all data. Black lines represent results after direct travel time calculation only, gray lines include the back-raytracing.

y = 6 050 000 m, z = −4 000 m in Lambert 93 (lon=-2.4899062°, lat=41.4078155° in WGS84). The box extends over 240 km, 320 km, and 59 km respectively along the the North, South, and depth directions. Travel time computations are performed for grid spacings of 2000, 1000, and 500 m (Table 3.1) and compared to the theoretical travel time given by eq. (3.14). The P wave velocity is uniform in each cell and is set to 5600 m/s at the surface, with a constant vertical gradient of b = 0.071 (m/s)/m. At the bottom of the box, it reaches between 9789.00 m/s (2000 m spacing) and 9771.25 m/s (500 m spacing).

Figure 3.5 shows the comparison of computation times and travel time residuals between the two methods. Travel time residuals before and after a-posteriori raytracing are given as a function of the source receiver distance in figures 3.5a and 3.5b. For all tested grids, the residuals increase with the epicentral distance. The code `FTeik3D` [Noble et al., 2014] yields a slightly better precision (up to 0.03 s). A-posteriori raytracing allows us to reduce the residuals by a factor between three and four.

Figures 3.5c and 3.5d show the average residuals and the computation times as a function of grid spacing. Residuals obtained from the two routines differ by less than 0.02 s, `FTeik3D` being more precise. However, `time3D` requires much less computation time. Figure 3.5e demonstrates that the computation time in order to obtain the same travel time residuals is 12 to 16 times smaller with `time3d`, depending on the grid spacing.

Finally we judge that a residual improvement of a factor 2 does not justify a computation time 12 to 15 times larger. For this reason, we decide to use `time3d` for our modeling. In order to still keep the residuals reasonably small, we choose a grid spacing of 500 m, which represents a good compromise between computation time and precision.

3.3 Implementation of Seismic Travel Time Inversion

During the inversion process, the seismic velocity model is perturbed and new travel times are calculated. For efficiency, we do not recompute the ray paths in the new velocity model at each

iteration. Instead, we calculate the effect of the velocity perturbation on the rays computed in the original model. This approach is justified by Fermat's principle, as described e.g. in Zhdanov [2015], Romanowicz and Dziewonski [2010], or Sen and Stoffa [2013], stating that small velocity perturbations result in very small perturbations of the ray geometry. Differences between the new and the old ray paths are thus negligible, and new paths need to be computed only after a large number of iterations, when the velocity model shows strong deviations from the a-priori model. The cells that are crossed by seismic rays are stored in a sparse matrix, the inversion of which is described below.

The computation of the new travel times is done via a matrix-vector multiplication

$$\mathbf{d} = \mathbf{G} \cdot \mathbf{x}, \tag{3.15}$$

where $\mathbf{G}(nray \times n)$ represents the lengths of the ray segments for each of the $nray$ rays (rows) and each of the n cells (columns), $\mathbf{x}(n)$ describes the slowness perturbation in each cell, and $\mathbf{d}(nray)$ is the resulting travel time perturbation for each ray.

In order to reduce the size of the problem and the memory requirements, the sparse matrix $\mathbf{G}$ is decomposed into vectors. Press et al. [2003] describe how to generate a sparse matrix representation with two vectors: one vector **sa** containing the non-zero elements of $\mathbf{G}$, starting with the diagonal, then listing the other ones row-wise, and another vector **ija** indicating which elements of **sa** belong to which row of $\mathbf{G}$.

Following a similar method, we decompose the sparse matrix $\mathbf{G}(nray \times n)$ into three vectors: The first vector, $\mathbf{ma}(nma)$, contains the nma non-zero elements of $\mathbf{G}$. These elements are stored row-wise and, in contrast to the method by Press et al. [2003], without any distinction between diagonal and other entries. The second vector $\mathbf{il}(nray + 1)$ is a simplified version of **ija** mentioned above. Its i^{th} element is the index at with the ith row of $\mathbf{G}$ starts in $\mathbf{ma}(nma)$. Its last element is $nma + 1$. The third vector is a column index vector $\mathbf{ic}(nma)$. Its j^{th} entry indicates the column in $\mathbf{G}$ to which the j^{th} element of **ma** belongs.

For example, the sparse matrix

$$\mathbf{G} = \begin{pmatrix} 10 & 20 & 0 & 0 & 30 & 40 & 0 \\ 0 & 50 & 0 & 60 & 0 & 0 & 70 \\ 80 & 0 & 0 & 0 & 90 & 0 & 0 \end{pmatrix}$$

is decomposed as follows:

$$\begin{aligned} \mathbf{ma} &= \begin{pmatrix} 10 & 20 & 30 & 40 & 50 & 60 & 70 & 80 & 90 \end{pmatrix} \\ \mathbf{il} &= \begin{pmatrix} 1 & 5 & 8 & 10 \end{pmatrix} \\ \mathbf{ic} &= \begin{pmatrix} 1 & 2 & 5 & 6 & 2 & 4 & 7 & 1 & 5 \end{pmatrix} \end{aligned}$$

This decomposition allows us to calculate the product of the sparse matrix $\mathbf{G}$ and a vector $\mathbf{x}$ with this very simple algorithm (modified after Press et al. [2003]):

```
d(i) = 0
for i = 1,nray
   for j = il(i), il(i+1)-1

                    d(i) = d(i) + ma(j) * x(ic(j))                    (3.16)
```

.

During the inversion in `GeoModeller`, only one cell is perturbed per iteration. The vector $\mathbf{x}$ in equation (3.16) is thus zero for all elements but one, and we may save computation time by solving (3.16) only for rays that pass through this cell:

```
for i in rays crossing current cell ic(j):
      d(i) = d(i) + ma(j) * x(ic(j))
```

For joint inversion, several options are available: Invert for gravity only (in this case we do not call the above algorithm), P waves only, P and S waves only, or P and S waves and gravity jointly. If more than one field is inverted, options for coupling are:

- Impose a relation between density and velocity: Instead of taking the perturbed velocity value from its probability density function (pdf), a new density is computed randomly from its pdf and used to calculate the new velocity according to the relationship proposed by Ludwig et al. [1970] (eq. (5.5)).
- Impose v_P/v_S ratio. Default is v_P/v_S=1.71±0.01, but other values may be chosen.

Since travel time computation requires less computational effort than gravity modeling, seismic fields are always the first fields to be computed. If a perturbed model is rejected by seismic inversion, its Bouguer anomalies are not calculated.

Chapter 4

Construction of the 3D Geological Model

Contents

This chapter has been submitted as: "A Three-dimensional model of the Pyrenees and their foreland basins from geological and gravimetric data" by Hannah Wehr, Sébastien Chevrot, Gabriel Courrioux, and Antonio Guillen to Tectonophysics in October 2017. Modeling with the `GeoModeller` software requires orthogonal coordinates, but geological data are usually referenced in WGS84

latitude and longitude. The transformation between WGS84 coordinates and the orthogonal Lambert93 system is explained in appendix A.1. Details of the borehole analysis are shown in A.2, and the stratigraphic pile as used in `GeoModeller` is described in A.3.

4.1 Abstract

We construct a three-dimensional geological model of the Pyrenees and their foreland basins with the `GeoModeller`. This model, which accounts for all the geological and geophysical information available, covers the whole Pyrenees, from the Atlantic Ocean to the Mediterranean Sea, and from the Iberian range to the Massif Central, down to 70 km depth. We model the geological structure with a stratigraphic column composed of a superposition of layers representing the mantle, lower crust, middle crust, and upper crust. The sedimentary basins are described by two layers which allow us to make the distinction between the Mesozoic consolidated sediments and the Cenozoic unconsolidated sediments. Since the Pyrenees result from the convergence between the Iberian and European plates, we ascribe to each plate its own stratigraphic column in order to be able to model the indentation and superposition of the Iberian and European crusts. We also introduce two additional units which describe the accretionary prism and the water column in the Bay of Biscay and in the Mediterranean Sea. The last ingredient is a unit that represents the bodies of shallow exhumed serpentinized mantle, which are assumed to produce the positive Bouguer gravity anomalies observed beneath the North Pyrenean Zone. A first 3D model is built using only the geological information coming from geological maps, drill-hole surveys, and seismic sections. We use the potential field method implemented in `GeoModeller` to interpolate these geological data. This model is then refined in order to better explain the observed Bouguer gravimetric anomalies by adding new constraints on the main lithological interfaces by trial-and-error. The final model explains the observed Bouguer anomalies with a standard deviation less than 3.5 mGal.

4.2 Introduction

The Pyrenees are a collisional system produced by the convergence between the European and Iberian plates during the Cenozoic [e.g Le Pichon and Sibuet, 1971; Vergés et al., 2002; Choukroune, 1992; Beaumont et al., 2000; Muñoz, 1992; Mouthereau et al., 2014]. It is an east-west, bivergent orogen, flanked by two flexural foreland basins. It is classically divided into five units: (1) The Aquitaine Basin (AB), overthrusted by (2) the North Pyrenean Zone (NPZ), the Axial Zone (AZ) mainly composed of hercynian basement rocks, the South Pyrenean Zone (SPZ), which overthrusts the Ebro Basin (EB) (Figure 4.1).

Many different models have been proposed for the kinematics of the Iberian plate during the Mesozoic [e.g. Sibuet et al., 2004; Jammes et al., 2009; Vissers and Meijer, 2012; Barnett-Moore et al., 2016]. Since the rotation of Iberia occurred during the Cretaceous Normal Superchron, there is thus no seafloor anomaly to document intermediate stages between magnetic anomalies M0 (118 Ma) and 34 (85 Ma). In addition, the nature of anomaly M0, which is key to reconstruct the motion of Iberia from magnetic anomalies, is now strongly debated [Bronner et al., 2011; Tucholke and Sibuet, 2012; Barnett-Moore et al., 2016]. Therefore, the relative movement of Iberia with respect to Europe during the Mesozoic remains highly controversial, and consequently one has to consider geological information as well as constraints coming from geophysical studies to reconstruct the Pyrenean architecture.

4.2.1 A Quick Overview of Past Geophysical Investigations in the Pyrenees

There are rich and varied sources of information coming from geological studies to constrain the shallow upper crust. However, the results of previous geophysical studies hold the key to constrain the deep architecture of the Pyrenees.

A pioneering study exploited the critical reflections on the Moho from two fan profiles deployed in the central and eastern Pyrenees [Daignières et al., 1982] and evidenced thick crustal roots beneath the Axial Zone in the central Pyrenees. A sharp vertical 15 km Moho offset, located

approximately beneath the North Pyrenean Fault, marked the limit between the thickened Iberian crust and the European crust. In the eastern Pyrenees, this Moho jump is reduced to about 5 km, reflecting the crustal thinning related to the opening of the western Mediterranean basin and the retreat of the Tyrrhenean slab [Wortel and Spakman, 2000; Gunnell et al., 2008]. A few years later, the ECORS-Pyrenees profile [Choukroune, 1989; Roure et al., 1989; Teixell, 1998] was shot across the central Pyrenees. The shallow reflectors confirmed the bivergent geometry of the range, with south-vergent thrusts in the south and north-vergent thrusts in the north. Deep reflectors provided the first evidence for the underthrusting of the Iberian plate beneath the European plate. However, the nature and depth extent of the subducted material remained poorly constrained. Owing to strong uncertainties regarding the fate of the Iberian lower crust, different balanced cross-sections were proposed to reconstruct crustal structures along the ECORS line. According to Roure et al. [1989], the deep Iberian crust is currently stacked beneath the axial zone, while Muñoz [1992] favors continental subduction, with a minimum of 65 km of Iberian lower crust that would have disappeared beneath the European plate. For the same reason, the exact amount of convergence in the Pyrenees is still debated, with values ranging from 100 km [Roure et al., 1989] to 147 km [Muñoz, 1992].

Owing to the small number of permanent broadband stations installed in the Pyrenees, the deep structures beneath the Pyrenees were poorly illuminated with telesesimic waves which severely limited the resolution of passive tomographic studies at depth. The PYROPE and IberArray temporary deployments [Chevrot et al., 2014], with a backbone of about 130 broadband stations and a station spacing of around 70 km, provided a dense and homogeneous coverage of the deep architecture of the Pyrenees. The regional P-wave travel-time tomography by Chevrot et al. [2014] did not find any evidence for a coherent high-velocity anomaly at depth, which seems to preclude the subduction of an oceanic domain beneath the Pyrenees. In contrast, the tomographic images suggested a non-cylindricity of the range, with lithospheric structures segmented by major NE-SW transfer zones such as the Toulouse Fault and the Pamplona Fault. More detailed images were obtained by migrating the receiver functions from two dense transects [Chevrot et al., 2015]. The migrated sections revealed the geometry of the Iberian and European Moho, which were in

excellent agreement with the ECORS-Pyrenees migrated section. A dipping interface corresponding to a downward negative velocity jump, interpreted as the top of the subduction Iberian crust was detected beneath both transects, down to at least 60 km depth. However, the nature of the subducted material and its depth penetration remained poorly constrained.

Another long standing debate is related to the nature and geometry of the dense bodies that produce the strong Bouguer gravity anomalies beneath the NPZ in the western Pyrenees (west of the Toulouse Fault). An early interpretation of Bouguer anomalies along the ECORS-Pyrenees profile [Torné et al., 1989] explained the positive anomaly beneath the NPZ as a slice of mantle or lower crustal material in the upper crust. A later study focused on profiles across the Labourd and Saint-Gaudens anomalies, and across the eastern Pyrenees [Casas et al., 1997]. The strong positive anomalies in the western and central profiles were interpreted as slices of upper mantle exhumed during the transtensional motion of Iberia with respect to Europe, later emplaced at shallow crustal levels during the convergence. They also pointed out that the large positive anomalies are present beneath the NPZ in the central and western Pyrenees, but are absent in the east. This important observation was interpreted as an indication for a smaller amount of extension in the east before the oregenesis, and thus limited exhumation of deep material. An important limitation of these studies was that they relied on two-dimensional modeling, making an implicit assumption of structural cylindricity. A salient feature of the Labourd and Saint-Gaudens anomalies is their limited width of a few tens of km, which would suggest that 2D modeling would tend to overpredict the anomaly produced by a slice of dense material in the upper crust. The only real attempt to build a 3-D density model of the lithosphere able to explain the Bouguer and geoid anomalies is found in Vacher and Souriau [2001]. However, their modeling suffered from a very crude description of basin geometry and crustal structures and quite large misfits between observed and modeled anomalies. Important insight on the source of the positive Bouguer anomalies in the Pyrenees came from Wang et al. [2016]. In this study, very detailed tomographic images of the western Pyrenees were obtained by full waveform inversion of short period teleseismic P waveforms. The images showed a pronounced, north-dipping, low-velocity anomaly, beneath the European plate, providing further support for continental subduction. But the most salient feature was the fast velocity anomaly beneath the

Mauléon basin connected to the European lithospheric mantle, which spatially coincides with the Labourd Bouguer anomaly. Since the thickness of the Mauléon basin is comprised between 6 to 8 km and the top of this fast mantle body is at a depth of about 10 km, this implies that the crust beneath the Mauléon basin has experienced an extreme thinning. This very anormalous structure was interpreted as the results of mantle exhumation during the Cretaceous episode of rifting, with the crust beneath the Mauléon basin representing the remnants of the distal rift margin. In this study, we will assume as a guiding rule that the other positive Bouguer anomalies observed in the central and western Pyrenees have a similar origin. However, these anomalies disappear in the eastern Pyrenees, which would suggest that the rifting was less intense in that region. An alternative explanation would be that the polarity of the rift opening was opposite in the eastern Pyrenees, as recently suggested by Tugend et al. [2014] from detailed geological field observations. If this hypothesis is correct, this would imply a major influence of inheritance in the structuration of this mountain range.

To summarize, after several decades of detailed geological and geophysical studies, the first-order structure of the Pyrenees is now rather well understood. However, several controversies remain, regarding the lateral variations of the deep architecture, in particular the dichotomy between the eastern and western Pyrenees, the nature of the material from the Iberian plate that subducts beneath the European plate, and the depth extent of the subduction.

4.2.2 Objectives and Outlines of this Study

Here, we want to test the hypothesis that positive Bouguer anomalies are produced by exhumed mantle bodies and make a first attempt to better understand the apparently strong dichotomy between the eastern and western Pyrenees. The other motivation is to obtain a 3-D model that can be used as an a priori model in future crustal tomographic studies of the Pyrenees or for refining the location of the Pyrenean seismicity. After describing the main ingredients that were retained to build our 3-D geological model, we present the `GeoModeller` [Calcagno et al., 2008; Lajaunie et al., 1997], a versatile and interactive software which allows us to describe complex 3-D geological models with simple geometrical rules. We then introduce the gravimetric data that were exploited

to refine the model. The final model provides a complete description of this intricated fossile plate boundary, in particular of the complex geometry of sedimentary basins and of the Iberian and European Moho.

4.3 Geological Data

To build our 3D model, we have compiled all the currently available geological information for the Pyrenees. This includes maps of sediment and crustal thickness, seismic and geological sections, and drill-hole data. The topography of the free surface is taken from the SRTM[1]-90 data. The points at altitudes lower than the surface of the sea are put at the base of the sea water unit and an altitude of zero is ascribed to these points.

From the different data sources described below, we extract the bases of lower, middle, and upper crust, as well as of Mesozoic and Cenozoic sediments. In case of inconsistency between different sources, priority is given to 1. geological maps and 3D model of Lourdes, 2. borehole data, 3. shallow cross-sections for the sediments, and 4. deep seismic profiles for the Moho. The distribution of the geological data sources is depicted in Figure 4.2, the extracted 3D points in figure 4.3.

4.3.1 Geological Maps

The surface geology is taken from the 1/400 000 geological map of the Pyrenees published by BRGM/IGME, the synthesis by Barnolas and Courbouleix [2001], as well as the 1/50 000 Geological Maps of France published by the BRGM[2]. For the Spanish side, the 1/50 000 maps and 1/200 000 maps published by the IGME[3] (Instituto Geológico y Minero de España) are used. We only account for geological structures which are at least kilometric in scale, in order to ensure the coherence and continuity between the different maps. In addition, we discard all the faults except the South and North Pyrenean Frontal Thrusts (SPFT and NPFT), since they describe the main interfaces that

[1] https://www2.jpl.nasa.gov/srtm/
[2] namely maps 879-885, 903-909, 929-935, 955-961, 977-988, 1002-1014, and 1026-1101
[3] maps 31 (Soria) and 32 (Zaragoza)

delimit the accretionary prism.

The geological map shows basement outcrops along the Axial Zone (AZ) (Figure 4.1). These outcrops are surrounded by a band of Mesozoic sediments in the North and South Pyrenean Zones (NPZ and SPZ) while in the foreland basins, mainly Cenozoic sediments are found. The dips of layer boundaries constitute another useful source of information to constrain the model. They are indicated on the 1/50 000 maps only. Along the basement outcrops in the AZ, Mesozoic sediments have a dip of 30° in the west, 40° to 60° in the central zone and 20° in the very east. Dip directions are southward in the south and northward in the north. The tectonic contact yielding the crustal outcrop in the south-west is simulated by a Mesozoic base dipping 30° NE in the north and 50° SW in the south. Cenozoic dips range between 20° NE and 50° NE in the north, constrained by the Cenozoic isobaths described below, and between 20° SW and 30° SW in the south. Around the outcrop in the south-east, Cenozoic and Mesozoic dips are set to 30°, while 3° to 20° are used for the sediments around the Massif Central. In both cases, dip directions are orthogonal to the crustal outcrop. The NPFT is modeled as the base of the accretionary prism, dipping 50° S, while the SPFT is modeled as fault, dipping 40° N (60° N in the very east).

4.3.2 Isobaths of Main Geological Interfaces

Base of Sedimentary Layers

The Pyrenees are surrounded by flexural sedimentary basins. The Aquitaine Basin in the north developed by flexure of the European plate during orogeny [Brunet, 1986; Desegaulx et al., 1990]. It contains late Cretaceous sediments [Deramond et al., 1993], early Eocene, fluvial deposits, and lowermost Oligocene sediments [Fischer, 1984]. The Ebro Basin is marked by Paleocene red beds and Eocene carbonates, evaporites, and marls [Vergés et al., 1995].

The synthesis by Barnolas and Courbouleix [2001] provides isobaths of the base of Cenozoic sediments in the foreland basins (olive green lines in Figure 4.2). Cenozoic sediments have a maximum thickness of 4 km in France and 5 km in Spain. Off-shore, these isobaths are taken from Pellen et al. [2016] and Leroux et al. [2015] for the Mediterranean Sea, and from Tugend et al. [2014]

for the Bay of Biscay. Mesozoic depths are not described by these isobaths but modeled according to cross-sections described below (4.3.4).

Moho

We use the data from Tugend et al. [2014] to constrain the crustal thickness in the Bay of Biscay. Díaz and Gallart [2009] compiled the results of deep seismic sounding experiments to obtain a map of Moho depth for the entire Iberian peninsula. These measurements were recently complemented by Diaz et al. [2016] with receiver function data from the IberArray[4] experiment. A similar model more focused on the Pyrenean region was built by Chevrot et al. [2014] from a compilation of old seismic reflection and refraction experiments and from the receiver functions of the PYROPE temporary deployment. These independent sources of information on crustal thickness show spatial patterns that are strikingly coherent (Figure 4.4). The most salient features on these maps are the thick crustal roots beneath the central and western Pyrenees, and the crustal thinning beneath the eastern Pyrenees, resulting from the opening of the western Mediterranean basin which started around 30 Ma.

However, Díaz and Gallart [2009] and Diaz et al. [2016] point out that their models are not very well constraint around the Pyrenean belt. They acknowledge a lack of data in the southern Pyrenees, near the Ebro basin and an inconsistency between the results of deep seismic soundings and receiver functions, which may be caused by "the complex geometry of the Iberia-Eurasia crustal imbrication" [Diaz et al., 2016]. The interpolated model from Chevrot et al. [2014] does not resolve the sharp contrast between European and Iberian Moho depths. This is why we do not rely on these models. The isobath from Tugend et al. [2014] is taken for the Bay of Biscay, but the Moho beneath the continent will be taken from the deep seismic profiles described below (4.3.3).

[4] http://iberarray.ictja.csic.es/

4.3.3 Deep Seismic Cross-Sections

The ECORS Profiles

In 1985/86, the 250 km long, deep seismic ECORS[5]-Pyrenees section was deployed approximately from Toulouse (France) to Balaguer (Spain) [e.g Choukroune, 1989; Roure et al., 1989]. This was the first seismic survey to cross an entire orogenic belt. The seismic section confirmed the thick Iberian crustal roots beneath the Axial Zone, reaching about 55 km depth south of the NPF, and the fan-shape structure of the belt, with north-vergent thrusts in the north and south-vergent thrusts in the south [Choukroune, 1989]. In addition, deep reflectors beneath the North Pyrenean Fault (NPF) were detected, suggesting that the Iberian plate is underthrusted [Roure et al., 1989] or subducted [Muñoz, 1992] beneath the European plate (Figure 4.5). From this profile, we take Moho depth down to 55 km and the top of the Iberian slab down to 45 km. At this point, we do not decide between subduction and stacking. The accretionary prism is retraced as the top of Iberian crust in Spain and as the base of the prism in France.

A second profile, the ECORS-Arzacq line, was shot in the western Pyrenees in 1989 [Daignières et al., 1989; Teixell, 1998]. This second profile provided more ambiguous results. The seismic section did not show a coherent European Moho, and the Iberian Moho was also poorly constrained, because the acquisition did not cover the Spanish side of the belt. However, deep reflectors were interpreted as evidence for the underthrusting of the Iberian plate beneath the European plate [Daignières et al., 1989; Teixell, 1998]. From this very imperfect information, Teixell [1998] proposed a reconstruction model in which the European crust indents the Iberian crust so that only the lower Iberian crust subducts (cf. Figure 4.6). Such a model, however, cannot explain the positive Bouguer anomaly observed on top of the Mauléon basin. This is why we do not consider Teixell's reconstruction in our 3D model, but instead rely on the interpretation of the PYROPE02 profile described below.

[5]Etude continentale et Oceanique par Reflexion et Refraction Sismique; engl.: continental and oceanic seismic reflection and refraction study

The PYROPE and OROGEN Transects

Between 2012 and 2016, five transects were deployed across the Pyrenees, during the PYROPE[6] and OROGEN projects (Figure 4.2). PYROPE-01 approximately follows the ECORS-Pyrenees line, PYROPE-02 was deployed close to the ECORS-Arzacq profile, crossing the Labourd gravity anomaly. PYROPE-03 crosses the central Pyrenees, just west of the Saint-Gaudens anomaly. OROGEN-01 consists of two transects in the eastern Pyrenees, one oriented SSW-NNE in the east of the negative axial zone gravity anomaly and the second one oriented WE crossing the first one in the middle. Finally, OROGEN-02 is located between the first and fourth transect, around the longitude of Carcassonne.

Common conversion point (CCP) stacking of receiver functions from PYROPE-01 and PYROPE-02 provided detailed geometries of the Iberian and European Moho [Chevrot et al., 2015]. Beneath both profiles, the Moho is gently dipping toward the north beneath the AZ, where the thickest crustal roots are observed. It dips more strongly beneath the NPZ, where it can be followed down to about 50 to 60 km depth. Another striking feature observed in both profiles is the negative polarity interface which roughly parallels the Iberian Moho, interpreted as the top of the subducted Iberian crust. Beneath the NPZ, the Iberian and European Moho are thus superposed. For this reason, we had to consider two distinct stratigraphic columns for the Iberian and European plates in order to be able to describe the complex imbrication of the two plates along this fossil plate boundary. Finally, the migrated sections suggest an upwelling of the European Moho beneath the NPZ, moderate in the central profile with an uplift up to about 25 km depth and more pronounced in the west, around 10-15 km. The tomographic images obtained by inverting teleseismic P waveforms recorded by the western profile [Wang et al., 2016] provided a clear and undisputable evidence for this mantle exhumation. Further north, the European Moho is around 30 km depth beneath the Aquitaine Basin. The migrated sections obtained with the three additional profiles [Chevrot et al., 2015] provided crucial constraints to characterize the lateral variations of the main crustal interfaces along the Pyrenean range.

For our 3D model, we take the Moho revealed by the PYROPE and OROGEN profiles, divide

[6]Pyrenean Observational Portable Experiment

the crust into upper, middle, and lower crusts, and estimate the base of the accretionary prism. Furthermore, we introduce a unit for the exhumed mantle revealed by the PYROPE profiles, and model its base at ∼20 km depth.

4.3.4 Geological Sections

Barnolas and Courbouleix [2001] constructed geological sections across the Pyrenees (green lines in Figure 4.2). In their sections, the thickness of sediments varies mainly between 3 and 7 km but reaches a maximum of 10 km beneath the Arzacq Basin and the Alavais Synclinal. However, as shown in Figure 4.7, owing to their poor georeference, their localisation in the model is approximate. Horizontal offsets in topography between the cross-sections and the 3D model, as well as in geology between the cross-sections and other 2D or 3D data are met in all sections of Barnolas and Courbouleix [2001] and may reach 14 km in the case of topography and 17 km for the location of the NPFT as in the example presented in Figure 4.7. This is why we use these sections as rough information only, i.e. we retrace the geometry but move it according to the shift estimated for each transect. In case of inconsistency, we grant these sections less priority than other data, such as surface maps or drill-holes.

4.3.5 Shallow Seismic Sections in the Aquitaine Basin

Serrano et al. [2006] present shallow seismic sections across the Aquitaine Basin (orange transects in Figure 4.2). The thickness of sediments in these sections is comprised between 2 and 9 km. The geology is constrained by nearby drill-holes (see below). Discontinuities in the data points suggest the presence of thrusts and faults which are, however, too small to be modeled at the scale of our project. They are thus interpolated instead.

4.3.6 Borehole Data

Data from 117 drill holes provided by Serrano et al. [2006] and mainly located in the Aquitaine Basin were also exploited (triangles in Figure 4.2). They reach depths from a few hundreds to nearly

7000 m and cross mainly Cenozoic and Mesozoic structures. They are used to verify the data of the shallow seismic sections in the Aquitaine Basin. Additional information come from Filleaudeau [2011] who compiled the geological information from drill holes in the French and Spanish foreland basins. From these data, 75 points can be extracted and imported to `GeoModeller` as 3D points describing the base of Cenozoic and Mesozoic sedimentary layers (points in Figure 4.2). As drill-hole logs contain very localized information which might differ from regional structures, we use these points in order to verify realistic interpolation, but we do not include these 2D points in interpolation.

4.3.7 3D Model of Lourdes Area

BRGM [not published] built a 3D geological model of the Lourdes region, where a small positive Bouguer anomaly is observed, approximately located at equal distance from the Saint-Gaudens and Labourd anomalies. The model extension is 65 km along the east-west direction, 51 km along the north-south direction, and 15 km in depth. Its main structural units (crust, Mesozoic and Cenozoic sediments) are imported into our 3D model of the whole Pyrenees (purple lines in Figure 4.2).

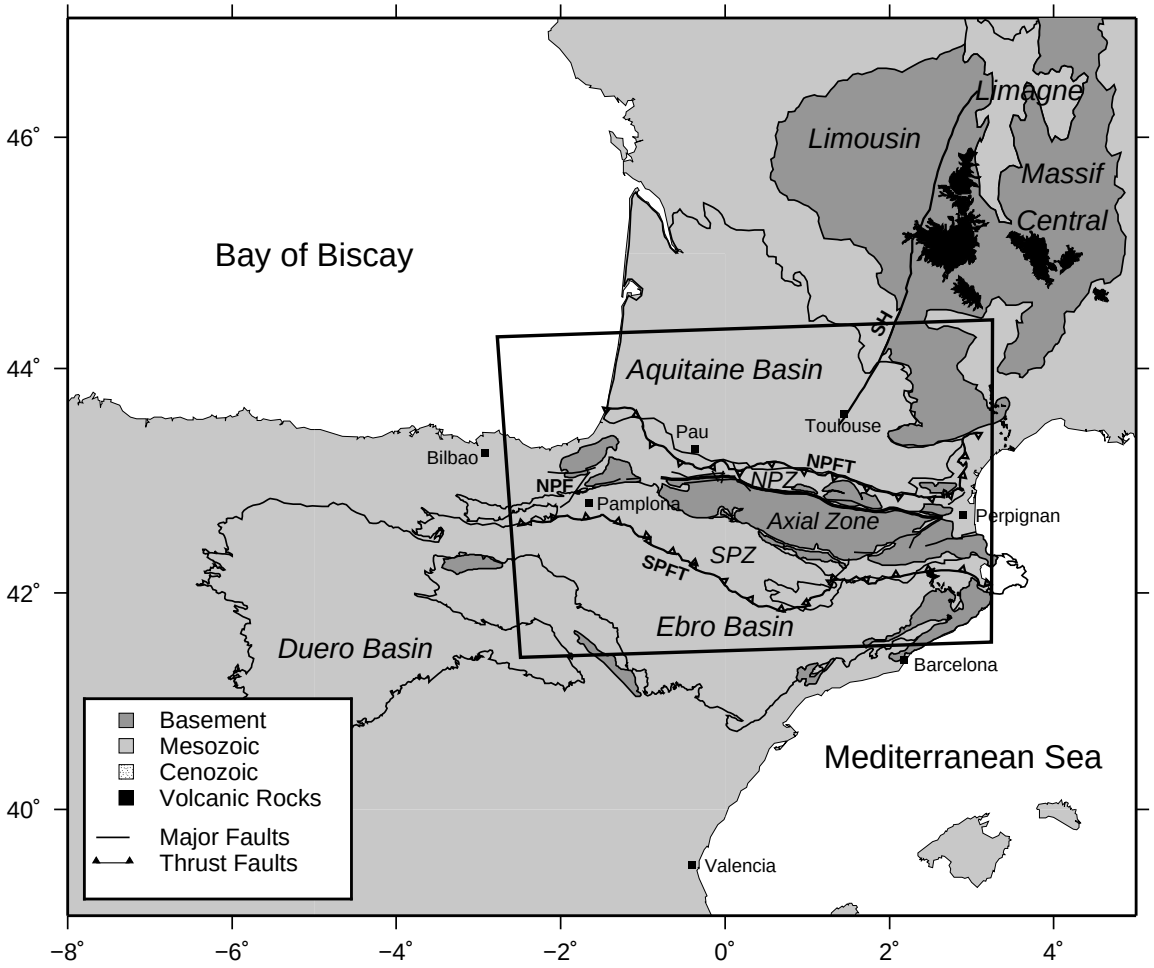

Figure 4.1: Main structural units in of Pyrenean region. The black rectangle delimits our model. NPF: North Pyrenean Fault; NPFZ: North Pyrenean Frontal Thrust; NPZ: North Pyrenean Zone; SPFZ: South Pyrenean Frontal Thrust; SPZ: South Pyrenean Zone.

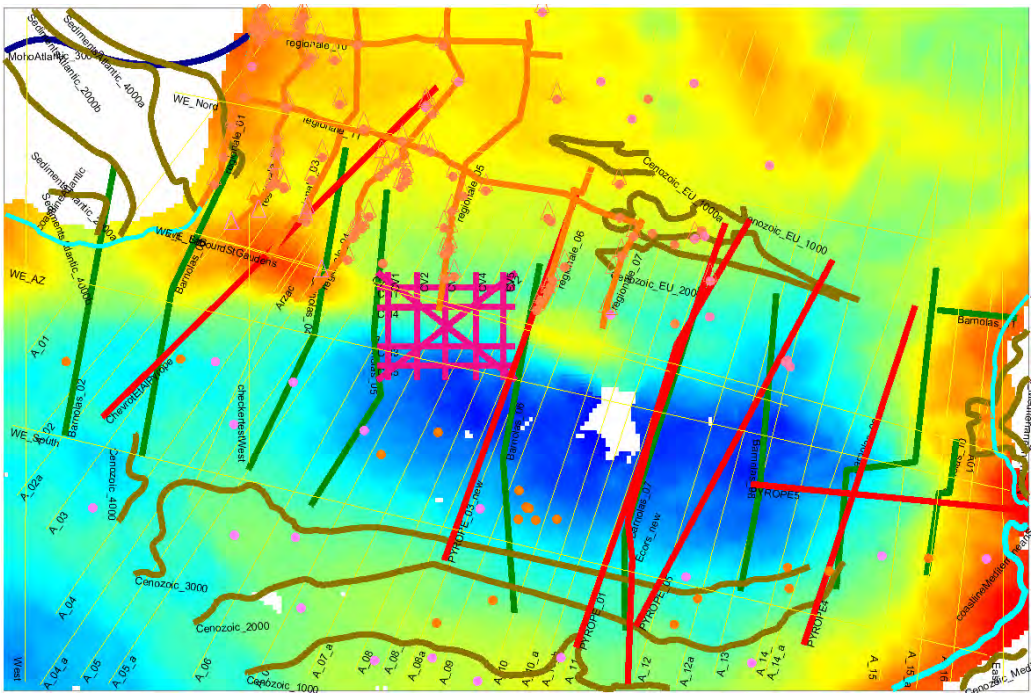
MohoAtlantic_3000
MohoAtlantic_2000b
MohoAtlantic_4000a
WE_Nord
WE_AZ
WE_South
Barnolas_01
Barnolas_02
Barnolas_03
Barnolas_04
Barnolas_05
Barnolas_06
Barnolas_07
Barnolas_08
Barnolas_09
Barnolas_10
Barnolas_11
Barnolas_12
Barnolas_13
Barnolas_14
Barnolas_15
Barnolas_16
Barnolas_17
Barnolas_18
Barnolas_19
Barnolas_20
Barnolas_21
Barnolas_22
Barnolas_23
Barnolas_24
Barnolas_25
Barnolas_26
Barnolas_27
Barnolas_28
Barnolas_29
Barnolas_30
Barnolas_31
Barnolas_32
Barnolas_33
Barnolas_34
Barnolas_35
Barnolas_36
Barnolas_37
Barnolas_38
Barnolas_39
Barnolas_40

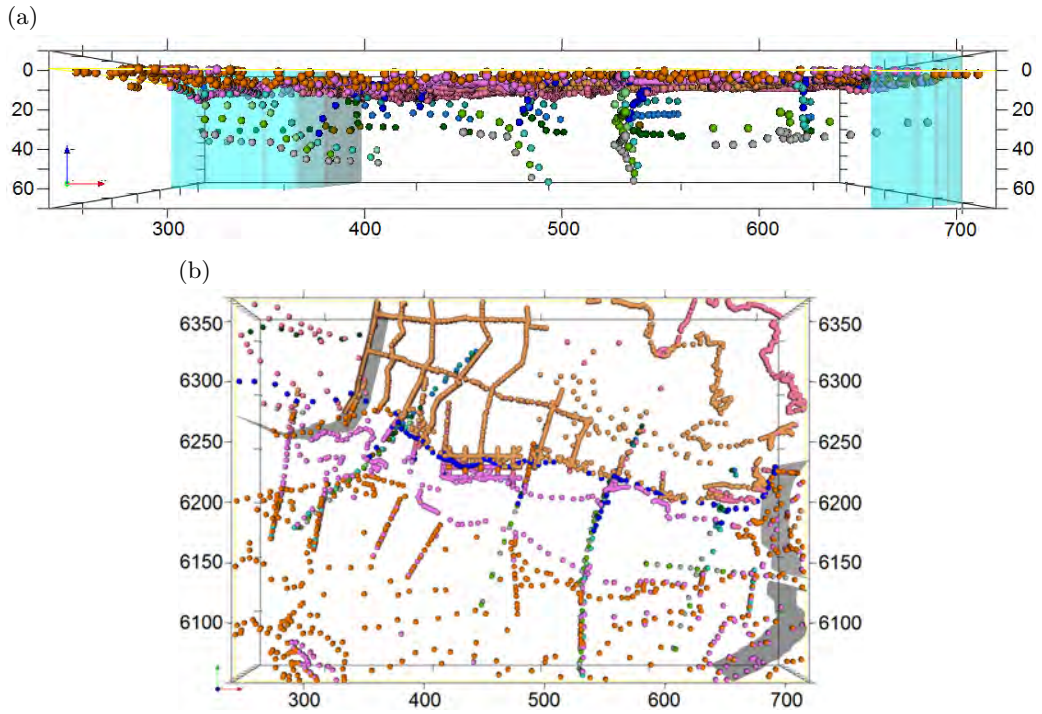

Figure 4.3: Distribution of the geological data used for modeling: View from south (top) and from the top (bottom). Shaded surfaces show coastlines. Colored points indicate the bases of Cenozoic (orange) and Mesozoic (pink) sediments, the accretionnary prism (dark blue), European upper, middle, and lower crusts (turquoise, blue, and dark green), and Iberian upper, middle, and lower crusts (light blue, light green, gray). Data points describing the sea floor are not depicted here, as priority is given to geological structures. Labels are depth and Lambert93 coordinates in kilometers.

(a)

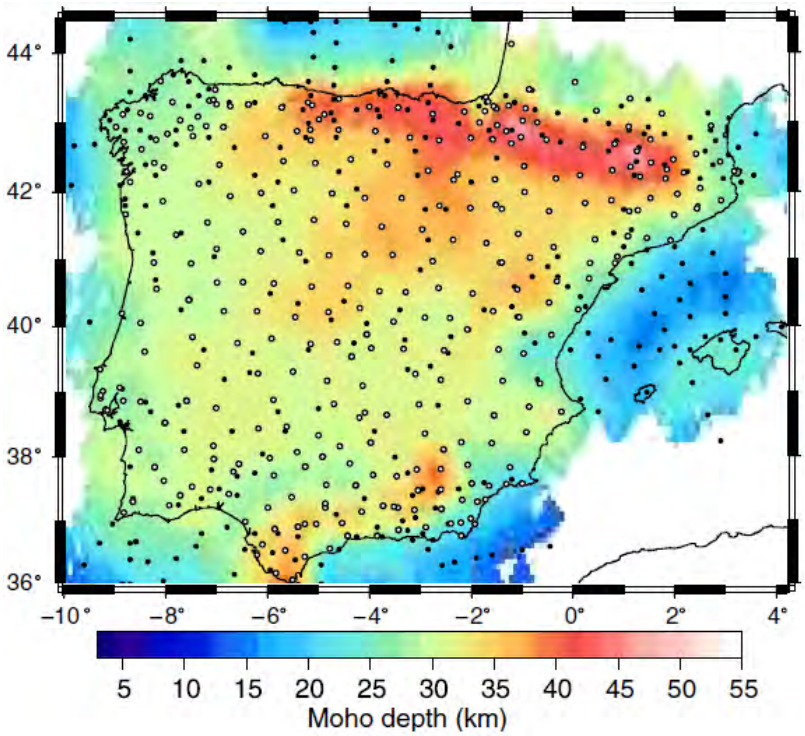

(b)

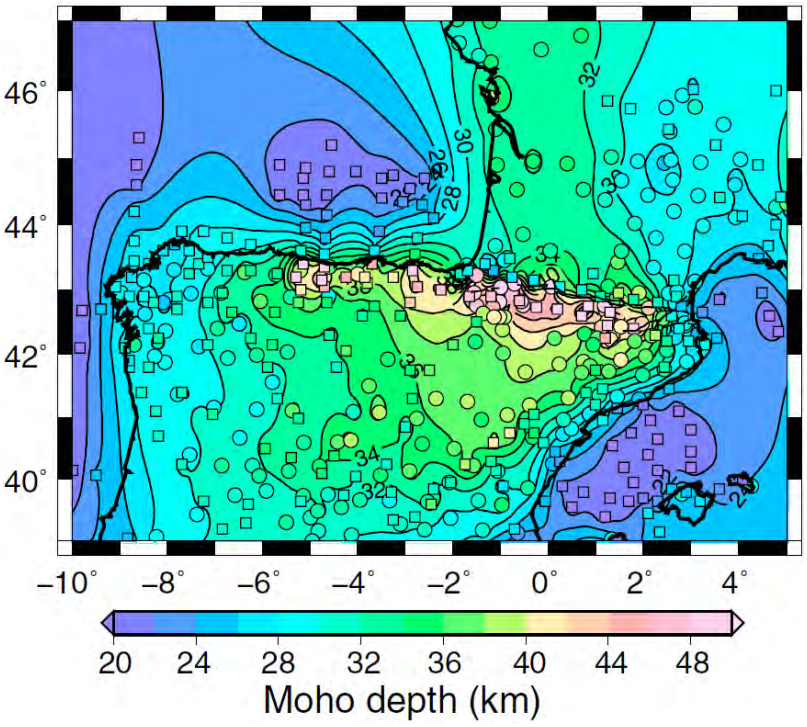

Figure 4.4: **(a):** Moho depth after Diaz et al. [2016]. Black and white dots show locations of data from deep seismic sounding (DSS) and from receiver functions (RF). **(b):** Moho depth after Chevrot et al. [2014]. Circles and squares indicate positions of data from DSS and RF.

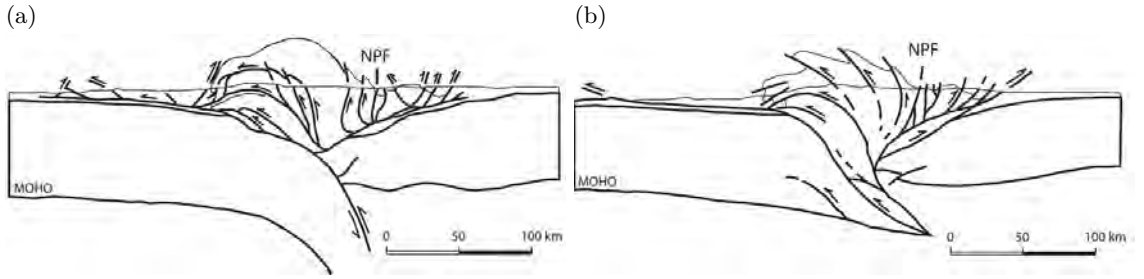

Figure 4.5: Interpretations of the ECORS-Pyrenees profile from Muñoz [1992] **(a)** and from Roure et al. [1989] **(b)**.

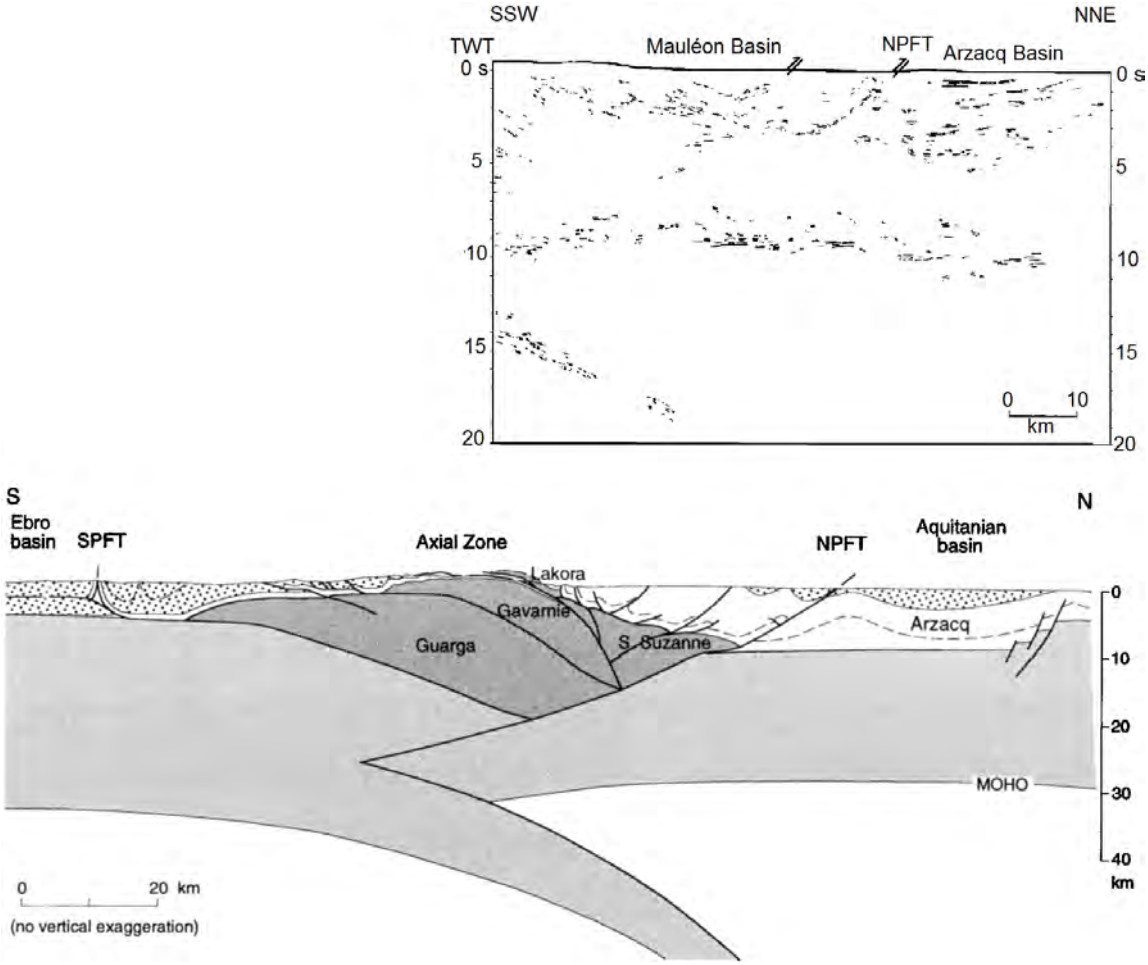

Figure 4.6: Two-way-travel times (**top**) and interpretation (**bottom**) of the ECORS-Arzacq profile (after Teixell [1998]).

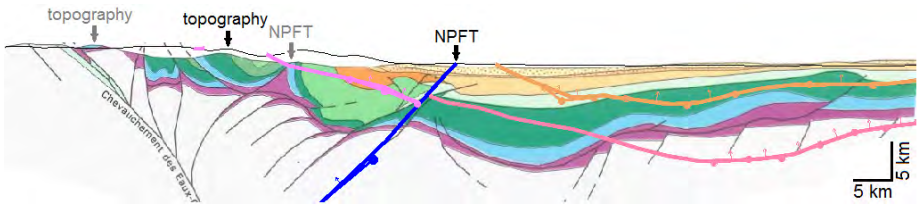

Figure 4.7: Extract of Barnolas 05 transect [Barnolas and Courbouleix, 2001]. Violet, blue, green: Mesozoic; orange, yellow: Cenozoic). The black line represents the model topography. Black arrows mark the NPFT trace from surface data and a local maximum of the model topography. Gray arrows mark the same points in the cross-section. Note the offset between model and cross-section topography due to poor georeference.

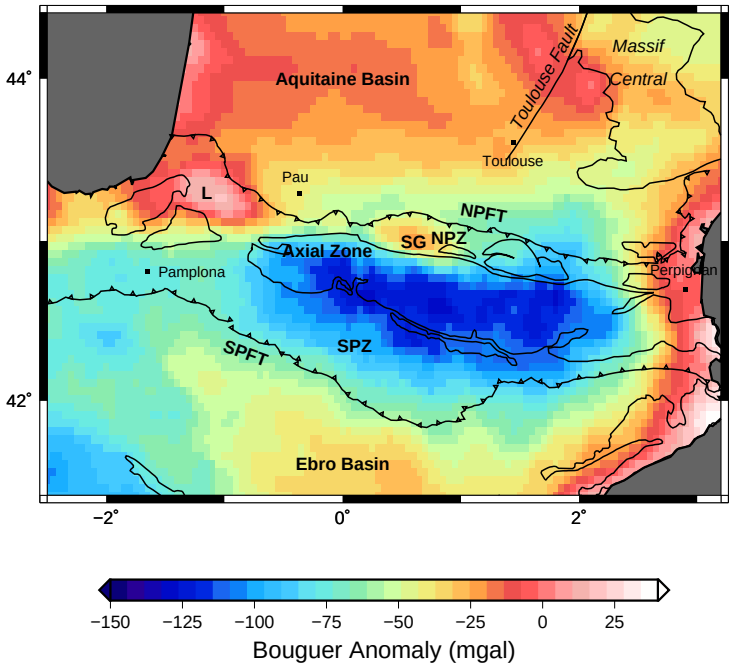

Figure 4.8: Bouguer Anomalies extracted from the BGI data base. L and SG design the positive anomalies of Labourd and Saint-Gaudens, respectively. NPFT- North Pyrenean Frontal Thrust, NPZ- North Pyrenean Zone, SPFT- South Pyrenean Frontal Thrust, SPZ- South Pyrenean Zone.

4.4 Gravimetric Data

Figure 4.8 shows the Bouguer gravity anomalies in the Pyrenean region extracted from the International Gravimetric Bureau (BGI[7]) database. A strong negative anomaly of less than -100 mGal is present along the Axial Zone, and less pronounced negative anomalies (<-70 mGal and <-30 mGal respectively) appear near the foothills in the SW Iberian Chain and in the Massif Central. The foreland basins reveal Bouguer anomalies between -25 mGal and -40 mGal for the Ebro basin and between -10 mGal and -30 mGal for the Aquitaine Basin. Positive anomalies can be observed along the coast lines.

These regional structures reflect the main structural elements of the region. The negative anomalies along the Axial Zone are related to the deep crustal roots (Figure 4.4), and the positive anomalies are related to crustal thinning in the oceans and the continental basins [Torné et al.,

[7]http://bgi.omp.obs-mip.fr/

1989].

However, two local anomalies, located near the Labourd Massif (L) and Saint-Gaudens (SG), do not correlate with the crustal thickness shown in Figure 4.4. They amount to +20 mGal (L) and -20 mGal (SG) and are limited by strong negative gradients towards the Axial Zone and the Aquitaine Basin. These anomalies have been explained by dense "intra-crustal bodies" [Daignières et al., 1989; Torné et al., 1989], upper mantle material emplaced in the upper crust [Casas et al., 1997], or exhumed mantle [Velasque et al., 1989]. As pointed out above, recent tomographic images obtained by Wang et al. [2016] strongly support the latter hypothesis.

4.5 Method

We use `GeoModeller` [Calcagno et al., 2008; Guillen et al., 2008] to construct the 3D model. This software allows us to import the different kinds of geological data (cross-sections, maps, boreholes), to visualize, and to edit them. After the definition of a stratigraphic pile describing the relations between the different geological units, the 3D model is computed using the method of potential field interpolation.

4.5.1 Stratigraphic Pile

The stratigraphic pile that describes our model is depicted in Figure 4.9. In order to describe the complex geometry of the plate boundary, we introduce two distinct stratigraphic columns to model the Iberian and European domains. Both columns contain sedimentary, crustal, and mantle units. The basement unit represents the accretionary prism squeezed between the European and the Iberian plate. It is delimited by the SPFT in the south and the NPFT in the north. Like the sea water series, this unit is considered independent from the Iberian and European blocks.

In order to account for the increase of mass density and seismic velocity with depth, the crust is divided into upper, middle, and lower crust. The upper crust is of particular importance where it reaches the surface, e.g. in the Massif Central in France or in the Cantabrian Mountains in Spain. In those regions, fitting the Bouguer anomalies with a two-layer crust is impossible because

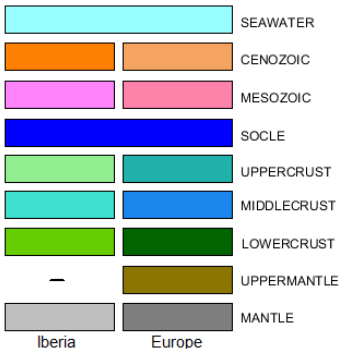

Figure 4.9: Stratigraphic Column. The European units are modeled with the crust eroding the mantle and with the sediments eroding the crust. The basement then erodes European units along the NPFT. Iberian sediments overlay the basement; Iberian crust and mantle are then modeled with inverse polarization: The Iberian crust erodes the basement and remaining European units along the SPFT and is overlain by the mantle. The seawater series erodes both the Iberian and the European block beyond the coast lines. These erosion and polarization rules assure the geometry shown in the figure.

the mass deficit in this area would be too important. We also include a unit that represents the European serpentinized upper mantle in order to model the exhumed mantle bodies beneath the NPZ in the central and western Pyrenees.

We describe the structure of sedimentary basins by two layers of consolidated and unconsolidated sediments, since physical properties like mass density or seismic velocities show important contrasts between these kinds of sediments. The analysis of density and sonic logs, mainly located in the Aquitaine Basin, reveals that the limit between these two units approximately corresponds to the transition between Eocene and Paleocene. However, only a small fraction of the available geological data provides sufficient information to define this limit. Indeed, most maps and cross-sections only give indications of geological eras (Cenozoic/Mesozoic) or systems (Paleogene/Cretacious). In most cases when the series (Eocene/Paleocene) are available, the extent of Paleocene is negligible. Therefore, we distinguish between Cenozoic (unconsolidated) and Mesozoic (consolidated).

4.5.2 Modeling with `GeoModeller`

The interpolation method in `GeoModeller` is based on an implicit approach for modeling surfaces: the potential-field approach [Lajaunie et al., 1997; Chilès et al., 2004; Aug, 2004] uses a function $T(x, y, z)$ which can be interpolated by cokriging from points located on interfaces, considered as

having a common (unknown) potential value for each interface, and directional data representing the gradient of T. The effect of faults is modeled by introducing discontinuous external drift functions in the cokriging system. Thanks to dual form of the cokriging, it is possible to solve the system for once, and then to use it as an interpolator where estimates of T at any point P of space can be easily performed. This property allows designing each interface as a specific isovalue of the potential field.

A complete geological model is made up of a set of different horizons which are assembled with respect to their chronology and relationships. Giving the chronology and relations (conform, erosion, on-lapping, intrusion) allows building a model of the geological formations by combining different potential field functions into one function. This function associates a geological formation to any point of space. It is the exploitation of this function that allows different representations of the model: maps, sections, isohyps, 3D visualisations, meshes, voxels representations. The methodology and examples for building models are fully described in Calcagno et al. [2008].

Assigning a density to each geological formation allows the calculation of gravity effect of the model which can be compared to the observed one. This can be performed through a direct forward modeling [Courrioux et al., 2001; Martelet et al., 2004] or inverse problem approach [Guillen et al., 2008].

4.6 Results

4.6.1 Model I: Geological Data Only

2D sections extracted from the 3D model resulting from the interpolation of the geological data (in the following referred to as Model I) are presented in Figure 4.10. The localisation of these sections is shown in Figure 4.11. Two E-W transects through the Aquitaine and the Ebro basins show Moho depths between 30 and 35 km. In another E-W section, crossing the Labourd and Saint-Gaudens gravity anomalies, the European Moho lies between 15 km depth beneath Labourd and 25-30 km in the central part. In the east, the European crust is replaced by the basement and the Iberian crust. The Iberian crust extends from 40 to 50 km depth beneath the Labourd and 40 to 70 km depth in the central Pyrenees. Between the central and the eastern third of the cross-section, the Moho steeply raises up to about 35 km depth and the Iberian crust replaces the European crust beneath the basement.

Six approximately SSW-NNE sections show the Iberian crust underthrusting the European crust in the west, with the uplift of European at 12 km depth beneath the Labourd Massif. In the central third of the model, the Iberian lower crust subducts down to at least 70 km, which is the lower boundary of our model. In the east, we find a nearly continuous Moho beneath both Iberia and Europe.

4.6.2 Gravity Anomalies Computed from Model I

Model I described above provides a satisfactory description of the available geological data. We will now compare its gravimetric response to the Bouguer anomalies provided by the BGI (Bureau gravimetrique international) using a reference density 2.67 as usual for French data. For this, a homogeneous mass density is assigned to each geological unit (cf. Table 4.1): Densities are assumed to be similar for the European and the Iberian domain. They range from 3.2 g/cm^3 for the mantle (3.1 for the serpentinized exhumed mantle) to 2.8, 2.7, and 2.64 g/cm^3 respectively for the lower, middle, and upper crusts. These values are the results of applying Brocher's Law on the tabular velocity model of Souriau and Pauchet [1998] (For the mantle, this conversion yields 3.29. In this

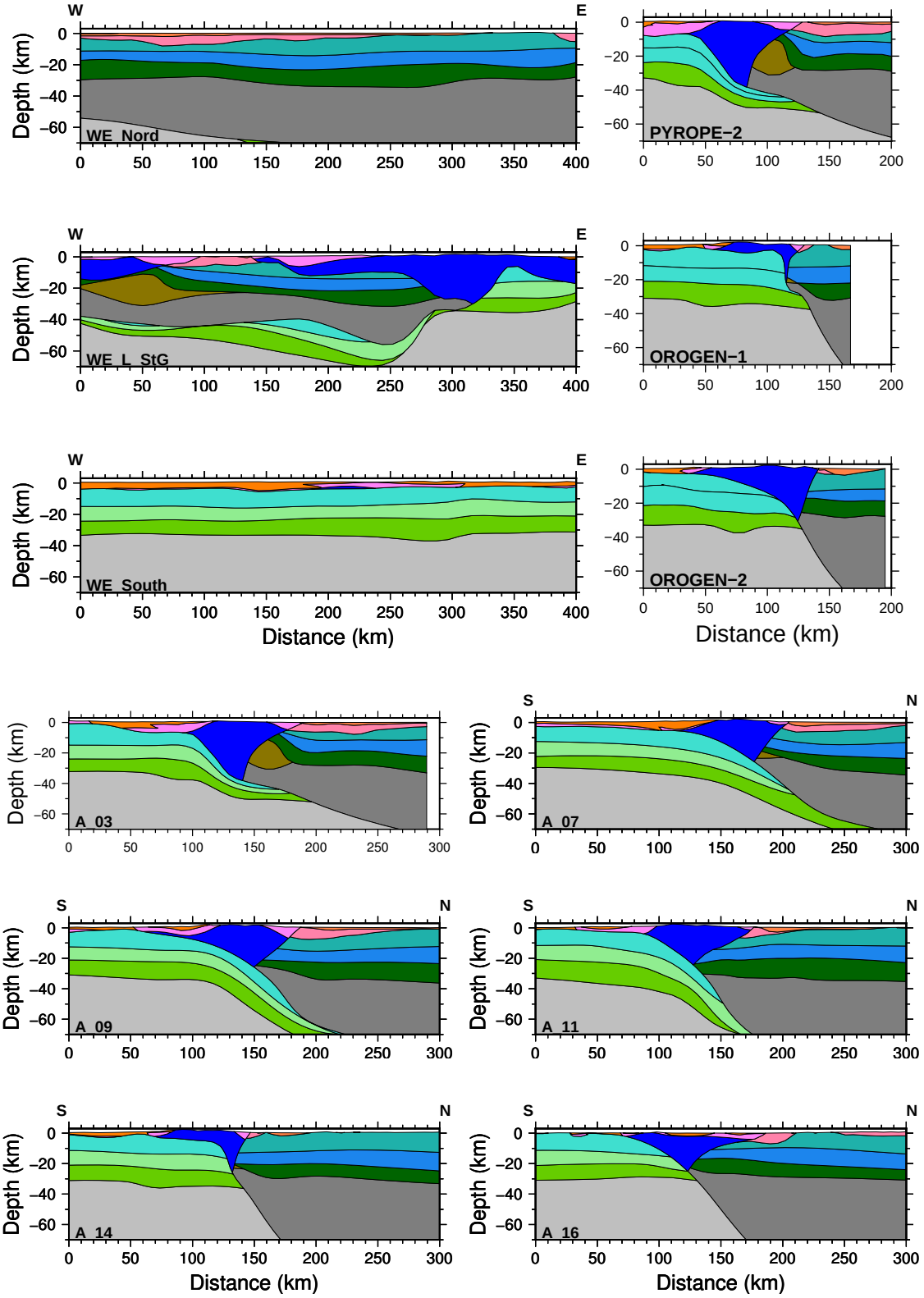

Figure 4.10: Cross sections in model I (localizations in Figure 4.11). Geological units from bottom to top: Mantle (gray), lower, middle, upper crust (green, light blue), basement (dark blue), Mesozoic (pink), Cenozoic (orange).

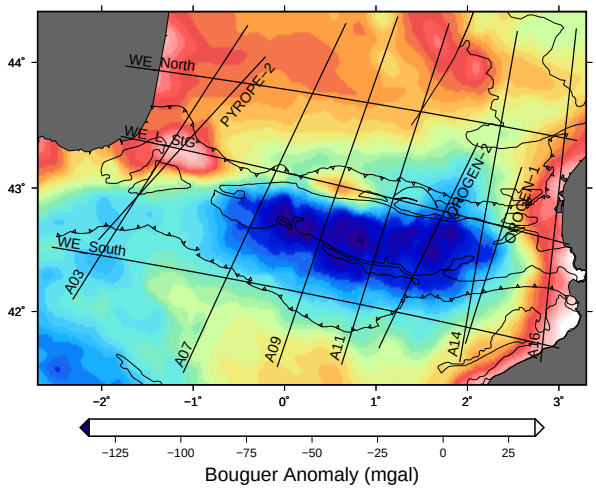

Figure 4.11: Localization of cross-sections presented in figures 4.10 and 4.13, overlain by Bouguer anomalies.

model, however, we consider the less dense upper mantle only). We adopt values of 2.62 g/cm^3 for the consolidated and 2.3 g/cm^3 for unconsolidated sediments, as a compromise between the analysis of drill-hole density logging data, available in northern Pyrenean units, and literature data in southern Pyrenees [Santolaria et al., 2017]. The density of sea water is set to 1.025 g/cm^3, the one of the basement to 2.67 g/cm^3, corresponding to the reference density.

Gravity computation is done in `GeoModeller`, with a reference density of 2.67 g/cm^3 and in a grid of 5000 m $\times$ 5000 m blocks in the horizontal directions. The layer thickness amounts to 200 m between 3 km altitude and 10 km depth. Below, layer thickness increases incrementally by 10% and reaches a value of 5.5 km at 70 km depth. This yields a discretized model of 96 $\times$ 64 $\times$ 101 cells (65 above, 36 below 10 km).

In `GeoModeller`, the gravity response is calculated under the assumption that all necessary information is contained in the model. The observed gravity field, however, and thus the Bouguer anomalies we want to explain, are caused by the entire Earth, i.e. they contain information that we cannot fit with our model. The Bouguer Anomalies are thus computed near to a constant and shifted so that the misfit can be interpreted in the same range of variations. Edge effects are adressed by reproducing the model symmetrically on the 8 lateral neighbouring blocks.

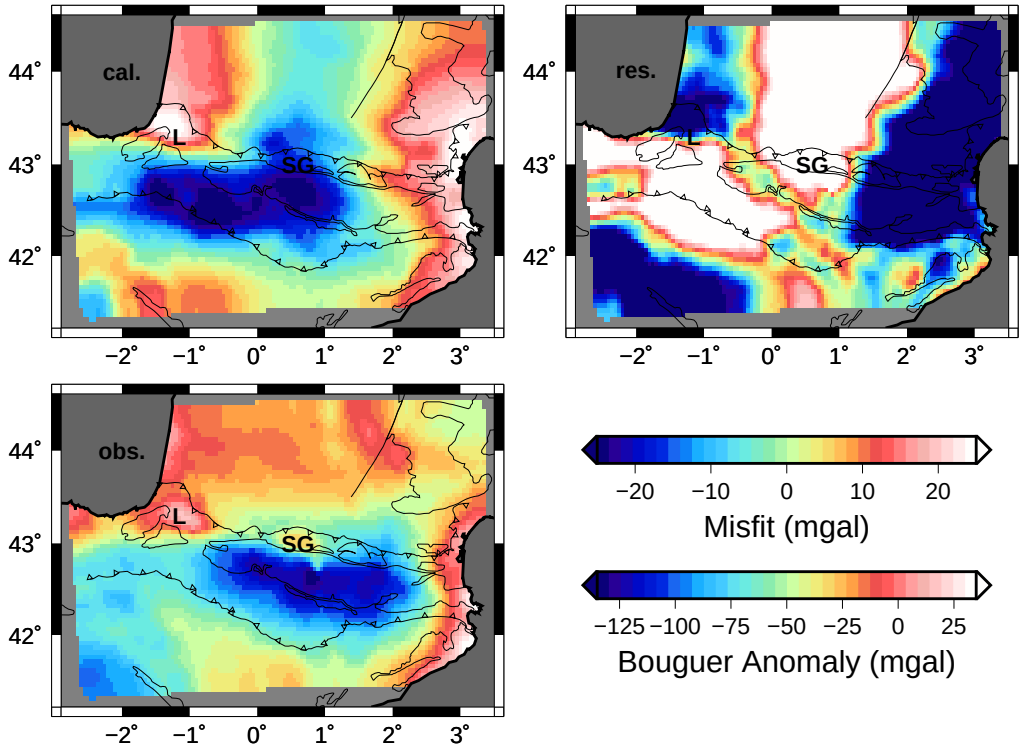

Figure 4.12: Top: Map of Bouguer anomalies (left) and residual misfits (right) calculated in Model I using the density values listed in table 4.1. Bottom: Oberserved Bouguer Anomalies.

Unit	ρ_I (g/cm^3)	ρ_{II} (g/cm^3)
Sea water	1.025	1.035
Cenozoic	2.300	2.400
Mesozoic	2.620	2.600
Basement	2.670	2.660
Upper crust	2.640	2.610
Middle crust	2.670	2.755
Lower crust	2.800	2.810
Upper mantle	3.100	3.090
Mantle	3.200	3.259

Table 4.1: Densities of Models I and II.

The top part of Figure 4.12 displays the Bouguer anomalies and misfits obtained from the 3D model. A strong negative anomaly is observed in the SPZ, to the south of the Labourd anomaly, and in the central part of the AZ. Positive anomalies are present along the coast lines, the western Aquitaine Basin, and in the south of the Ebro basin. The positive Labourd anomaly is approximately reproduced but cannot be distinguished from the Aquitaine Basin. The Saint-Gaudens anomaly is not reproduced at all.

In general, the calculated anomalies are too strong. The predictions range between -156.73 and +47.64 mGal versus a range of [-135.70 +40.83] mGal in the observed data. The misfits range from from -89.33 to +91.22 mGal. Therefore, our preliminary Model I poorly explains the gravimetric data. We thus decided to add further constraints in order to refine the gravitational response of the model.

4.6.3 Model II: Geological and Gravimetric Data

We now modify the geological model in order to improve the fit between computed and observed Bouguer anomalies. In large parts of the model, the sedimentary thickness is well constrained by seismic profiles, drill holes, surface, and isobath data. For this reason, we kept the geometry of the

sedimentary basins and adjusted the Moho and the crustal interfaces. However, small adjustments are also made on the sedimentary thickness obtained from Barnolas and Courbouleix [2001] cross sections which is justified from their poor georeference.

In a first step, we focus on the Labourd and St Gaudens anomalies. We introduce additional points to describe the Moho depth in the PYROPE-02 section and in transects A09 and A10. The Moho depth is set to ∼11 km beneath the Labourd, ∼10 km beneath Saint-Gaudens, and ∼25 km in between these two anomalies. It reaches ∼28 km depth west of the Labourd Massif and east of Saint-Gaudens. The Moho uplifts extend approximately over 45 km WNW-ESE and 28 km SSW-NNE beneath the Mauléon basin and over 48 km WNW-ESE and 14 km SSW-NNE beneath Saint-Gaudens.

In a second step, we adjust the geometry of the negative Axial Zone anomaly. Assuming that Chevrot et al. [2015] and Wang et al. [2016] might have underestimated the effect of the sedimentary cover, we move the lower crustal bases of the PYROPE sections 1 to 3 km upwards beneath the Aquitaine and Ebro basins. Furthermore, we allow a larger Moho depth of ∼35 km beneath the Massif Central, in order to better explain the gravity data in the north-eastern corner of the model. Finally, we add constraints on crustal and mantle units along the boundaries of the study area, especially beneath the Aquitaine and Ebro basins.

Several 2D sections extracted from the interpolated 3D model (Model II) are shown in Figure 4.13. In the new model, the E-W sections in the foreland basins still show Moho depths between 28 and 35 km. In the sections crossing the positive Labourd and Saint-Gaudens gravity anomalies, the European Moho lies between 25 and 30 km depth, interrupted by the mantle uplifts beneath the gravity anomalies. In the eastern part, the basement is now limited to the upper 10 km. The Iberian crust is present between 40 and 55 km depth in the western and central Pyrenees. In the east, it raises up to 30 km. The SSW-NNE cross-sections show the Iberian crust underthrusting the European plate down to 50 km in A03 and A11 and down to 60 km depth in A07 and A09. In the east, the Iberian crust reaches a maximum thickness of 40 km. A14 reveals the upper Iberian crust to be as thick as the cumulative middle and lower crusts. In fact, the PYROPE-04 profile does not show any evidence for subduction, and a strong low density anomaly in the crust is thus

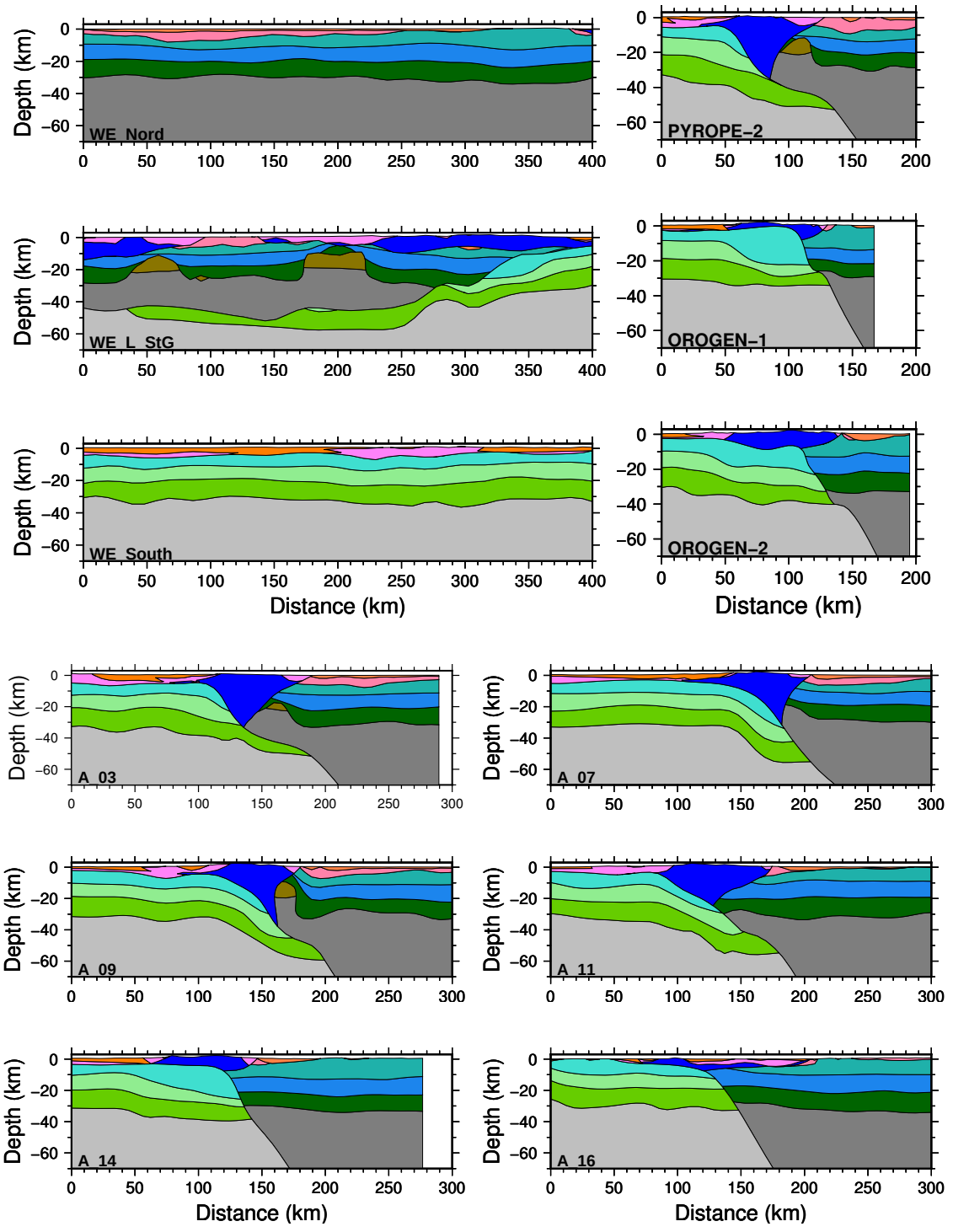

Figure 4.13: Model II, obtained from geological and gravimetric data. The localizations of the sections are shown in Figure 4.11). Geological units from bottom to top: Mantle (gray), lower, middle, upper crust (green, light blue), basement (dark blue), Mesozoic (pink), Cenozoic (orange).

(a)

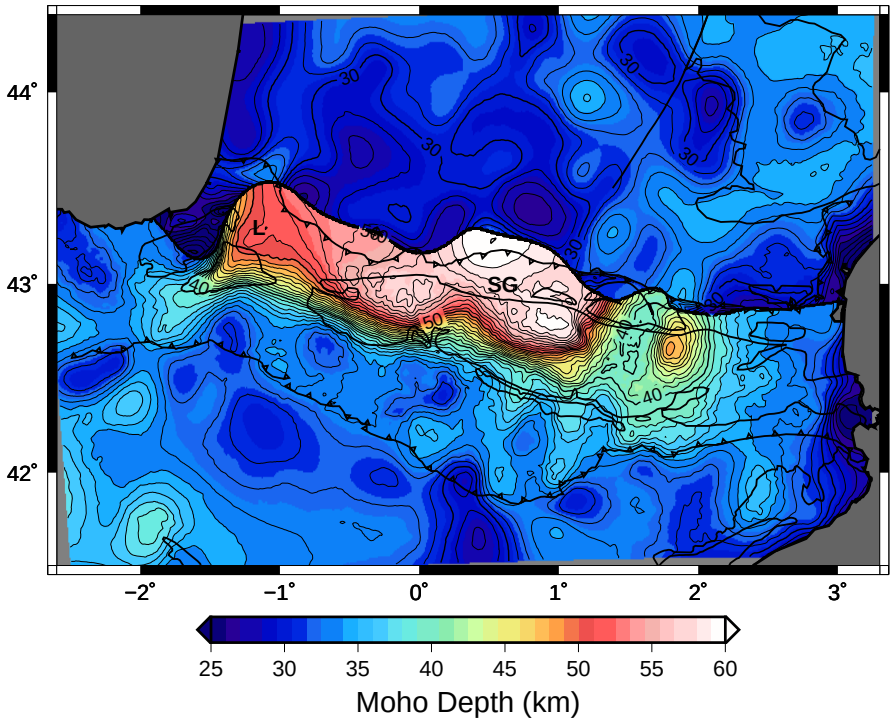

(b)

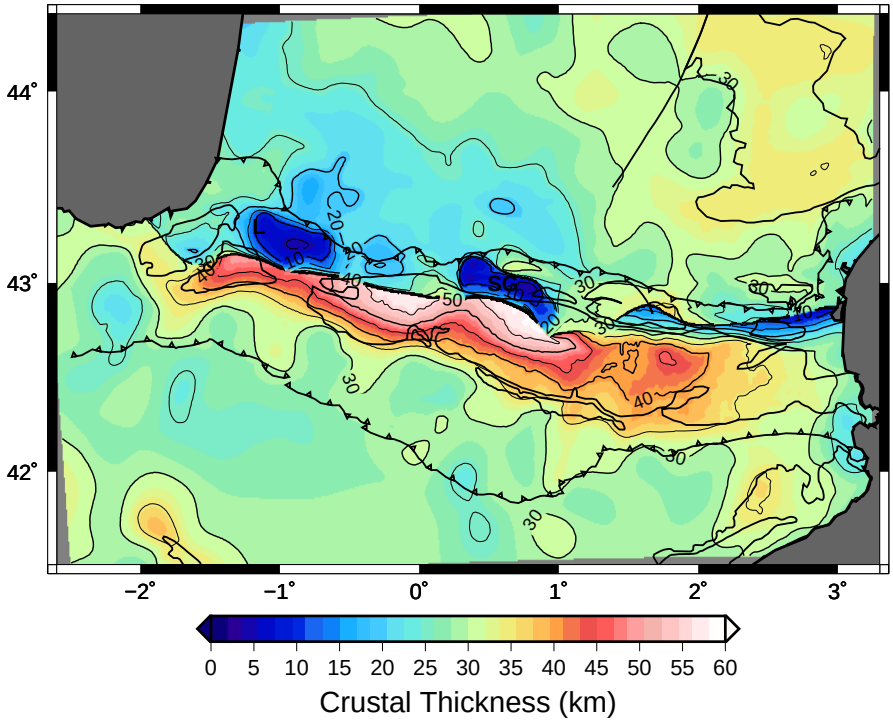

Figure 4.14: Moho depth (**a**) and crustal thickness (without sediments) (**b**) and of Model II. In the case of superposed Iberian and European crust, the Iberian one is taken into account for the Moho depth but not for the crustal thickness.

needed to explain the negative Bouguer Anomaly in the eastern Axial Zone. Thickening the upper crust is one possibility, an alternative explanation could be a low density body within the crust or in the mantle.

Detailed maps of Moho depth and crustal thickness (upper, middle, and lower crust, without sediments) are given in Figure 4.14. The Moho depth reaches 30 to 35 km beneath the Ebro basin, 28 to 33 km beneath the Aquitaine Basin, and 33 to 35 km beneath the Massif Central. Crustal roots beneath the axial zone reach depths of 53 km in the west (beneath the Mauléon basin) and 60 km beneath the SPFT north of Saint-Gaudens. The Moho raises up to the east, reaching 25 to 30 km depth along the Mediterranean coast, but showing a local minimum of 48 km at about 1.8° longitude.

The European crust is about 40 km thick beneath the Massif Central, 20 to 25 km thick beneath the Aquitaine Basin, and reaches a minimum thickness beneath the Saint-Gaudens and Labourd gravity anomalies of about 5 to 10 km. The Iberian crust is the thinnest beneath the western Ebro basin (21 - 25 km). It thickens to 30 km in the rest of the foreland basin and the SPZ. Crustal thickness is about 40 km around the basement outcrops in the SW and the SE and has a maximum of 60 km in the central Axial Zone, S and SW of Saint-Gaudens.

4.6.4 Gravity Anomalies Computed from Model II

The Bouguer anomalies and residuals computed in Model II are shown in Figure 4.15. In order to better fit the Bouguer anomalies, the densities have been slightly modified. We now use densities of 3.259 (3.090) g/cm^3 for the (upper) mantle, 2.810, 2.755, and 2.610 g/cm^3 respectively for the lower, middle, and upper crusts, and 2.600 (2.400) g/cm^3 for Mesozoic (Cenozoic) sediments. Density is set to 1.035 g/cm^3 for sea water and to 2.660 g/cm^3 for the basement.

The range of Bouguer Anomalies decreases to [-131.57 +48.54] mGal with a misfit in the interval [-21.72 +23.83] mGal. Figure 4.16 shows the histogram of residuals compared to those obtained from Model I. It shows a characteristic Gaussian distribution with standard deviation of σ =3.4 mGal. This result gives us, using the simple equation of infinite horizontal plate [Lindner and Casten, 2005], a possible variation of 1159 m in Moho depth or 601 m in the thickness of Cenozoic

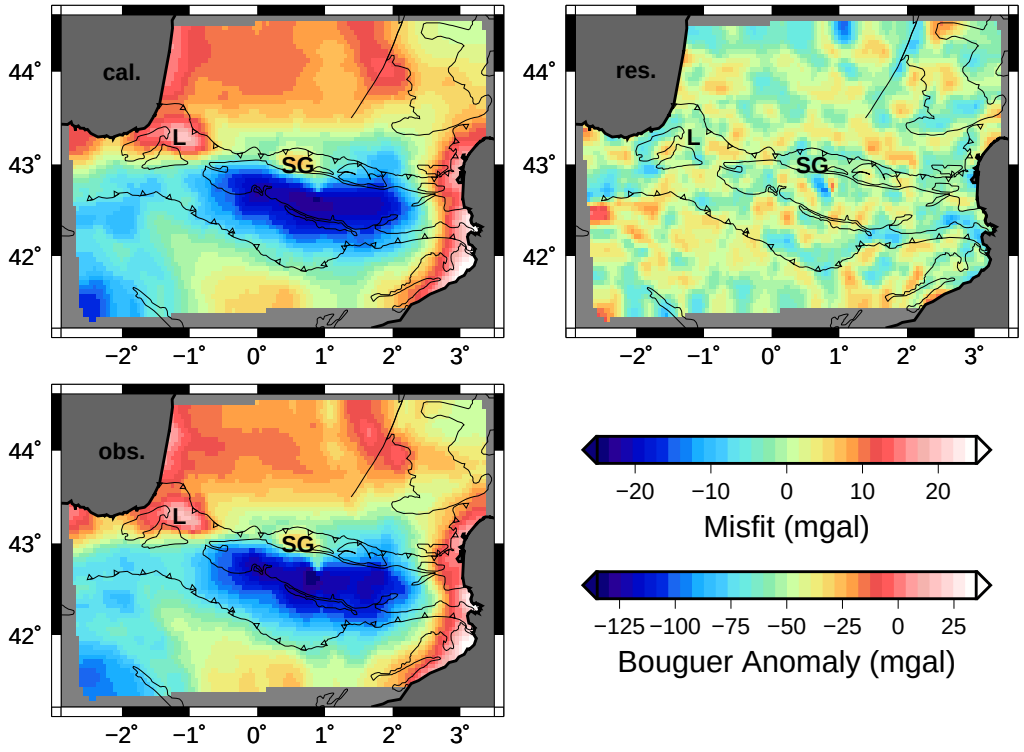

Figure 4.15: Top: Map of Bouguer anomalies (left) and residual misfits (right) calculated in Model II using the density values listed in table 4.1. Bottom: Oberserved Bouguer Anomalies.

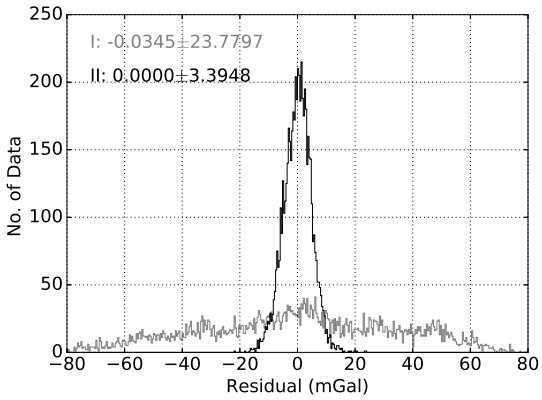

Figure 4.16: Residuals of Bouguer anomalies predicted by Model II (black) compared to those from Model I (gray). Text inset indicates mean values and standard deviations.

sediments. Given the grid size used to build the model, we are at the limit of what can be achieved with our trial-and-error direct modeling approach.

4.7 Discussion

The final 3D model provides direct insight into the detailed architecture of the Pyrenees. It can be used to estimate the volumes of the different units and to characterize their contribution to the gravity field. In the following, we will illustrate and discuss several types of information that can be extracted from our 3D model.

4.7.1 Volume Estimates

Integration over the 3D model yields allows us to estimate the volumes of the different units. For the sediments, we obtain a total volume of 454 357 km^3 sediments for both the Aquitaine and the Ebro Basin. Vanderhaeghe and Grabkowiak [2014] estimate the amount of sediments in the Ebro and the Aquitaine Basins to 112 500 km^3 and 315 000 km^3, respectively, which yields to 427 500 km^3 for both basins. However, this computation does not consider sediments inside a "zone of deformation perpendicular to the Pyrenees" [Vanderhaeghe and Grabkowiak, 2014], the width of which is 150 km and comprises the North and South Pyrenean Zones (NPZ and SPZ). We approximate the SPZ and NPZ as two bands of 40 km width south and 10 km width north of the Axial Zone, extending over 400 km EW. This gives a surface of 20 000 km^2. Assuming an average depth of 4 km in the NPZ and SPZ, we need thus to add 80 000 km^3 to the estimation of Vanderhaeghe and Grabkowiak [2014]. In addition, our model is missing the southernmost $\sim$10 000 km^2 of the Ebro Basin and the northernmost $\sim$14 000 km^2 of the Aquitaine Basin (Figure 4.1). Taking an average depth of 1.5 km for the missing parts of the foreland basins, we have to add 36 000 km^3 to our sedimentary volume. This gives total volumes of sediments of 507 500 km^3 based on the estimates of Vanderhaeghe and Grabkowiak [2014] and 490 357 km^3 based on our 3D model. The difference of only 3.4 % demonstrates an excellent agreement between the two models.

The volume of crustal roots beneath 35 km depth and the subduction slab amounts to $2.2 \cdot 10^6$ km^3, in good agreement with the estimate of crustal volume affected by convergence made by Vanderhaeghe and Grabkowiak [2014] ($2.36\ ^{+0.30}/_{-0.28} \cdot 10^6$ km^3).

4.7.2 Bouguer Anomalies: The contributions of Sediments and Crustal Roots

Figure 4.17a shows the Cenozoic thickness in Model II. In France, Cenozoic thickness is almost everywhere less than 1.5 km, but it increases to about 2 km near the Atlantic coast and in the vicinity of the NPFZ. Three regions are characterized by a Cenozoic thickness larger than 3 km: one located to the NW of the Saint-Gaudens gravity anomaly and two between the NPFT and the Massif Central. The easternmost region is connected to the only spot where Cenozoic sediments are present in the NPZ and in the AZ. This accumulation of sediments is constrained by a geological cross-section from Barnolas and Courbouleix [2001] (sec. 4.3.4). In the Ebro Basin, the Cenozoic sediments are about 1 km thick near the southern border of our model and thicken northwards. Along the SPFT, their thickness reaches up to 5 km in the west and 3 to 4 km in the east. In the western and central parts of the SPZ, it also reaches 3 to 4 km depth before flattening towards and disappearing in the AZ. In the east, only a small amount of Cenozoic sediments are present between the SPFT and the AZ, with a maximum depth of 1.8 km.

The contribution of the Cenozoic sediments to the Bouguer anomalies is shown in Figure 4.17b. It is calculated as the difference between the Bouguer anomalies from Model II and from the same geometry but with Cenozoic densities being replaced by the reference density of 2.67 g/cm^3. In most parts of the French basins, the contribution is beneath -5 to -7 mGal but it increases southwards and towards the Atlantic coast. Along the coast it reaches -12 to -16 mGal, and north of the NPFT it is -18 to -30 mGal. In Spain, the contribution increases from -7 mGal in the south to -28 mGal in the north-east and -36 mGal in the north-west of the Ebro basin. The western anomaly continues through the SPZ and reaches the border of the Axial Zone. In places where no Cenozoic sediments are present, such as the AZ and the Massif Central, the influence of the basins is still up to -5 mGal. On the whole, 1 km of Cenozoic thickness contributes about -7.5 mGal to the modeled Bouguer anomalies.

Figure 4.18a presents the thickness of Mesozoic sediments in Model II. In the French part, it follows a NE-SW trend from 0 km near the Massif Central to 9 km in the Mauléon basin. North

(a)

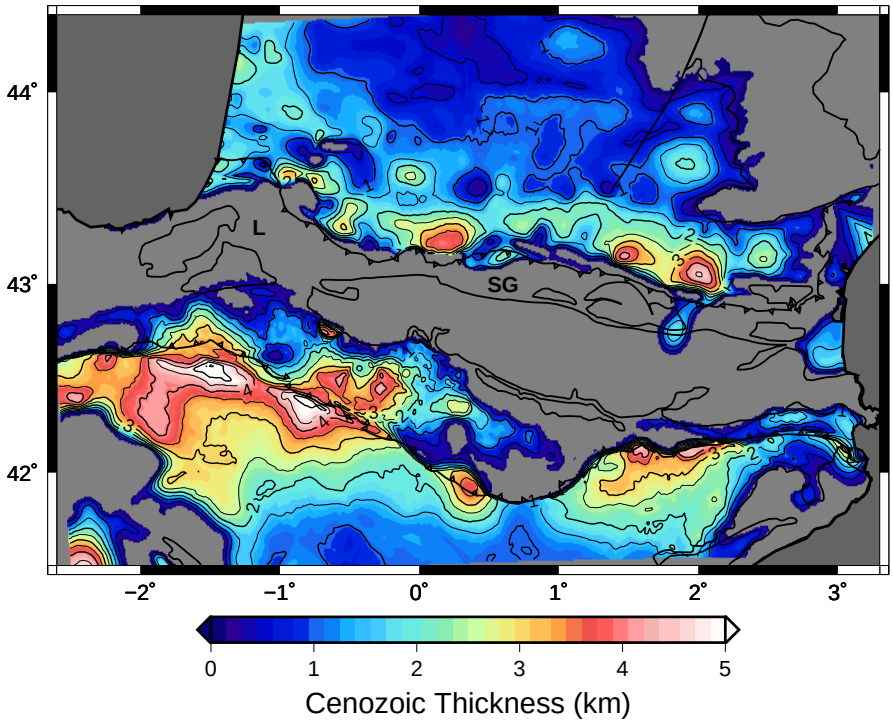

(b)

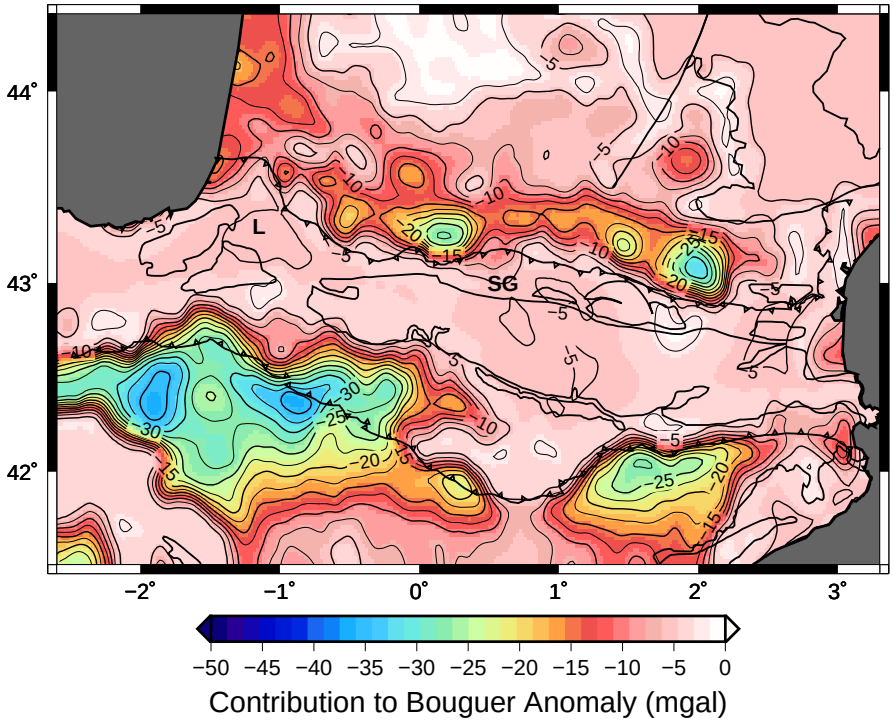

Figure 4.17: **a:** Thickness of Cenozoic sediments in Model II. **b:** Contribution of Cenozoic sediments to Bouguer anomalies.

(a)

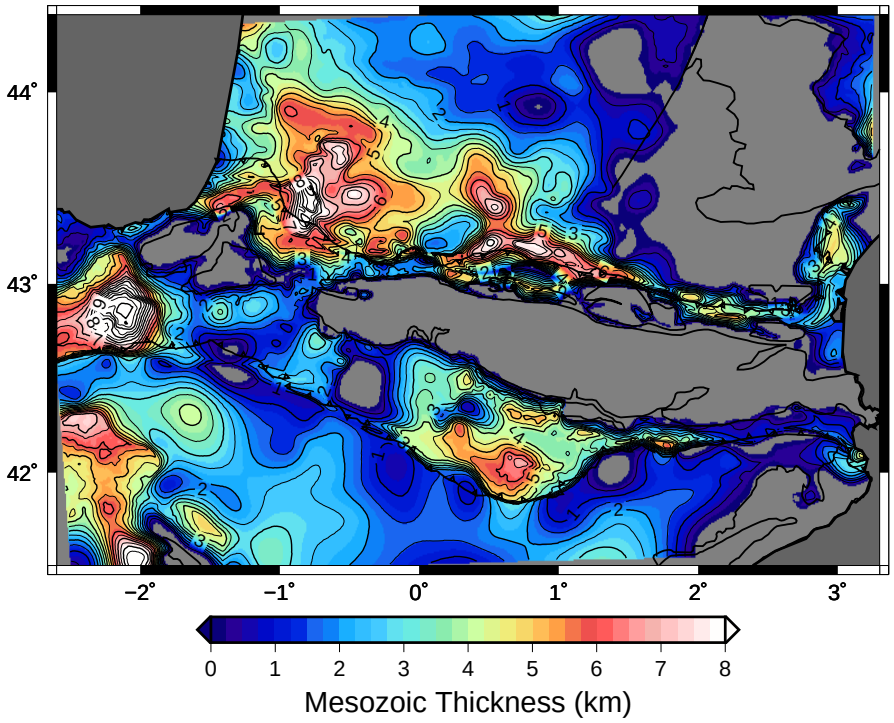

(b)

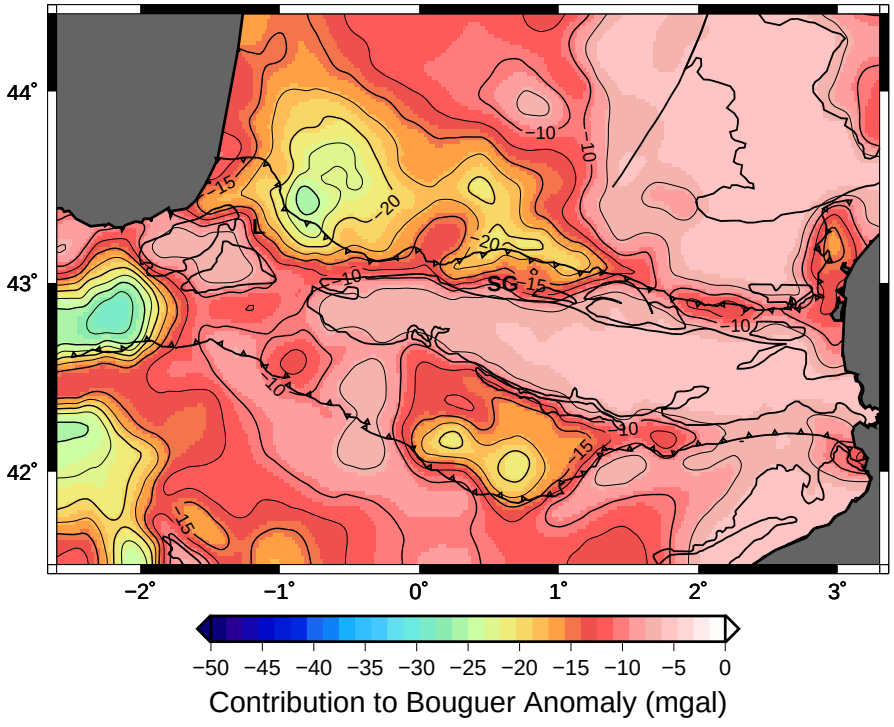

Figure 4.18: **a:** Thickness of Mesozoic sediments in Model II. **b:** Contribution of Mesozoic sediments to Bouguer anomalies.

of Saint-Gaudens, another narrow basin shows a maximum depth of 6 km. In the Spanish part, Mesozoic sediment thickness lies roughly between 1 km and 3 km, interrupted by 5 5.5 km deep basin in the eastern center of the SPZ and a 9 km to 10 km deep basin in the very west of the SPZ. In the SW corner of the study area, the maximum depth is 6 to 7.5 km.

Figure 4.18b shows the contribution of Mesozoic sediments to the modeled Bouguer anomalies, following the same procedure as for the contribution of Cenozoic sediments described above. In France, it is around 5 mGal at the Massif Central and reaches values smaller than -20 mGal in the deep basins. In Spain, it is mostly between -5 mGal and -15 mGal but reaches -21 mGal in the eastern center of the SPZ, more than -25 mGal in the SW, and -28 mGal in the west. The overall contribution of 1 km thick Mesozoic sediments to the Bouguer anomaly is about -2.9 mGal, 2.5 times smaller than for the Cenozoic sediments.

The maps for all sediments (Mesozoic and Cenozoic) are shown in Figure 4.19. Here, no general relationship can be drawn between the sediment thickness and the Bouguer anomalies because of varying amounts of Cenozoic and Mesozoic sediments. For example, the 8 km deep western Ebro basin contributes -50 mGal, whereas the influence of the 10 km deep Aquitaine Basin is only -35 to -40 mGal. This difference results from the equal relative contributions of Mesozoic and Cenozoic sediments in the Ebro Basin, while the Aquitaine Basin is largely dominated by consolidated Mesozoic sediments.

In order to obtain the contribution of the Iberian crustal root and subducted crust, we define the Iberian Moho depth of 35 km beneath the Axial Zone and recompute the Bouguer anomalies. Figure 4.20 shows the difference from the Bouguer anomalies computed in Model II. The contribution of the slab and crustal root is larger than 85 mGal in the central AZ, where the crust is the thickest. In the eastern Axial Zone, where subduction is absent in our 3D model, the contribution is between -10 and -20 mGal.

4.7.3 Moho Depth

Chevrot et al. [2014] compiled a map of apparent Moho depth obtained from the interpolation of receiver function measurements and of seismic reflection and refraction profiles from Díaz and

(a)

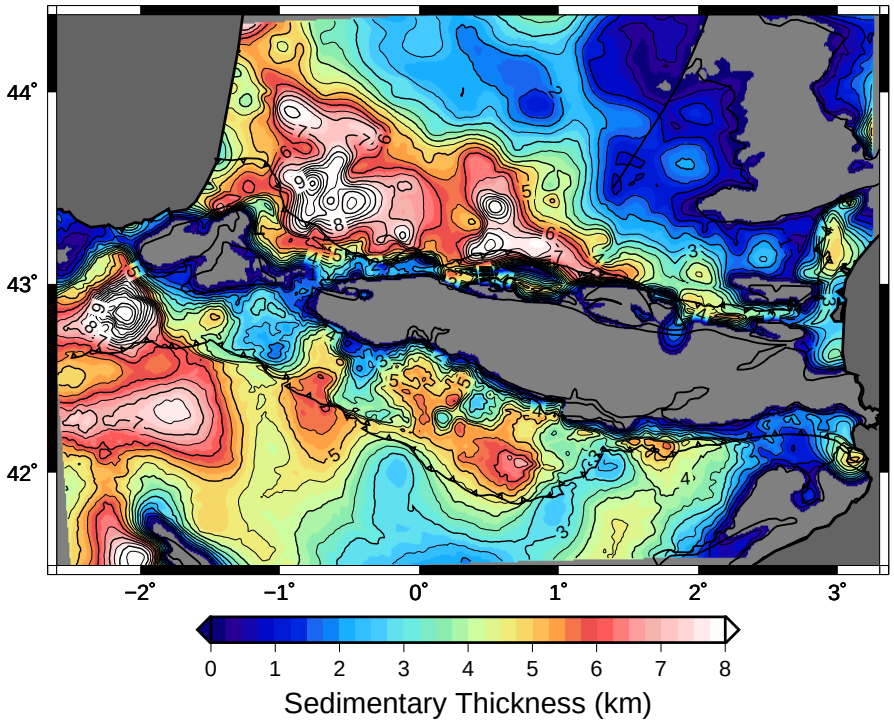

(b)

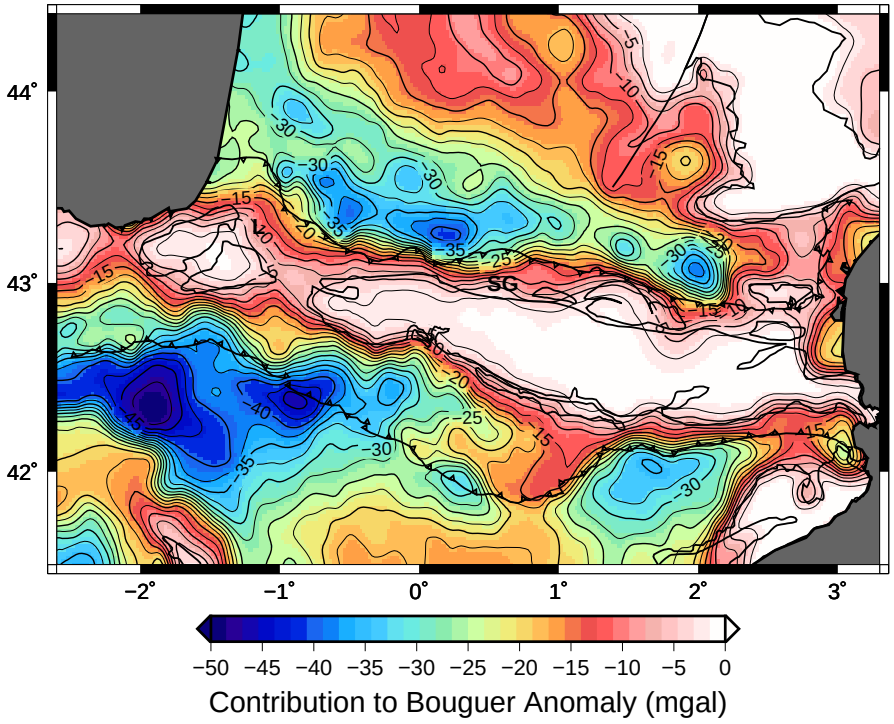

Figure 4.19: **a:** Total sediment thickness in Model II. **b:** Contribution of sediments to Bouguer anomalies.

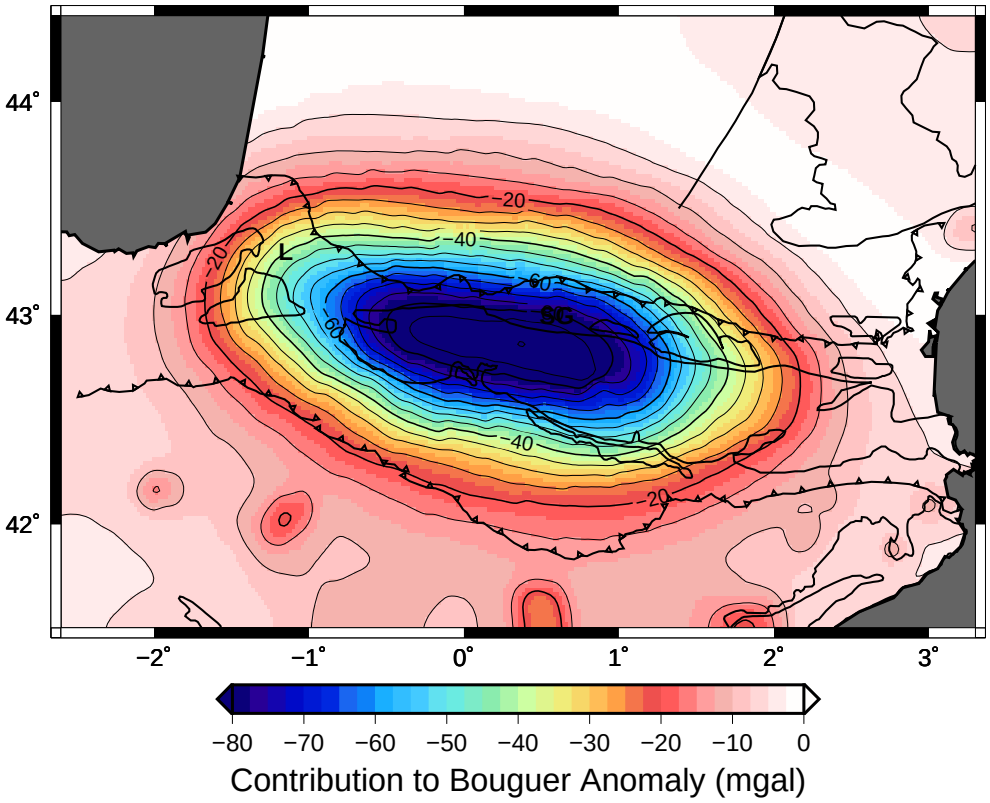

Figure 4.20: Contribution of crustal roots to Bouguer anomalies. The map shows the difference of Bouguer anomalies computed in Model II and in a model with the Iberian Moho fixed at 35 km depth beneath the AZ.

Gallart [2009], Sapin and Prodehl [1973], Sapin and Hirn [1974], and Perrier and Ruegg [1973]. Figure 4.21 shows the Moho depth in Model II and the interpolated Moho depth of Chevrot et al. [2014]. Where the Iberian and European Mohos are superposed, only the shallower European Moho is taken into account. Both maps show a deeper Moho beneath the Axial Zone than beneath the foreland basins, but significant differences are observed in absolute depths and gradients, mainly because of the coarse coverage and interpolation in the model of Chevrot et al. [2014].

Chevrot et al. [2014] computed the apparent Moho depth without considering the contribution of the low velocities in the sedimentary layers. This can explain the fact that they observe greater depths beneath the foreland basins (35 km to 40 km versus 30 km to 35 km beneath the Ebro basin and 30 km to 35 km versus 28 km to 32 km beneath the Aquitaine Basin). Beneath the Axial Zone

(a)

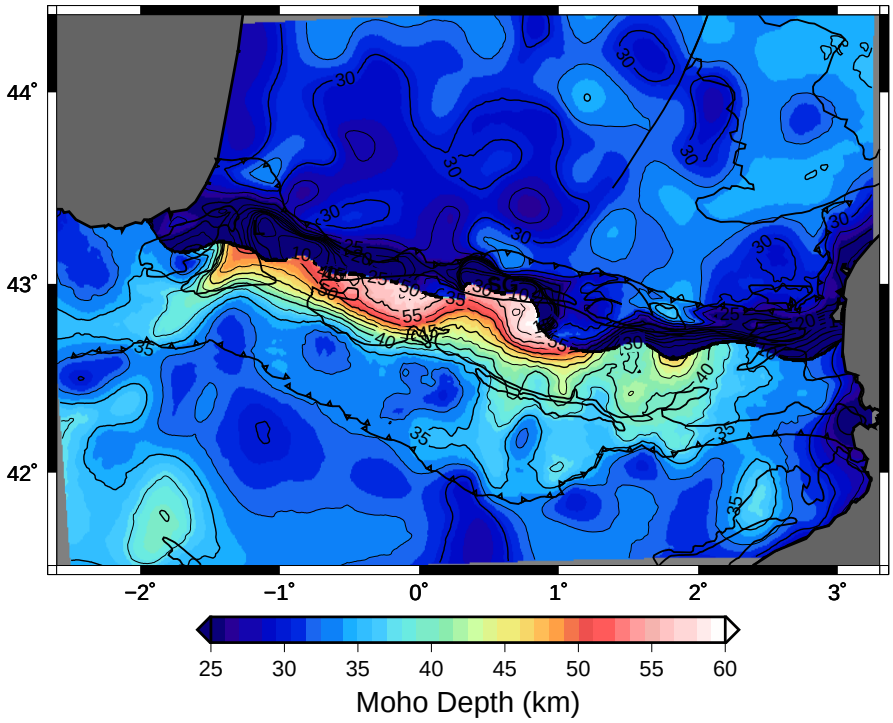

(b)

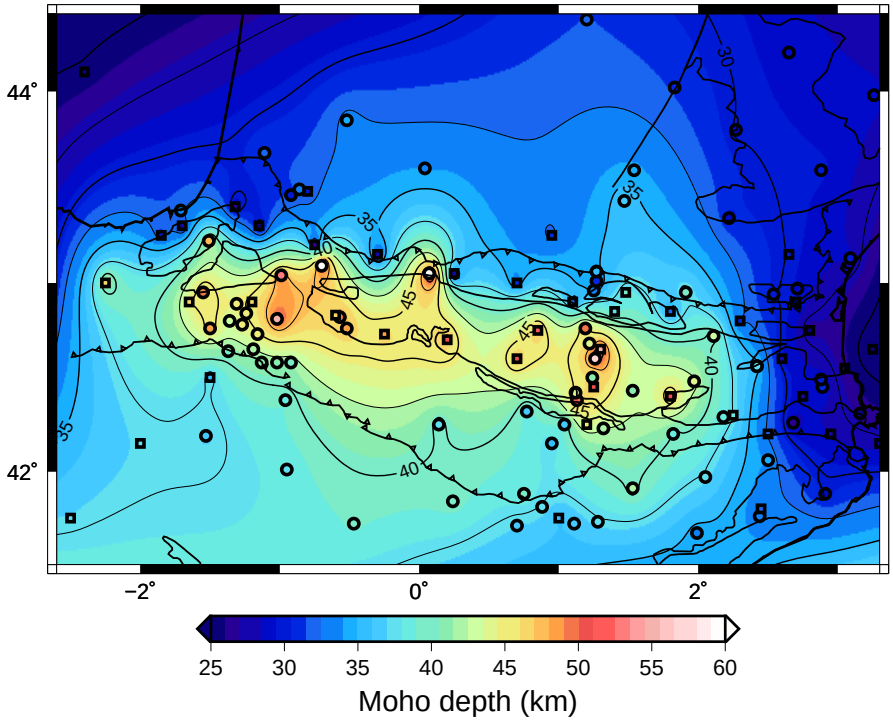

Figure 4.21: Moho depth (thickness of crust plus sediments) in our 3D model II **(a)** compared to the Moho depth model from Chevrot et al. [2014], obtained by interpolating estimates coming from receiver functions (circles) and deep seismic soundings (squares)**(b)**. Where the European and Iberian crusts are superposed, the map shows the European Moho.

and the Massif Central, however, the Moho in their model is significantly shallower (maximum of 50 km versus 59 km beneath the AZ and 28 km to 30 km versus 32 to 34 km in the Massif Central).

Yet, the most obvious difference between the two models is the gradient between the Iberian and European domains. Our map results from a continuous 3D model that has been discretized every 500 m and thus shows the sharp contrast between the underthrusting, thickened Iberian crust and the flattened European crust. In contrast, Chevrot et al. [2014] present a smooth interpolation of discrete data points that are separated by 25 km or more. Event though steep gradients can be observed between the data points, especially in the vicinity of the Mauléon basin between the 60 km deep Iberian and the <26 km deep European Moho, these gradients are not resolved in the interpolated map. Our 3D model resolves such sharp contrasts and thus provides more detailed and more precise information about the Moho depth than Chevrot et al. [2014]'s map. Therefore, our model may provide more accurate crustal corrections for regional tomography.

4.7.4 The Eastern Pyrenees

Our 3D geological model reproduces the main aspects of the Bouguer anomalies. The negative anomalies in the central Axial Zone are well explained by the crustal roots and the underthrusting of the Iberian plate beneath Europe. The Positive Labourd and Saint-Gaudens anomalies are explained by sharp Moho uplifts, and the negative anomalies in the foreland basins are also well reproduced by sedimentary basins. Subtracting the effects of these three contributions from the Bouguer anomalies indicates where further complexity need to be incorporated into the model in to explain the gravity data. For this, we predict Bouguer Anomalies with a reference 3D model that is in large parts equal to our Model II but differs is three important aspects: (1) The crustal roots are cut off at 35 km depth and replaced by mantle, (2) the sedimentary density is set to the upper crustal density of 2.61 g/cm^3, and (3) the Moho uplifts introduced to explain the Labourd and Saint-Gaudens gravity anomalies are filled with lower crust. We then subtract these predicted Bouguer anomalies from those computed with Model II in order to obtain the contribution of the three changes. Finally, we subtract this contribution from the true Bouguer anomalies.

In the map of Bouguer anomalies without the influence of crustal roots and sediments (Figure

4.22a), large parts of the negative Axial Zone anomaly are removed. Instead, a sharp contrast can be observed between positive anomalies above 20 mGal in the western and central Pyrenees and a large negative pattern of less than -150 mGal in the eastern Pyrenees. The positive anomalies can be explained by the Moho uplift beneath the Labourd and Saint-Gaudes anomalies and disappear when removing the influence of the exhumed mantle (Figure 4.22b). In this latter map, anomalies of -20 mGal to -40 mGal remain in the sedimentary basins but can be explained by changes of 1 km to 2 km of Moho depth. However, the large negative anomaly of -150 mGal is still present in the eastern Axial Zone. Preliminary results of the PYROPE and OROGEN experiments revealed that the Moho in this region lays between 28 km and 35 km depth, with an uncertainty of 3 km. This implies that this anomaly cannot be explained by thick crustal roots. A possible explanation for the shallow Moho under the pronounced topography in the eastern Pyrenees is thermal erosion of the lithosphere and crustal extension during Oligocene, going along with the opening of the western Mediterranean back-arc basin and resulting in crustal buoyancy and topographic uplift[Gunnell et al., 2008]. For our 3D model, we have fully exploited this uncertainty and modeled the Moho $\sim$3 km beneath the depth indicated in the seismic profiles, but this is not sufficient to reproduce the negative Bouguer anomalies.

Inspired by the structure revealed in OROGEN-01, we replaced the middle crust by upper crust and parts of the lower crust by middle crust beneath the eastern Axial Zone, thus introducing a low-density anomaly. With these changes, the model explains the data satisfactorily. In any case, the results of our modeling clearly point towards and anomalous crust in the eastern Pyrenees, compatible with an extreme crustal thinning accompanied by a removal of the lower crust and produced by the retreat of the Thyrhenean slab.

4.8 Conclusion

Combining geological and gravimetric data, we are able to construct a 3D model that respects the known geological information and that also explains the observed Bouguer anomalies. Residuals of

Bouguer anomalies in the final model have a standard deviation of less than 4 mGal, which would correspond to the effect of shifting the Moho by less than 1 km. Further refinement of the model requires 3D inversion. This will be presented in a forthcoming study.

The positive Labourd and Saint-Gaudens gravity anomalies can be explained by significant Moho uplifts up to depths of 11 km beneath the Mauléon basin and 10 km beneath Saint-Gaudens. Their horizontal extents are 45 km×28 km for the Labourd and 48 km×14 km for the Saint-Gaudens anomaly. In the eastern parts of the Axial Zone, a low-density anomaly is needed to explain gravity data. Since Moho depth and sedimentary thickness are well constrained in this area, we have introduced a significant thickening of the Iberian upper crust from 10 to 25 km without changing the total crustal thickness. This allowed us to model the anomalous density structure of the eastern Pyrenean crust, where our modeling results clearly suggest crustal thinning and the removal of the lower Crust. This might go along with an anomalously hot lithosphere maybe resulting from the retreat of the Thyrhenean slab during the opening of the western Mediterranean basin.

The maps of sediment thickness and their contribution to the Bouguer anomalies show that it is crucial to consider the unconsolidated sediments in the 3D model. A 1 km thick layer of unconsolidated sediments contributes as much as about -7.5 mGal to the total Bouguer anomaly.

Thanks to the potential field interpolation, our continuous 3D model may be discretized at any resolution and may thus serve as an a-priori 3D model for future investigations. In particular the sedimentary and crustal depths may be used to refine crustal corrections and to improve local and regional tomography. This model should also allow us to improve the localization of seismic events in the Pyrenees. The use of our 3D geological model is not limited to gravimetric or seismic studies. It can also be useful for other types of geophysical studies such as magneto-telluric or magnetic anomalies, which may yield new information to constrain the Pyrenean architecture.

(a)

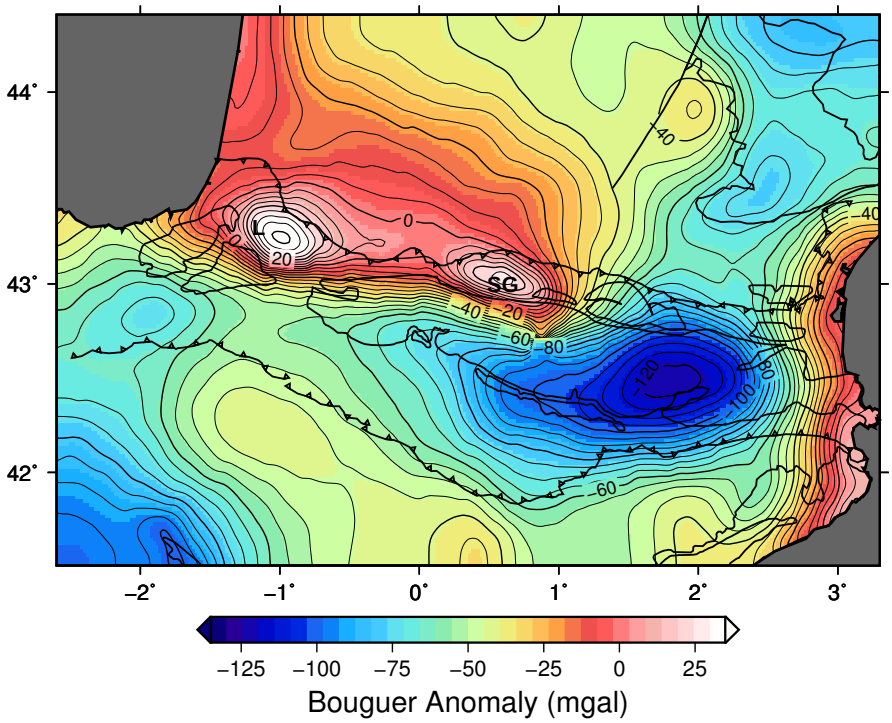

(b)

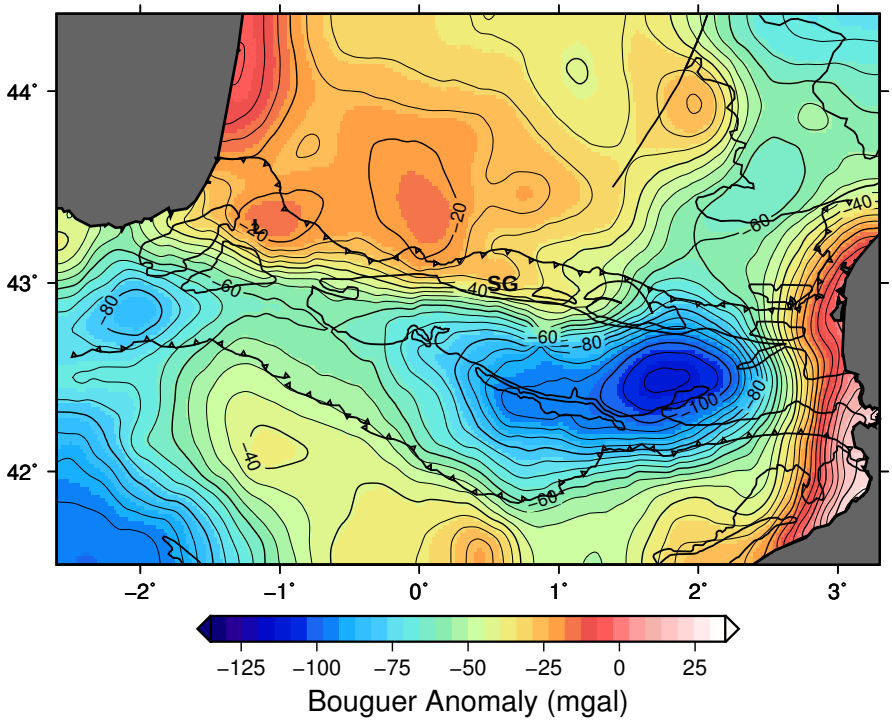

Figure 4.22: Bouguer Anomalies of the Pyrenean region minus the contribution of crustal roots, sediments **(a)**, and exhumed mantle **(b)**.

Chapter 5

3D Geophysical Imaging of the Pyrenees

Contents

5.1 Introduction

As it is shown in the previous chapter, the European crust is extremely thinned beneath the Labourd and Saint-Gaudens gravity anomalies (section 4.6.3), and the crust of the eastern Pyrenees differs from the western and central part of the belt (section 4.7.4). But this EW dichotomy is not the only source of lateral heterogeneities. Geological data (section 4.3) reveal small-scale heterogeneities all over the belt that are still not captured by our 3D model. For example, thrusts and faults are present in the North and South Pyrenean Zones [e.g. Daignières et al., 1982; Choukroune, 1989; Velasque et al., 1989], and the petrophysical properties of the sedimentary foreland basins differ from those of the basement in the mountain range [e.g. Grandjean, 1994]. These heterogeneities motivate the need to further refine our 3D a-priori model. Since the tomographic problem of imaging the very heterogeneous crust is strongly non-linear, the influence of the starting model used in the

inversion may be crucial. One of our motivations is thus to test our 3D a-priori model versus a standard 1D model to quantify the benefits of using more a-priori information in the inversion. We will use two approaches, a standard iterative 3D local travel time tomography and a Monte Carlo method. Monte Carlo methods take into account the non-uniqueness of the solution by creating large sets of models that satisfy the data within the measurement errors [Mosegaard and Tarantola, 1995]. The Metropolis algorithm [Metropolis et al., 1953] randomly perturbs a model following a given a-priori probability density function on the model parameters. After inversion, an a-posteriori probability density can be computed from all models that satisfy the data. The inversion algorithm implemented in `GeoModeller` is based on the Metropolis approach. After inversion, it allows us to compute a-posteriori density functions to estimate for example the average and standard deviation of a given parameter or to characterize the covariance of two distinct parameters.

Many geophysical investigations have been performed in the Pyrenees using various types of data: gravimetric [e.g. Grandjean, 1994; Casas et al., 1997], seismic [Hirn et al., 1980; Gallart et al., 1981; Roure et al., 1989; Grandjean, 1994, e.g], and magneto-telluric [e.g. Pous et al., 1995; Campanyà et al., 2012; Benjumea et al., 2013], to name a few.

The idea to combine different geophysical methods in a joint inversion is to better constrain the model and thus reducing the non-uniqueness of the solution of the inverse problem. In the present study, regional seismic travel times and Bouguer gravity anomalies are inverted to refine our 3D a-priori model. The a-priori model is described in section 5.2, the geophysical data in section 5.3. After introducing the discretization of our model in section 5.4, the results will be presented in section 5.5 and discussed in section 5.6.

5.2 3D A-Priori Model

As it is shown in section 4.7.4, a low-density anomaly is needed in the eastern Pyrenees to reproduce the Bouguer Anomalies. For forward modeling, this low-density body has been modeled by replacing lower crust by middle crust and middle crust by upper crust. Let us now consider a new 3D model, Model III, which is in large parts the same as Model II but has a standard layered crust also in

the east. Cross-sections of this model are shown in Figure 5.1; a 3D view of the crustal units is presented in Figure 5.2. The map of Bouguer anomalies (Figure 5.3) predicted by this model shows negative anomalies up to -50 mGal in the eastern Axial Zone, while positive anomalies of 5 to 10 mGal are observed in the rest of the model. Applying equation (2.13), the amplitude of the negative anomaly corresponds to a deepening of 2.7 km of the Moho or to 21.7 km of middle crust replacing the lower crust. The difference in Moho depth is not compatible with the seismic data since their uncertainty of 3 km has already been exploited to push the Moho downward by this amount when constructing the model. The seismic transects do not reveal intracrustal boundaries; however the OROGEN-01 section indeed shows anomalous structures beneath the Axial Zone.

5.3 Geophysical Data

5.3.1 Seismic Data

The data set used in our tomographic inversions is based on a catalog compiled by Theunissen et al. [2017]. It covers the period between 1975 and 2013 and is mainly composed of arrival times extracted from the bulletins of the "Réseau de Surveillance Sismique des Pyrénées" (RSSP, http://rssp.irap.omp.eu/), the "Institut Cartographic i Geologic de Catalunya" (ICGC), and the "Instituto Geografico Nacional" (IGN) as well as on manual picks on stations from the IBERARRAY and PYROPE temporary deployments and smaller, temporary experiments [Dubos et al., 2004; Ruiz et al., 2006a,b; Sylvander et al., 2008].

For the inversion, we only keep the first P and S wave arrivals, because the algorithm used to compute travel times only provides arrival times of the first P and S arrivals at a receiver [Podvin and Lecomte, 1991]. Figure 5.4a shows P wave arrival times as a function of epicentral distance. Two linear branches can be distinguished: one starting near the origin of the graph and representing the P_g waves, which propagate through the crust, and a second one starting at about 100 km source-receiver distance and representing the P_n waves, which reach the mantle. For distances above approximately 150 km, the P_n phase arrives before the P_g phase. In order to keep the first arrivals only, we first fit a straight line through the P_g data below 150 km distance and a second

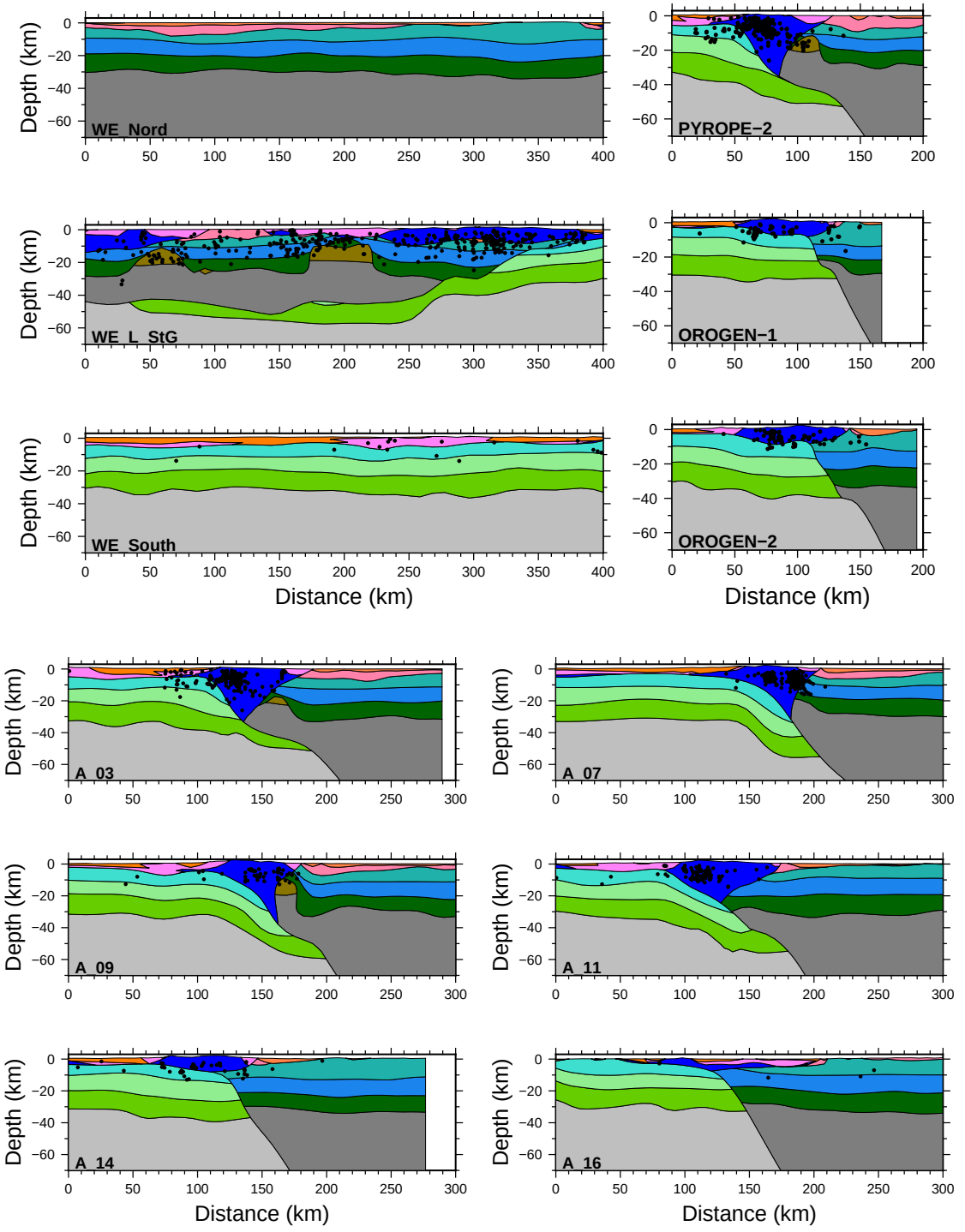

Figure 5.1: Cross-sections in Model III with seismicity displayed as black dots (see Figure 4.11 for the localizations of the sections and Figure 5.5b for the description of the stratigraphic pile.

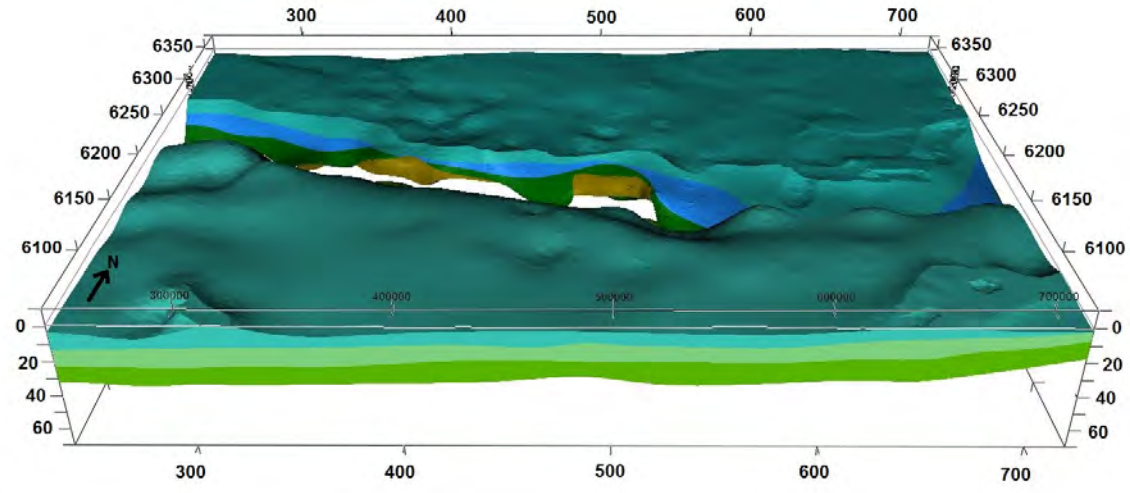

Figure 5.2: Crustal units (green and blue colors) and exhumed mantle (brown) of Model III. Axes are depth in km and Lambert93 coordinates in km.

straight line through the P_n branch above 300 km distance. For distances below 100 km, we keep arrival times that are closer than four standard deviations to the P_g. Above 100 km, we retain data that differ by less than one standard deviation from the P_n branch. The filtered data set is represented in dark gray in Figure 5.4. We follow the same procedure to filter the S wave travel times, shown in Figure 5.4b.

The Wadati diagram [e.g. Lowrie, 2007; Lay and Wallace, 1995; Havskov and Ottemoller, 2010] is shown in Figure 5.4c. It is obtained by plotting the difference $t_S - t_P$ between the S and P arrivals as a function of the P wave travel time t_P:

$$t_S - t_P = a \cdot t_P \tag{5.1}$$

The distance x between the source and the receiver is the same for P and S waves, so that the slope

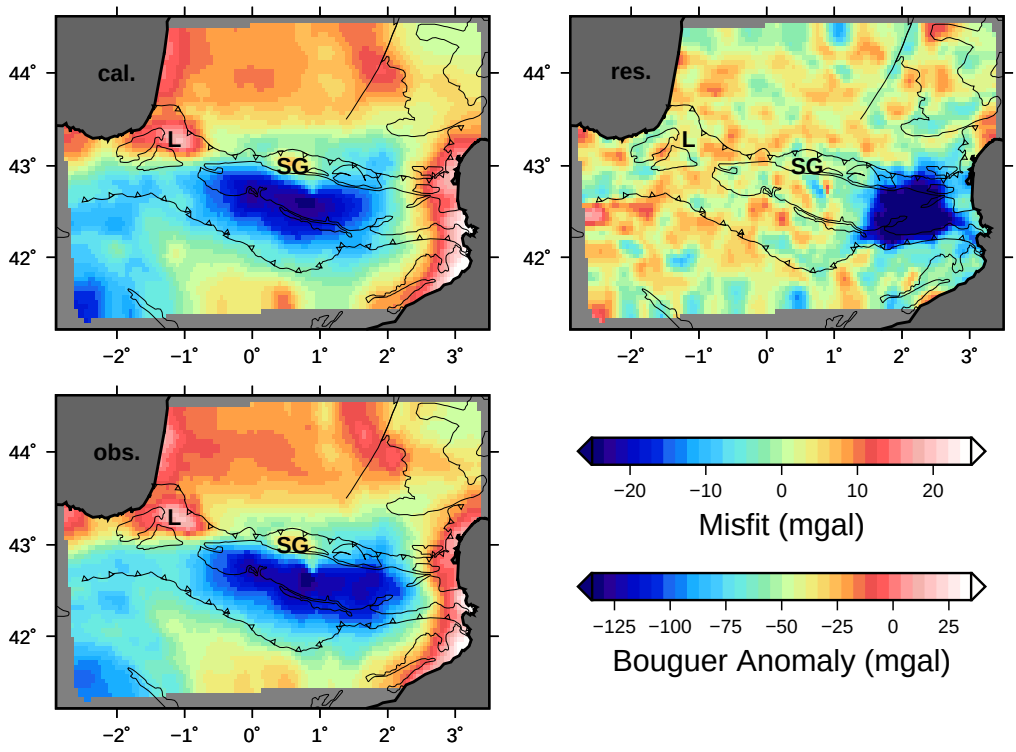

Figure 5.3: Top: Map of Bouguer anomalies (left) and residual misfits (right) calculated in Model III using the density values listed in table 4.1. Bottom: Observed Bouguer Anomalies.

a in the Wadati diagram is related to the v_P-to-v_S ratio:

$$a = \frac{t_S - t_P}{t_P} = \frac{t_S}{t_P} - 1. \tag{5.2}$$

$$a + 1 = \frac{\frac{x}{v_S}}{\frac{x}{v_P}} = \frac{v_P}{v_S}. \tag{5.3}$$

The original data set (light gray points) consists of three branches. The main central branch shows S_g and P_g phases beneath and S_n and P_n phases above ∼25 s P wave travel time. At ∼25 s P wave travel time, two branches corresponding to the S_g and P_n phases and to the S_n and P_g phases start respectively above and beneath the main branch. In the filtered data set (dark gray points), large parts of the S_n-P_g and S_g-P_n branches have been eliminated. We now compute a

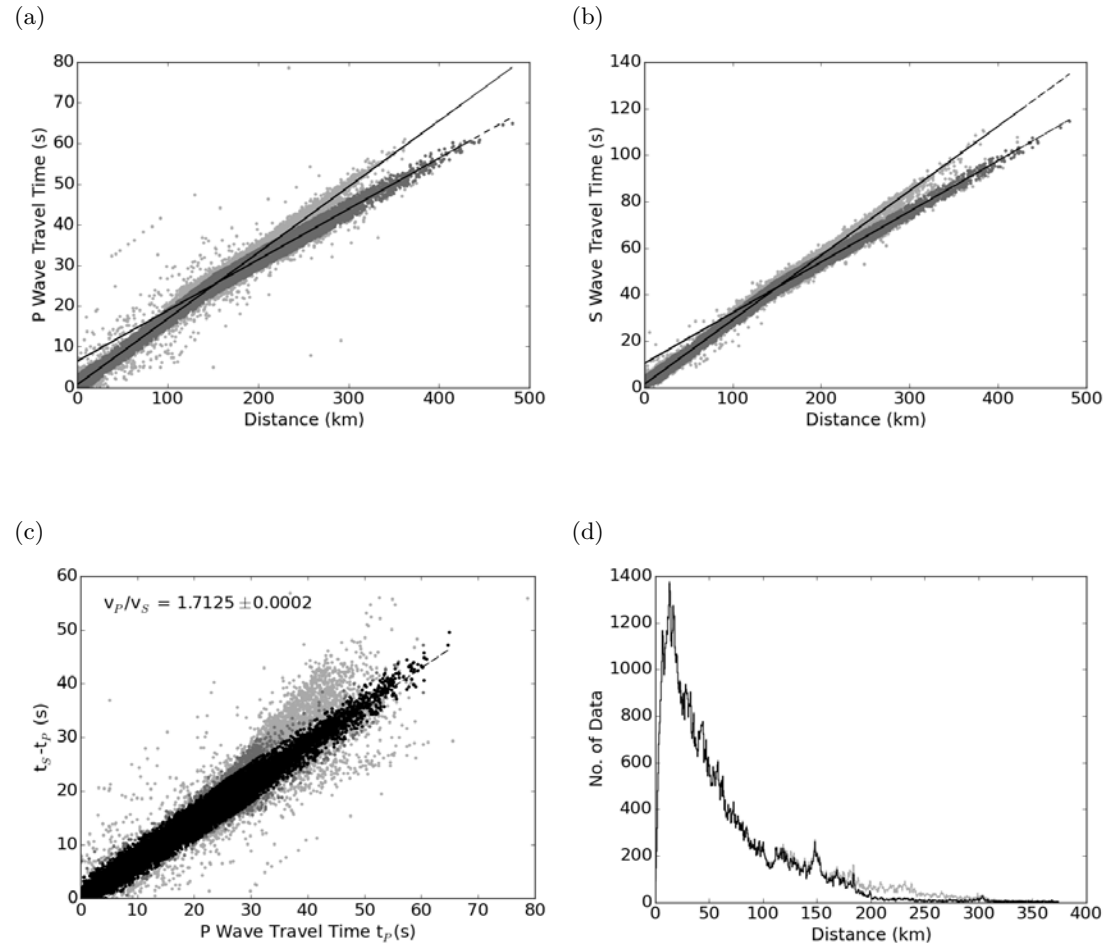

Figure 5.4: Seismic data selection. **(a):** P wave travel times as a function of epicentral distance. The P_g branch starts at the origin, the P_n branch starts at about 100 km distance. Linear fits are computed for both branches, and data differing by less than 4 standard deviations from the P_g trend are kept below 100 km, one standard deviation from P_n is kept above. The remaining data are represented in dark gray. **(b):** Same diagram for S waves corresponding to the paths kept in (a). The same filter is applied to the S waves, resulting in the dark gray data set. **(c):** Wadati diagramm. All available data are represented in light gray. First P and S arrivals (remaining after (b) are dark gray. They are fitted with a straight line and only data deviating by less than 4 standard deviations are kept (black points). The new fit gives a v_P/v_S ratio of 1.71. **(d):** Number of data per distance before (gray) and after (black) filtering.

linear fit considering only the filtered points that differ by less than four standard deviations from the mean branch. The remaining data set (black points) contains 150 005 arrival times for both P and S waves. A linear fit through these data yields a v_P/v_S ratio of 1.7125±0.0002.

Finally, in order to keep only the well located earthquakes, we reject those that have been recorded at less than five stations. This final data set contains 146 773 P and S waves from 19 470 sources, recorded at 314 stations.

Figure 5.5a shows the selected events and receivers, and Figure 5.5c gives the distribution of the seismic events in different depth levels of Model III. The seismicity in different cross-sections is shown in Figure 5.1. Most of the seismicity occurs in the accretionary prism. The narrow band of seismicity in the western NPZ is located between the prism and the sediments near the surface. The diffuse distribution in the east approximately coincides with the reduction of the volume of the accretionary prism. Earthquakes occur all over the exhumed mantle beneath the Labourd gravity anomaly, but are concentrated above the exhumed mantle in the section crossing the Saint-Gaudens anomaly.

5.3.2 Densities and Seismic Velocities

Gravity is often used to infer crustal structures [Rivero et al., 2002; Coron and Guillaume, 1971], but densities of deep rocks are difficult to retrieve by solving an inverse problem. For this reason, many scientists estimate densities from seismic velocities, as proposed e.g. by Nafe and Drake [1957], Birch [1952], Gardner et al. [1974], Rybach and Buntebarth [1982], or Brocher [2005].

Brocher [2005] summarizes different empirical relationships between density and seismic compressional wave speeds as well as between seismic P and S wave velocities. The Nafe-Drake relation (Eq. 1 in Brocher [2005]) relates density to seismic velocity according to:

$$\rho = 1.6612v_P - 0.4721v_P^2 + 0.0671v_P^3 - 0.0043v_P^4 + 0.000106v_P^5 \tag{5.4}$$

where ρ is the density in g/cm^3 and v_P is the compressional wave speed between 1.5 km/s and 8.5 km/s. He further proposes a regression formula for the inverse relation, based on Ludwig et al.

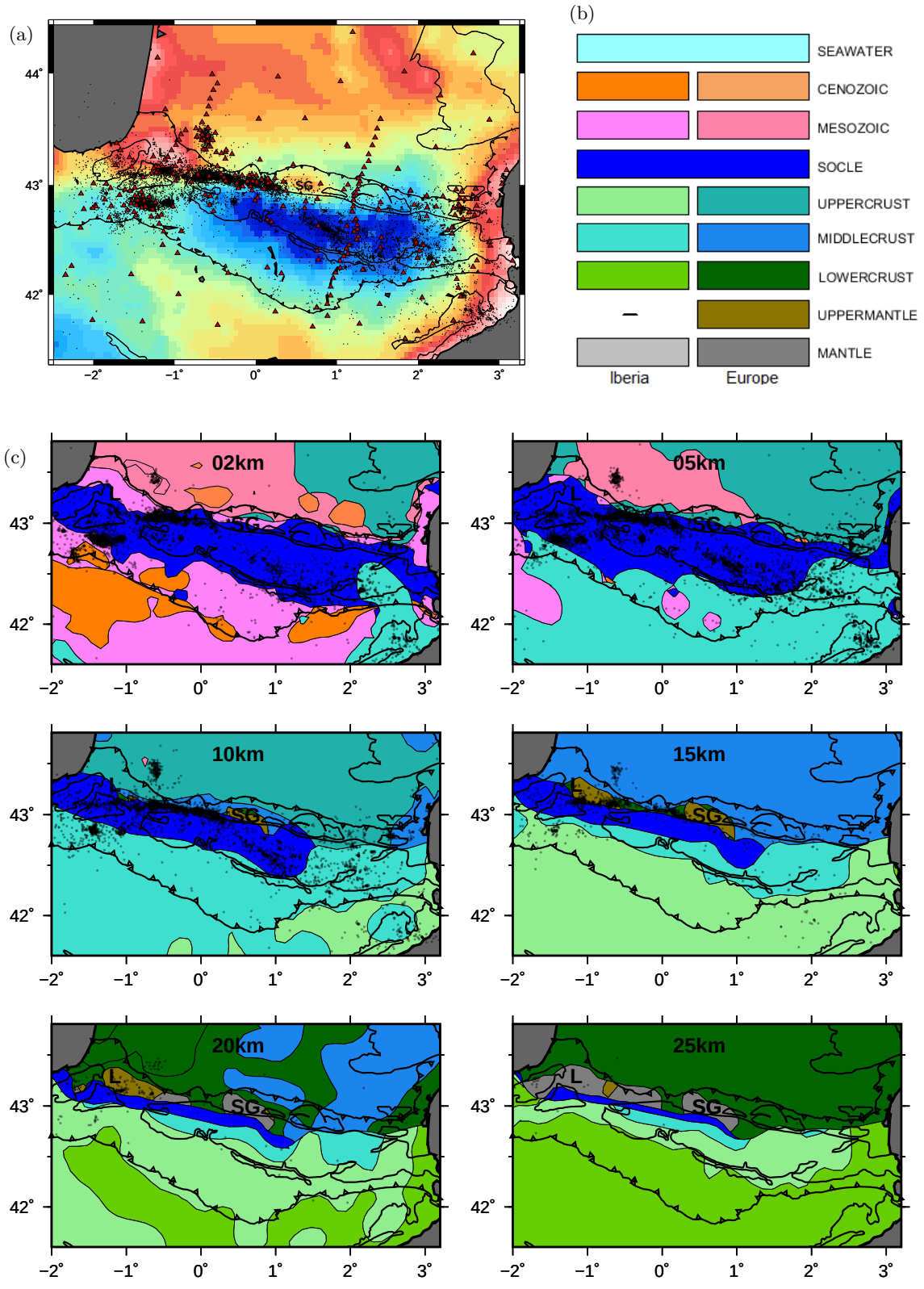

Figure 5.5: **a:** Map of earthquakes (black dots) and receivers (red triangles), overlain by Bouguer anomalies. **b:** Stratigraphic pile. **c:** Distribution of earthquakes at different depth levels. The letters L and SG indicate the locations of the Labourd and Saint-Gaudens gravity anomalies.

Unit	P wave velocity (km/s)	density (g/cm^3)
Sediments	5.3 - 5.6	2.4 - 2.52
Upper Crust	6.1	2.75
Lower Crust	6.3 - 6.4	2.93
Mantle	8.0 - 8.1	3.28

Table 5.1: Seismic compressional wave speed and density in the Pyrenees after Rivero et al. [2002]

[1970] (Eq. 5 in Brocher [2005]):

$$v_P = 39.128\rho - 63.064\rho^2 + 37.083\rho^3 - 9.1819\rho^4 + 0.8228\rho^5 \tag{5.5}$$

with v_P being the P wave speed in km/s for densities ρ between 2 g/cm^3 and 3.5 g/cm^3.

However, measurements show a wide scatter around these relations and their applicability to real problems is controversial. While Fountain [1986] rejects scaling relations between these two petro-physical properties, Barton [1986] acknowledges the use of such functions as long as they are not the only source of information. He states that using density-velocity relations as the only constraint to determine densities yields to important uncertainties for layer thicknesses of several kilometers. At the scale of the continental crust (25 - 35 km thickness), he estimates the error to be "one order of magnitude larger than observed gravity anomalies". Therefore, he suggests to take into account additional constraints like isostasy or the fact that large lateral changes in density are as unrealistic as very different densities for neighboring rocks with similar seismic velocity.

Casas et al. [1997] and Rivero et al. [2002] propose values for seismic velocities and mass densities in the Pyrenees (cf. Table 5.1). Seismic velocities derived from deep seismic refraction profiles range from 5.3 to 5.6 km/s in the uppermost sedimentary layers, from 6.1 to 6.4 km/s in the upper and middle crust, and from 8.0 to 8.1 km/s in the mantle. Densities derived from samples and gamma logs or at larger depth from density-velocity relationships range from 2.40 - 2.52 g/cm^3 in

sediments over 2.75 (2.93) g/cm^3 in the upper (lower) crust to 3.28 g/cm^3 in the mantle [Rivero et al., 2002].

A huge number of borehole logs are available at the Office for Exploitation and Production of hydrocarbons (BEPH: Bureau Exploration-Production des Hydrocarbures, www.beph.net) for the Pyrenean foreland basin (mainly the Aquitain Basin), but only 35 of them contain both mass density and sonic logs.

These logs contain data in different depth ranges, sampled every five meters. While density logs directly yield the density in g/cm^3 at a given depth in m, sonic logs reveal interval transit times (ITT) in μs/ft which have to be transformed to velocity v in km/s by

$$v = \frac{10^3 \mu\text{s/s}}{3.28084\text{ft/m} \cdot \text{ITT}}. \tag{5.6}$$

The logs are present as scanned images only, so before being exploited, they have to be digitized. This is done with the free software QGIS [Team, 2016] by referencing the axes first and then re-sampling the lines point by point. As this procedure is very time-consuming (it takes up to one working day per drillhole), it could not be performed on the entire set of drillholes. Figure 5.6a shows the location of the available logs and the ones chosen for this study.

Once the logs are digitized, they can be used to establish a regional density-velocity relationship and to choose realistic values for the starting model. We re-sample by calculating averaged values every 50 meters in depth. The average densities are then plotted against the average velocities and vice versa. Figures 5.6d and 5.6e depict the data points $\rho(v)$ and $v(\rho)$ obtained from all analyzed boreholes. In general, the data follow the Nafe and Drake [1957] and Ludwig et al. [1970] relations but with a wide scatter.

We can distinguish different ranges of seismic velocity and mass density for Cenozoic (circles in Figure 5.6) and Mesozoic sediments (diamonds in Figure 5.6; plots for all boreholes are given in appendix A.2). While Cenozoic densities range between 2.2 and 2.4 g/cm^3 and 2.5 and 3.5 km/s, Mesozoic ones range from 2.55 to 2.75 g/cm^3 and from 4.0 to 6.2 km/s. The only Cenozoic

sediments lying in the Mesozoic range date from Paleocene. Mesozoic rocks of lower densities are mostly anhydrites. These observations lead us to distinguish between Cenozoic as unconsolidated and Mesozoic plus Paleocene as consolidated sediments.

5.4 Discretization

In order to obtain further information on the nature of the anomaly in the eastern Pyrenees, we will perform 3D gravity and seismic inversions. Seismic travel times are computed with `time3d` as explained in section 3.1. This routine requires the velocity model to be discretized into a regular grid of cubic blocks. The block size is a compromise between precise modeling of geological units on one hand and computation time and memory demands on the other hand. We compute travel times and perform raytracing in a grid of 500×500×500 m^3 from 3 km altitude to 69 km depth. This leads to a grid size of 960×640×144=88 473 600 cells.

In `GeoModeller`, in contrast, block dimensions may differ between the three directions, and thickness may increase with depth. It is thus possible to precisely model the sedimentary basins near the surface and to use a coarser grid at depth in order to save computation time. For gravity computations, we use a grid of 5×5 km^2 in horizontal directions. The layer thickness is 200 m from 3 km altitude to 10 km depth and then increases incrementally by 10% until it reaches 5.5 km at 70 km depth. This grid has 96×64×101=620 544 cells (65 layers above 10 km depth, 36 beneath).

For joint inversion, all geophysical fields have to be computed on the same grid. This means that a compromise must be found between the seismic and the gravity grid. The results from seismic forward modeling are resampled to 5×5×0.5 km^3, i.e. 96×64×144=884 736 cells, and this grid is adopted for joint inversion. The large dimensions in the horizontal directions allow us to perform the gravity computations in a reasonable time, while the smaller layer thickness allows us to describe the complex geometry of the sedimentary basins. However, the coarser grid implies a less precise velocity model, since the new cells are averages of the smaller cells. Furthermore, travel time inversion will be less precise because ray segments of the old cells are summed up for the new ones, and travel time perturbations are computed using the average velocities. For example, if one

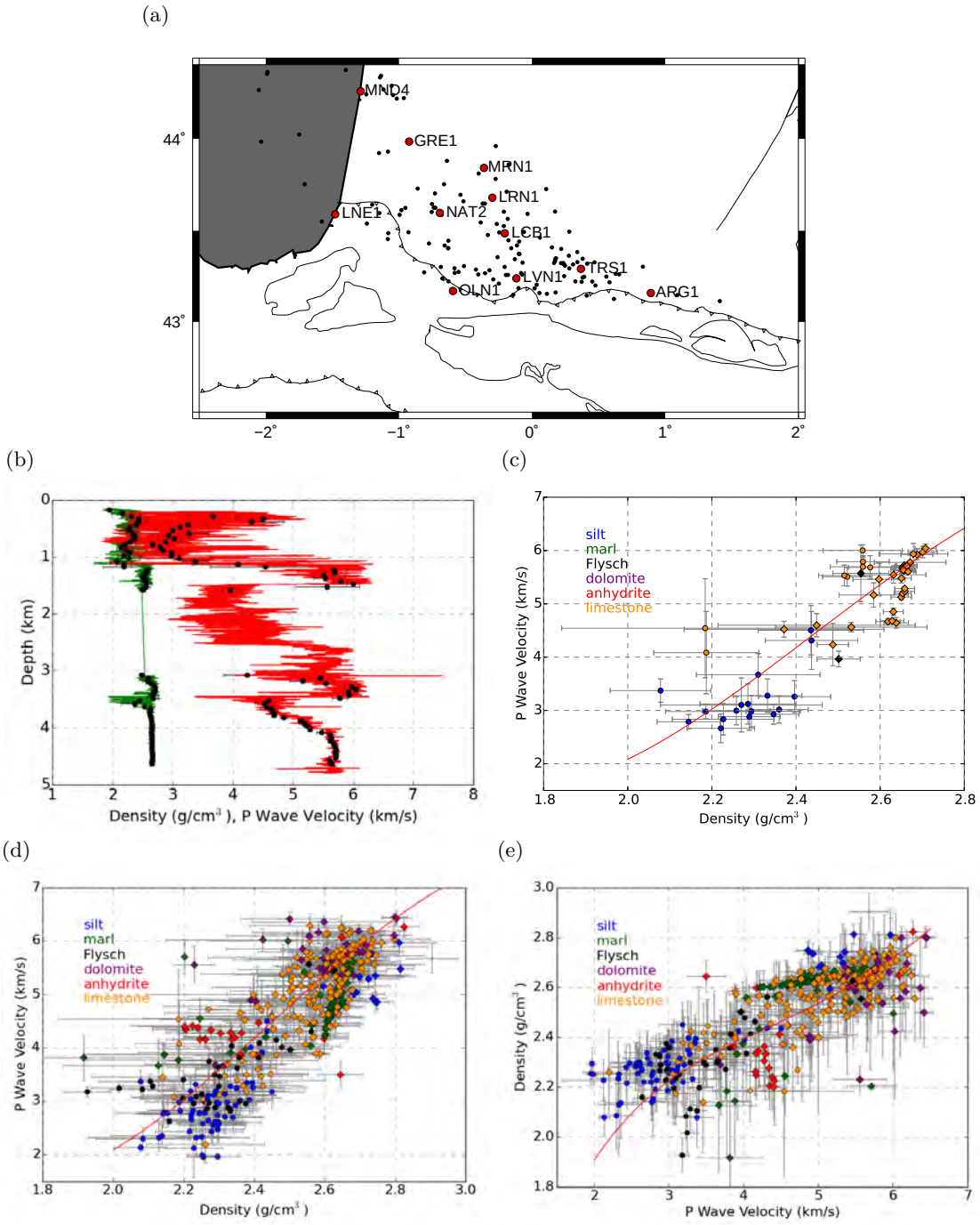

Figure 5.6: Seismic P wave velocities and mass densities from borehole logs. **(a):** Positions of density and sonic logs from the BEPH database. Black circles indicate positions of available density and sonic logs; red circles represent those that we used for our analysis. **(b):** Seismic P wave velocities (red) and mass densities (green) obtained from sonic and density logs of borehole TRS-1. Black points show averages calculated every 50 m. **(c):** Cross-plots of average velocities and densities from (b). **(d-e):** Same cross-plots for all analyzed logs. Diamonds show sediments of Mesozoic age, circles of Cenozoic age. Red lines show the relations proposed by Nafe and Drake [1957] (c-d) and Ludwig et al. [1970](e).

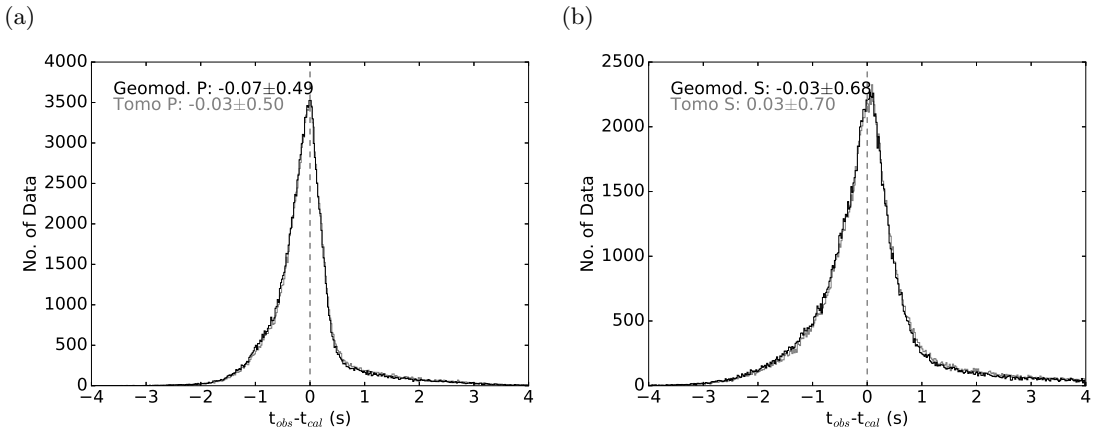

Figure 5.7: Travel time residuals of Model II obtained in the joint grid (black) compared to discretization used for travel time computation (gray). Left: P waves, right: S waves.

new block contains the average of two or more velocities, no difference is made whether the ray touches all of them or whether it just travels through one uniform velocity. Figure 5.7 shows the travel time residuals obtained directly from Model II compared to those after rediscretization for the `GeoModeller` inversion. The maxima of the curves change from -0.03 for the P waves and +0.03 for S waves to -0.07 and -0.03, respectively, i.e. the curves obtained in the `GeoModeller` grid are slightly shifted towards negative values with respect to the original ones. The standard deviations, however decrease slightly from 0.50 to 0.49 for P waves and from 0.7 to 0.68 for S waves. All in all, the differences between the travel time residuals obtained in the two grids are small enough to validate our choices for the parametrization of the problem.

5.5 Results

5.5.1 Inversion of Bouguer Anomalies

For the inversion of Bouguer anomalies, we assume an uncertainty of 1.0 mGal on each gravimetric measurement. At each iteration, the density perturbation is selected at random within the

propability density function of the current cell. This function is defined as a Gaussian distribution around the current density of the cell and a standard deviation. This standard deviation is set to ± 0.08 g/cm^3 for most of the geological units. The densities of the sediments, however, being well defined from the logging data, have a standard deviation of ± 0.05 g/cm^3. For sea water, the value is set to ± 0.001 g/cm^3. 60 000 000 iterations are performed, and the constant shift between modeled Bouguer anomalies and true data (cf. sec. 2.4) is recalculated every 10 000 iterations. The computation is performed in a grid of $96 \times 64 \times 144 = 884\,736$ blocks of $5 \times 5 \times 0.5$ km^3.

Figure 5.8 shows the misfit between observed and predicted Bouguer anomalies during the inversion. It converges from 8.52 mGal to 1.67 mGal during the first $30 \cdot 10^6$ iterations and oscillates around this value until the end.

The densities resulting from the last 50%, i.e. the last $30 \cdot 10^6$ iterations, are kept for statistical analysis. Since the images seem noisy, we apply a Gaussian filter with a correlation length of 30 km. The smoothed images are shown in Figure 5.9, the unsmoothed ones are in the appendix (Figure A.6). Figure 5.9 shows negative density perturbations of $\sim$-0.04 g/cm^3 are retrieved near the surface along the SPF. The most striking feature, however, is a large pattern of negative perturbations in the eastern Axial Zone, which are the strongest in the uppermost 10 km and still present down to 40 km depth.

In order to test the discretization, we rerun the inversion with $60 \cdot 10^6$ iterations in the grid used for forward modeling: The layer thickness is 200 m from 3 km altitude to 10 km depth and increases incrementally by 10% beneath, reaching a value of 5.5 km at 70 km depth.

Figure 5.10 shows the evolution of the misfit between observed and modeled Bouguer anomalies. It decreases from 8.52 mGal before inversion to 1.44 mGal after $10 \cdot 10^6$ iterations and oscillates around this value until the end. We compute the average of the last $40 \cdot 10^6$ iterations and apply the same filter as before for smoothing. The density perturbations differ significantly from those obtained with the regular grid, as shown in Figure 5.11. The negative density perturbations in the eastern Axial Zone are now concentrated at depth with their top lying at $\sim$20 km and their base lying beneath 50 km depth. They are the most pronounced between 30 and 40 km depth. Their

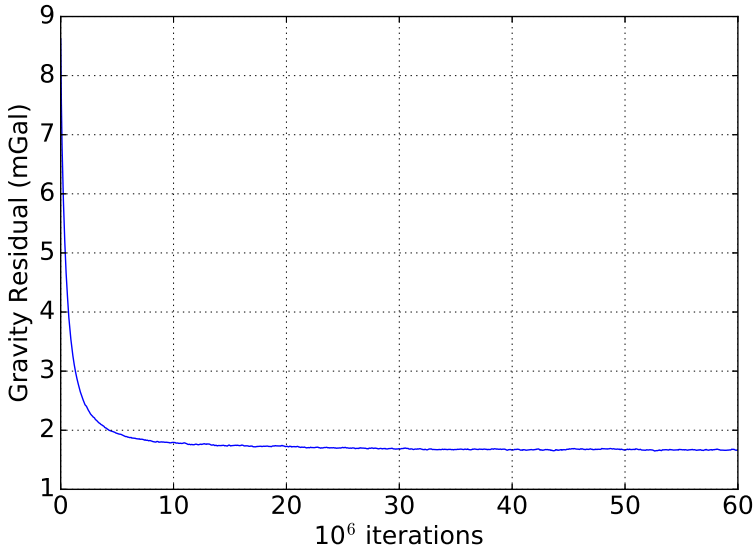

Figure 5.8: Misfit of Gravity inversion in the regular grid.

amplitudes reach -0.05 to -0.1 g/cm^3 at 30 km depth. Positive perturbations of more than 0.4 g/cm^3 are scattered over the foreland basins at 30 km depth, and migrate towards the Axial Zone with increasing depth. Between 40 and 50 km depth, strong positive and negative patterns are present in the Axial Zone and the North Pyrenean Zone. An explanation for these strong perturbations can be seen in Figure 5.12, showing the smoothed density perturbations in cross-sections: They are mostly located at interfaces between the mantle and crustal units. The application of strong density perturbations along these boundaries corresponds to a change in topography of the interfaces. The inversion results thus indicate that the geometry of the Moho and in particular of the Iberian slab can still be refined. Figure 5.13 shows the a-posteriori standard deviation of the density. It lies between 0.006 and 0.007 g/cm^3 in most parts of the model and is thus less than the a-priori standard deviation.

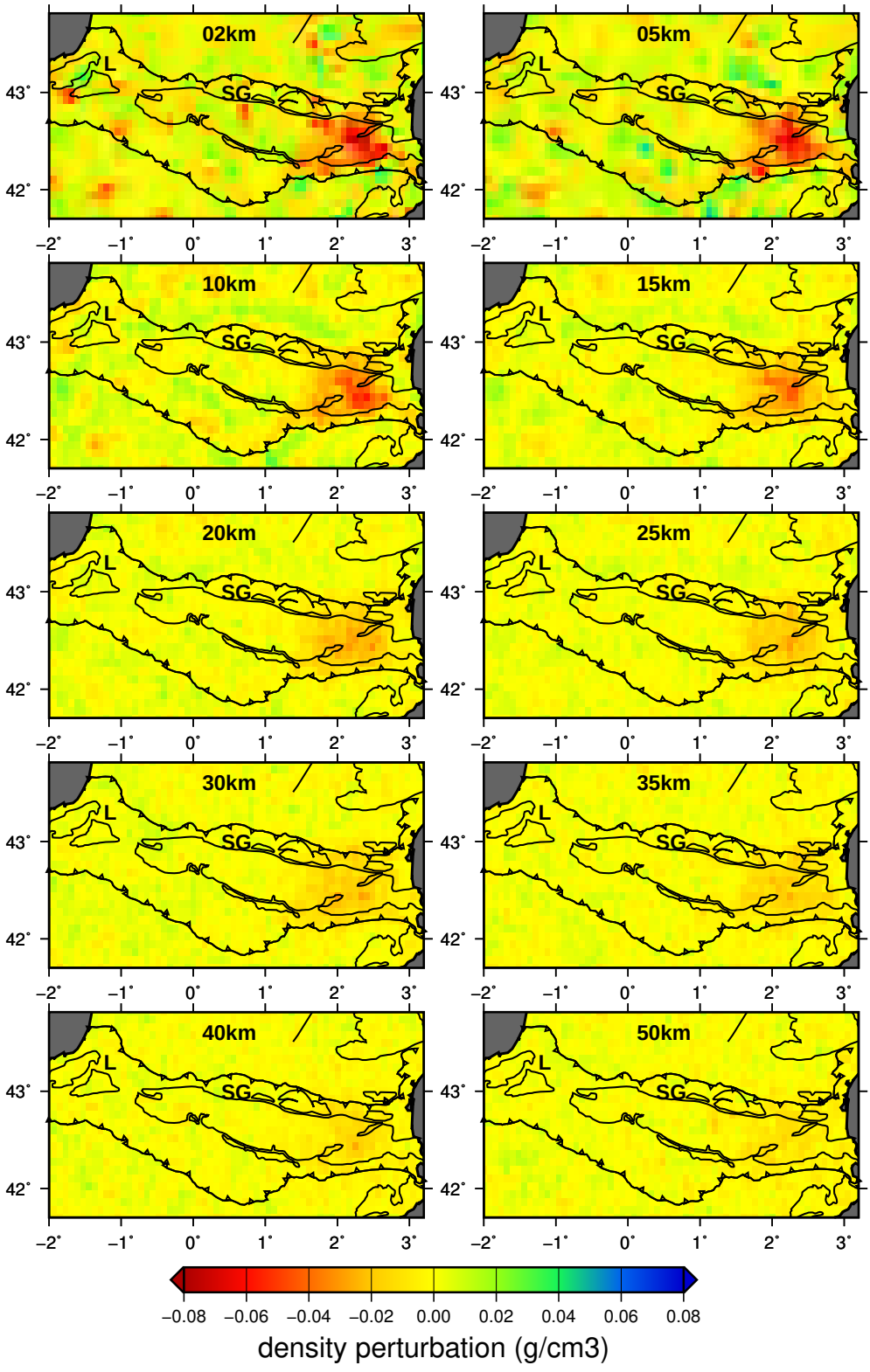

Figure 5.9: Smoothed density perturbation after gravity inversion in the regular grid, starting from Model III. Average from the last $30{\cdot}10^6$ out of $60{\cdot}10^6$ iterations.

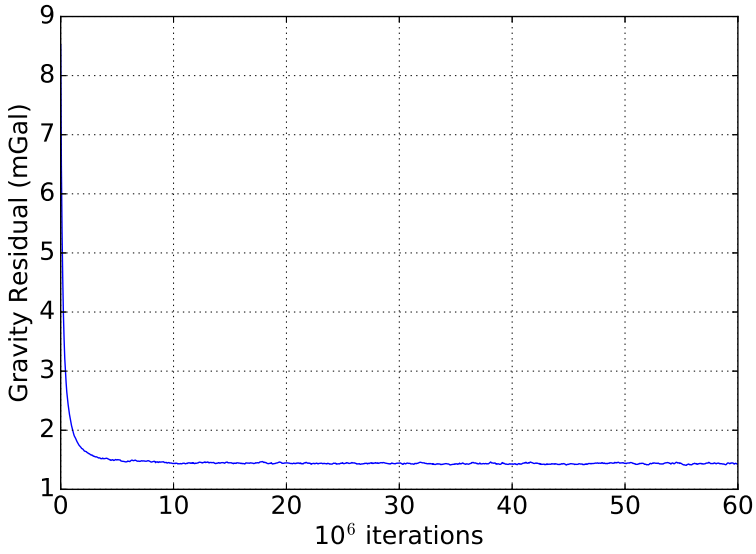

Figure 5.10: Misfit of Gravity inversion in irregular grid.

5.5.2 Seismic Travel Times Predicted from the 3D Model

We will now exploit our 3D model to compute regional seismic travel times and compare the results to travel times obtained from a 1D model of homogeneous velocity layers. We use relation from Ludwig et al. [1970] (eq. (5.5)) to transform the densities used for gravity modeling into P wave velocities for the 3D model. This gives values between 4.5 km/s and 5.2 km/s for Cenozoic and Mesozoic sediments, 5.2 km/s to 6.6 km/s for the crust, and 8 km/s for the mantle (Table 5.2). Sea water velocity is set to 1500 km/s. S wave velocities are obtained from the Wadati diagram (Figure 5.4c) as

$$\frac{v_P}{v_S} = 1.71. \tag{5.7}$$

The 1D velocity model [Souriau and Pauchet, 1998] is used at the Observatoire Midi-Pyrénées (OMP) for earthquake localization. It starts at the surface with a P wave velocity of 5.5 km/s and has its last discontinuity at 34 km depth where it reaches a maximum P-wave velocity of 8.0 km/s

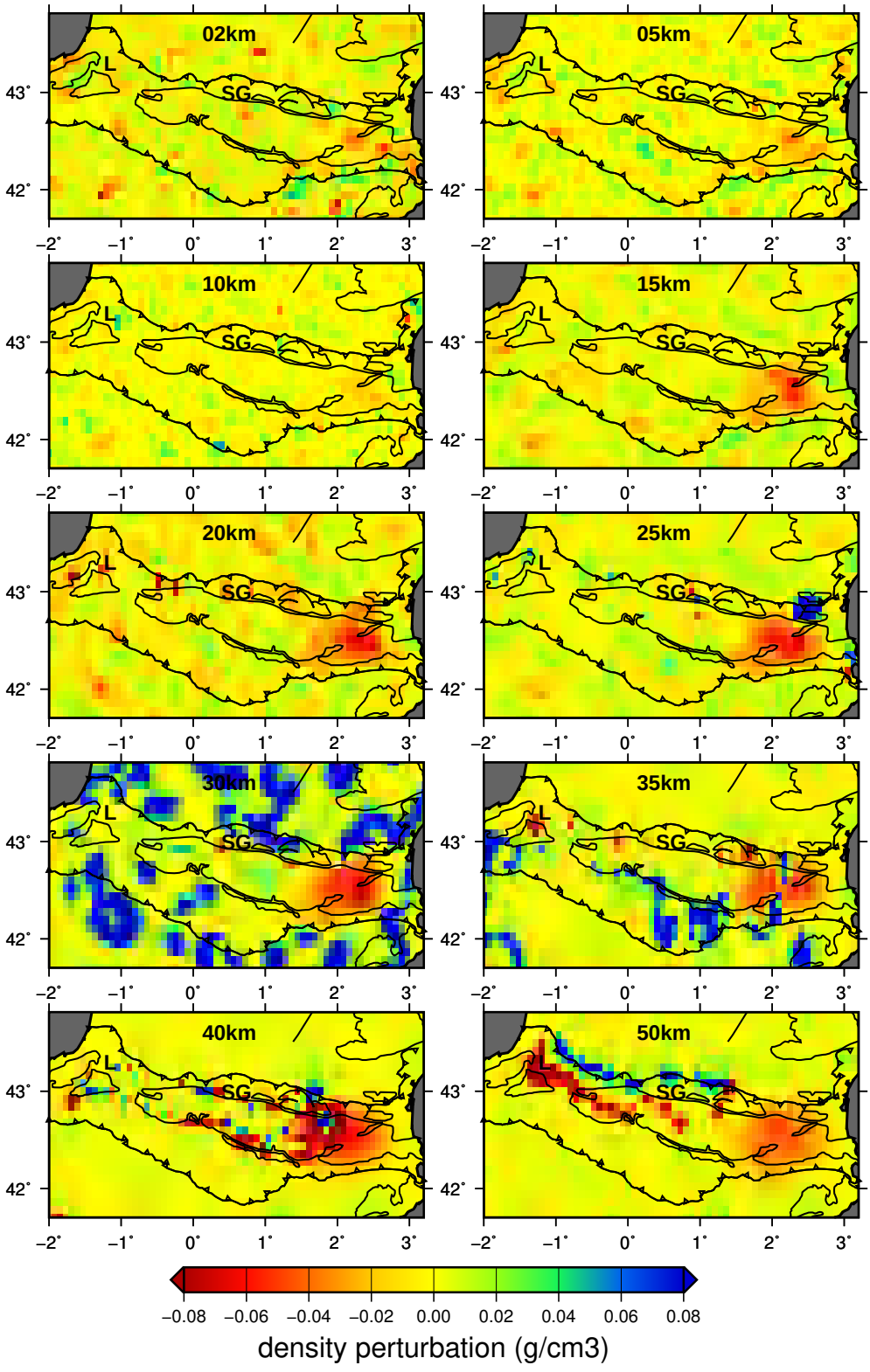

Figure 5.11: Smoothed density perturbation after gravity inversion in irregular grid, starting from Model III. Average from the last $40{\cdot}60^6$ out of $60{\cdot}10^6$ iterations.

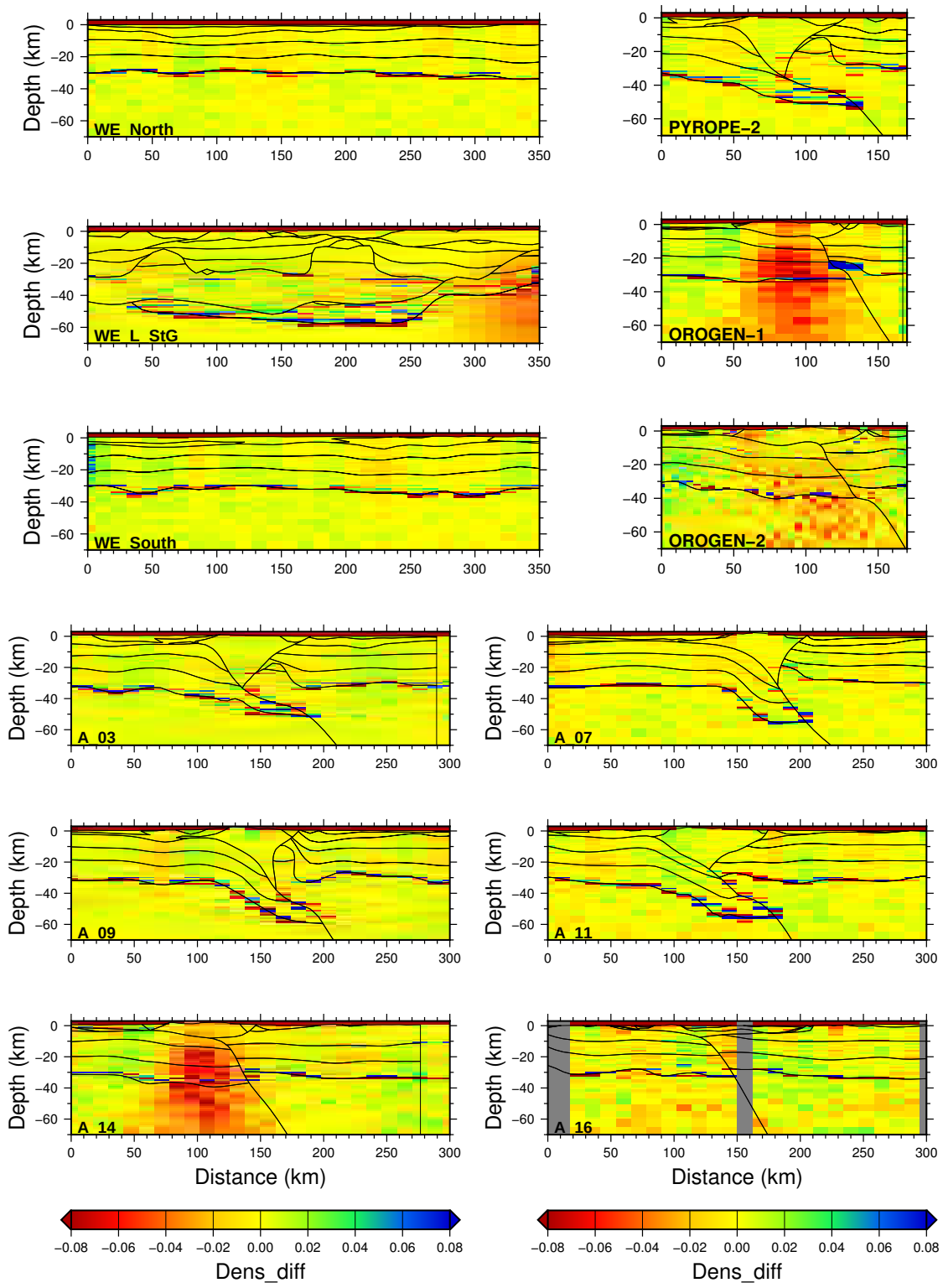

Figure 5.12: Smoothed density perturbations after inversion in semi-regular grid (see Figure 4.11 for the localizations of the sections). Black lines describe the geological units, vertical black lines indicate the end of a cross-section. Gray columns in A 16 are due to a bug in the model export.

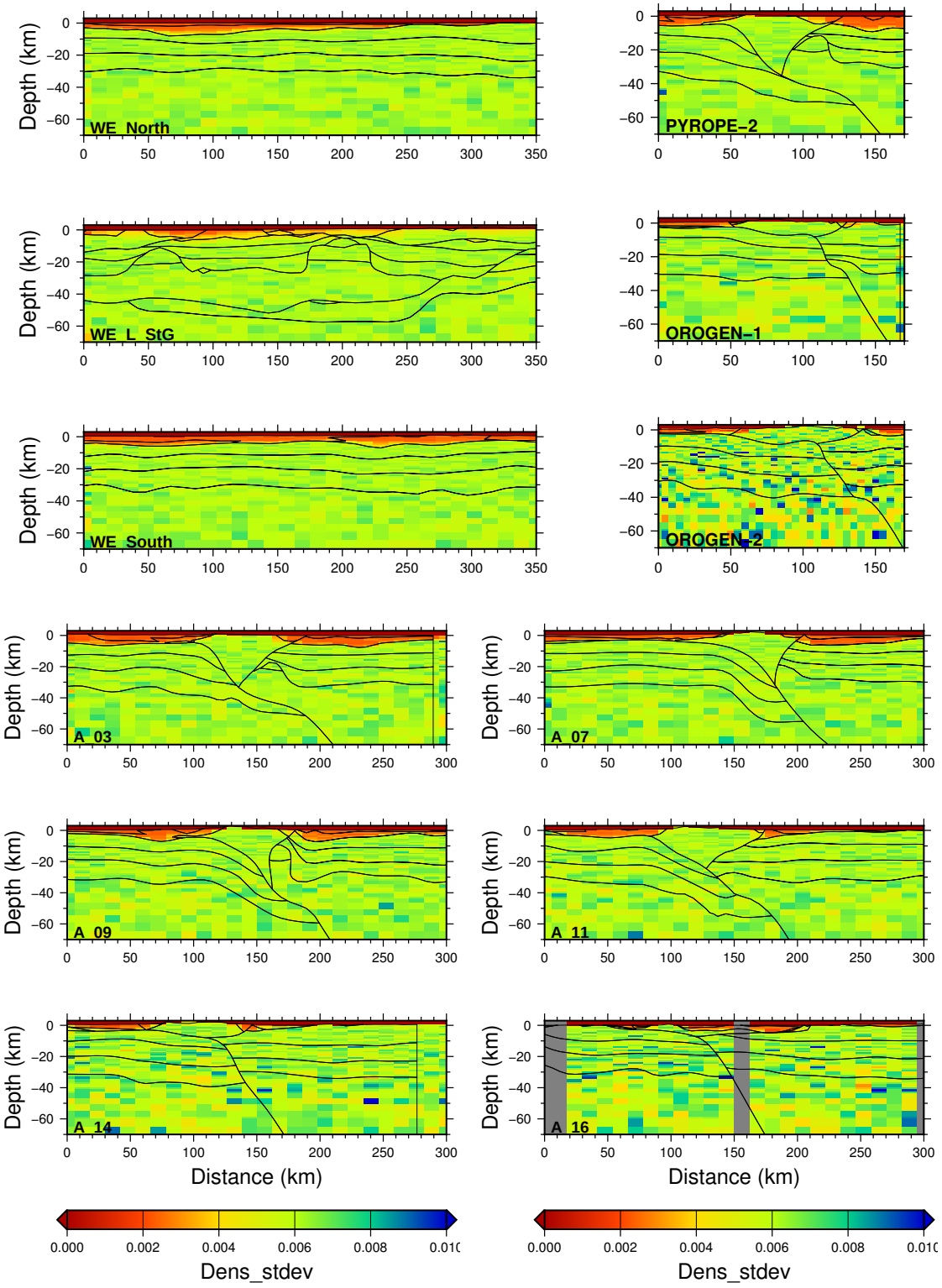

Figure 5.13: Smoothed standard deviations after density inversion in semi-regular grid (see Figure 4.11 for the localizations of the sections). Black lines describe the geological units, vertical black lines indicate the end of a cross-section. Gray columns in A 16 are due to a bug in the model export.

Geological Unit	**P-wave velocity (m/s)**	**S-wave velocity (m/s)**
Sea Water	1500	877
Cenozoic	4177	2443
Mesozoic	5360	3135
Prism	5698	3332
Upper Crust	5417	3168
Middle Crust	6197	3624
Lower Crust	6466	3781
Exhumed Mantle	7554	4417
Mantle	8013	4686

Table 5.2: Seismic velocities obtained from densities following Ludwig et al. [1970]. The P-to-S-wave ratio is 1.71.

(cf. Table 5.3). The P-to-S-wave ratio in this model is

$$\frac{v_p}{v_s} = 1.75. \tag{5.8}$$

Figures 5.14a and 5.14b show the travel time residuals obtained from the 1D and from the 3D Models II and III. Histograms produced with the 3D models have a slight trend towards negative residuals instead of the positive trend of the 1D model. Furthermore, they now have a larger standard deviation (0.5 vs. 0.4 for P and 0.7 vs. 0.5 for S waves), but their maxima are closer to zero. The average misfit for Model III is slightly higher than for Model II (0.03 s vs. -0.03 s for P and 0.12 s vs. 0.03 s for S). This is due to the fact that the eastern crust is layered sub-horizontally in Model III but dominated by the low-velocity upper crust in Model II.

However, the larger standard deviations in both 3D models with respect to the 1D model indicate that the seismic velocities can still be improved, in particular in the accretionary prism and in the upper crust. The velocities obtained from Brocher [2005] for the upper and middle crusts are lower than those at corresponding depths in the 1D model. The relation between density and velocities

depth	**P-wave**	**S-wave**
km	**velocity (m/s)**	**velocity (m/s)**
0	5500	3142
1	5600	3200
4	6100	3486
11	6400	3657
34	8000	4571

Table 5.3: 1D velocity model after Souriau and Pauchet [1998]. The P-to-S-wave ratio is 1.75.

is supposed to be valid for densities between 2.0 g/cm^3 and 3.5 g/cm^3 [Brocher, 2005], i.e. for the entire 3D model, but is based on samples from the surface or from well-logs that do not reach the basement. Assuming that the relation is applicable for the sediments but might differ for basement rocks, we test different velocities for the crustal units in order to improve the predictions of travel times. The velocity distributions are listed in Table 5.4.

The resulting values for the mean and standard deviations of residuals are shown in Figure 5.15a. While the mean values cover a large spectrum from 0.01 for vel17 to 0.54 for vel1, the standard deviation varies only between 0.47 and 0.51. Figure 5.15b shows the histograms of the residuals in four models presenting a good compromise between mean value and standard deviation, compared to the 1D model and Model III. Among these models, vel10 yields the most narrow Gaussian distribution with the highest maximum. For further seismic modeling, we set the velocities of the lower, middle, and upper crust and of the basement to 6400 m/s, 6150 m/s, 5900 m/s, and 5800 m/s, respectively. Figure 5.15c shows the same histograms for S wave residuals, obtained with a v_P/v_S ratio of 1.713. While for the P waves, the four tested models yield smaller residuals compared to the 1D model, larger residuals are obtained with the S waves. This may simply result from stronger lateral heterogeneities in shear velocities. Different v_P/v_S ratios tested between 1.71 and 1.75 do not improve the results. For this reason, P and S wave inversion will be performed separately, without imposing any ratio.

Model	P Wave Velocity (m/s)			
	Lower Crust	Middle Crust	Upper Crust	Basement
vel0	6466	6197	5417	5698
vel1	6466	6400	6100	6100
vel2	6466	6300	6100	6100
vel3	6466	6300	6100	6000
vel4	6466	6250	6100	6100
vel5	6466	6250	6100	6000
vel6	6400	6200	6000	6000
vel7	6400	6150	6000	6000
vel8	6400	6200	6000	5900
vel9	6400	6150	6000	5900
vel10	6400	6150	5900	5800
vel11	6400	6150	5900	5900
vel12	6400	6200	5900	5900
vel13	6400	6200	5900	5800
vel14	6400	6150	5800	5800
vel15	6400	6150	5800	5700
vel16	6400	6150	5700	5700
vel17	6400	6150	5600	5600
vel18	6400	6200	5600	5600
vel19	6400	6200	5800	5800
vel20	6400	6200	5800	5700
vel21	6400	6200	5700	5700
vel22	6400	6200	5750	5700
vel23	6400	6150	5750	5700

Table 5.4: P wave velocities tested for Model III. Vel0 corresponds to the velocities obtained from densities following Ludwig et al. [1970] (Tab. 5.2). The values of vel10 are adopted for seismic modeling.

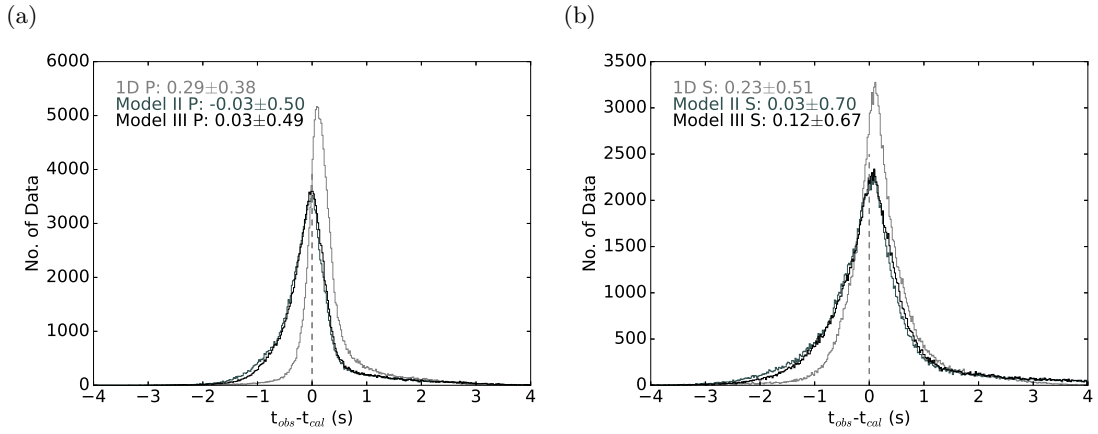

Figure 5.14: Travel time residuals obtained from Model III (black) compared to Model II (dark gray) and the 1D model (light gray). **(a):** P waves, **(b):** S waves.

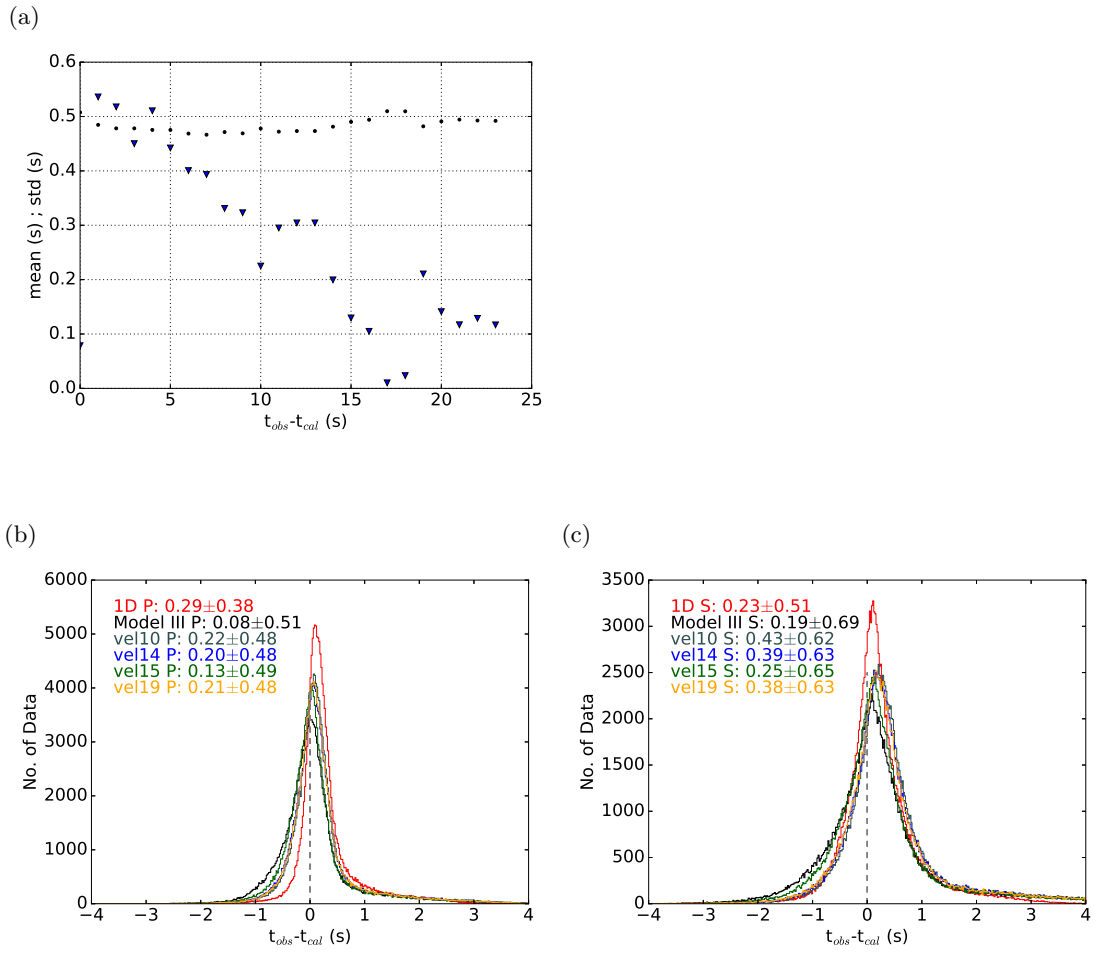

Figure 5.15: Travel time residuals obtained from the tested velocity models. **(a):** mean values (blue triangles) and standard deviations (black circles) for all tested models. **(b):** Histograms obtained from selected models compared to 1D and Model III. **(c):** Same for S waves with a $v_{P/S}$ ratio of 1.713.

5.5.3 Seismic Travel Time Inversion in `GeoModeller`

In order to validate the seismic data set and the inversion algorithm, we first perform a resolution test on synthetic data. The inversion of the 3D model is described afterwards.

All seismic inversions are performed in `GeoModeller` inside a 5×5×0.5 km^3 grid. The standard deviation allowed for velocity is 300 m/s. We run 200 000 000 iterations and compute the average from the last 40 % of the models, i.e. from the last 80 000 000 iterations.

Resolution Test

We estimate the resolution of our seismic tomography with a checkerboard model. For this synthetic test, we use the 1D layered model from Souriau and Pauchet [1998] (Table 5.3, Figures A.7 to A.8) as a reference model and apply to it velocity perturbations of ±7% in 25×25×2.5 km^3 blocks (Figure 5.16). Synthetic travel times are calculated as described in section 3.1 in a 960×640×144=88 473 600 grid of 0.5×0.5×0.5 km^3 cells. For inversion, velocities and rays lengths are averaged over 96×64×144 = 884 736 coarser blocks of 5×5×0.5 km^3 (cf. sec. 5.4), and the 1D layered velocity model is used as a starting model. A standard deviation of 0.02 s for the travel time data is used to compute the likelihood (Equation 2.22). At each iteration, the P wave velocity is perturbed within a standard deviation of 300 m/s, and a new S wave velocity is computed using a constant v_P/v_S ratio of 1.75. After 200·10^6 iterations, averages are computed over the results of the last 40 %. Having a grid of 884 736 cells, each cell has been perturbed on average 90 times during these last 80·10^6 iterations.

During this inversion, the travel time residuals converge from 0.239 s to 0.085 s for P and from 0.418 s to 0.147 s for S waves (Figure 5.17), which is more than four times larger than the expected value of 0.02.

Again, the images of the resulting perturbations seem noisy, so we apply a Gaussian filter with a correlation length of 30 km. Figure 5.18 shows the average P wave velocity perturbation at different depth levels for cells in which the cumulative ray length is at least 10 km. The unsmoothed images are shown in the appendix (Figure A.9). At 5 km depth, the checkerboard is well reproduced in the Axial Zone, the NPZ, and parts of the SPZ. At 2 km and 15 km, it reasonably well retrieved around the Labourd Massif, but at other depths, it is not recovered at all. This can in parts be explained by

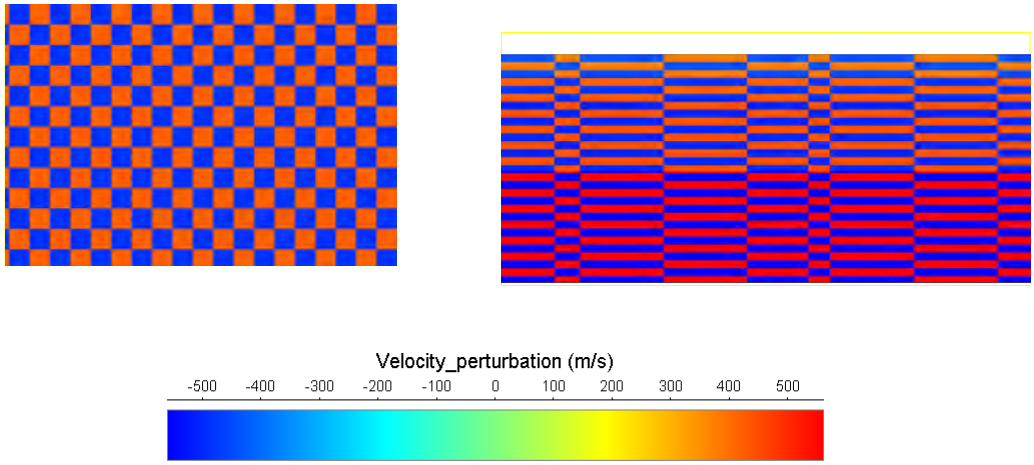

Figure 5.16: Checkerboard model giving the perturbations of P wave velocities at 5 km depth (left) and along OROGEN-1 (right). The checkerboard blocks are 5×5 km^2 large and 500 m thick. Cell widths in OROGEN-1 are not uniform since the transect is not perpendicular to the grid.

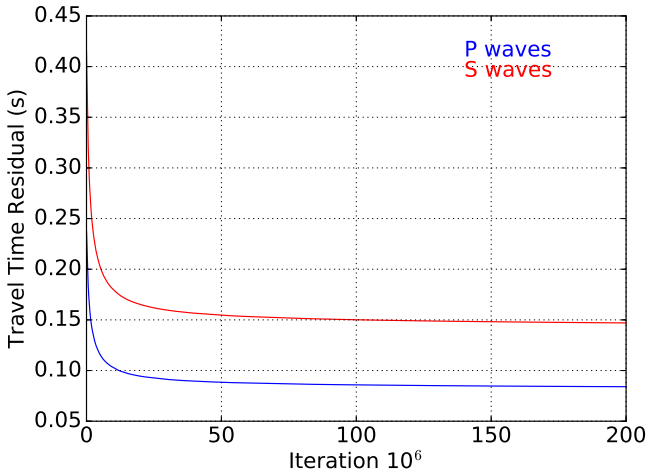

Figure 5.17: Residuals (s) from checkerboard test with joint P and S wave inversion.

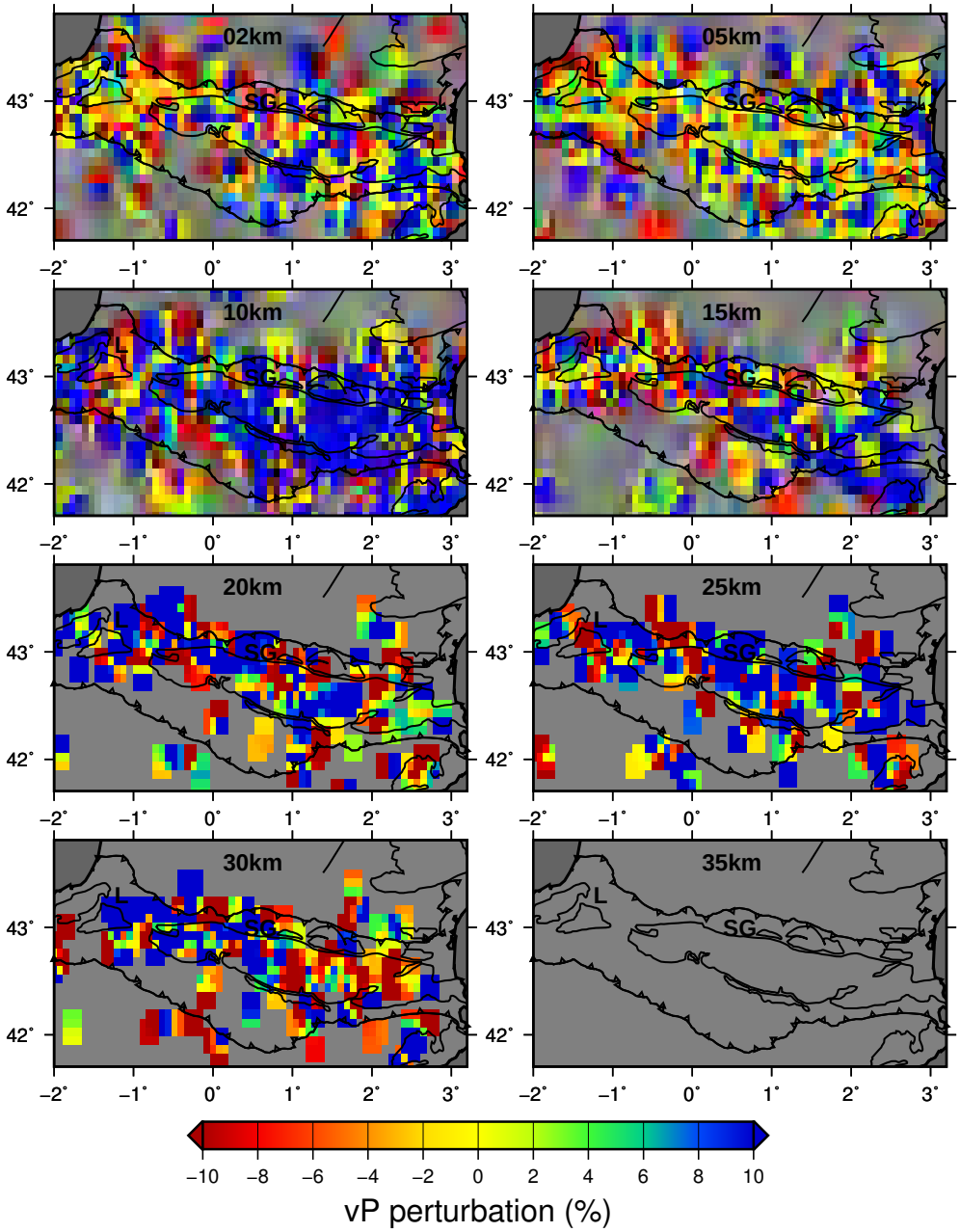

Figure 5.18: P wave velocity perturbation (%) after checkerboard joint P and S wave inversion (smoothed).

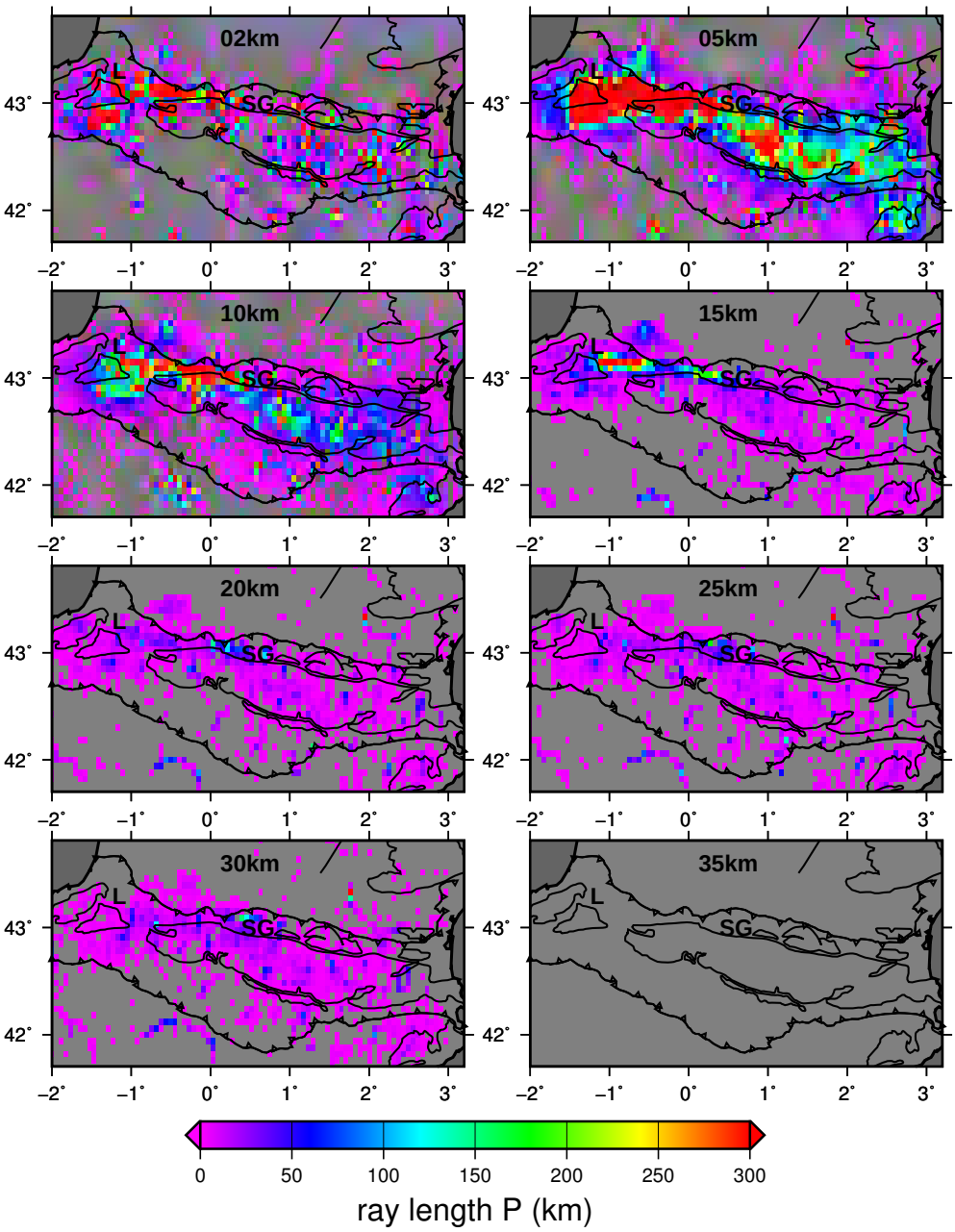

Figure 5.19: Rays lengths of P waves in 1D layered velocity model.

the ray coverage, which is shown in Figure 5.19. Ray coverage is very uneven, with a maximum at 5 km and 10 km depth. A narrow band between Labourd and Saint-Gaudens is still well covered at 15 km depth, but below that depth, the rays are not dense enough for proper imaging. Nevertheless, regarding the good coverage at 10 km depth, one would expect the checkerboard to be reproduced at this depth. However, velocity perturbations at 10 km depth are much stronger than those of the checkerboard. This suggests that further constraints should be added to the inversion algorithm. For example, a penalty function on the model norm would prevent the occurrence of too strong perturbations, and a covariance matrix would allow us to recover smooth models.

The results for the S waves and for P only inversion are very similar. The corresponding figures are shown in the appendix (Figures A.9 to A.12).

Seismic Inversion of the 3D model

Figure 5.20 shows the P ray coverage in the 3D model. Since the Iberian Moho lies at greater depth than in the 1D model, the P_n and S_n waves, which refract below the Moho, reach larger depths in the 3D model. This is why we do now have rays at 35 km depth. Moreover, more rays are present beneath the western and central NPZ down to 25 km depth.

Inversion in the 3D model is performed in the same grid as for the checkerboard test, and $200{\cdot}10^6$ iterations are computed. The results of the last 40 %, i.e. the last $80{\cdot}10^6$ iterations are then determined.

Figure 5.21 shows the evolution of the residuals during inversion. For the P waves, the standard deviation of travel time residuals decrease from 0.67 s before inversion to 0.26 s after $200{\cdot}10^6$ iterations. For the S waves, it decreases from 1.08 s to 0.36 s. In both cases, these values are far above the 0.01 s standard deviation that was assumed on the arrival time picks.

Figure 5.22 shows the P wave velocity perturbations, smoothed with the same Gaussian filter as for the checkerboard test described above. The unsmoothed images are in the appendix (Figure A.16). The perturbations do not reveal any satisfying structure.

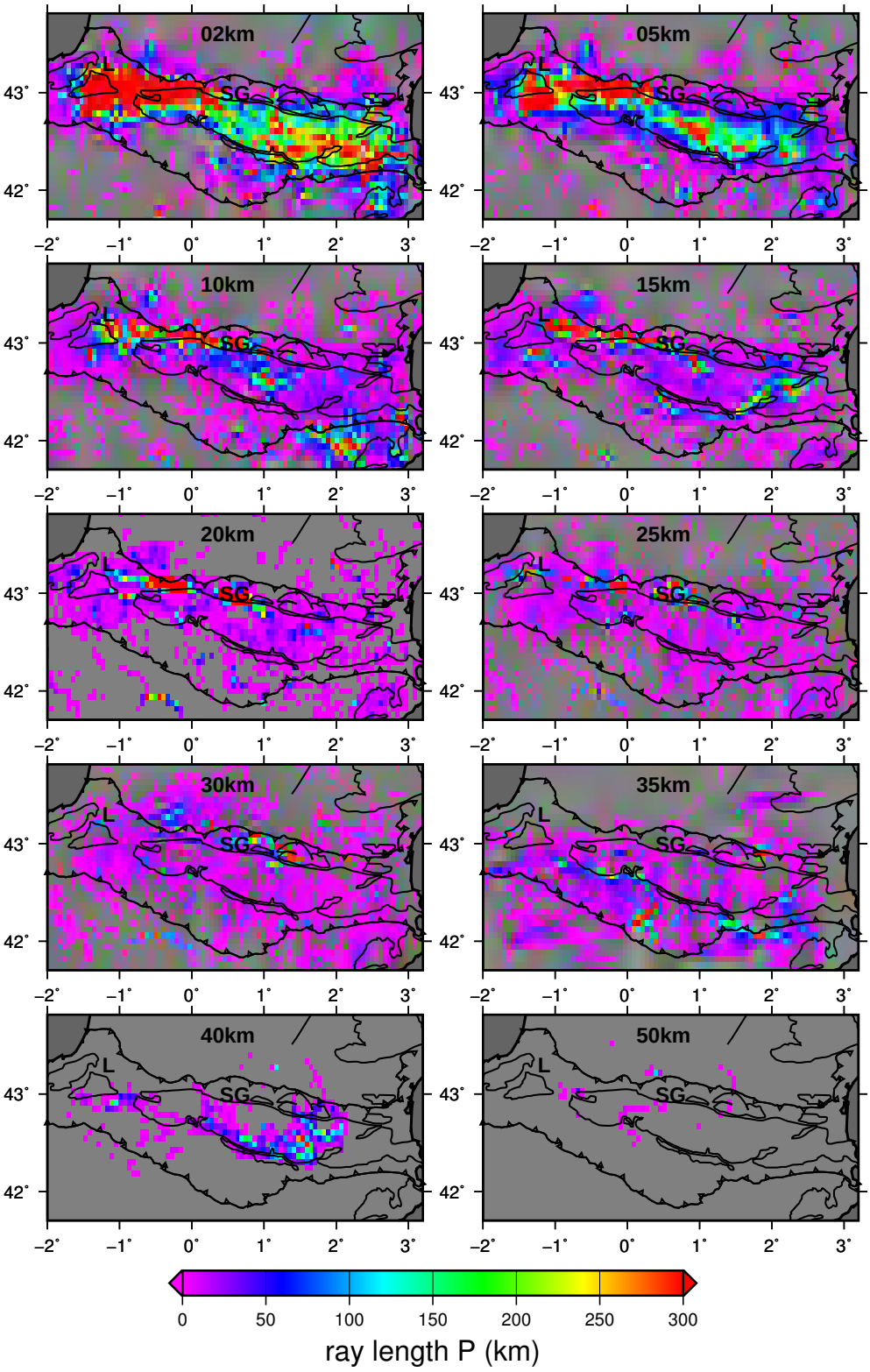

Figure 5.20: Rays lengths of P waves in the 3D model.

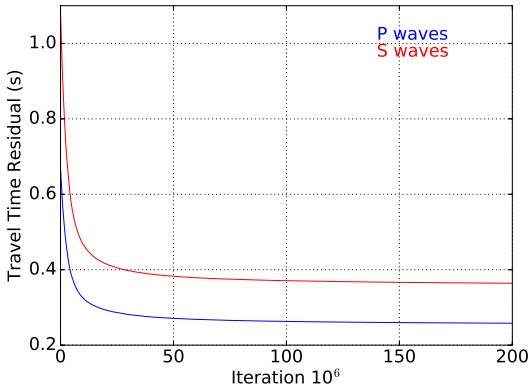

Figure 5.21: Residuals from separate and joint (1.71) P and S wave inversion.

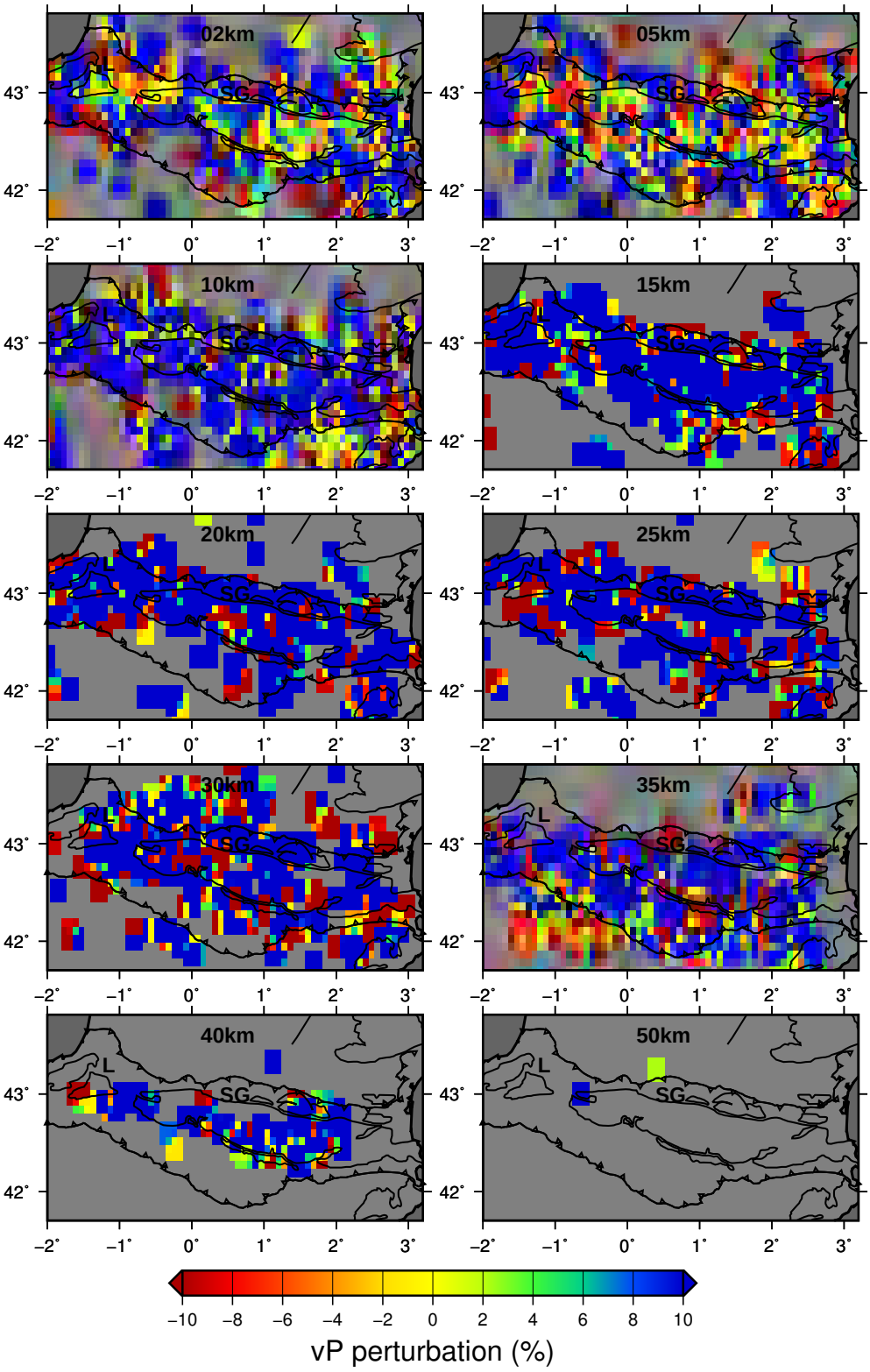

Figure 5.22: Smoothed velocity perturbations (in %) after separate P and S inversions.

5.5.4 Seismic LSQR inversion

Since the algorithm implemented in `GeoModeller` does not give satisfying results, seismic inversion is performed with a LSQR algorithm. After a brief description of the LSQR method, the resolution test and the 3D inversion will be presented.

The LSQR method searches the model that minimizes the L2-norm data misfit:

$$||\Delta \mathbf{t} - \mathbf{G}\Delta \mathbf{u}||^2 = 0. \tag{5.9}$$

Here, the matrix $M \times N$ matrix $\mathbf{G}$ contains the lengths of the M seismic rays in the N blocks of the model. The N-length element model vector $\Delta \mathbf{u}$ contains the slowness perturbation inside each cell, and the M-length data vector $\Delta \mathbf{t}$ contains the travel time residuals.

Since geophysical inverse problems are generally under-determined, i.e. many different models can explain the observed data, additional constraints may be added such as imposing to the model to not deviate too strongly from the starting model or to be smooth. These constraints are usually imposed by extending the system of equations to include the Identity matrix $\mathbf{I}$ and the Laplacian matrix $\mathbf{L}$ to damp the norm and the roughness of model perturbations. This leads to the new damped LSQR problem [e.g. Paige and Saunders, 1982]:

$$\begin{bmatrix} \mathbf{G} \\ \gamma_1 \mathbf{I} \\ \gamma_2 \mathbf{L} \end{bmatrix} \Delta \mathbf{u} = \begin{bmatrix} \Delta \mathbf{t} \\ 0 \\ 0 \end{bmatrix}. \tag{5.10}$$

Checkerboard Resolution Test

In order to test the resolution of this inversion scheme, we apply this method on the checkerboard model as described in section 5.5.3. Figure 5.23 shows the P wave velocity perturbations obtained with the regularization parameters $\gamma_1 = 5$ for the model norm and $\gamma_2 = 10$ for the Laplacian, for cells that are crossed by at least five rays. The variance reduction is 95%. In agreement with the ray coverage shown in Figure 5.19, the LSQR inversion recovers the checkerboard pattern down to

10 km depth, and in the western and central part down to 15 km depth. Between 20 and 30 km depth, the checkerboard is partly resolved, but with amplitudes that are much weaker than in the upper depth levels. Beneath, the synthetic model is not resolved at all, owing to poor ray coverage.

LSQR Inversion of the 3D Model

Figure 5.24 shows the P velocity perturbations obtained from 3D LSQR inversion with the regularization parameters $\gamma_1 = 10$ for the model norm and $\gamma_2 = 50$ for the Laplacian. Small-scale heterogeneities can be seen in the uppermost 5 km of depth. The most striking features are positive perturbations of 10 to 15% all along the western and central Axial Zone between 10 and 15 km depth and negative perturbations of ∼-15% beneath Labourd and Saint-Gaudens from 15 to 25 km depth. In the eastern Axial zone, positive perturbations of 5 to 10% are present at 10 km depth. At 15 km depth the eastern Axial Zone show a negative perturbation of ∼-5%. This anomaly, however, is located very close to the limit of resolution and cannot be observed in greater depths due to missing ray coverage.

Figures 5.25 and 5.26 show the final P wave velocity distribution after LSQR inversion starting with the 3D and, respectively, starting with the 1D model from Souriau and Pauchet [1998]. In both cases, a variance reduction of 63.7% is obtained. The Labourd and Saint-Gaudens anomalies are better resolved when starting from the 3D a-priori model. With the 1D a-priori model, none of the two anomalies can be distinguished down to 15 km, and the Saint-Gaudens anomaly is very poorly resolved. For the exhumed mantle beneath the Labourd Massif, both a-priori models yield similar final velocities of ∼7 km/s.

Figures 5.26 and 5.28 show the difference between the respective final velocity distributions and the initial 1D model. None of the two figures reveals a low-velocity anomaly in the eastern Axial Zone as we would expect from the gravity data.

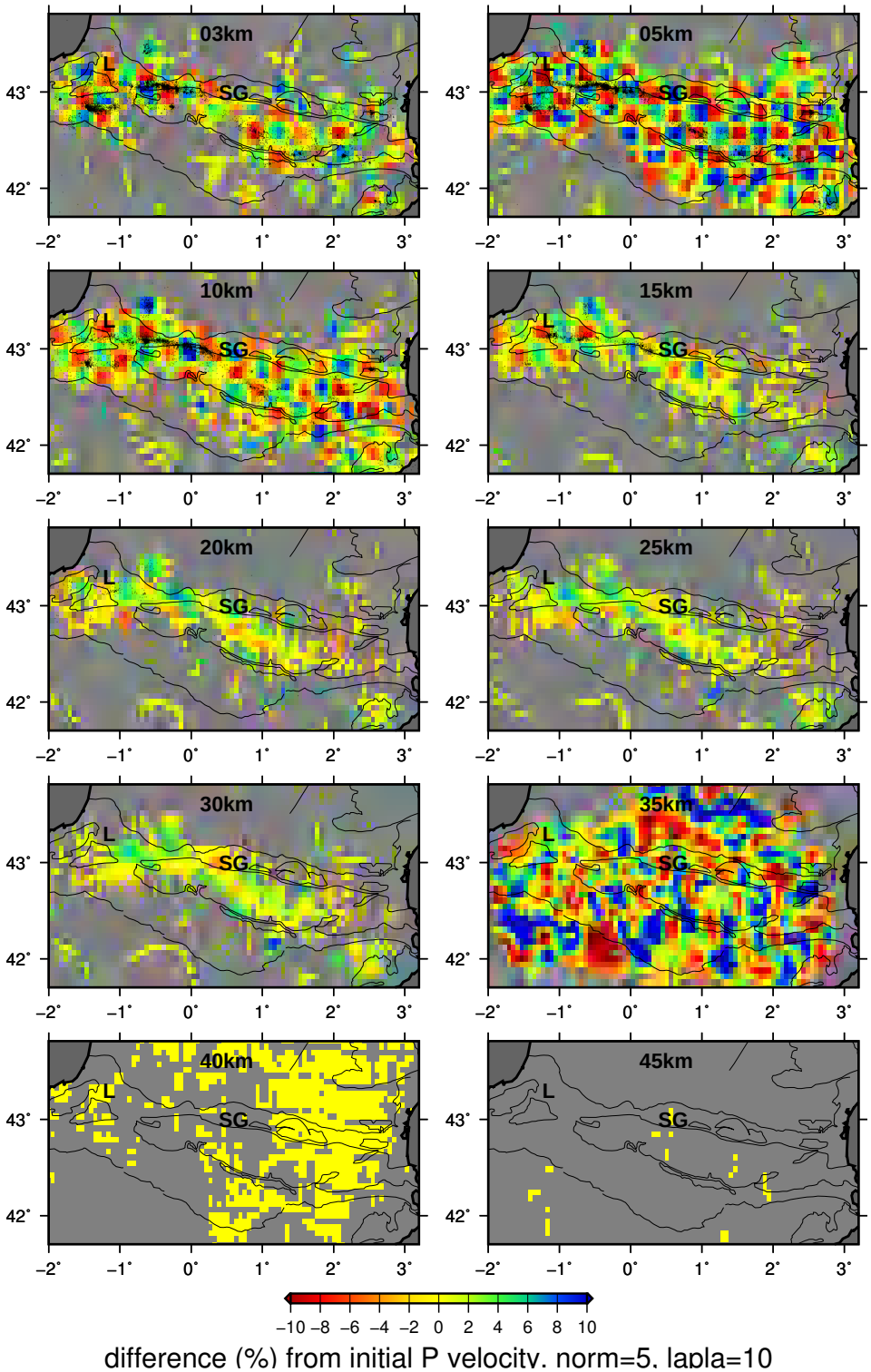

Figure 5.23: Results of the checkerboard test in the 3D model.

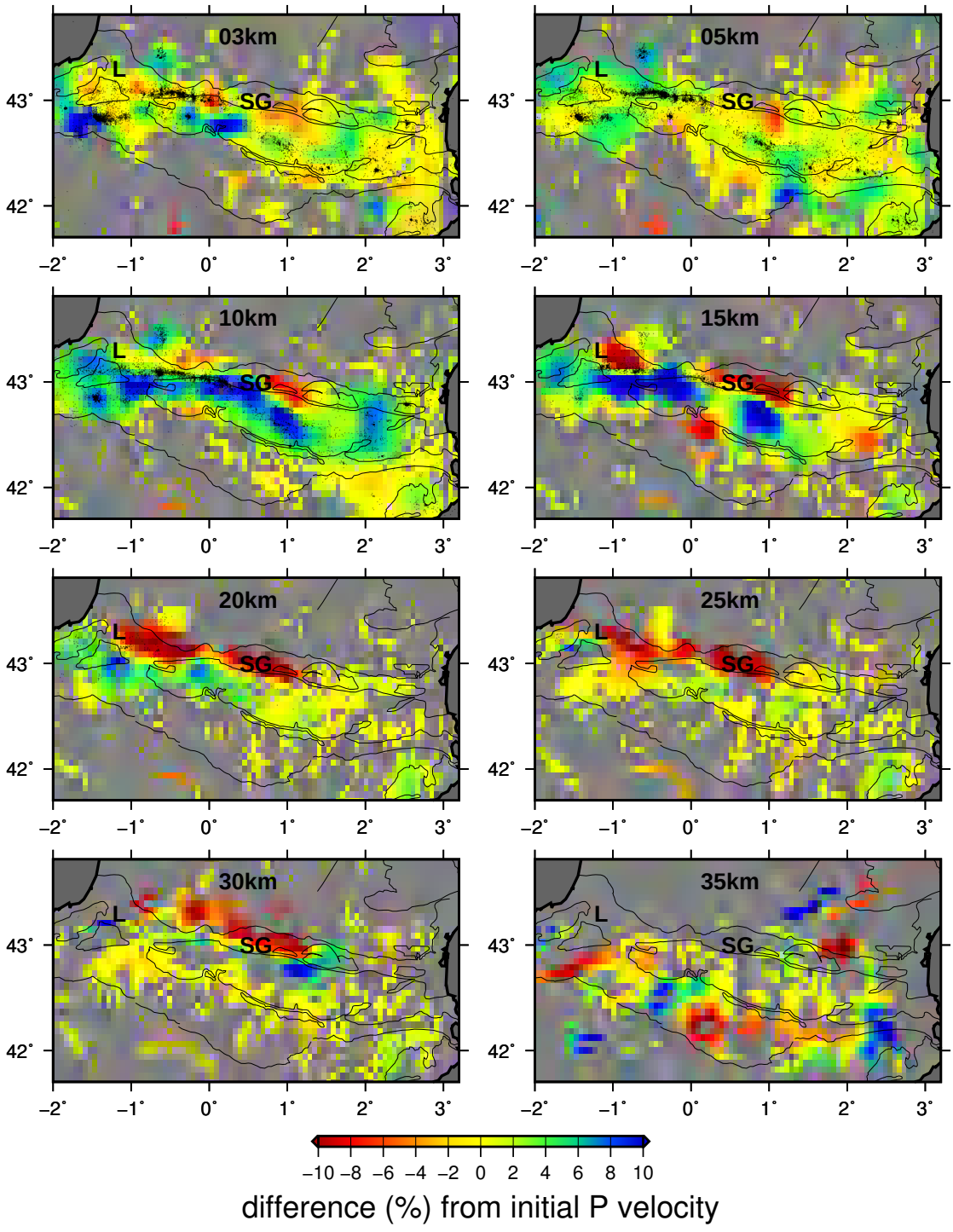

Figure 5.24: P wave velocity perturbations from LSQR inversion.

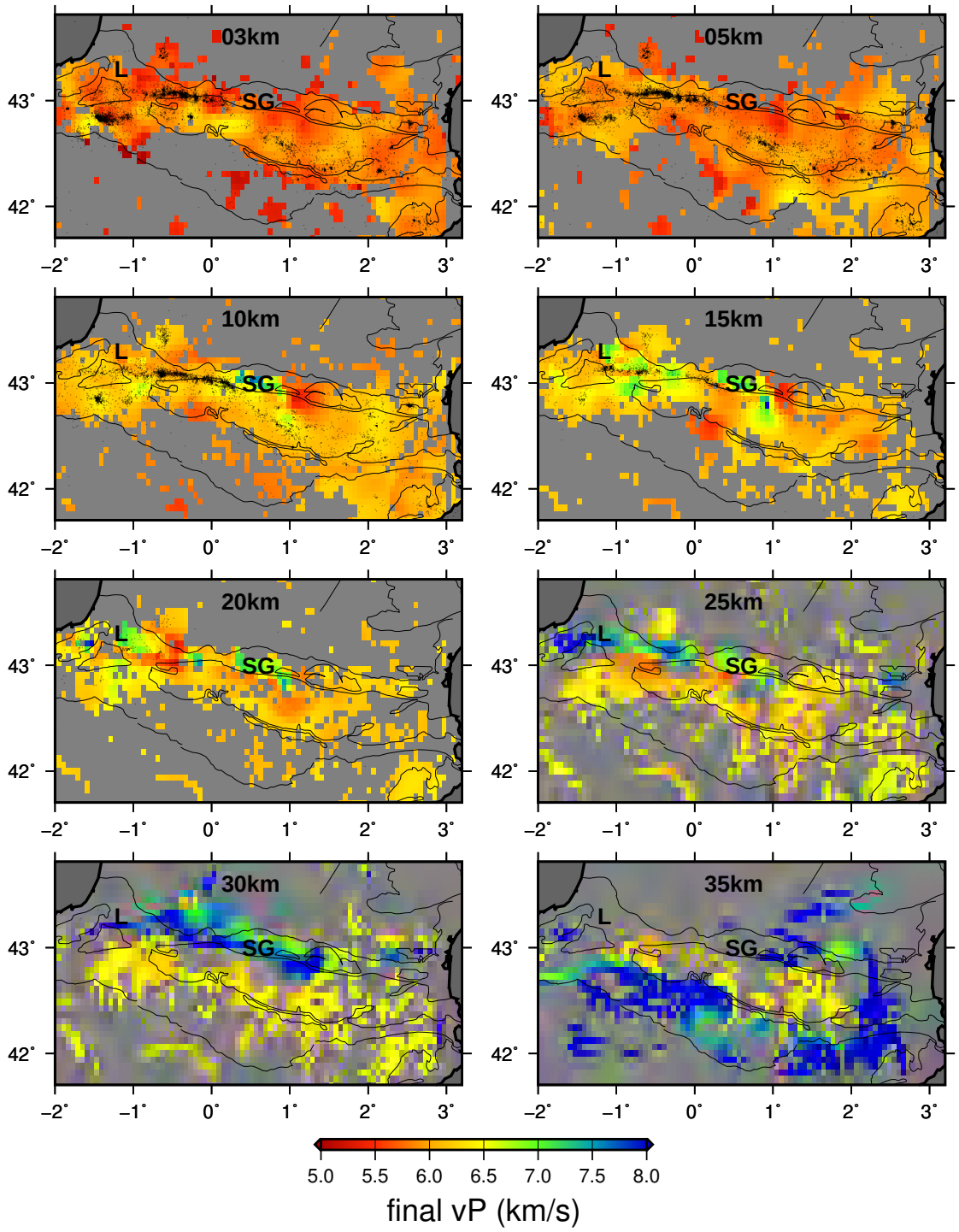

Figure 5.25: P wave velocity after 3D LSQR inversion.

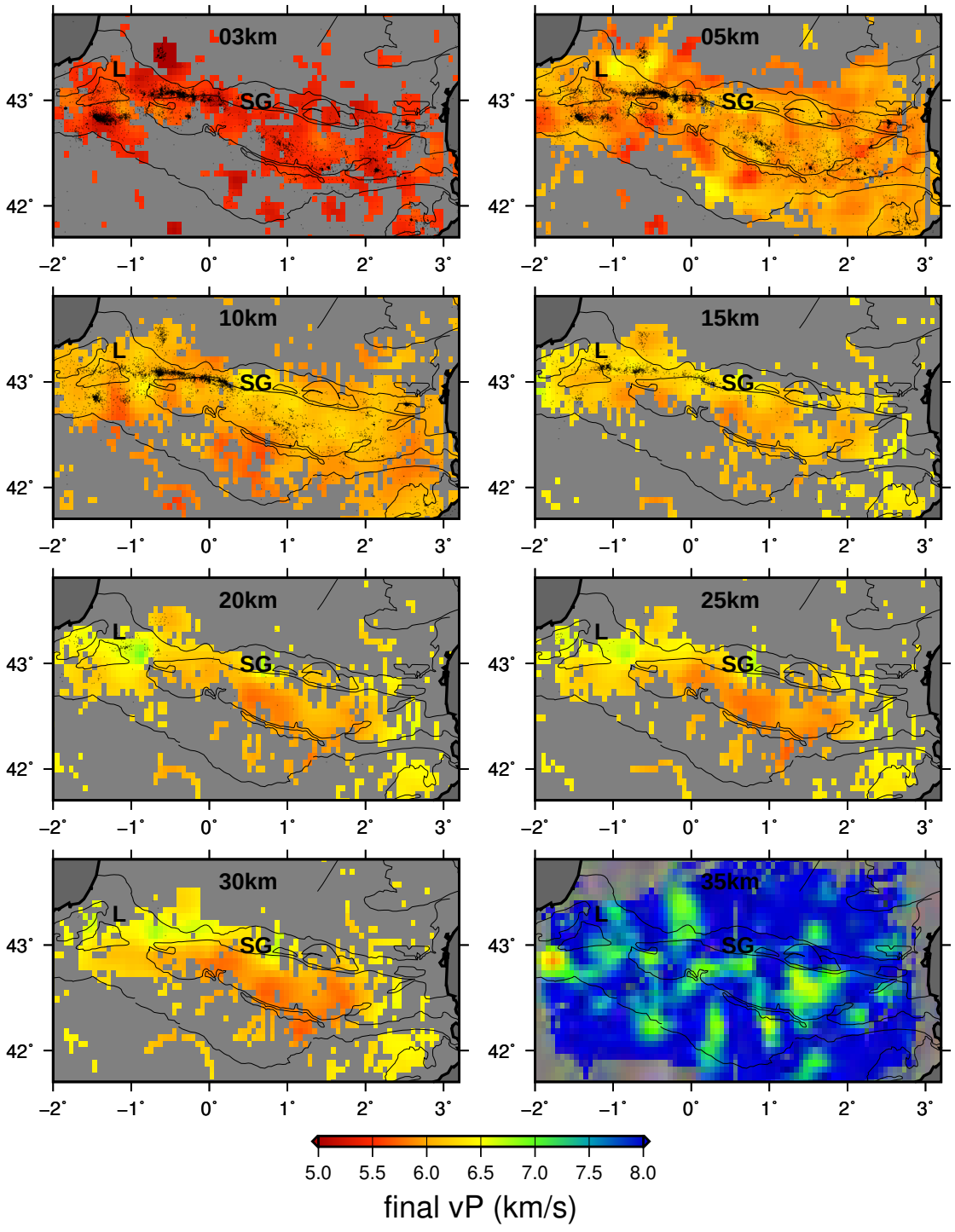

Figure 5.26: P wave velocity after 1D LSQR inversion.

5.6 Discussion

Travel time prediction from the 3D model has shown that the densities used for fitting the Bouguer anomalies cannot be simply transformed into seismic velocities. Velocities of the crustal units had to be adjusted in order to obtain better residuals. One possible explanation is that the relation proposed by Brocher [2005] is not valid in depth, maybe because of different pressure and thermal conditions. A second explanation is the fact that Bouguer anomalies can only be modeled within a certain constant. The shift between observed and modeled Bouguer anomalies changes if densities change. That means that a certain density distribution can fit the data as well as another one, but with a different offset. This option can easily be verified in the near future by reconverting the used velocities into densities and predicting Bouguer anomalies from those.

Gravity inversion in two different grids illustrates the problematic principle of equivalence. Regular, small cell thicknesses yield negative anomalies in the uppermost 15 km of the eastern Axial Zone, while the semi-regular grid with increasing cell thicknesses results in negative anomalies between 15 and 50 km depth. The latter grid furthermore yields to strong perturbations along the boundaries between mantle and crustal units, and thus indicates that the geometry of the Moho and especially of the Iberian slab beneath the Axial Zone may still be refined. Indeed, the increase of cell thickness with depth counteracts the decrease of contribution to the gravity field and seems better suited for gravity inversion than the regular grid.

Seismic LSQR inversion yields to small-scale heterogeneities in the uppermost 5 km of the Axial Zone. These are resolved both, starting from the 3D and from the 1D layered a-priori model. The serpentinized mantle beneath the Labourd Massif and Saint-Gaudens, as well as deep crustal roots, however, are better resolved with the 3D model. Here, positive perturbations are obtained in the western and central Axial Zone between 10 and 15 km depth, indicating that at these levels, the initial velocity of the accretionary prism can still be improved. The same conclusion can be taken from positive perturbations beneath the Labourd and Saint-Gaudens gravity anomalies, where the initial velocity of the serpentinized mantle is too far from crustal values. The comparison of the final models obtained from the 3D and the 1D starting model underlines the interest in using a

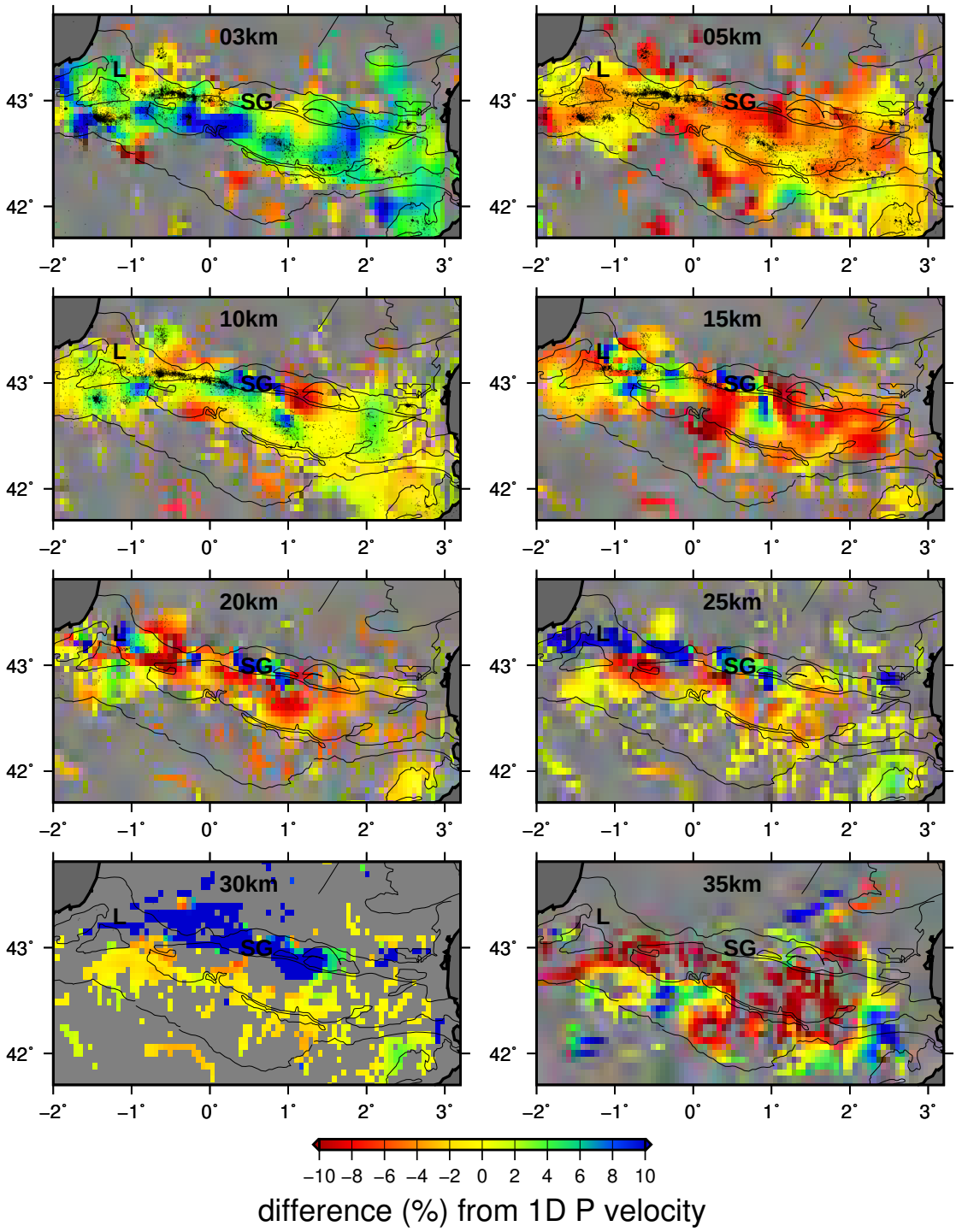

Figure 5.27: 3D P wave perturbation with respect to the 1D model.

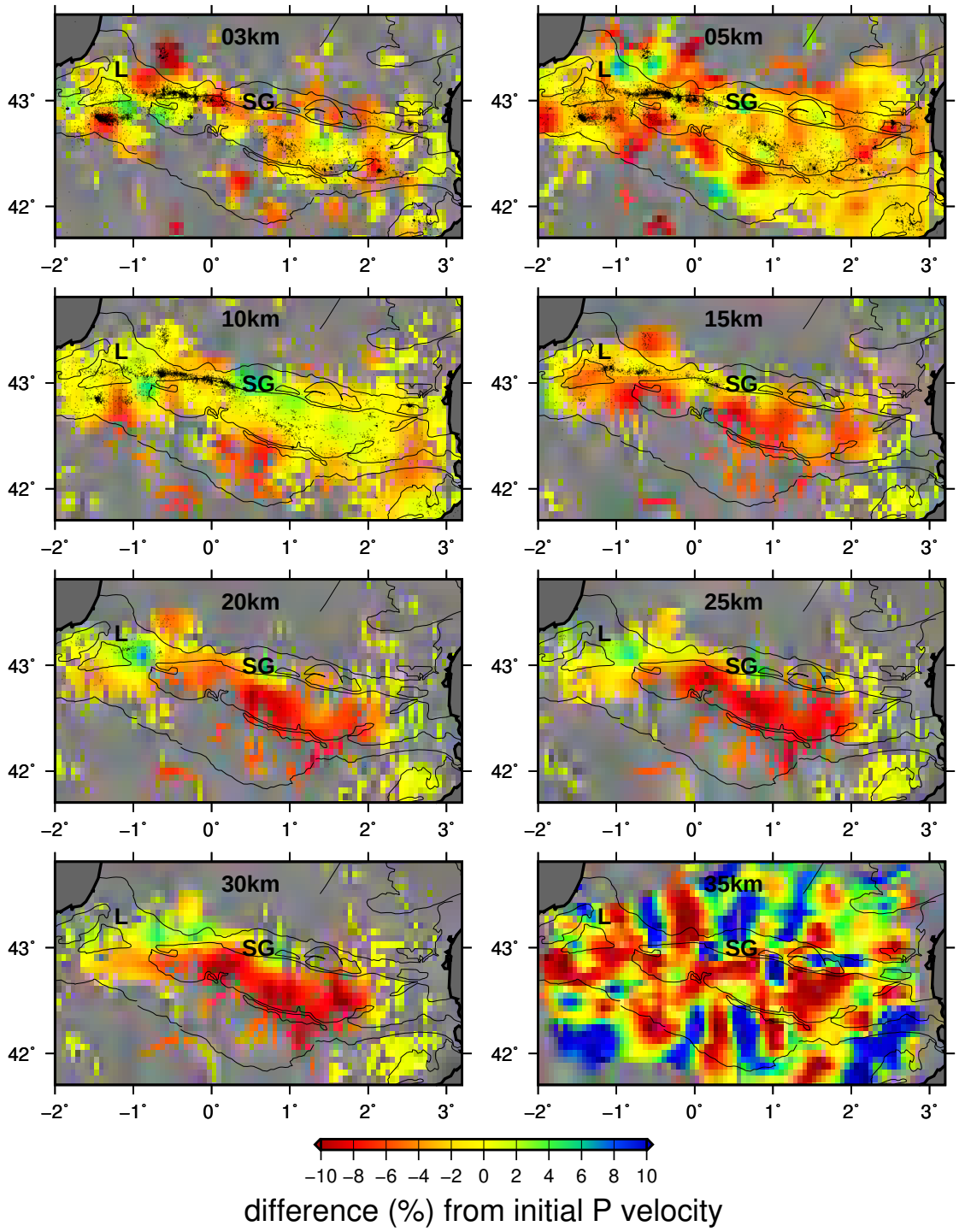

Figure 5.28: P wave velocity perturbations from LSQR inversion starting from the 1D model.

detailed 3D a-priori model. The Labourd and Saint-Gaudens anomalies are well resolved with the 3D model and their structures and velocities may be refined on the basis of the inversion results. Inversion on the 1D a-priori model, however, hardly resolves the Saint-Gaudens anomaly.

The absence of strong anomalies in the eastern Axial Zone both, starting from the 1D or from the 3D model, suggests that the negative anomaly needed to explain the Bouguer anomalies lies at greater depths which are not resolved by the seismic data. This supports the gravity results obtained from the inversion in the semi-regular grid.

However, the ray coverage differs importantly between the 1D and the 3D a-priori model. This indicates that the LSQR inversion should be expanded to an iteration between the computation of new ray paths and travel times in velocity model obtained from inversion and LSQR inversion of these newly computed data. This will refine the final velocity distribution and yield a better basis for the comparison of inversion starting from a 3D and a 1D a-priori model.

More certain information concerning the anomalous structures should be obtained by joint inversion. For this, further efforts have to be made on the inversion algorithm of both gravity and seismics in `GeoModeller`. The transform between the seismic and the `GeoModeller` grid has to be more bearable and options for damping and smoothing have to be added. Furthermore, only one iteration has been performed for each LSQR inversion. It would be interesting to see how far the results can be refined by tracing the rays in the velocity model obtained from LSQR and running more inversions starting from the respective current velocity model.

Chapter 6

Conclusion

Contents

6.1 Conclusion (English)

Available geological data such as geological maps, drill-hole surveys, or cross-sections are not sufficient to constrain a 3D geological model of the Pyrenees and their foreland basins. Including gravity data, namely Bouguer anomalies, enabled us to construct a 3D model that respects the geological information and that reproduces Bouguer anomalies within an uncertainty of ±3.5 mGal. The positive Bouguer anomalies of Labourd and Saint-Gaudens can be explained by exhumed mantle connected to the European upper mantle as proposed for the western Pyrenees by Velasque et al. [1989] and recently confirmed by the full wave-form inversion of [Wang et al., 2016]. In this study, the mantle wedge beneath the Mauleon basin was interpreted as the remnants of hyperextended rifted margin produced during the Cretaceous episode of rifting. The top of the exhumed mantle is located at 11 km depth beneath the Mauleon basin and 9.5 km depth beneath the Saint-Gaudens anomaly. Horizontal extents of mantle bodies are 45 km along the EW direction, and 28 km along the NS direction for the Labourd and 48 km along the EW direction, and 14 km along the NS direction for Saint-Gaudens. Given a sediment thickness of 3 to 4 km in the Mauleon basin, the European crust is thus thinned to less than 7 km. In the eastern part of the Axial Zone, where the recent seismic cross-sections from the OROGEN project [Chevrot, pers. comm., 2017] evidence a Moho depth of 30 to 35 km, a low-density body is needed to reproduce the negative Bouguer anomalies. Volume estimates obtained from the 3D model for the sediments in the foreland basins ($490{\cdot}10^3 \mathrm{km}^3$) and for the crustal roots ($2.2{\cdot}10^6$ km^3) are in excellent agreement with the estimates of Vanderhaeghe and Grabkowiak [2014].

The densities used for gravity modeling have been converted to seismic P wave velocities using the empirical relationship from Ludwig et al. [1970], quantified by Brocher [2005] but needed to be corrected for the crustal units in order to better explain seismic travel times.

Regional seismic arrival times show a $\mathrm{v}_P/\mathrm{v}_S$ ratio of 1.71 in the Pyrenees. P and S wave travel times predicted by the 3D model agree with observed data within 0.5 s (0.7 s in the case of S waves).

Gravity inversion localizes the negative anomaly which is needed to fit the Bouguer anomalies in

the eastern Pyrenees in the uppermost 15 km when using a regular grid with a small cell thickness, but in larger depths when using a semi-regular grid with block thicknesses increasing with depth. The semi-regular grid, furthermore, yields strong density perturbations along the interfaces between mantle and crustal units. These are interpreted as corrections on the geometry of these boundaries and as an indication that this grid is better suited for gravity inversion than the regular one. Indeed, the increase of cell thickness with depth compensates for the decrease of contribution to the gravity field.

In order to better constrain the inversion with `GeoModeller` , seismic travel time inversion has been implemented. Checkerboard resolution tests show that travel time tomography suffers from a poor resolution in the deep crust. Furthermore, gravity and seismic inversions reveal the necessity of implementing further constraints, such as a covariance matrix for smoothing or a penalty function on the model norm to prevent too strong perturbations.

Since seismic inversion in `GeoModeller` does not yield satisfying results, we have also performed direct inversions with the LSQR method. In these new inversions, near-surface heterogeneities are well resolved, either starting from the 3D model or from a 1D layered velocity model. Deeper anomalies, however, are better resolved with the 3D a-priori model. The LSQR inversion does not reveal any large-scale low-velocity anomaly in the eastern Axial Zone as it would be expected from the gravity data. This indicates that the anomaly might be located deeper, at a depth that cannot be resolved by the seismic data set. However, further iterations need to be performed, including ray tracing in the velocity models obtained from inversion and LSQR inversion of the newly retrieved data.

Moreover, in order to further refine the tomographic images, improvements on the tomographic grid are required. The discretization of a cubic grid for travel time computation always results from a compromise between the resolution needed to describe the detailed geometry of geological structures such as sedimentary basins and computational costs. In a first step, an increase of layer thickness with depth would allow us to perform joint inversion in a grid that is well suited for both seismic and gravity computations. Ina second step, an irregular, non-cubic grid would allow us to

describe the complex geometries of the basins, crustal roots, or anomalous intra-crustal bodies, and at the same time provide a coarser resolution in depth. In other words, we need a more flexible parameterization of the model to capture the complex geometry of geological structures. Regarding the Monte Carlo inversions performed with the `GeoModeller`, damping and smoothing constraints should clearly be added.

More generally, future work shall focus on:

- Inversion of isostatic anomalies. Bouguer anomalies reflect regional structures and are dominated by surface-near structures and the long wavelength signature of the thick crustal roots. Isostatic anomalies reflect shorter wavelengths and thus more local uncompensated anomalies. Inverting isostatic anomalies should thus provide more detailed images than the inversion of Bouguer anomalies.
- Including new types of geophysical data in order to further constrain the model, e.g. dispersion curves extracted from noise correlations, receiver functions, complete waveforms, etc...

Future applications of our 3D geological model will focus on improving the localization of seismic events in the Pyrenees. This might provide further insights into the spatial distribution of seismicity and its relations with geological structures. Moreover, the 3D model may be useful as a starting model for more local studies and for future joint inversions of teleseismic waveforms and gravimetric data.

6.2 Conclusion (French)

Les données géologiques disponibles telles que les cartes géologiques, les sondages de forage ou les coupes 2D ne sont pas suffisantes pour contraindre un modèle géologique 3D des Pyrénées et de leurs bassins d'avant-pays. Cependant, en ajoutant des données gravimétriques, plus précisement les anomalies de Bouguer, nous sommes en mesure de construire un modèle 3D qui respecte la géologie et qui reproduit les anomalies de Bouguer avec une incertitude de ± 3,5 mGal. Les anomalies positives de Bouguer de Labourd et de Saint-Gaudens peuvent être expliquées par du manteau exhumé relié au manteau supérieur européen comme l'ont proposé Velasque et al. [1989] pour les Pyrénées occidentales, une hypothèse confirmée récemment par l'inversion de formes d'ondes complètes [Wang et al., 2016]. Dans cette étude, le corps de manteau sous le bassin de Mauléon a été interprété comme une vertige témoignant de l'hyper-extension pendant l'épisode de rifting crétacé. Le sommet du manteau exhumé est situé à 11 km de profondeur sous le bassin de Mauléon et à 9,5 km de profondeur sous l'anomalie de Saint-Gaudens. Les dimensions horizontales des corps de manteau sont de 45 km dans la direction EW et de 28 km dans la direction NS pour le Labourd, et 48 km dans la la direction EW et 14 km dans la direction NS pour Saint-Gaudens. Compte tenu de l' épaisseur de sédiments de 3 à 4 km dans le bassin de Mauléon, la croûte européenne est donc amincie à moins de 7 km. Dans la partie orientale de la Zone Axiale, où les sections sismiques récentes du projet OROGEN [Chevrot, comm. comm., 2017] montrent une profondeur de Moho de 30 à 35 km, un corps de faible densité est nécessaire pour reproduire l'anomalie négative de Bouguer. Les estimations de volume obtenues à partir du modèle 3D pour les sédiments dans les bassins d'avant-pays ($490 \cdot 10^3$ km^3) et pour les racines crustales ($2.2 \cdot 10^6$ km^3) sont en excellent accord avec les estimations de Vanderhaeghe et Grabkowiak [2014].

Les densités utilisées pour la modélisation gravimétrique ont été converties en vitesses d'onde P en utilisant la relation proposée par Ludwig et al. [1970] et quantifiée par Brocher [2005], mais il est nécessaire de les corriger pour les unités crustales afin de mieux expliquer les temps de trajet sismiques. Les temps d'arrivée montrent un rapport vP / vS de 1,71 dans les Pyrénées. Les temps de trajet prédits par le modèle 3D sont en accord avec les données observées plus ou moins 0,5 s (0,7

s dans le cas des ondes S). Les anomalies de Bouguer sont fortement influencées par les structures peu profondes car les inversions de gravité ont tendance à perturber les parties les moins profondes du modèle géologique. Afin de mieux contraindre les modèles, l'inversion des temps de trajet a été implémentée dans `GeoModeller`. Des tests de résolution sur un modèle en damiers montrent que la tomographie souffre d'une mauvaise résolution dans la croûte profonde. En outre, les inversions gravimétriques et sismiques révèlent la nécessité d'ajouter d'autres contraintes, comme une matrice de covariance pour le lissage ou une fonction de pénalité sur la norme du modèle afin d'éviter des perturbations trop fortes. Puisque l'inversion sismique dans `GeoModeller` ne donne pas de résultats satisfaisants, nous avons également réalisé des inversions directes avec la méthode du LSQR. Dans ces nouvelles inversions, les hétérogénéités proches de la surface sont bien résolues, que l'on démarre l'inversion à partir du modèle 3D ou d'un modèle 1D. Cependant, les anomalies plus profondes sont mieux résolus avec le modèle a-priori 3D. L'inversion gravimétrique localise l'anomalie négative qui est nécessaire pour ajuster les anomalies de Bouguer à l'est des Pyrénées dans les 15 premiers kilomètres en utilisant une grille régulière avec une petite épaisseur des cellules, mais à de plus grandes profondeurs lorsque les épaisseurs de blocs augmentent avec la profondeur. L'inversion LSQR ne révèle aucune anomalie de grande échelle dans la zone axiale orientale, contrairement à ce que montrent les modélisations gravimétriques. Ceci indique que l'anomalie pourrait être localisée plus profondément, à un niveau mal résolu par l'inversion des données sismiques.

Pour affiner d'avantage les images tomographiques, des améliorations sur la grille tomographique sont nécessaires. La discrétisation d'une grille cubique pour le calcul du temps de trajet résulte toujours d'un compromis entre la résolution nécessaire pour décrire la géométrie détaillée des structures géologiques telles que les bassins sédimentaires et les coûts de calcul. Une grille irrégulière non cubique nous permettrait de décrire les géométries complexes des bassins, des racines crustales ou des corps hétérogènes intra-crustaux, et en même temps de permettre une résolution plus grossière en profondeur. En d'autres termes, nous avons besoin d'une plus grande flexibilité dans la paramétrisation du modèle, afin de capturer la géométrie complexe des structures géologiques. En ce qui concerne les inversions Monte Carlo réalisées avec le `GeoModeller`, des contraintes de damping et de lissage devraient clairement être ajoutés.

Plus généralement, les travaux futurs porteront sur:

- Inversion des anomalies isostatiques. Les anomalies de Bouguer reflètent les structures régionales et sont dominées par des structures proches de la surface et la signature à grande longueur d'onde des racines épaisses de la croûte. Les anomalies isostatiques reflètent des longueurs d'onde plus courtes et donc plus d'anomalies locales et non compensées. L'inversion des anomalies isostatiques devrait donc fournir des images plus détaillées que l'inversion de Anomalies de Bouguer.

- Inclure de nouveaux types de données géophysiques pour contraindre le modèle davantage, p. ex. des courbes de dispersion des corrélations de bruit, des fonctions de récepteurs, des formes d'ondes, etc ...

Les applications futures de notre modèle géologique 3D se concentreront sur l'amélioration de la localisation des séismes dans les Pyrénées. Cela pourrait fournir des informations supplémentaires sur la répartition spatiale de la sismicité et ses relations avec les structures géologiques. De plus, le modèle peut aussi être utile comme modèle de départ pour des études locales et pour de futures inversions conjointes des formes d'onde télésismiques et des données gravimétriques.

Appendix

Contents

A.1 Coordinate Transform

The `GeoModeller` software requires orthogonal coordinates, but geological and geophysical data, are commonly georeferenced in WGS84 latitude and longitude This section describes the conversion between WGS84 coordinates and the orthogonal Lambert93 system.

A.1.1 Geographical Coordinates ⟶ Lambert93

The conversion from lon/lat to Lambert93 is computed as follows [Courrioux, 2015, pers. comm.]: The origin of Lambert93 is defined as:

$$x_0 = 700000 \tag{A.1}$$

$$y_0 = 6600000 \tag{A.2}$$

with x pointing eastwards and y pointing northwards. We furthermore define the following projection parameters:

$$
\begin{aligned}
l_c &= 3\frac{\pi}{180} && \text{reference longitude}\\
\varphi_0 &= 46.5\frac{\pi}{180} && \text{latitude of origin in radiant}\\
\varphi_1 &= 44\frac{\pi}{180} && \text{1st parallel automcoque}\\
\varphi_2 &= 49\frac{\pi}{180} && \text{2nd parallel automcoque}\\
\varphi &= lat\frac{\pi}{180} && \text{latitude in radiant}\\
l &= lon\frac{\pi}{180} && \text{longitude in radiant}
\end{aligned}
$$

With

$$g_{N1} = \frac{A}{\sqrt{1-E^2\sin^2(\varphi_1)}} \tag{A.3}$$

$$g_{N2} = \frac{A}{\sqrt{1-E^2\sin^2(\varphi_2)}} \tag{A.4}$$

$$g_{l1} = \ln\left(\tan\left(\frac{\pi}{4}+\frac{\varphi_1}{2}\right)\left(\frac{1-E\sin(\varphi_1)}{1+E\sin(\varphi_1)}\right)^{E/2}\right) \tag{A.5}$$

$$g_{l2} = \ln\left(\tan\left(\frac{\pi}{4}+\frac{\varphi_2}{2}\right)\left(\frac{1-E\sin(\varphi_2)}{1+E\sin(\varphi_2)}\right)^{E/2}\right) \tag{A.6}$$

$$g_{l0} = \ln\left(\tan\left(\frac{\pi}{4}+\frac{\varphi_0}{2}\right)\left(\frac{1-E\sin(\varphi_0)}{1+E\sin(\varphi_0)}\right)^{E/2}\right) \tag{A.7}$$

$$g_{l} = \ln\left(\tan\left(\frac{\pi}{4}+\frac{\varphi}{2}\right)\left(\frac{1-E\sin(\varphi)}{1+E\sin(\varphi)}\right)^{E/2}\right) \tag{A.8}$$

$$a_n = \ln\left(\frac{g_{N2}\cos(\varphi_2)}{g_{N1}\cos(\varphi_1)}\right)\frac{1}{g_{l1}-g_{l2}} \tag{A.9}$$

$$a_c = \frac{g_{N1}\cos(\varphi_1)}{a_n e^{a_n g_{l1}}} \tag{A.10}$$

$$y_s = y_0 + a_c e^{-a_n g_{l0}}, \tag{A.11}$$

the coordinates in Lambert 93 are then given as:

$$x = x_0 + a_c e^{-a_n g_l} \sin\left(a_n(l - l_c)\right) \tag{A.12}$$

$$y = y_s - a_c e^{-a_n g_l} \cos\left(a_n(l - l_c)\right) \tag{A.13}$$

A.1.2 Lambert93 $\longrightarrow$ Geographical Coordinates

For the transform from Lambert93 to lon/lat, the longitude computation follows directly from the above equations as:

$$\text{lon} = \frac{180}{\pi}\left(\frac{\arctan(\frac{x-x_0}{y_s-y})}{a_n} + l_c\right). \tag{A.14}$$

The isometric latitude also follows from above to:

$$g_l = -\frac{1}{a_n}\log\left(\frac{x - x_0}{a_c \sin\left(a_n(\text{lon}\frac{\pi}{180} - l_c)\right)}\right) \tag{A.15}$$

The latitude φ in radiant can than be approximated by setting:

$$\varphi_{old} = 2\arctan\left(e^{g_l}\right) - \frac{\pi}{2} \tag{A.16}$$

and by iterating between

$$\varphi = 2\arctan\left(\left(\frac{1 + E\sin(\varphi_{old})}{1 - E\sin(\varphi_{old})}\right)^{E/2} e^{g_l}\right) - \frac{\pi}{2} \tag{A.17}$$

and

$$\varphi_{old} = \varphi \tag{A.18}$$

until the difference $|\varphi - \varphi_{old}|$ is insignificantly small [IGN, 1995].

A.2 Drillhole Data

Figures A.1 to A.4 show mass densities and seismic velocities revealed by the boreholes that have been analyzed in order to get (a) the relationship between mass density and seismic velocity and (b) the differentiation between consolidated and non-consolidated sediments. Table A.1 gives stratigraphic information.

ID	Name	Cenozoic						Mesozoic								Paleozoic			bot.
		Qu.	Neogene		Paleogene			Cretac.		Jurassic			Triassic			Per.	Car.	Dev.	
		Plei.	Pli.	Mio.	Oli.	Eo.	Pal.	Late	Ear.	Late	Mi.	Ear.	Late	Mi.	Ear.				
1700	**MND4**	*	-	*	*	1236	-	?	bot.	-	-	-	-	-	-	-	-	-	1597
1880	**SVT1**	-	-	-	-	-	-	?	4452	-	-	-	*	*	4594		-	bot.	4637
1952	**LCY101**	-	?	*	?	?	?	?	?	?	?	3059	?	?	3995	bot.	?	-	4002
1966	**GRE1**	-	-	-	-	-	-	*	2954	?	?	bot.	-	-	-	-	-	-	3336
1986	**OGC1**	-	-	-	-	*	1808	3965	6374	bot.	?	?	-	-	-	-	-	-	6549
1994	**ARG1**[a]	-	-	-	-	-	-	-	-	?	?	4147	bot.	?	?	-	-	-	5138
1995	**GAR1**	-	-	*	661	*	-	2149	*	bot.	?	?	-	-	-	-	-	-	3590
2014	**SZE1**	-	-	-	-	*	2483	3812	-	bot.	?	?	-	-	-	-	-	-	4200
2029	**MLG1**	-	*	388	-	*	902	3152	bot.	-	-	-	-	-	-	-	-	-	3400
2048	**MRN 1**	-	-	-	-	1420	-	?	3118	?	?	bot.	-	-	-	-	-	-	3800
2061	**LNE1**	*	-	*	722	2007 3031	2034	*	2683 3624	-	-	-	bot.	?	?	-	-	-	4244
2073	**LBG1**	-	-	*	*	*	-	2149	*	bot.	?	?	-	-	-	-	-	-	3590
2077	**TRS1**	-	-	-	-	1124	1478	?	?	-	-	-	bot.	-	-	-	-	-	4816
2086	**LVN1**	-	-	-	-	2232	2320	?	bot.	-	-	-	-	-	-	-	-	-	2350
2095	**LCB1**	-	-	*	*	536	940	?	2476	?	?	bot.	-	-	-	-	-	-	3224
2096	**CRB1**	-	-	*	*	*	1998	?	2378	bot.	?	?	-	-	-	-	-	-	2940
2107	**NAT2**	-	-	*	*	1417	-	2714	bot.	-	-	-	-	-	-	-	-	-	5452
2123	**LRN1**	-	-	*	*	1412	1665	?	2881	?	?	bot.	-	-	-	-	-	-	3150
2250	**SL3**	-	-	-	-	1107	-	?	*	bot.	?	?	-	-	-	-	-	-	2406
2298	**OLN1**	-	-	-	-	-	-	?	bot.	-	-	-	-	-	-	-	-	-	4410
2339	**LAV5**	-	-	-	-	*	*	bot.	?	-	-	-	-	-	-	-	-	-	2498
2350	**GAA1**	-	*	*	*	1320	bot.	-	-	-	-	-	-	-	-	-	-	-	1524
2371	**COG1**	*	*	*	*	*	2230	*	2420	bot.	?	?	-	-	-	-	-	-	2840
2374	**LVG1**	*	?	?	?	?	?	*	3762	bot.	?	?	-	-	-	-	-	-	3873
2410	**LAV1**	*	?	?	?	?	?	bot.	-	-	-	-	-	-	-	-	-	-	2150

Table A.1: Geological information obtained from borehole surveys. Qu.-Quarternary; Cretac.-Cretacious; Plei.-Pleistocene; Pli.-Pliocene; Mio.-Miocene; Oli.-Oligocene; Eo.-Eocene Pal-Paleocene; Per.-Permian; Car.-Carboniferous; Dev.-Devonian; Mi.-Middle; Ear.-Early, underlined-contains salt or anhydrite, bot.-bottom

[a]geological observation for ARG1 starts at 1993 m depth.

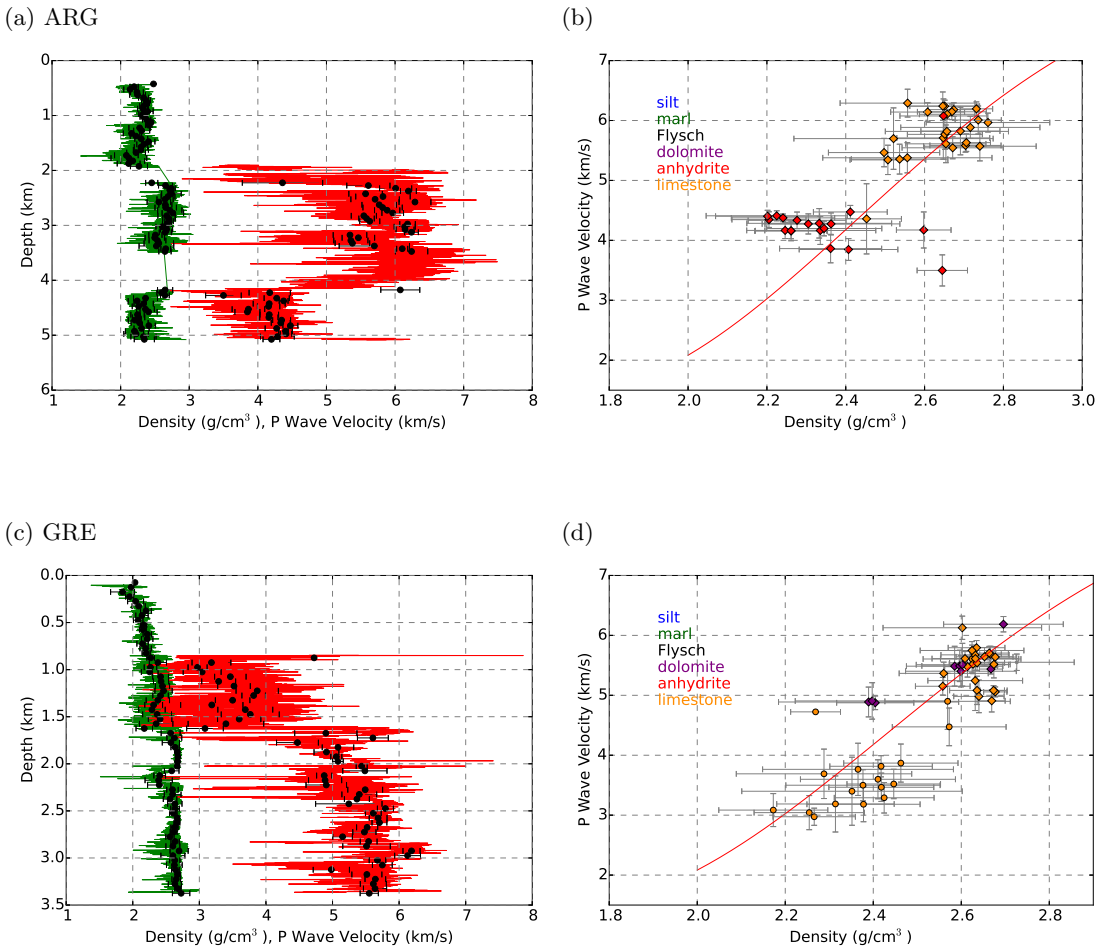

Figure A.1: Seismic P wave velocities (red) and mass densities (green) obtained from sonic and density logs. Black points show averages calculated every 50 m. Diamonds are of Mesozoic, circles of Cenozoic age. Red lines show the relationship proposed by Ludwig et al. [1970].

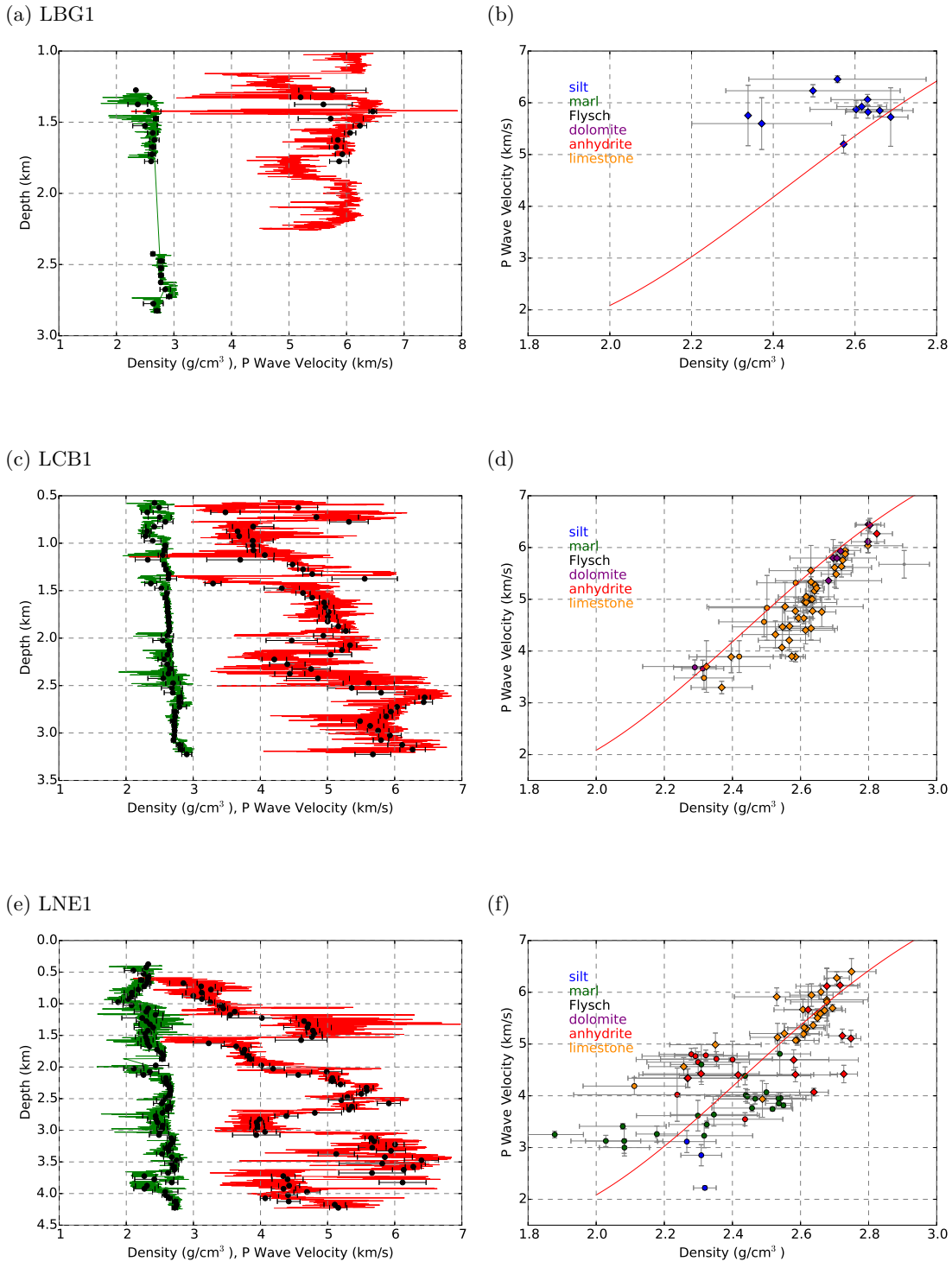

Figure A.2: Seismic P wave velocities (red) and mass densities (green) obtained from sonic and density logs. Black points show averages calculated every 50 m. Diamonds are of Mesozoic, circles of Cenozoic age. Red lines show the relationship proposed by Ludwig et al. [1970]. No Cross-plot is available for LBG1, since density and sonic logs do not cover the same depth range.

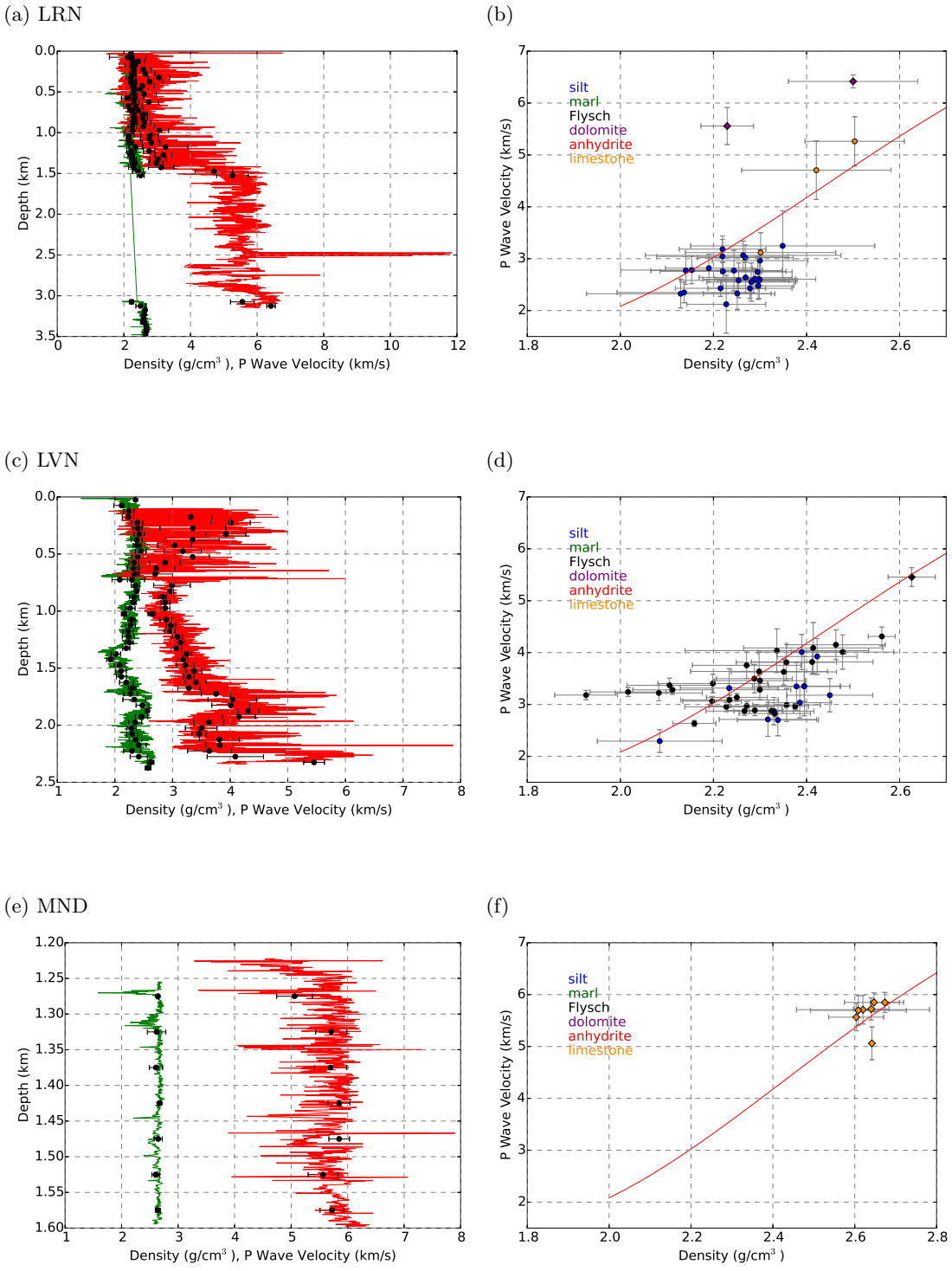

Figure A.3: Seismic P wave velocities (red) and mass densities (green) obtained from sonic and density logs. Black points show averages calculated every 50 m. Diamonds are of Mesozoic, circles of Cenozoic age. Red lines show the relationship proposed by Ludwig et al. [1970].

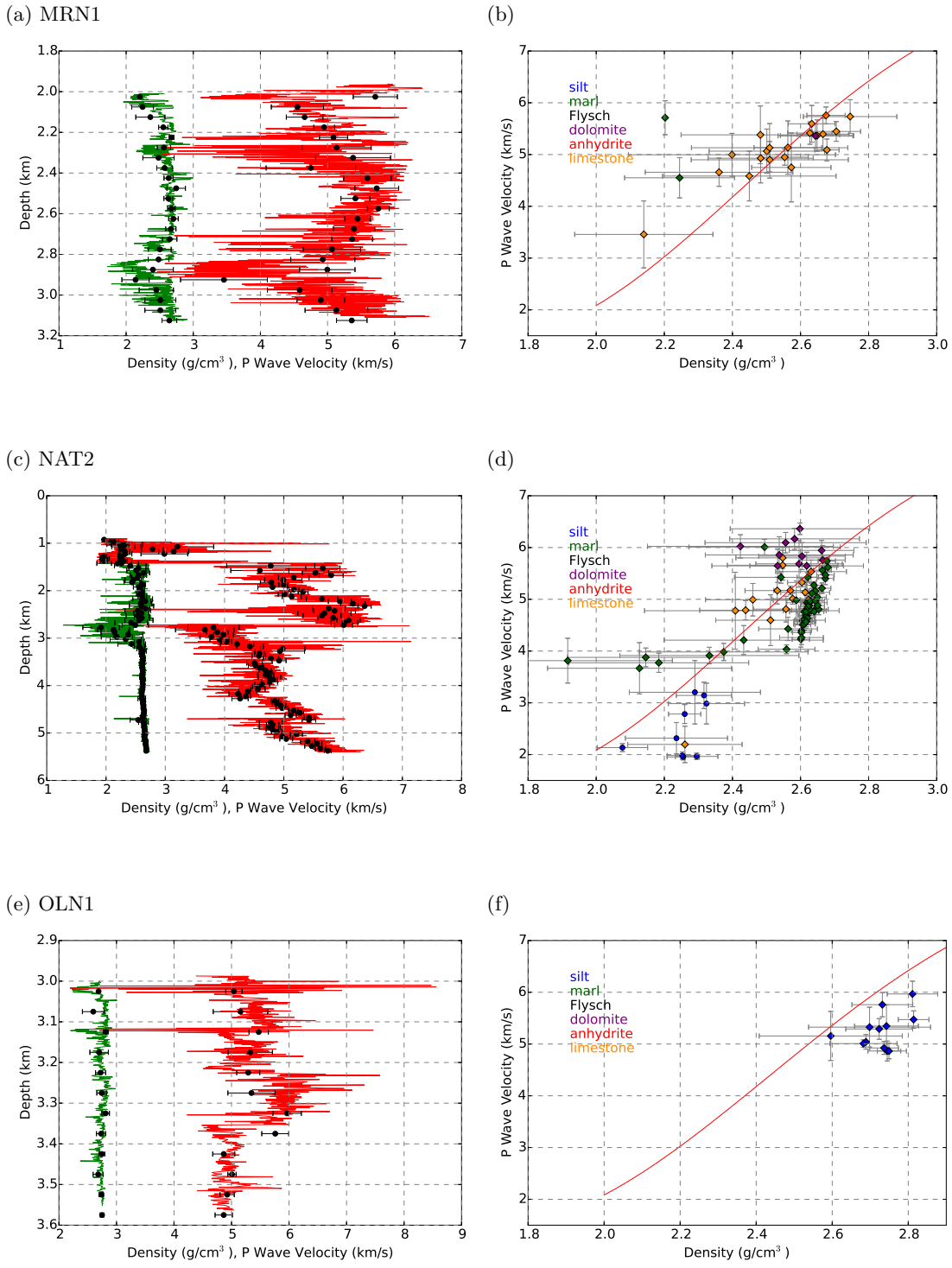

Figure A.4: Seismic P wave velocities (red) and mass densities (green) obtained from sonic and density logs. Black points show averages calculated every 50 m. Diamonds are of Mesozoic, circles of Cenozoic age. Red lines show the relationship proposed by Ludwig et al. [1970].

A.3 Stratigraphic Pile

The stratigraphic pile in `GeoModeller` does not necessarily correspond to the geological time scale. It describes the structural relations between the different units. A series is marked as 'onlap' if it deposits above another series without changing the latter's geometry (the corresponding potential field is of less consequence than the field of the series below), or it is marked as 'erode' if it may erode the series beneath (the potential field takes precedence over the field of the lower series).

Figure A.5 illustrates these relations in our 3D model. Iberian and European units are marked by the respective prefixes IB_ and EU_. The European ones are at the bottom of the `GeoModeller` pile with the crust eroding the mantle and the sediments eroding the crust. The basement then erodes European units along the NPFT. Iberian sediments overlay the basement; Iberian crust and mantle are then modeled with inverse polarization: The Iberian crust erodes the basement and remaining European units along the SPFT and is overlain by the mantle. The seawater series erodes both the Iberian and the European block beyond the coast lines. The inverse polarization of Iberian crust and mantle allows to ensure the correct geological layering with the deepest units (Iberian and European mantle) at the bottom and the uppermost series (sediments and sea water) at the top.

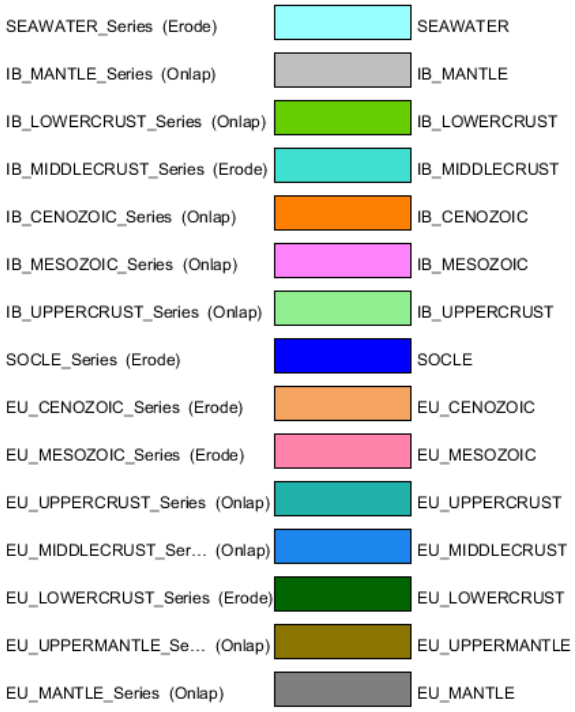

Figure A.5: Stratigraphic pile in `GeoModeller`. The Iberian units are placed above the European ones with the accretionnary prism (socle) in the collision zone eroding the European units, and the Iberian crust eroding the European crust and the basement.

A.4 3D Imaging

The following figures are meant to supplement the 3D imaging in section 5.

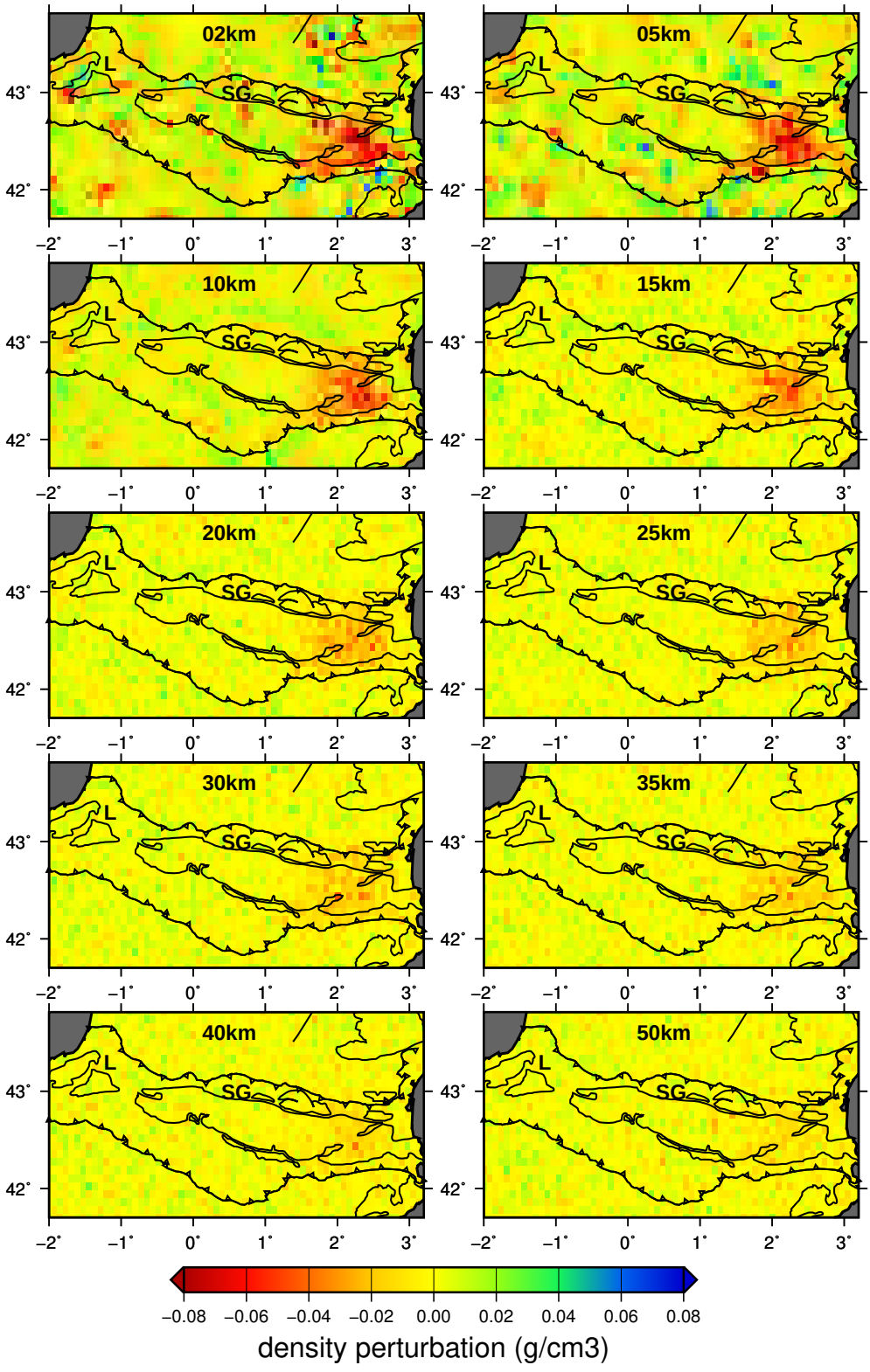

Figure A.6: Density perturbation after gravity inversion starting from Model III. Average from the last $8{\cdot}10^6$ out of $20{\cdot}10^6$ iterations.

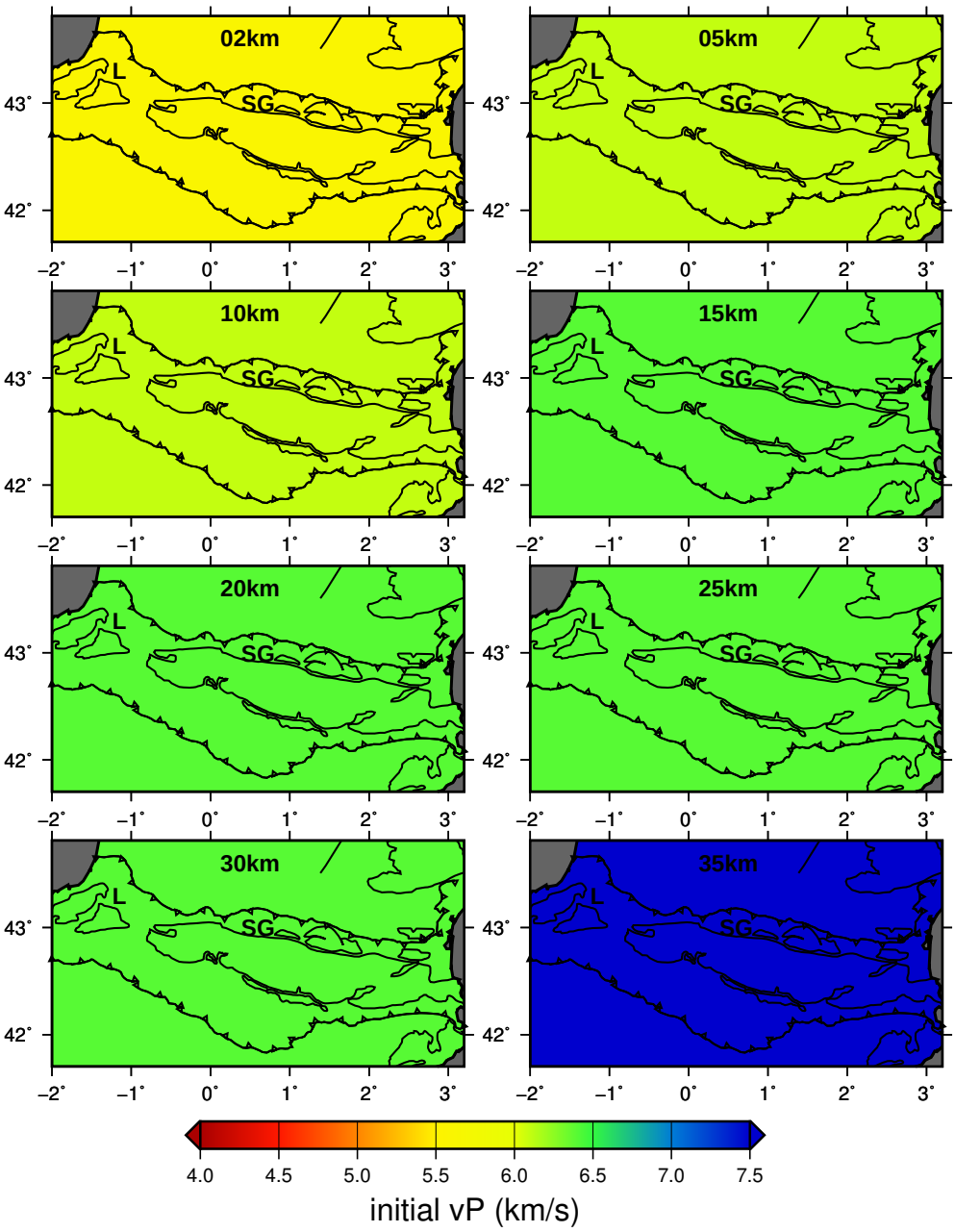

Figure A.7: P wave velocity of the 1D starting model.

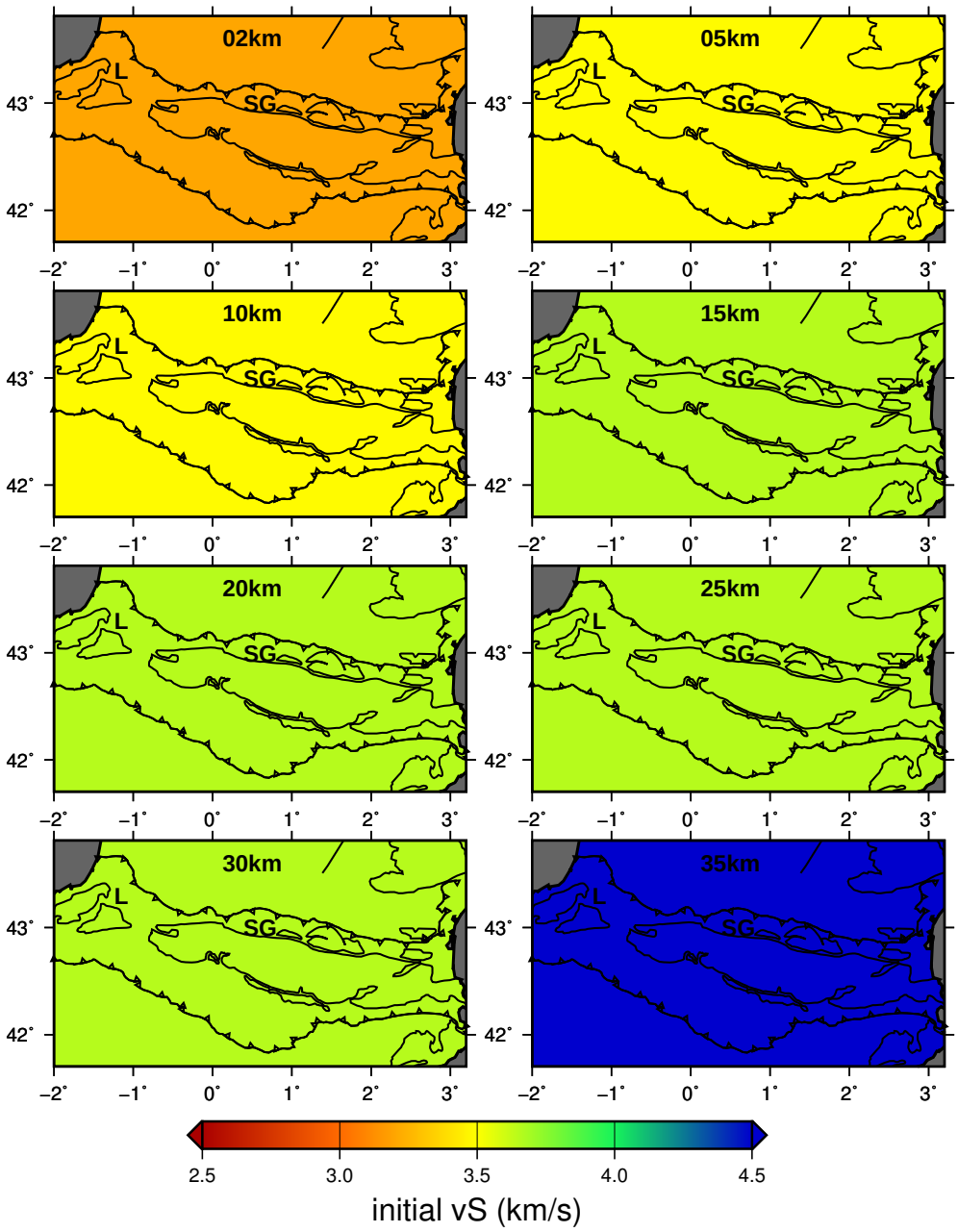

Figure A.8: S wave velocity of the 1D starting model.

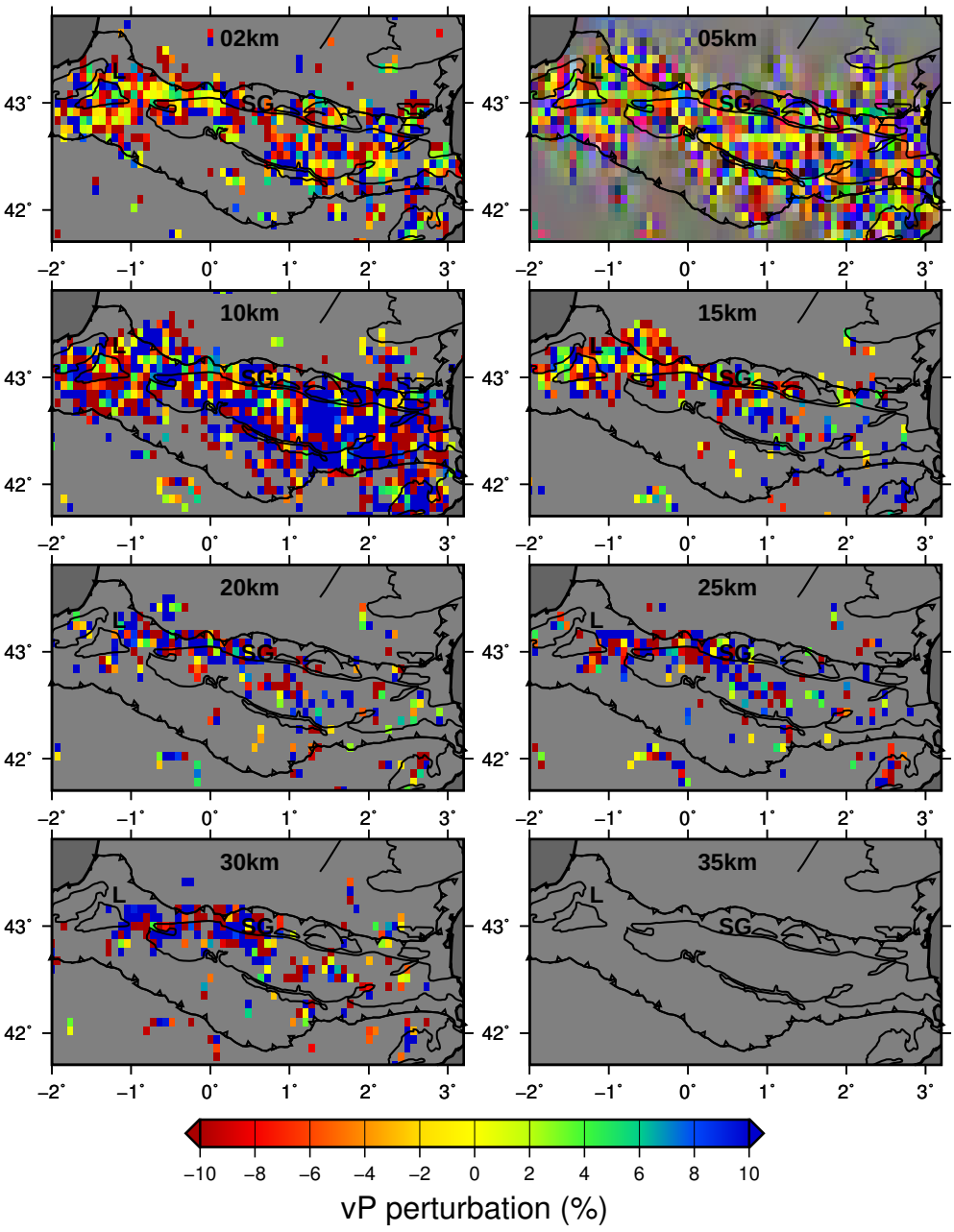

Figure A.9: P wave velocity perturbation(%) after checkerboard joint P and S wave inversion.

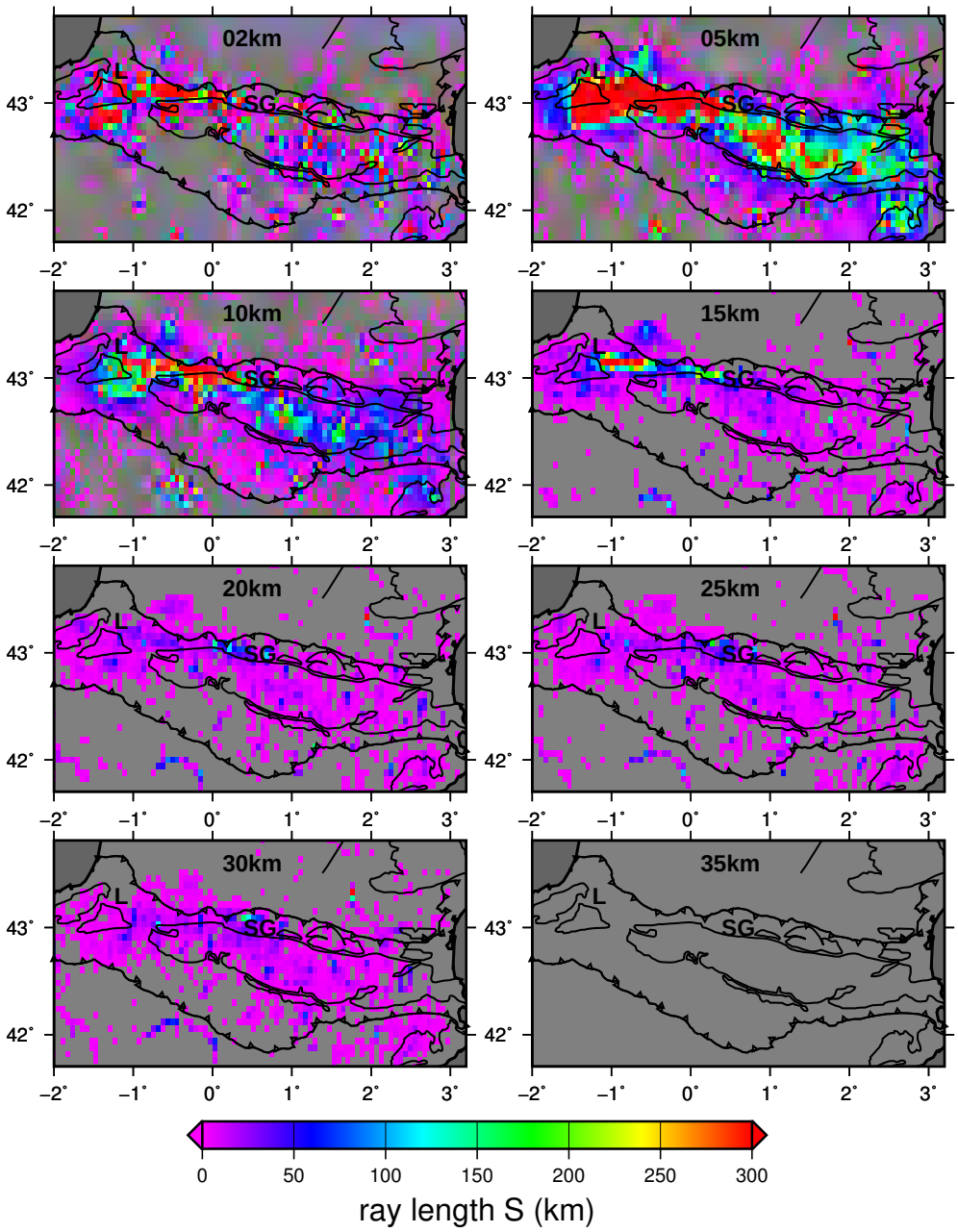

Figure A.10: Rays lengths of S waves in 1D layered velocity model.

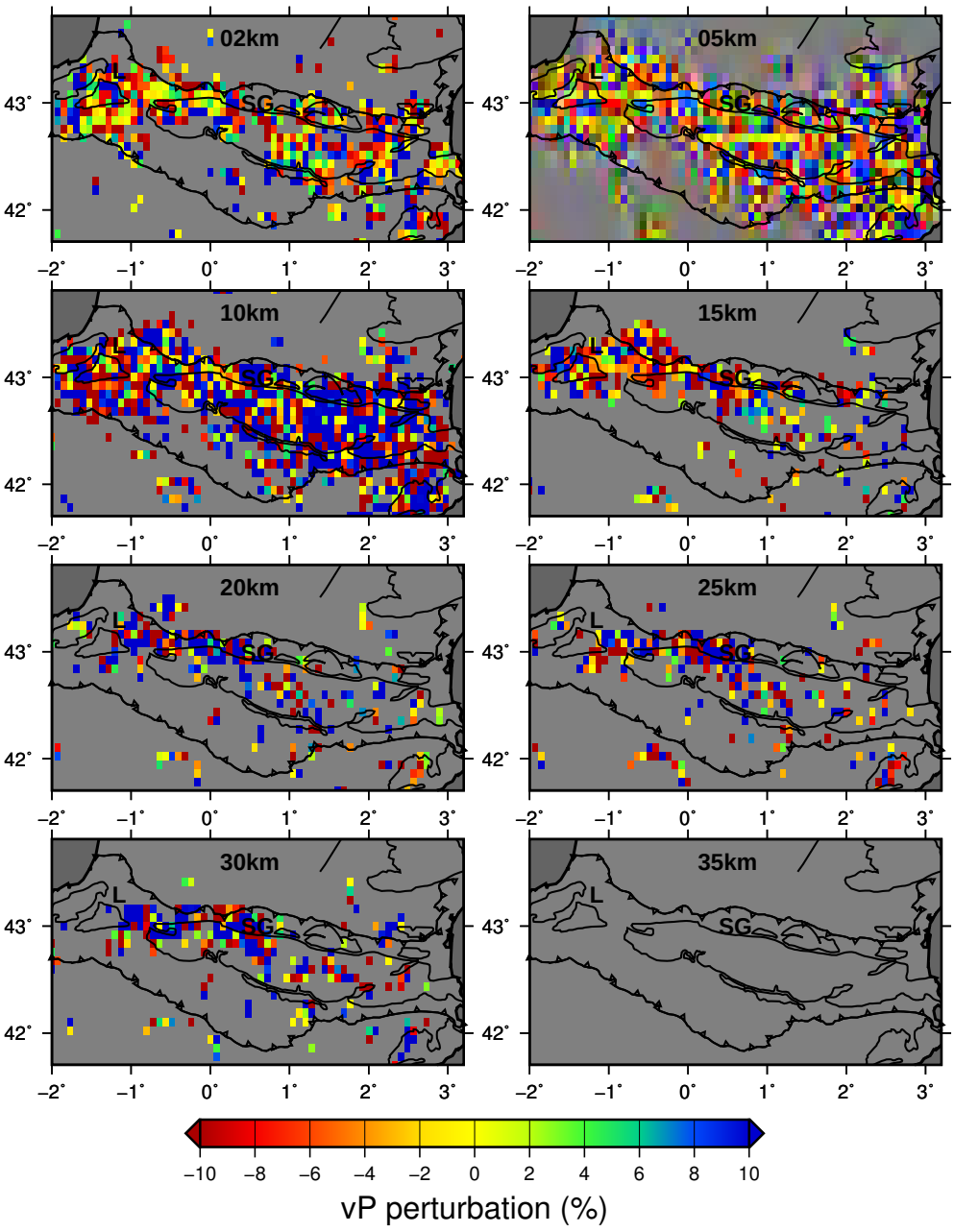

Figure A.11: Velocity perturbation(%) after checkerboard P wave inversion.

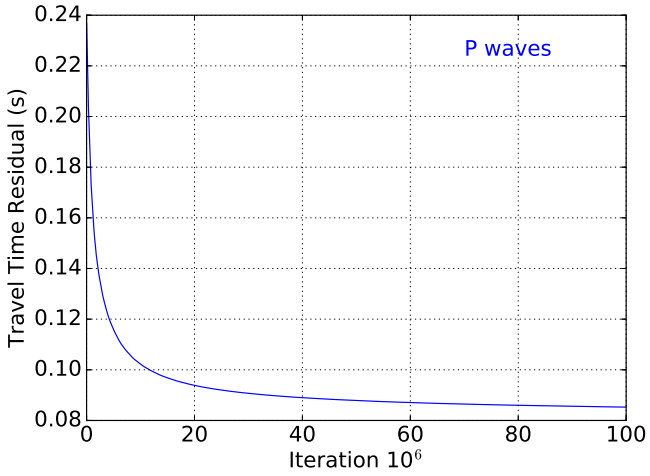

Figure A.12: Residuals from checkerboard test with P wave inversion.

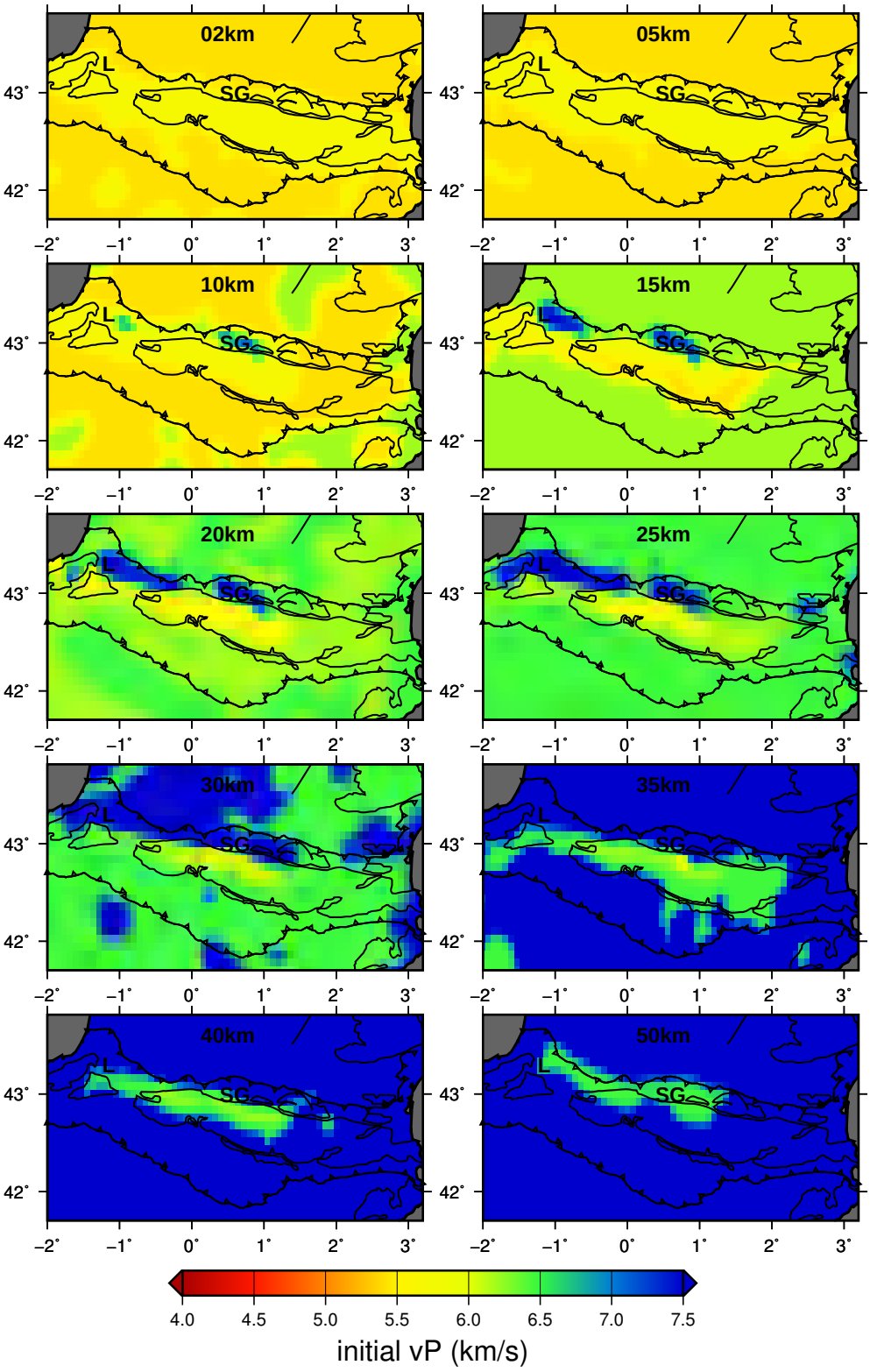

Figure A.13: P wave velocity of the 3D starting model.

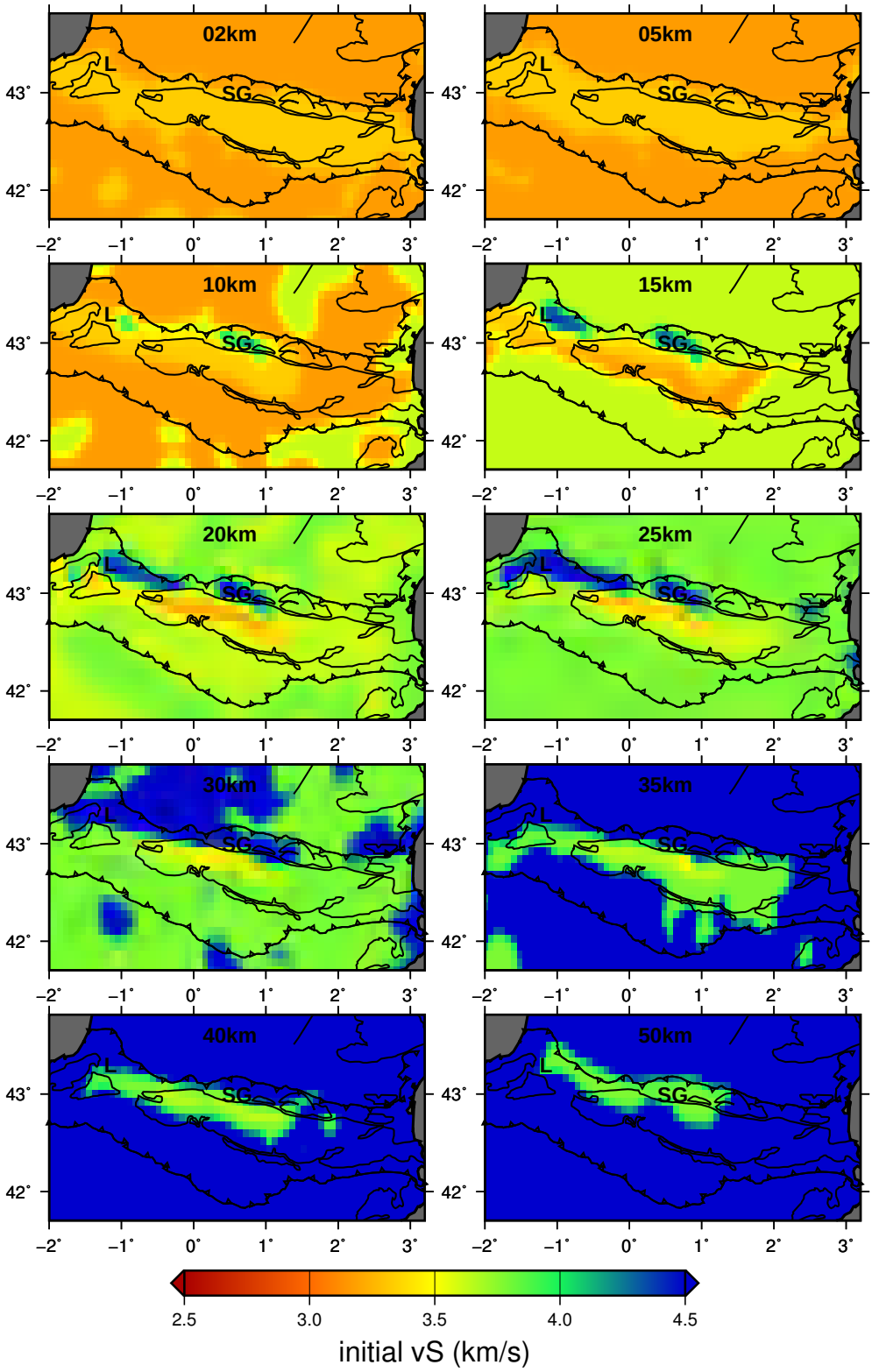

Figure A.14: S wave velocity of the 3D starting model.

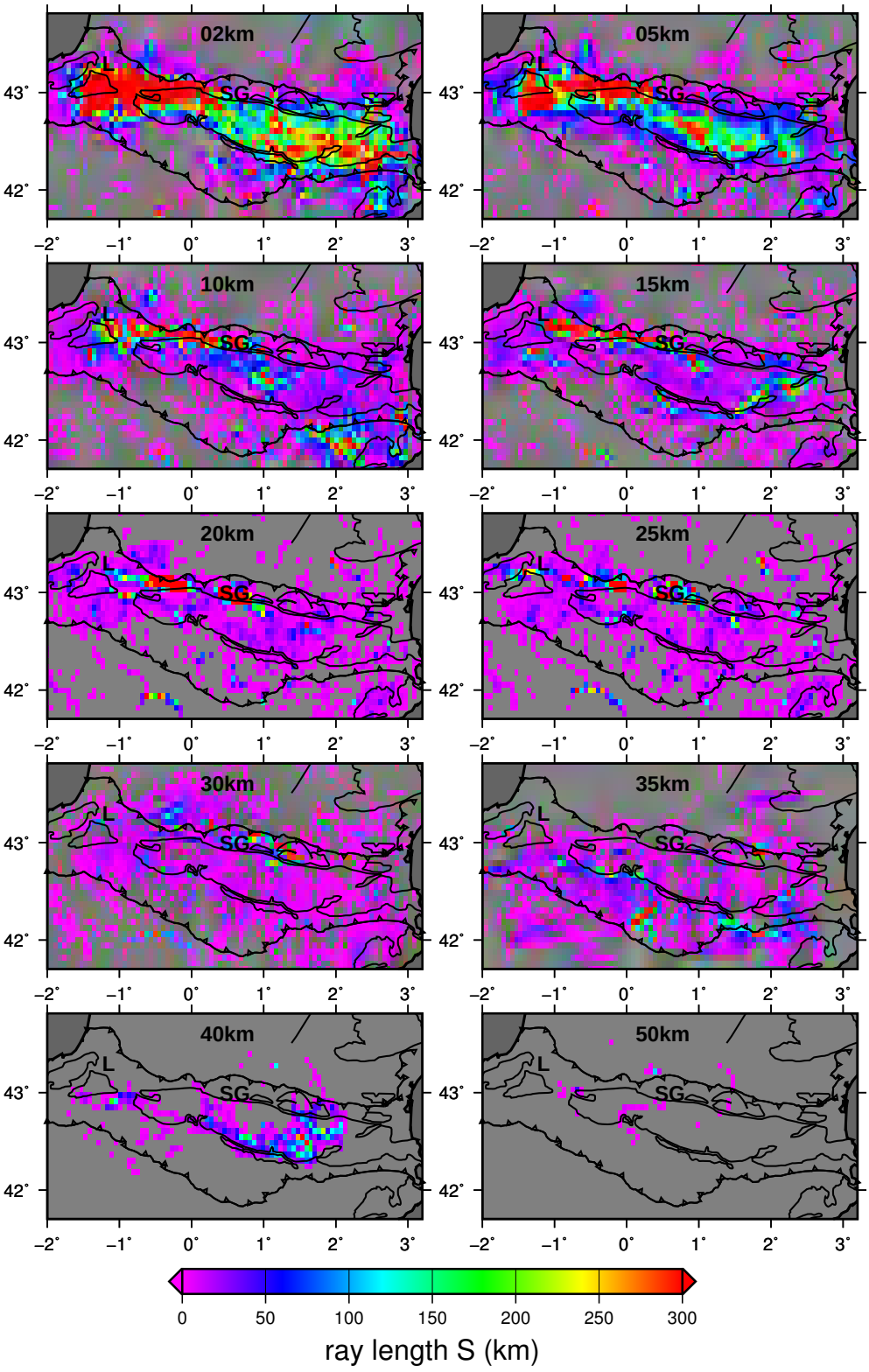

Figure A.15: Rays lengths of S waves in the 3D model.

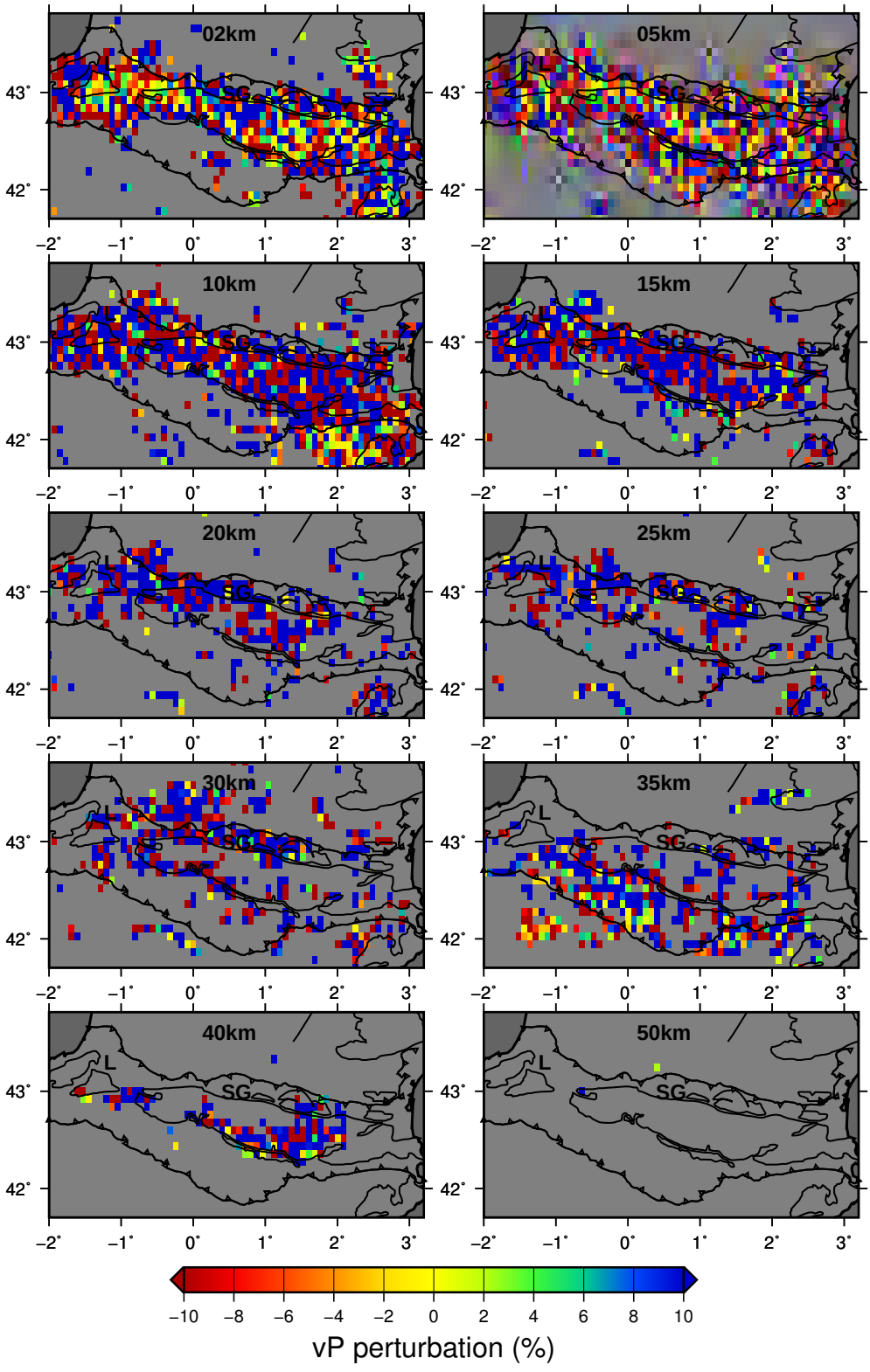

Figure A.16: Velocity perturbations (in %) after Inversion in `GeoModeller`.

Bibliography

Afnimar and Kazuki Koketsu (2000). Finite difference traveltime calculation for head waves travelling along an irregular interface. *Geophysical Journal International*, 143(3):729–734.

Asensio, E., Khazaradze, G., Echeverria, A., King, R. W., and Vilajosana, I. (2012). GPS studies of active deformation in the Pyrenees: GPS active deformation in the Pyrenees. *Geophysical Journal International*, 190(2):913–921.

Aug, C. (2004). *Modélisation géologique 3D et caractérisation des oncertitudes par la méthode du champ de potentiel*. PhD thesis, École des Mines de Paris.

Bardainne, T., Dubos-Sallée, N., Sénéchal, G., Gaillot, P., and Perroud, H. (2008). Analysis of the induced seismicity of the Lacq gas field (Southwestern France) and model of deformation. *Geophysical Journal International*, 172(3):1151–1162.

Barnett-Moore, N., Hosseinpour, M., and Maus, S. (2016). Assessing discrepancies between previous plate kinematic models of Mesozoic Iberia and their constraints: DIFFERENCES BETWEEN MODELS OF IBERIA. *Tectonics*, 35(8):1843–1862.

Barnolas, A. and Courbouleix, S. (2001). *Synthèse géologique et géophysique des Pyrénées*, volume 3 : Cycle Alpin: Phénomènes alpins. Edition BRGM, ITGE.

Barton, P. J. (1986). The relationship between seismic velocity and density in the continental crust—a useful constraint? *Geophysical Journal International*, 87(1):195–208.

Beaumont, C., Muñoz, J. A., Hamilton, J., and Fullsack, P. (2000). Factors controlling the Alpine evolution of the central Pyrenees inferred from a comparison of observations and geodynamical models. *Journal of Geophysical Research*, 105(B4):8121–8145.

Benjumea, B., Macau, A., Gabàs, A., Ledo, J., Queralt, P., and Figueras, S. (2013). Magnetotelluric and Seismic Noise Techniques Combination for the Cerdanya Basin Characterization (Eastern Pyrenees).

BGI (2012). Gravity anomalies (formulas).

Birch, F. (1952). Elasticity and constitution of the Earth's interior. *Journal of Geophysical Research*, 57(2):227–286.

Bosch, M., Guillen, A., and Ledru, P. (2001). Lithologic tomography: an application to geophysical data from the Cadomian belt of northern Brittany, France. *Tectonophysics*, 331(1-2):197–227.

Brocher, T. M. (2005). Empirical Relations between Elastic Wavespeeds and Density in the Earth's Crust. *Bulletin of the Seismological Society of America*, 95(6):2081–2092.

Bronner, A., Sauter, D., Manatschal, G., Péron-Pinvidic, G., and Munschy, M. (2011). Magmatic breakup as an explanation for magnetic anomalies at magma-poor rifted margins. *Nature Geoscience*, 4(8):549–553.

Brückl, E., Dresen, L., Edelmann, H. A. K., Fertig, J., Gaertner, H., Gelbke, C., Kirchheimer, F., Krummel, H., Liebhardt, G., Orlowsky, D., Reimers, L., Sandmeier, K.-J., Schneider, C., Utecht, T., and Witka, T. (2005). Seismik. In *Geophysik*, number 3, pages 405–706. Knödel, K., Krummel, H., Lange, G., springer-verlag berlin heidelberg edition.

Brunet, M. F. (1986). The influence of the evolution of the Pyrenees on adjacent basins. *Tectonophysics*, 129(1-4):343–354.

Calcagno, P., Chilès, J.-P., Courrioux, G., and Guillen, A. (2008). Geological modelling from field data and geological knowledge: Part I. Modelling method coupling 3d potential-field interpolation and geological rules. *Physics of the Earth and Planetary Interiors*, 171(1):147–157.

Campanyà, J., Ledo, J., Queralt, P., Marcuello, A., Liesa, M., and Muñoz, J. A. (2012). New geoelectrical characterisation of a continental collision zone in the West-Central Pyrenees: Constraints from long period and broadband magnetotellurics. *Earth and Planetary Science Letters*, 333-334:112–121.

Casas, A., Kearey, P., and Adam, C. R. (1997). Gravity nomaly map of the Pyrenean region and a comparison of the deep geological structure of the western and eastern Pyrenees. *Earth and Planetary Science Letters*, 150:65–78.

Chevrot, S., Sylvander, M., Diaz, J., Ruiz, M., Paul, A., and others (2015). The Pyrenean architecture as revealed by teleseismic P-to-S converted waves recorded along two dense transects. *Geophysical Journal International*, 200(2):1096–1107.

Chevrot, S., Villaseñor, A., Sylvander, M., Benahmed, S., Beucler, E., Cougoulat, G., Delmas, P., de Saint Blanquat, M., Diaz, J., Gallart, J., Grimaud, F., Lagabrielle, Y., Manatschal, G., Mocquet, A., Pauchet, H., Paul, A., Péquegnat, C., Quillard, O., Roussel, S., Ruiz, M., and Wolyniec, D. (2014). High-resolution imaging of the Pyrenees and Massif Central from the data of the PYROPE and IBERARRAY portable array deployments. *Journal of Geophysical Research: Solid Earth*, 119(8):6399–6420.

Chilès, J.-P., Aug, C., Guillen, A., and Lees, T. (2004). Modelling the geometry of geological units and its uncertainty in 3d from structural data: the potential-field method. In *Proceedings of International Symposium on Orebody Modelling and Strategic Mine Planning, Perth, Australia*, volume 22, page 24.

Choukroune, P. (1989). The ECORS Pyrenean deep seismic profile reflection data and the overall structure of an orogenic belt. *Tectonics*, 8(1):23–39.

Choukroune, P. (1992). Tectonic Evolution of the Pyrenees. *Annual Review of Earth and Planetary Sciences*, 20(1):143–158.

Choukroune, P. and Mattauer, M. (1978). Tectonique des plaques et Pyrenees; sur le fonctionnement

de la faille transformante nord-pyreneenne; comparaisons avec des modeles actuels. *Bulletin de la Société Géologique de France*, 7(5):689–700.

Coron, S. and Guillaume, A. (1971). Etude gravimétrique sur le Golfe de Gascoge et les Pyrénées. In *Histoire Structurale du Golfe de Gascogne*. Technip, IFP, Paris.

Courrioux, G., Nullans, S., Guillen, A., Boissonnat, J. D., Repusseau, P., Renaud, X., and Thibaut, M. (2001). 3d volumetric modelling of Cadomian terranes (Northern Brittany, France): an automatic method using Voronoı diagrams. *Tectonophysics*, 331(1):181–196.

Daignières, M., De Cabissole, B., Gallart, J., Surinach, E., and Torne, M. (1989). Geophysical constraints on the deep structure along he ECORS Pyrenees line. *Tectonics*, 8(5):1051–1058.

Daignières, M., Gallart, J., Banda, E., and Hirn, A. (1982). Implications of the seismic structure for the orogenic evolution of the Pyrenean range. *Earth and Planetary Science Letters*, 57(1):88–100.

Deramond, J., Souquet, P., Fondecave-Wallez, M.-J., and Specht, M. (1993). Relationships between thrust tectonics and sequence stratigraphy surfaces in foredeeps: model and examples from the Pyrenees (Cretaceous-Eocene, France, Spain). *Geological Society, London, Special Publications*, 71(1):193–219.

Desegaulx, P., Roure, F., and Villien, A. (1990). Structural evolution of the Pyrenees: tectonic heritage and flexural behavior of the continental crust. In *Petroleum and Tectonics in Mobile Belts*, pages 31–48. Editions TECHNIP, Paris.

Díaz, J. and Gallart, J. (2009). Crustal structure beneath the Iberian Peninsula and surrounding waters: A new compilation of deep seismic sounding results. *Physics of the Earth and Planetary Interiors*, 173(1-2):181–190.

Diaz, J., Gallart, J., and Carbonell, R. (2016). Moho topography beneath the Iberian-Western Mediterranean region mapped from controlled-source and natural seismicity surveys. *Tectonophysics*, 692:74–85.

Dubos, N., Sylvander, M., Souriau, A., Ponsolles, C., Chevrot, S., Fels, J.-F., and Benahmed, S. (2004). Analysis of the 2002 May earthquake sequence in the central Pyrenees, consequences for the evaluation of the seismic risk at Lourdes, France. *Geophysical Journal International*, 156(3):527–540.

Durá-Gómez, I. and Talwani, P. (2010). Reservoir-induced seismicity associated with the Itoiz Reservoir, Spain: a case study. *Geophysical Journal International*, 181(1):343–356.

Fabriès, J., Lorand, J.-P., and Bodinier, J.-L. (1998). Petrogenetic evolution of orogenic lherzolite massifs in the central and western Pyrenees. *Tectonophysics*, 292(1-2):145–167.

Filleaudeau, P.-Y. (2011). *Croissance et dénudation des Pyrénées du Crétacé Supérieur au Paléogène : Apports de l'analyse de bassin et thermochronométrie détritique*. PhD thesis, Université Pierre et Marie Curie - Paris VI.

Fischer, M. W. (1984). Thrust tectonics in the North Pyrenees. *Journal of structural geology*, 6(6):721–726.

Flood, W. E. and West, M. (1952). *An explaining and pronouncing dictionary of scientific and technical words: 10.000 scientific and technical words in 50 subjects explained as to a person who has little or no knowledge of the particular subject*. Longsmans, London. OCLC: 474726799.

Fomel, S., Luo, S., and Zhao, H. (2009). Fast sweeping method for the factored eikonal equation. *Journal of Computational Physics*, 228(17):6440–6455.

Fountain, D. M. (1986). Is there a relationship between seismic velocity nd heat production? *Earth and Planetary Science Letters*, 79:145–150.

Gallart, J., Banda, E., and Daignières, M. (1981). Crustal structure of the Paleozoic Axial Zone of the Pyrenees and transition to the North Pyrenean Zone. *Ann. Geoph.*, 37(3):457–480.

Gallart, J., Díaz, J., Nercessian, A., Mauffret, A., and Reis, T. D. (2001). The eastern end of the Pyrenees: seismic features at the transition to the NW Mediterranean. *Geophysical research letters*, 28(11):2277–2280.

Gardner, G. H. F., Gardner, L. W., and Gregory, A. R. (1974). Formation Velocity and Density - the Diagnostic Basics for Stratigraphic Traps. *GEOPHYSICS*, 39(6):770–780.

Grandjean, G. (1994). Study of crustal structures in a section of a mountain-range-relationship with sedimentary basins - application to western pyrenees. *BULLETIN DES CENTRES DE RECHERCHES EXPLORATION-PRODUCTION ELF AQUITAINE*, 18(2):391–419.

Guillen, A., Calcagno, P., Courrioux, G., Joly, A., and Ledru, P. (2008). Geological modelling from field data and geological knowledge. *Physics of the Earth and Planetary Interiors*, 171(1-4):158–169.

Gunnell, Y., Zeyen, H., and Calvet, M. (2008). Geophysical evidence of a missing lithospheric root beneath the Eastern Pyrenees: Consequences for post-orogenic uplift and associated geomorphic signatures. *Earth and Planetary Science Letters*, 276(3-4):302–313.

Havskov, J. and Ottemoller, L. (2010). *Routine Data Processing in Earthquake Seismology: With Sample Data, Exercises and Software*. Springer Science & Business Media.

Hirn, A., Daignières, M., Gallart, J., and Vadell, M. (1980). Explosion seismic souding of throws and dips in the continental Moho. *Geophysical Research Letters*, 7(4):263–266.

Hole, J. A. and Zelt, B. C. (1995). 3-D finite-difference reflection travel times. *Geophysical Journal International*, 121(2):427–434.

Holstein, H. (2003). Gravimagnetic anomaly formulas for polyhedra of spatially linear media. *GEOPHYSICS*, 68(1):157–167.

IGN, I. G. N. (1995). Algorithmes néccessaires à la projection carthographique conique conforme de Lambert. Notes Techniques NT/G 71.

Jammes, S., Manatschal, G., Lavier, L., and Masini, E. (2009). Tectonosedimentary evolution related to extreme crustal thinning ahead of a propagating ocean: Example of the western Pyrenees: EXTREME CRUSTAL THINNING IN THE PYRENEES. *Tectonics*, 28(4):n/a–n/a.

Lajaunie, C., Courrioux, G., and Manuel, L. (1997). Foliation fields and 3d cartography in geology: principles of a method based on potential interpolation. *Mathematical Geology*, 29(4):571–584.

Lay, T. and Wallace, T. C. (1995). *Modern Global Seismology*. Academic Press.

Le Pichon, X., Bonnin, J., Francheteau, J., and Sibuet, J. (1971). Une hypothèse d'évolution tectonique du golfe de gascogne. *Histoire structurale du Golfe de Gascogne*, 2:1–44.

Le Pichon, X. and Sibuet, J.-C. (1971). Western extension of boundary between European and Iberian plates during the Pyrenean orogeny. *Earth and Planetary Science Letters*, 12(1):83–88.

Leroux, E., Rabineau, M., Aslanian, D., Gorini, C., Molliex, S., Bache, F., Robin, C., Droz, L., Moulin, M., Poort, J., Rubino, J.-L., and Suc, J.-P. (2015). High resolution evolution of terrigenous sediment yields in the Provence Basin during the last 6 Ma: relation with climate and tectonics. *Basin Research*.

Lindner, H. and Casten, U. (2005). Gravimetrie. In Knödel, D. K., Krummel, H., and Lange, G., editors, *Geophysik*, number 3, pages 43–69. Springer Berlin Heidelberg.

Lowrie, W. (2007). *Fundamentals of Geophysics*. Cambridge University Press.

Ludwig, W. J., Nafe, J. E., and Drake, C. L. (1970). Seismic refraction. In *The Sea, Maxwell, A. E. (Editor)*, volume 4, pages 53–84. Wiley-Interscience, New York.

Martelet, G., Calcagno, P., Gumiaux, C., Truffert, C., Bitri, A., Gapais, D., and Brun, J. (2004). Integrated 3d geophysical and geological modelling of the Hercynian Suture Zone in the Champtoceaux area (south Brittany, France). *Tectonophysics*, 382(1-2):117–128.

Martín González, F. (2011). Geometría, estructuras y evolución de la terminación occidental de los relieves del Orógeno Alpino-Pirenaico (NO Península Ibérica). *Journal of Iberian Geology*, 37(2).

Mattauer, M. (1968). Les traits structuraux essentiels de la chaîne pyrénéenne. *Rev. Geogr. Phys. Geol. Dyn.*, 10(3).

Metropolis, N., Rosenbluth, A. W., Rosenbluth, M. N., Teller, A. H., and Teller, E. (1953). Equation of State Calculations by Fast Computing Machines. *The Journal of Chemical Physics*, 21(6):1087–1092.

Monteiller, V., Got, J.-L., Virieux, J., and Okubo, P. (2005). An efficient algorithm for double-difference tomography and location in heterogeneous media, with an application to the Kilauea volcano. *Journal of Geophysical Research*, 110(B12).

Montigny, R., Azambre, B., Rossy, M., Thuisat, R., and Boutin, R. (1992). New 40ar-39ar data on time relationships between hot spot activity, lherzolite ascent, and metamorphism in the Cretaceous rift of the Pyrenees. *Abstract to EUG VII Meeting*, page 429.

Mosegaard, K. and Tarantola, A. (1995). Monte Carlo Sampling of Solutions to Inverse Problems. *Journal of Geophysical Research*, 100(B7):12,431–12,447.

Mouthereau, F., Filleaudeau, P.-Y., Vacherat, A., Pik, R., Lacombe, O., Fellin, M. G., Castelltort, S., Christophoul, F., and Masini, E. (2014). Placing limits to shortening evolution in the Pyrenees: Role of margin architecture and implications for the Iberia/Europe convergence: Plate convergence in the Pyrenees. *Tectonics*, 33(12):2283–2314.

Muñoz, J. A. (1992). Evolution of a continental collision belt: ECORS-Pyrenees crustal balanced cross-section. In McClay, K. R., editor, *Thrust Tectonics*, pages 235–246. Springer Netherlands, Dordrecht. DOI: 10.1007/978-94-011-3066-0_21.

Nafe, J. E. and Drake, C. L. (1957). Variation with depth in shallow and deep water marine sedients of porosity, density and the velocities of compressional and shear waves. *GEOPHYSICS*, XXII(3):523–552.

NIMA (1997). Department of Defense World Geodetic System 198,. Its definition and Relationships with Local Geoditic Systems. Technical Report TR8350.2, National Imagery and Mapping Agency.

Noble, M., Gesret, A., and Belayouni, N. (2014). Accurate 3-D finite difference computation of traveltimes in strongly heterogeneous media. *Geophysical Journal International*, 199(3):1572–1585.

Nocquet, J.-M. (2012). Present-day kinematics of the Mediterranean: A comprehensive overview of GPS results. *Tectonophysics*, 579:220–242.

Nocquet, J.-M. and Calais, E. (2003). Crustal velocity field of western Europe from permanent GPS array solutions, 1996–2001. *Geophysical Journal International*, 154(1):72–88.

Nocquet, J.-M. and Calais, E. (2004). Geodetic Measurements of Crustal Deformation in the Western Mediterranean and Europe. *Pure and Applied Geophysics*, 161(3):661–681.

Okabe, M. (1979). ANALYTICAL EXPRESSIONS FOR GRAVITY-ANOMALIES DUE TO HOMOGENEOUS POLYHEDRAL BODIES AND TRANSLATIONS INTO MAGNETIC-ANOMALIES. *GEOPHYSICS*, 44(4):730–741.

Paige, C. C. and Saunders, M. A. (1982). LSQR: An algorithm for sparse linear equations and sparse least squares. *ACM Transactions on Mathematical Software (TOMS)*, 8(1):43–71.

Parasnis, D. S. (1997). *Principles of Applied Geophysics*. Springer Science & Business Media, fifth edition.

Pellen, R., Aslanian, D., Rabineau, M., Leroux, E., Gorini, C., Silenziario, C., Blanpied, C., and Rubino, J.-L. (2016). The Minorca Basin: a buffer zone between the Valencia and Liguro-Provençal Basins (NW Mediterranean Sea). *Terra Nova*, 28(4):245–256.

Perrier, G. and Ruegg, J. C. (1973). Structure profonde du Massif Central français. *Ann. Geoph.*, 29:435–502.

Plouff, D. (1976). GRAVITY AND MAGNETIC-FIELDS OF POLYGONAL PRISMS AND APPLICATION TO MAGNETIC TERRAIN CORRECTIONS. *GEOPHYSICS*, 41(4):727–741.

Podvin, P. and Lecomte, I. (1991). Finite difference computation of traveltimes in very contrasted velocity models: a massively parallel approach and its associated tools. *Geophysical Journal International*, 105(1):271–284.

Pous, J., Ledo, J., Marcuello, A., and Daignières, M. (1995). Electrical resistivity model of the crust and upper mantle from a magnetotelluric survey through the central Pyrenees. *Geophysical Journal International*, 121(3):750–762.

Press, W. H., Teukolsky, S. A., Vetterling, W. T., and Flannery, B. P. (2003). *Numerical recipes in Fortran 77: the art of scientific computing*. Number the art of scientific computing / William H. Press ... ; Vol. [1,1] in Numerical recipes in FORTRAN. Cambridge Univ. Press, Cambridge, 2. ed., reprinted with corr edition.

Rigo, A., Vernant, P., Feigl, K. L., Goula, X., Khazaradze, G., Talaya, J., Morel, L., Nicolas, J., Baize, S., Chery, J., and Sylvander, M. (2015). Present-day deformation of the Pyrenees revealed by GPS surveying and earthquake focal mechanisms until 2011. *Geophysical Journal International*, 201(2):947–964.

Rivero, L., Pinto, V., and Casas, A. (2002). Moho Depth Structure Of The Eastern Pyrenean Belt derived from Gravity Data. *Journal of Geodynamics*, 33:315–332.

Romanowicz, B. and Dziewonski, A. (2010). *Seismology and Structure of the Earth: Treatise on Geophysics*. Elsevier. Google-Books-ID: 5DEBDsisDEQC.

Rosenbaum, G., Lister, G. S., and Duboz, C. (2002). Relative motions of Africa, Iberia and Europe during Alpine orogeny. *Tectonophysics*, 359(1):117–129.

Roure, F., Choukroune, P., Berastegui, X., Muñoz, J., Villien, A., Matheron, P., Bareyt, M., Seguret, M., Camara, P., and Deramond, J. (1989). Ecors Deep Seismic Data and Balanced Cross Sections: Geometric Constraints on the Evolution of the Pyrenees. *Tectonics*, 8(1):41–50.

Ruiz, M., Díaz, J., Gallart, J., Pulgar, J. A., González-Cortina, J. M., and López, C. (2006a).

Seismotectonic constraints at the western edge of the Pyrenees: aftershock series monitoring of the 2002 February 21, 4.1 Lg earthquake. *Geophysical Journal International*, 166(1):238–252.

Ruiz, M., Gaspà, O., Gallart, J., Díaz, J., Pulgar, J., García-Sansegundo, J., López-Fernández, C., and González-Cortina, J. (2006b). Aftershocks series monitoring of the September 18, 2004 M=4.6 earthquake at the western Pyrenees: A case of reservoir-triggered seismicity? *Tectonophysics*, 424(3-4):223–243.

Rybach, L. and Buntebarth, G. (1982). Relationships between the petrophysical properties density, seismic velocity, heat generation, ans mineralogical constitution. *Earth and Planetary Science Letters*, 57:367–376.

Santolaria, P., Casas-Sainz, A. M., Soto, R., and Casas, A. (2017). Gravity modelling to assess salt tectonics in the western end of the south pyrenean central unit. *Journal of the Geological Society*, 174(2):269–288.

Sapin, M. and Hirn, A. (1974). Results of explosion seismology in the Southern Rhone Valley. *Ann. Geoph.*, 30:171–202.

Sapin, M. and Prodehl, C. (1973). Long-range profiles in Western Europe: I. Crustal structure between the Bretagne and the Central Massif of France. *Ann. Geoph.*, 29:127–145.

Sen, M. K. and Stoffa, P. L. (2013). *Global Optimization Methods in Geophysical Inversion*. Cambridge University Press. Google-Books-ID: FVshAwAAQBAJ.

Serrano, O., Delmas, J., Hanot, F., Vially, R., Herbin, J., Houel, P., and Tourlière, B. (2006). *Le Bassin d'Aquitaine : valorisation des données sismiques, cartographie structurale et potentiel pétrolier*. BRGM.

Sibuet, J.-C., Srivastava, S. P., and Spakman, W. (2004). Pyrenean orogeny and plate kinematics: PYRENEAN OROGENY AND PLATE KINEMATICS. *Journal of Geophysical Research: Solid Earth*, 109(B8).

Slawinski, R. A. and Slawinski, M. A. (1999). On Raytracing in Constant Velocity-Gradient Media: Calculus Approach. *Canadian Journal of Exploration Geophisics*, 35(1/2):24–27.

Sleep, N. and Fujita, K. (1997). *Principles of Geophysics*. Wiley.

Souriau, A. and Pauchet, H. (1998). A new synthesis of Pyrenean seismicity and its tectonic implications. *Tectonophysics*, 290(3):221–244.

Sylvander, M., Souriau, A., Rigo, A., Tocheport, A., Toutain, J.-P., Ponsolles, C., and Benahmed, S. (2008). The 2006 November, $M_{\,l} = 5.0$ earthquake near Lourdes (France): new evidence for NS extension across the Pyrenees. *Geophysical Journal International*, 175(2):649–664.

Team, Q. D. (2016). QGIS Geographic Information System.

Teixell, A. (1998). Crustal structure and orogenic material budget in the west central Pyrenees. *Tectonics*, 17(3):395–406.

Teixell, A., Labaume, P., and Lagabrielle, Y. (2016). The crustal evolution of the west-central Pyrenees revisited: Inferences from a new kinematic scenario. *Comptes Rendus Geoscience*, 348(3-4):257–267.

Theunissen, T., Chevrot, S., Sylvander, M., Monteiller, V., Calvet, M., Villaseñor, A., Benahmed, S., Pauchet, H., and Grimaud, F. (2017). Absolute earthquake locations using 3-D versus 1-D velocity models below a local seismic network: example from the Pyrenees. *Geophysical Journal International*.

Torné, M., De Cabissole, B., Bayer, R., Casas, A., Daignières, M., and Rivero, A. (1989). Gravity constraints on the deep structure of the Pyrenean belt along the ECORS profile. *Tectonophysics*, 165(1):105–116.

Tucholke, B. E. and Sibuet, J.-C. (2012). Problematic plate reconstruction. *Nature Geoscience*, 5(10):676–677.

Tugend, J., Manatschal, G., Kusznir, N. J., Masini, E., Mohn, G., and Thinon, I. (2014). Formation and deformation of hyperextended rift systems: Insights from rift domain mapping in the Bay of Biscay-Pyrenees. *Tectonics*, 33(7):1239–1276.

Twiss, R. J. and Moores, E. M. (2007). *Structural geology*. W.H. Freeman, New York, NY, 2nd ed edition.

Vacher, P. and Souriau, A. (2001). A three-dimensional model of the Pyrenean deep structure based on gravity modelling, seismic images and petrological constraints. *Geophysical Journal International*, 145(2):460–470.

Van der Voo, R. and Zijderveld, J. D. A. (1971). Renewed Paleomagnetic Study of the Lisbon Volcanics and Implications fot The Rotation of the Iberian Peninsula. *Journal of Geophysical Research*, 76(17):3913–3921.

Vanderhaeghe, O. and Grabkowiak, A. (2014). Tectonic accretion and recycling of the continental lithosphere during the Alpine orogeny along the Pyrenees. *Bulletin de la Societe Geologique de France*, 185(4):257–277.

Vassal, P. and Derenne, J.-L. (2013). Référentiel Géologique de la France. *géorama Le journal d'information du BRGM*, 28.

Velasque, P. C., Ducasse, L., Muller, J., and Scholten, R. (1989). The influence of inherited extensional structures on the tectonic evolution of an intracratonic chain: the example of the Western Pyrenees. *Tectonophysics*, 162(3):243–264.

Vergés, J., Fernàndez, M., and Martìnez, A. (2002). The Pyrenean orogen: pre-, syn-, and post-collisional evolution. *Journal of the Virtual Explorer*, 08.

Vergés, J., Millán, H., Roca, E., Muñoz, J. A., Marzo, M., Cirés, J., Den Bezemer, T., Zoetemeijer, R., and Cloetingh, S. (1995). Eastern Pyrenees and related foreland basins: pre-, syn-and post-collisional crustal-scale cross-sections. *Marine and Petroleum geology*, 12(8):903–915.

Vidale, J. E. (1990). Finite-difference calculation of traveltimes in three dimensions. *Geaophysics*, 55(5):521–525.

Vissers, R. and Meijer, P. (2012). Mesozoic rotation of Iberia: Subduction in the Pyrenees? *Earth-Science Reviews*, 110(1-4):93–110.

Wang, Y., Chevrot, S., Monteiller, V., Komatitsch, D., Mouthereau, F., Manatschal, G., Sylvander, M., Diaz, J., Ruiz, M., Grimaud, F., Benahmed, S., Pauchet, H., and Martin, R. (2016). The deep roots of the western Pyrenees revealed by full waveform inversion of teleseismic P waves. *Geology*, 44(6):475–478.

Wortel, M. J. R. and Spakman, W. (2000). Subduction And Slab Detachment In The Mediterranean-Carpathian Region. *SCIENCE'S COMPASS*, 290.

Zhdanov, M. S. (2015). *Inverse Theory and Applications in Geophysics*. Elsevier. Google-Books-ID: L0ibBwAAQBAJ.

Author: Hannah Wehr

Title: 3D Modeling of the Pyrenees based on Geological, Gravimetric, and Seismic Data

Doctoral advisor: Sébastien Chevrot

Place and date of the defence : Toulouse, 6 December 2017

A three-dimensional geological model of the Pyrenees and their foreland basins is constructed with the GeoModeller software. This model accounts for all the geological and geophysical information available and covers the whole Pyrenees, from the Atlantic Ocean to the Mediterranean Sea, and from the Iberian Range to the Massif Central, down to 70 km depth. It is able to explain main features of Bouguer gravity anomalies and of seismic travel times. 3D inversion is performed to refine this model. Joint geological and geophysical modeling and inversion reveal differences in the crustal structure between the western and central Pyrenees and the eastern Pyrenees. They show furthermore the presence of exhumed mantle material enclosed in the crust beneath the Labourd Massif and Saint-Gaudens, as well as the necessity of a low density anomalie in the eastern Pyrenees.

Keywords: Pyrenees, 3D Modeling, Probabilistic Inversion, GeoModeller, Bouguer anomaly, Seismic travel time computation

---

Discipline: Earth and Planetary Sciences

Laboratory:

Géosciences Environnement Toulouse (UMR 5563)

14, avenue Edouard Belin

31400 Toulouse

Auteur : Hannah Wehr

Titre : Modélisation des Pyrénées à partir des données géologiques, gravimétriques et sismiques

Directeur de thèse : Sébastien Chevrot

Lieu et date de soutenance : Toulouse, le 06 décembre 2017

Un modèle géologique tridimensionnel des Pyrénées et de leurs bassins d'avant-pays est construit avec le logiciel GeoModeller. Ce modèle tient compte de toutes les informations géologiques et géophysiques disponibles et couvre l'ensemble des Pyrénées, de l'Océan Atlantique à la Mer Méditerranée, et de la Chaîne Ibérique au Massif Central, jusqu'à 70 km de profondeur. Il est capable d'expliquer les principales caractéristiques des anomalies de Bouguer et des temps de trajet sismiques. Des inversions 3D sont réalisées pour affiner ce modèle. La modélisation et l'inversion géologiques et géophysiques révèlent des différences dans la structure crustal entre les Pyrénées occidentales et centrales et les Pyrénées orientales. Elles montrent en outre la présence de manteau exhumé et enfermé dans la croûte sous le Massif du Labourd et à Saint-Gaudens ainsi que la nécessité d'une anomalie de faible densité dans les Pyrénées orientales.

Mots clés : Pyrénées, Modélisation 3D, Inversion stochastique, GeoModeller, Anomalie Bouguer, Temps de Trajet Sismiques

---

Discipline administrative : Sciences de la Terre et des Planètes Solides

---

Laboratoire :

Géosciences Environnement Toulouse (UMR 5563)

14, avenue Edouard Belin

31400 Toulouse